

Title	Crystal Engineering of Porous Lanthanide Coordination Polymers with Multicarboxylate Ligands
Author(s)	Thammakan, Supaphorn
Citation	大阪大学, 2023, 博士論文
Version Type	VoR
URL	https://doi.org/10.18910/92173
rights	Reproduced in part with permission from Thammakan S., Rodlamul P., Semakul N., et al. Gas Adsorption, Proton Conductivity, and Sensing Potential of a Nanoporous Gadolinium Coordination Framework. <i>Inorganic Chemistry</i> 59, 3053 (2020); https://doi.org/10.1021/acs.inorgchem.9b03395 . Copyright 2020 American Chemical Society.
Note	

Osaka University Knowledge Archive : OUKA

<https://ir.library.osaka-u.ac.jp/>

Osaka University

**CRYSTAL ENGINEERING OF POROUS
LANTHANIDE COORDINATION POLYMERS
WITH MULTICARBOXYLATE LIGANDS**

SUPAPHORN THAMMAKAN

**DOCTOR OF PHILOSOPHY
IN CHEMISTRY**

**GRADUATE SCHOOL
CHIANG MAI UNIVERSITY**

2023

**CRYSTAL ENGINEERING OF POROUS
LANTHANIDE COORDINATION POLYMERS
WITH MULTICARBOXYLATE LIGANDS**

SUPAPHORN THAMMAKAN

**DOCTOR OF PHILOSOPHY
IN SCIENCE**

**DEPARTMENT OF CHEMISTRY
GRADUATE SCHOOL OF SCIENCE
OSAKA UNIVERSITY**

2023

**CRYSTAL ENGINEERING OF POROUS LANTHANIDE
COORDINATION POLYMERS WITH
MULTICARBOXYLATE LIGANDS**

SUPAPHORN THAMMAKAN

**A THESIS SUBMITTED TO CHIANG MAI UNIVERSITY AND OSAKA
UNIVERSITY IN PARTIAL FULFILLMENT OF THE REQUIREMENTS FOR
THE DEGREE OF DOCTOR OF PHILOSOPHY**

**GRADUATE SCHOOL, CHIANG MAI UNIVERSITY AND GRADUATE
SCHOOL, OSAKA UNIVERSITY**


2023

**CRYSTAL ENGINEERING OF POROUS LANTHANIDE
COORDINATION POLYMERS WITH
MULTICARBOXYLATE LIGANDS**

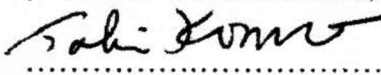
SUPAPHORN THAMMAKAN

THIS THESIS HAS BEEN APPROVED TO BE A PARTIAL FULFILLMENT OF
THE REQUIREMENTS FOR THE DEGREE OF
DOCTOR OF PHILOSOPHY
IN CHEMISTRY

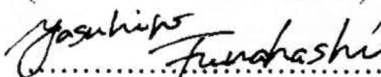
Examination Committee:

..... Chairman


(Prof. Dr. Naoto Ishikawa)

..... Member

(Prof. Dr. Takumi Konno)

..... Member

(Prof. Dr. Yasuhiro Funahashi)

..... Member

(Assoc. Prof. Dr. Apinpus Rujiwatra)


..... Member

(Assoc. Prof. Dr. Piyarat Nimmanpipug)

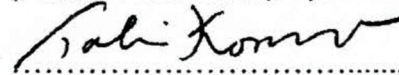
..... Member

(Assoc. Prof. Dr. Athipong Ngamjarurojana)

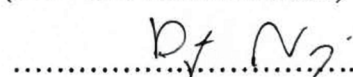
Advisory Committee:

..... Advisor


(Assoc. Prof. Dr. Apinpus Rujiwatra)

..... Co-advisor

(Prof. Dr. Takumi Konno)

..... Co-advisor

(Assoc. Prof. Dr. Piyarat Nimmanpipug)

..... Co-advisor

(Assoc. Prof. Dr. Athipong Ngamjarurojana)

15 February 2023

Copyright © by Chiang Mai University

ACKNOWLEDGEMENT

Although, there is only my name on the front cover of this thesis, it does not mean its sole contributors. A lot of people have been contributed in their own specific routes throughout my Ph.D study. This work could not be completed without their helps. I would like to acknowledge and many thanks from the bottom of my heart.

First of all, I would like to express my deepest appreciation to my beloved supervisor in Chiang Mai University, Assoc. Prof. Dr. Apinpus Rujiwatra who always give me the sincerely valuable guidance, encouragement, kindness, support and inspiration in both the academic and social life. Without her suggestions and constant help, this work would have not been achievable. I also would like to show my best regards to Prof. Dr. Takumi Konno and Prof. Dr. Yasuhiro Funahashi who provided me the valuable opportunities for being their DDP student in Osaka University. With their helpful advices and suggestions, I really enjoyed my research in Japan throughout a year. One important thing for my research in Prof. Konno's laboratory (Coordination Chemistry Laboratory), I would also like to share special thanks to Assoc. Prof. Dr. Nobuto Yoshinari, Asst. Prof. Dr. Naoto Kuwamura and Asst. Prof. Dr. Tatsuhiro Kojima for their kindness, very warmest helps, and valuable suggestions during my stay in Japan. I have learnt a lot since my first day in Japan. Without their helps, my thesis would not be completed. I am really thankful and appreciated them very much.

Besides my advisors, I would also like to deeply thank to my co-advisors, Assoc. Prof. Dr. Athipong Ngamjarurojana who always supported me the scientific instruments (proton conductivity and photoluminescent instruments) and Assoc. Prof. Dr. Piyarat Nimmanpipug who always helps me the computational information. I sincerely appreciate it.

I am really grateful to all examination committee, Prof. Naoto Ishikawa, Prof. Dr. Prof. Takashi Yoshimura, Prof. Dr. Takumi Konno and Prof. Dr. Yasuhiro Funahashi, Assoc. Prof. Dr. Apinpus Rujiwatra, Assoc. Prof. Dr. Athipong Ngamjarurojana, and Assoc. Prof. Dr. Piyarat Nimmanpipug for their valuable questions, comments, and

suggestions. I could have a chance to improve my research skills, concepts and others with them. Their useful guidance through this process made this thesis accomplish well. Thus, I would also like to take this opportunity to thank as being my examination committee members and all of their useful guidance through this process. Their discussion and ideas can help this thesis accomplish well.

I would like to give a big thank to Spring-8 (Japan) for supporting the synchrotron radiation experiments with the approval of JASRI (Proposal Nos. 2021A1295, 2021B1475, 2022A1578, 2022A1573, 2022B1806, 2022B1659).

I gratefully acknowledge the Human Resource Development in Science Project (Science Achievement Scholarship of Thailand, SAST) for scholarship and financial supports through my master study. In addition, many thanks to Department of Chemistry, Faculty of Science, Chiang Mai University as well as the Materials Chemistry Research Laboratory (MChemRL) for technical instruments and laboratory support.

Furthermore, my profoundly thanks to all the members of MChemRL at Chiang Mai University and Coordination Chemistry Laboratory (Prof. Konno's Lab) at Osaka University for the numerous assistances, useful guidance, admirable cooperation and inspiration. Completing this work would be more difficult without their support, encouragement and suggestion for many times.

I can never say "thanks" enough to my beloved family who always support and cheer me up in every moment of life, but I still would like to say thank you for everything that they have done for me. They always give me the constant love and encouragement. Without them, I would have not made it possible.

Finally, I also would like to give a special thanks to everyone who pay attention and be a part of this thesis as well as who involve a special part in my life, even though their names are not listed here.

Supaphorn Thammakan

หัวข้อคุณฉันทิพนธ์	วิศวกรรมผลึกของแลนทาไนด์โคออร์ดิเนชันพอลิเมอร์แบบมีรูพรุน โดยมัลติคาร์บอกซิเลตลิแกนด์	
ผู้เขียน	นางสาวสุภาพร ธรรมขัน	
ปริญญา	ปรัชญาดุษฎีบัณฑิต (เคมี)	
คณะกรรมการที่ปรึกษา	รองศาสตราจารย์ ดร. อภินิภัศ รุจิวัตร์ Prof. Dr. Takumi Konno รองศาสตราจารย์ ดร. ปิยรัตน์ นิมมานพิภักดิ์ รองศาสตราจารย์ ดร. อธิพงษ์ งามจาร์โรจน์	อาจารย์ที่ปรึกษาหลัก อาจารย์ที่ปรึกษาร่วม อาจารย์ที่ปรึกษาร่วม อาจารย์ที่ปรึกษาร่วม

บทคัดย่อ

แลนทาไนด์โคออร์ดิเนชันพอลิเมอร์แบบมีรูพรุนได้รับความสนใจ ด้วยว่าเป็นวัสดุที่สามารถถูกปรับแต่งโครงสร้างได้ และมีคุณสมบัติเฉพาะเจาะจง อย่างไรก็ตามการวิจัยในส่วนนี้ยังคงมีความท้าทายอยู่มาก เนื่องมาจากความเป็นไปได้ของเลขโคออดิเนชันและรูปร่างเชิงเรขาคณิตของไอออนแลนทาไนด์มีความหลากหลายและแปรเปลี่ยนได้มาก ลิแกนด์ที่มักจะถูกใช้ในการออกแบบแลนทาไนด์โคออร์ดิเนชันพอลิเมอร์แบบมีรูพรุน คือ มัลติคาร์บอกซิเลตลิแกนด์ ซึ่งจะถูปรับแต่งด้วยการเติมแต่งหมู่ฟังก์ชันหลายชนิด แต่ถึงอย่างไร การคิดค้นแลนทาไนด์โคออร์ดิเนชันพอลิเมอร์แบบมีรูพรุนเพื่อให้มีคุณสมบัติตามที่ต้องการด้วยการออกแบบลิแกนด์อินทรีย์นั้นยังคงเป็นไปได้ยากเนื่องจากขาดการศึกษาอย่างเป็นระบบในการปรับแต่งลิแกนด์ การศึกษาอิทธิพลของการเปลี่ยนแปลงโครงสร้างของลิแกนด์ที่ส่งผลต่อความเป็นรูพรุนของแลนทาไนด์โคออร์ดิเนชันพอลิเมอร์นั้นปราศจากข้อสรุปที่ชัดเจน และยังคงต้องการการศึกษาอีกมาก

ในงานวิจัยนี้ได้ทำการออกแบบและสังเคราะห์แลนทาไนด์โคออร์ดิเนชันพอลิเมอร์แบบมีรูพรุนโดยการปรับแต่งโครงสร้างของลิแกนด์ (ภาพที่ 1) ดังนี้ (i) เพิ่มลิแกนด์ตัวช่วยฟีนอกซีอะซิเตทเพื่อช่วยขยายพื้นที่ที่สามารถใช้งานได้และพัฒนาความเป็นรูพรุนให้เพิ่มขึ้น (ii) เติมกลุ่มไนโตรบนลิแกนด์ที่มีขนาดยาว อาทิเช่น ไบฟีนิล-4,4'-ไดคาร์บอกซิเลต เพื่อขยายขนาดและความเป็นรูพรุน (iii) แทนที่โรเดียมไอออนในสารประกอบเชิงซ้อนลิแกนด์โลหะของ $[Zn_4O\{Rh(L-cys)_3\}_4]^{6-}$ ด้วยเออร์เดียมไอออน เพื่อควบคุมความเป็นรูพรุนผ่านพันธะไฮโดรเจน ซึ่งทำให้สามารถสังเคราะห์สารประกอบโคออร์ดิเนชันพอลิเมอร์อนุกรมต่าง ๆ ดังนี้

- $[\text{Ln}(\text{poa})(2,5\text{-pydc})(\text{H}_2\text{O})_2] \cdot 3\text{H}_2\text{O}$ (1_{Ln}) เมื่อ $\text{Ln} = \text{Eu}^{\text{III}}, \text{Gd}^{\text{III}}, \text{Tb}^{\text{III}},$ และ Sm^{III} , $2,5\text{-pydc}^{2-} = 2,5\text{-ไพริดีนไดคาร์บอกซิเลต}$ และ $\text{poa}^- = \text{พีนอกซีอะซิเตท}$ (บทที่ 2) ที่แสดงความสามารถในการตรวจวัดแอมโมเนีย
- $[\text{Ln}_4(\text{di-nitro-BPDC})_4(\text{NO}_2)_3(\text{OH})(\text{H}_2\text{O})_5] \cdot (\text{solvent})$ (2_{Ln}) เมื่อ $\text{di-nitro-BPDC}^{2-} = 2,2'\text{-ไดไนโตรฟีนิล-4,4'\text{-ไดคาร์บอกซิเลต}$ และ $\text{Ln} = \text{Pr}^{\text{III}}, \text{Nd}^{\text{III}}, \text{Sm}^{\text{III}}, \text{Eu}^{\text{III}},$ และ Gd^{III} (บทที่ 3) ที่แสดงศักยภาพการนำไปใช้งานได้หลากหลาย (การนำโปรตรอน และการเป็นสารตรวจวัดความชื้นและอุณหภูมิ)
- $\text{Ln}_2[\text{L}^{\text{Ir}}] \cdot n\text{H}_2\text{O}$ (3_{Ln}) เมื่อ $[\text{L}^{\text{Ir}}]^{6-} = [\text{Zn}_4\text{O}\{\text{Ir}(\text{L-cys})_3\}_4]^{6-}$, $\text{L-cys} = \text{L-ซีสตีเนต}$, $\text{Ln} = \text{Sc}^{\text{III}}, \text{La}^{\text{III}}, \text{Ce}^{\text{III}}, \text{Pr}^{\text{III}},$ และ Nd^{III} และ $\text{Ln}_{0.33}[\text{Ln}_4(\mu_3\text{-OH})_4(\mu_2\text{-OAc})_3(\text{H}_2\text{O})_7][\text{L}^{\text{Ir}}] \cdot n\text{H}_2\text{O}$ (4_{Ln}) เมื่อ $\text{Ln} = \text{Sm}^{\text{III}}, \text{Eu}^{\text{III}}, \text{Gd}^{\text{III}}, \text{Tb}^{\text{III}}, \text{Dy}^{\text{III}}, \text{Ho}^{\text{III}}, \text{Er}^{\text{III}}, \text{Tm}^{\text{III}}, \text{Yb}^{\text{III}}, \text{Lu}^{\text{III}},$ และ Y^{III} (บทที่ 4)

$[\text{Ln}(\text{poa})(2,5\text{-pydc})(\text{H}_2\text{O})_2] \cdot 3\text{H}_2\text{O}$ (1_{Ln}). การใช้ลิแกนด์ผสมระหว่าง $2,5\text{-H}_2\text{pydc}$ และ Hpoa นำไปสู่โครงสร้างหนึ่งมิติของ $[\text{Ln}(\text{poa})(2,5\text{-pydc})(\text{H}_2\text{O})_2] \cdot 3\text{H}_2\text{O}$ (1_{Ln} ; $\text{Ln} = \text{Eu}^{\text{III}}, \text{Gd}^{\text{III}}, \text{Tb}^{\text{III}},$ และ Sm^{III}) โดยมีขนาดช่องเปิดของรูพรุนเท่ากับ $5.5 \times 4.2 \text{ \AA}^2$ และมีคุณสมบัติความเป็นรูพรุนเท่ากับ 21% การมีอยู่ของ poa^- ทำให้เกิดการขยายของขนาดรูพรุนใน 1_{Ln} ผ่านการลดจำนวนโคออดิเนตของ $2,5\text{-pydc}^{2-}$ กับแลนทาไนด์ไอออน ช่องเปิดหนึ่งมิติดังกล่าวถูกตกแต่งโดยหมู่ฟังก์ชันของลิแกนด์ ได้แก่ วงฟีนิล และ อะตอมออกซิเจนอิสระของ poa^- รวมไปถึงอะตอมออกซิเจนจากหมู่คาร์บอกซิเลตของลิแกนด์ $2,5\text{-pydc}^{2-}$ ในส่วนของฟังก์ชันการใช้งานของ 1_{Ln} พบว่า 1_{Eu} และ 1_{Tb} แสดงคุณสมบัติเชิงแสงที่ดีเยี่ยม ทั้งนี้เนื่องมาจากขนาดรูพรุนที่จำเพาะ หมู่ฟังก์ชันที่สามารถใช้งานได้ และการส่งต่อพลังงานอย่างมีประสิทธิภาพของลิแกนด์สู่แลนทาไนด์ไอออน ทำให้ 1_{Eu} มีศักยภาพในการใช้งานสำหรับการตรวจจับแอมโมเนีย โดยแสดงให้เห็นความจำเพาะเจาะจงอย่างมีนัยยะสำคัญและความไวในการตรวจจับที่สูง นอกจากนี้เพื่อพัฒนาวัสดุสำหรับการใช้งานได้สะดวกขึ้น ฟิล์ม $1_{\text{Eu}}/\text{PVA}$ จึงถูกประดิษฐ์ขึ้น โดยมีช่วงความเข้มข้นของแอมโมเนียที่ใช้งานได้ระหว่าง 0.50 ถึง 10.0 ppm สามารถตรวจจับความเข้มข้นต่ำสุดที่ 0.14 ppm ด้วยความไวในการตรวจจับสูงถึง $4.04 \% \cdot \text{ppm}^{-1}$ ค่าร้อยละการกลับคืนในช่วง 103 ถึง 111 % ค่าความเบี่ยงเบน 1.5 ถึง 8.2 %RSD และความสามารถในการถูกใช้งานซ้ำสูง 95 ถึง 97 %

$[\text{Ln}_4(\text{di-nitro-BPDC})_4(\text{NO}_2)_3(\text{OH})(\text{H}_2\text{O})_5] \cdot (\text{solvent})$ (2_{Ln}). การใช้ลิแกนด์ $\text{di-nitro-BPDC}^{2-}$ ทำให้เกิดโครงสร้างสามมิติของแลนทาไนด์โคออร์ดิเนชันพอลิเมอร์แบบมีรูพรุนของ $[\text{Ln}_4(\text{di-nitro-BPDC})_4(\text{NO}_2)_3(\text{OH})(\text{H}_2\text{O})_5] \cdot (\text{solvent})$ ($\text{Ln} = \text{Pr}^{\text{III}}, \text{Nd}^{\text{III}}, \text{Sm}^{\text{III}}, \text{Eu}^{\text{III}},$ และ Gd^{III}) โดยภายในโครงข่ายมีรู

พอร์แบบหนึ่งมิติที่แผ่ขยายไปตามทิศทางของแกน a และ b ช่องเปิดของรูพอร์มีขนาดตั้งแต่ 1.1 nm ถึง 2 nm การเติมหมู่ในโตรมีบทบาทสำคัญในการขยายขนาดของรูพอร์ อันเนื่องมาจากแรงผลักทางไฟฟ้าและผลจากความเกาะเกาะของหมู่ในโตร ทำให้จำนวนของการโคออดิเนตของลิแกนด์กับแลนทาไนด์ไอออนลดลง สารประกอบ 2_{Ln} แสดงประสิทธิภาพในการนำโปรตรอนที่ดีเยี่ยม และยังมี ความจำเพาะในการเลือกจับกับแก๊สคาร์บอนไดออกไซด์ และเป็นตัวเร่งปฏิกิริยาไฮโดรแอคดิชันของ คาร์บอนไดออกไซด์ด้วยอีพอกไซด์ โดยศักยภาพการใช้งานดังกล่าวสืบเนื่องมาจากผลของการมี ช่องเปิดที่มีทิศทางแน่ชัด หมู่ในโตรที่สามารถเข้าถึงและใช้งานได้ รวมไปถึงบริเวณความเป็นกรด ของลิแกนด์ในโครงสร้าง 2_{Ln}

$Ln_2[L^r] \cdot nH_2O$ (3_{Ln}) และ $Ln_{0.33}[Ln_4(\mu_3-OH)_4(\mu_2-OAc)_3(H_2O)_7][L^r] \cdot nH_2O$ (4_{Ln}). การ แทนที่โลหะอะตอมกลางในสารประกอบเชิงซ้อนลิแกนด์โลหะของ $[L^M]^{6-}$ จากโรเดียมไอออน (Rh^{III}) เป็นเอริเดียมไอออน (Ir^{III}) สามารถเพิ่มความมีรูพอร์ของโครงข่ายจาก 46% เป็น 53% และขนาดรู พอร์จาก $4.7 \times 11.5 \text{ \AA}$ เป็น $6.0 \times 12.2 \text{ \AA}$ ในส่วนของการสังเคราะห์แลนทาไนด์ควมบนคลัสเตอร์ $Ln_4(OH)_4$ ภายใน $[L^M]^{6-}$ สามารถจำแนกได้ดังนี้ ในกรณีของ $[L^r]^{6-}$ สามารถสังเคราะห์อนุกรมของ $Ln_{0.33}[Ln_4(\mu_3-OH)_4(\mu_2-OAc)_3(H_2O)_7][L^r] \cdot nH_2O$ (4_{Ln} ; $Ln = Sm^{III}, Eu^{III}, Gd^{III}, Tb^{III}, Dy^{III}, Ho^{III}, Er^{III}, Tm^{III}, Yb^{III}, Lu^{III}$, และ Y^{III}) และสำหรับ $[L^{Rh}]^{6-}$ สามารถสังเคราะห์ $Ln_{0.33}[Ln_4(\mu_3-OH)_4(\mu_2-OAc)_3(H_2O)_7][L^{Rh}] \cdot nH_2O$ (6_{Ln} ; $Ln = Gd^{III}, Tb^{III}, Dy^{III}, Ho^{III}, Er^{III}, Tm^{III}, Yb^{III}$, และ Lu^{III}) ได้ นอกเหนือจากนี้ยังพบว่าสามารถปรับปรุงคุณสมบัติเชิงแสงของ 4_{Ln} ได้โดยการแทนที่ไอออนอะตอม กลางจาก Rh^{III} เป็น Ir^{III} ใน $K_6[L^M] \cdot nH_2O$

โดยสรุป ในงานวิจัยนี้ได้เสนอแนวทางปฏิบัติสามรูปแบบสำหรับการออกแบบแลนทาไนด์ โคออร์ดิเนชันพอลิเมอร์แบบมีรูพอร์ผ่านระบบการปรับแต่งลิแกนด์ ได้แก่ (i) การใช้ลิแกนด์ไดคาร์ บอกซิเลตที่สามารถให้โครงสร้างที่มีมิติสูง ร่วมกับการเติมโมเลกุลขนาดเล็กเพื่อหลีกเลี่ยงการเกิด โครงสร้างแบบหนาแน่น (ii) การขยายรูพอร์ในโครงข่ายโดยใช้ลิแกนด์ที่ยาวขึ้นและมีการปรับแต่ง หมู่ฟังก์ชันด้วยหมู่ที่มีความเกาะเกาะมาก และ (iii) การใช้สารประกอบเชิงซ้อนลิแกนด์โลหะแบบมีลติ คาร์บอกซิเลตสามารถนำไปสู่การปรับแต่งพันธะไฮโดรเจนในโครงสร้างได้ด้วยการเปลี่ยนไอออน อะตอมกลางในสารประกอบเชิงซ้อนลิแกนด์โลหะดังกล่าว

Dissertation Title	Crystal Engineering of Porous Lanthanide Coordination Polymers with Multicarboxylate Ligands	
Author	Miss Supaphorn Thammakan	
Degree	Doctor of Philosophy (Chemistry)	
Advisory Committee	Assoc. Prof. Dr. Apinpus Rujiwatra	Advisor
	Prof. Dr. Takumi Konno	Co-advisor
	Assoc. Prof. Dr. Piyarat Nimmanpipug	Co-advisor
	Assoc. Prof. Dr. Athipong Ngamjarurojana	Co-advisor

ABSTRACT

Interest in porous lanthanide coordination polymers (LnCPs) originated from their tunable structures and unique properties. However, crystal engineering of LnCPs is challenging due to the large possibility of the coordination number and geometry of lanthanide ions (Ln^{III}). The commonly used ligands in the design of LnCPs are multicarboxylate ligands, which have been modified by adding various functional groups. Nevertheless, creating porous LnCPs with desired properties by designing organic ligands is still difficult, due to the lack of systematic study on ligand modification for developing LnCPs. In particular, the influence of the slight change in the ligand structures on the porosity of LnCPs is unclear.

In this research, the design and synthesis of porous LnCPs were examined through the structural modifications of conventional ligand systems (Fig. 1): (i) the introduction of auxiliary phenoxy acetate (poa^-) ligand to disrupt dense framework (chapter 2), (ii) the insertion $-\text{NO}_2$ groups on the lengthy biphenyl-4,4'-dicarboxylate (BPDC^{2-}) ligand to enlarge the porosity (chapter 3), and (iii) the replacement of Rh^{III} centers in $[\text{Zn}_4\text{O}\{\text{Rh}(\text{L-cys})_3\}_4]^{6-}$ ($[\text{L}^{\text{Rh}}]^{6-}$) metalloligands by Ir^{III} ion to control the void through the modified hydrogen bonding interactions (chapter 4). In addition, the plausible applications of the

resulting LnCPs were also explored. The several new series of porous LnCPs in this work were listed following;

Chapter 2: $[\text{Ln}(\text{poa})(2,5\text{-pydc})(\text{H}_2\text{O})_2] \cdot 3\text{H}_2\text{O}$ ($\mathbf{1}_{\text{Ln}}$) when $\text{Ln} = \text{Eu}^{\text{III}}, \text{Gd}^{\text{III}}, \text{Tb}^{\text{III}},$ and Sm^{III} , $2,5\text{-pydc}^{2-} = 2,5\text{-pyridine dicarboxylate}$, and $\text{poa}^- = \text{phenoxy acetate}$

Chapter 3: $[\text{Ln}_4(\text{di-nitro-BPDC})_4(\text{NO}_2)_3(\text{OH})(\text{H}_2\text{O})_5] \cdot (\text{solvent})$ ($\mathbf{2}_{\text{Ln}}$) when *di-nitro-BPDC*²⁻ = 2,2'-dinitrobiphenyl-4,4'-dicarboxylate and $\text{Ln} = \text{Pr}^{\text{III}}, \text{Nd}^{\text{III}}, \text{Sm}^{\text{III}}, \text{Eu}^{\text{III}},$ and Gd^{III}

Chapter 4: $\text{Ln}_2[\text{L}^{\text{Ir}}] \cdot n\text{H}_2\text{O}$ ($\mathbf{3}_{\text{Ln}}$) when $[\text{L}^{\text{Ir}}]^{6-} = [\text{Zn}_4\text{O}\{\text{Ir}(\text{L-cys})_3\}_4]^{6-}$, L-cys = L-cysteinate, $\text{Ln} = \text{Sc}^{\text{III}}, \text{La}^{\text{III}}, \text{Ce}^{\text{III}}, \text{Pr}^{\text{III}},$ and Nd^{III} and $\text{Ln}_{0.33}[\text{Ln}_4(\mu_3\text{-OH})_4(\mu_2\text{-OAc})_3(\text{H}_2\text{O})_7][\text{L}^{\text{Ir}}] \cdot n\text{H}_2\text{O}$ ($\mathbf{4}_{\text{Ln}}$) when $\text{Ln} = \text{Sm}^{\text{III}}, \text{Eu}^{\text{III}}, \text{Gd}^{\text{III}}, \text{Tb}^{\text{III}}, \text{Dy}^{\text{III}}, \text{Ho}^{\text{III}}, \text{Er}^{\text{III}}, \text{Tm}^{\text{III}}, \text{Yb}^{\text{III}}, \text{Lu}^{\text{III}},$ and Y^{III}

Chapter 2: Microporous Frameworks of Lanthanide-2,5-Pyridine-Dicarboxylate-Phenoxy Acetate and Selective Ammonia Sensing.

The use of mixed ligands of 2,5-H₂pydc and Hpoa for construction of LnCPs was reported in chapter 2. This combination of these two ligands led to one-dimensional porous LnCPs of $[\text{Ln}(\text{poa})(2,5\text{-pydc})(\text{H}_2\text{O})_2] \cdot 3\text{H}_2\text{O}$ ($\mathbf{1}_{\text{Ln}}$; $\text{Ln} = \text{Eu}^{\text{III}}, \text{Gd}^{\text{III}}, \text{Tb}^{\text{III}},$ and Sm^{III} , $2,5\text{-pydc}^{2-} = 2,5\text{-pyridine dicarboxylate}$, and $\text{poa}^- = \text{phenoxy acetate}$) with a window opening size of $5.5 \times 4.2 \text{ \AA}^2$ and 21% porosity. The presence of poa^- facilitates the extension of the void space in $\mathbf{1}_{\text{Ln}}$ through the reducing coordination of $2,5\text{-pydc}^{2-}$ to Ln^{III} centers. The one-dimensional channel was decorated by functional groups of the ligands, *i.e.* phenyl rings and free O atoms of poa^- as well as free O atoms from carboxylate groups of $2,5\text{-pydc}^{2-}$ ligands. Besides the expanded void space by the introduction of poa^- ligand, the functionalities of $\mathbf{1}_{\text{Ln}}$ were then promoted. The excellent photoluminescent properties of $\mathbf{1}_{\text{Eu}}$ and $\mathbf{1}_{\text{Tb}}$ were also investigated. Motivated by the specific pore size, available functional groups, and effective sensitization of the ligands to Ln^{III} , the potential application of ammonia sensing of $\mathbf{1}_{\text{Eu}}$ was evaluated, showing significant selectivity and high sensitivity among several common volatile organic compounds (VOCs). For further practical use, the fabricated $\mathbf{1}_{\text{Eu}}$ /PVA film was then prepared for ammonia sensing with a working concentration range of 0.50 to 10.0 ppm, low detection limit (0.14 ppm), high

sensitivity (4.04 %·ppm⁻¹), excellent recovery (103 to 111 %), narrow deviation (1.5 to 8.2 %RSD), and high repeatability (95 to 97 %).

Chapter 3: Nanoporous Frameworks of Lanthanide-2,2'-Dinitrobiphenyl-4,4'-Dicarboxylates as Multifunctional Materials.

In chapter 3, the –NO₂ insertion on the lengthy BPDC²⁻ ligand was studied to enlarge porosity. With the use of *di*-nitro-BPDC²⁻, the three-dimensional porous LnCPs structure of [Ln₄(*di*-nitro-BPDC)₄(NO₂)₃(OH)(H₂O)₅](solvent) (**2**_{Ln}; *di*-nitro-BPDC²⁻ = 2,2'-dinitrobiphenyl- 4,4'-dicarboxylate and Ln = Pr^{III}, Nd^{III}, Sm^{III}, Eu^{III}, and Gd^{III}) was successfully synthesized. Within the framework, there are two types of one-dimensional channels running along the a and b directions with the window opening size ranging from 1.1 nm to 2 nm. The insertion of –NO₂ group plays an important role in enlarging the porosity, which may be due to the electronic repulsion and steric effect. The coordination of organic ligands to Ln^{III} centers was then reduced. Owing to the highly directional channel, accessible –NO₂ groups as well as the Lewis acidic sites in the frameworks, **2**_{Ln} showed very high performance of various potential applications, *e.g.* proton conductivity, selective CO₂ capture, and catalysis for CO₂ cycloaddition reaction with epoxides.

Chapter 4: Tunable Installation of Lanthanide Cubane Clusters in Porous Supramolecular Frameworks Based on Multicarboxylate Metalloligands.

The tunable porosity by replacement of metal centers in multicarboxylate metalloligand of [L^M]⁶⁻ was investigated in Chapter 4. The use of a heavier and more rigid Ir^{III} instead of Rh^{III} in [L^M]⁶⁻ could enlarge the porosity from 46 to 53% with the expansion of pore size from 4.7 × 11.5 Å² to 6.0 × 12.2 Å². In addition, the border of the installation of lanthanide hydroxide cubane clusters Ln₄(OH)₄, in those [L^M]⁶⁻ was differentiated. In the case of [L^{Ir}]⁶⁻, a series of porous LnCPs Ln_{0.33}[Ln₄(μ₃-OH)₄(μ₂-OAc)₃(H₂O)₇][L^{Ir}]⁶⁻·nH₂O (**4**_{Ln}; Ln = Sm^{III}, Eu^{III}, Gd^{III}, Tb^{III}, Dy^{III}, Ho^{III}, Er^{III}, Tm^{III}, Yb^{III}, Lu^{III}, and Y^{III}) were synthesized from Sm^{III} to Lu^{III}, and Y^{III}. For the smaller porosity of [L^{Rh}]⁶⁻, the Ln₄(OH)₄ cluster could be grown in the crystal lattice of [L^{Rh}]⁶⁻ from Gd^{III} to Lu^{III} leading to the LnCPs Ln_{0.33}[Ln₄(μ₃-OH)₄(μ₂-OAc)₃(H₂O)₇][L^{Rh}]⁶⁻·nH₂O (**6**_{Ln}).

Furthermore, the photoluminescent properties in this class of LnCPs could also be improved by replacing the metal centers from Rh^{III} to Ir^{III} in K₆[L^M] \cdot nH₂O.

Conclusions

This study proposed three practical approaches for designing and fabricating porous LnCPs through modifying conventional ligand systems. First, the use of divergent dicarboxylate ligands could provide a high dimensionality of the framework. While introducing a small molecule to fulfill the coordination requirement of Ln^{III} centers could avoid the formation of dense frameworks. Second, the pore size could enlarge by using the longer ligands and functionalized ligands with steric groups of electron-rich moieties, which could also disrupt dense frameworks. Third, using multicarboxylate metalloligands could provide exceptional possibilities to control the hydrogen-bonded framework by the metal substitution in the metalloligands. The achievements presented in this thesis would provide effective ways for further designing and synthesizing porous LnCPs with desired structures and functionalities.

CONTENTS

	Page
Acknowledgement	c
Abstract in Thai	e
Abstract in English	h
List of Tables	p
List of Figures	r
List of Abbreviations and Symbols	z
Statement of Originality in Thai	aa
Statement of Originality in English	bb
Chapter 1 General Introduction	1
References	5
Chapter 2 Microporous Frameworks of Lanthanide-2,5-Pyridine-Dicarboxylate-Phenoxy Acetate and Selective Ammonia Sensing	8
2.1 Introduction	8
2.2 Experimental section	10
2.2.1 Synthesis of $\mathbf{1}_{Ln}$ ($Ln = Eu^{III}, Gd^{III}, Tb^{III},$ and Sm^{III})	10
2.2.2 X-ray crystallography	11
2.2.3 Preparation of $\mathbf{1}_{Eu}$ /PVA composite film using a drop-cast method	15
2.2.4 Photoluminescent study and ammonia sensing experiments	15
2.3 Results and discussions	17
2.3.1 Crystal structure description of $\mathbf{1}_{Ln}$	17
2.3.2 Purity and thermal stability of $\mathbf{1}_{Ln}$	20
2.3.3 UV-Vis and photoluminescent properties of $\mathbf{1}_{Ln}$	24

CONTENTS (Cont.)

	Page
2.3.4 Room temperature photoluminescent spectra of 1_{Ln}	25
2.3.5 Chemical robustness of 1_{Eu} and its selective sensing of ammonia gas	26
2.3.6 Characterization of 1_{Eu} /PVA composite film and its photoluminescence	30
2.3.7 Determination of ammonia gas concentration using 1_{Eu} /PVA film	32
2.3.8 Recyclability of 1_{Eu} /PVA film	36
2.4 Conclusions	39
2.5 References	40
Chapter 3 Nanoporous Frameworks of Lanthanide-2,2'-Dinitrobiphenyl-4,4'-Dicarboxylates as Multifunctional Materials	43
3.1 Introduction	43
3.2 Experimental section	45
3.2.1 Synthesis of <i>di</i> -nitro- H₂BPDC	45
3.2.2 Synthesis of 2_{Ln} (Ln = Pr ^{III} , Nd ^{III} , Sm ^{III} , Eu ^{III} , and Gd ^{III})	46
3.2.3 X-ray crystallography	47
3.2.5 Proton conductivity measurements	49
3.2.6 Gas adsorption experiments	51
3.2.7 Catalytic activities for CO ₂ cycloaddition reaction with epoxides	52
3.3 Results and discussions	53
3.3.1 Crystal structures description of 2_{Gd}	53
3.3.2 Phase and purity of 2_{Ln}	59
3.3.3 Thermogravimetric behavior and stability	60
3.3.4 Proton conductivity of 2_{Gd}	63
3.3.4.1 Superprotonic conductivity	63
3.3.4.2 Humidity- and temperature-dependent proton conductivities	67
3.3.5 Gas adsorption and selectivity	70

CONTENTS (Cont.)

	Page
3.3.6 Acidity and basicity of 2Pr , 2Eu , and 2Ga	74
3.3.7 Catalytic activities	75
3.3.7.1 CO ₂ cycloaddition reactions with epoxides	79
3.3.7.2 Influence of lanthanide contraction on the catalytic performance	80
3.4 Conclusions	84
3.5 References	84
Chapter 4 Tunable Installation of Lanthanide Cubane Clusters in Porous Supramolecular Frameworks Based on Multicarboxylate Metalloligands	90
4.1 Introduction	90
4.2 Experimental section	92
4.2.2 Synthesis (Δ_{LLL}) ₄ K ₆ [Zn ₄ O{Ir(L-cys) ₃ } ₄] \cdot 48H ₂ O (K₆[L^{Ir}] \cdot 48H ₂ O)	92
4.2.3 Synthesis of Ln ₂ [L ^{Ir}] \cdot nH ₂ O (3_{Ln}) and Ln _{0.33} [Ln ₄ (OH) ₄ (OAc) ₃ (H ₂ O) ₇][L ^{Ir}] \cdot nH ₂ O (4_{Ln})	92
4.2.4 X-ray crystallography	94
4.3 Results and discussions	100
4.3.1 Synthesis, characterizations, and crystal structures of K₆[L^{Ir}] \cdot 48H ₂ O	100
4.3.2 Synthesis, characterizations, and crystal structures of 3_{Ln}	104
4.3.3 Synthesis, characterizations, and crystal structures of 4_{Ln}	108
4.3.4 Photoluminescent properties of K₆[L^{Ir}] \cdot 48H ₂ O, 4_{Eu} and 4_{Tb}	118
4.3.5 Magnetic properties of 3_{Ln} and 4_{Ln}	122
4.4 Conclusions	123
4.5 References	124
Chapter 5 Concluding Remarks	128

CONTENTS (Cont.)

	Page
Curriculum Vitae	133

LIST OF TABLES

Table		Page
2.1	Coordination modes of 2,5-pydc ²⁻ or 2,5Hpydc ⁻ and dimensionality of LnCPs deposited to the Cambridge Structural Database	10
2.2	Crystallographic and refinement data of 1Eu , 1Ga , and 1Tb	12
2.3	Hydrogen bonding distance (<i>d</i> , Å) and angles (\angle , °) found in 1Eu	14
2.4	Band assignments of FT-IR spectra of 1Ln compared with Hpoa and 2,5-H ₂ pydc	22
2.5	CHN analyses of 1Ln	22
2.6	Performances of exemplified photoluminescent CP-films used for ammonia sensing	35
2.7	The read-out ammonia concentrations and statistical data	36
2.8	Read-out concentration (ppm) from the calibration curve for tenth measurements compared with the expected concentration of 3.50 and 8.50 ppm	37
3.1	Selected examples of LnCPs of BPDC ²⁻ and its derivatives possessing large pores	44
3.2	Crystallographic and refinement data of 2Ga	48
3.3	Elemental analysis of 2Ln	49
3.4	Thickness (<i>d</i> /cm) and surface areas (S/cm ²) of 2Ga used in proton conductivity experiments	50
3.5	Proton conductivities and activation energies of 2Ga compared with previously reported superprotonic conducting CPs and single crystal samples	68
3.6	The gas uptake capacities at 1 atm for 77 K, 195 K, and 298 K	72
3.7	Catalytic activities of 2Eu in CO ₂ cycloaddition reactions with ECH under solvent-free and ambient CO ₂ pressure conditions	77

LIST OF TABLES (Cont.)

Table		Page
3.8	Catalytic activities of 2_{Eu} in CO ₂ cycloaddition reactions with several epoxides under solvent-free and ambient CO ₂ pressure conditions	80
3.9	Catalytic activities of 2_{Ln} in CO ₂ cycloaddition reactions with ECH under solvent-free and ambient CO ₂ pressure conditions	81
3.10	Conversion, selectivity (if available), and the corresponding TON and TOF values reported for nanoporous CPs catalysts employed in the CO ₂ cycloaddition with ECH under various conditions	83
4.1	Crystallographic and refinement data of K ₆ [L ^{Ir}] \cdot 48H ₂ O	95
4.2	Crystallographic and refinement data of 3_{Ln}	96
4.3	Crystallographic and refinement data of 4_{Ln}	97
4.4	Comparisons of ratio Zn to Ln in XFA data and crystal structure data of 3_{Ln} and 4_{Ln}	105
4.5	The averaged distance of Ln ^{III} —O _{COO} and Ln \cdots Ln in the cubanes of 4_{Ln} compared to 6_{Ln}	116
4.6	The averaged N—H \cdots O _{COO} hydrogen bond distances in 3_{Ln} and 4_{Ln} compared to 5_{Ln} and 6_{Ln}	117

LIST OF FIGURES

Figure		Page
1.1	Examples of ligands employed in the synthesis of porous LnCPs.	4
1.2	Diagrams summarizing all reported LnCPs in this thesis	5
2.1	Coordination modes of 2,5-pydc ²⁻ found in LnCPs deposited to the Cambridge Structural Database [5] (frequency of appearance shown in brackets).	9
2.2	Schematic illustration of the setup for VOCs sensing experiments using (a) the finely ground 1_{Eu} and (b) the 1_{Eu}/PVA composite film	15
2.3	Crystallographic illustrations of 1_{Eu} : (a) asymmetric unit (drawn using 50% thermal ellipsoids), (b) modes of the coordination adopted by poa ⁻ and 2,5-pydc ²⁻ , (c) the <i>TPRS</i> -{EuNO ₈ } structural building motif, (d) the coordination environment of Eu ^{III} and (e) the formation of the edge-shared <i>TPRS</i> -{Eu ₂ N ₂ O ₆ } dimer	18
2.4	Illustrations of (a) the <i>TPRS</i> -{EuNO ₈ } ₂ dimer and a one-dimensional ladder in 1_{Eu} , and their assembly viewed along (b) <i>a</i> axis	19
2.5	PXRD patterns of 1_{Ln} compared with the patterns simulated from the corresponding single crystal data in the cases of 1_{Eu} , 1_{Gd} , and 1_{Tb}	21
2.6	FT-IR spectra of 1_{Ln} compared with those of H ₂ poa and 2,5-H ₂ pydc	21
2.7	TG/DTA curves of 1_{Eu}	23
2.8	PXRD patterns of 1_{Eu} before and after the treatment at 90 and 200 °C for 30 min compared with the patterns simulated from the single crystal data	23
2.9	UV-Vis spectra of 1_{Ln} (solid line) compared to the Hpoa (dash line) and 2,5-H ₂ pydc (dash-dot line) ligands	24
2.10	Room-temperature emission spectra (solid line) of (a) 1_{Eu} (b) 1_{Gd} (c) 1_{Tb} , and (d) 1_{Sm}	26

LIST OF FIGURES (Cont.)

Figure		Page
2.11	Simulated PXRD patterns of 1Eu (a) compared with the PXRD patterns after exposed to MeOH, EtOH, ammonia, acetone, MeCN, THF, <i>n</i> -hex, benzene, CHCl ₃ , and CH ₂ Cl ₂ (b-k), respectively	28
2.12	(a) Emission spectra of 1Eu after being exposed to VOCs and (b) the corresponding <i>R</i> values	29
2.13	UV-Vis spectra of 1Eu (solid-red line) and after being exposed to ammonia gas (solid-blank line) compared to the Hpoa (dash line) and 2,5-H ₂ pydc (dash-dot line) ligands	29
2.14	Emission spectrum of 1Ga before and after being exposed to ammonia compared with those of 2,5-H ₂ pydc and Hpoa	30
2.15	(a) PXRD pattern of 1Eu /PVA film (with a photo of the film in the inset (b) SEM images with the corresponding elemental mappings showing (b) the top surface) and (c) the cross-sectional area of the film	31
2.16	Photoluminescent spectra of the freshly prepared 1Eu /PVA film compared with that left at ambient condition for a month (photos of the films shown in insets)	32
2.17	Responses of 1Eu /PVA film in terms of (a) emission spectra and (b) the corresponding <i>R</i> values after contact with different VOCs vapors (15.0 ppm and 30 min)	33
2.18	(a, c) Emission spectra of 1Eu /PVA film for time-dependent at 10 ppm of ammonia vapor concentration and concentration-dependent at 30 min contact time and (b, d) the consisted <i>R</i> values calculated from triplicate data	34

LIST OF FIGURES (Cont.)

Figure		Page
2.19	(a) The R values of the $\mathbf{1Eu}$ /PVA films over ten cycles of the measurement-and-regeneration and the (b) corresponding concentrations of ammonia vapor determined using the standard calibration method for the expected concentrations of 3.50 ppm	38
2.20	(a) R values of the $\mathbf{1Eu}$ /PVA films over ten cycles of the measurement-and-regeneration and (b) the corresponding concentrations of ammonia vapor determined using the standard calibration method for the expected concentrations of 8.50 ppm	38
2.21	SEM images and the elemental mapping analysis of the $\mathbf{1Eu}$ /PVA-film after ten successive measurements of ammonia vapor sensing in (a, b) top-view and (c, d) cross-section for 3.50 ppm and 7.50 ppm, respectively	39
3.1	^1H NMR spectrum of the as-synthesized <i>di</i> -nitro- H_2BPDC	45
3.2	Diagram showing the experimental setting and the measurement chamber used in proton conductivity experiments	51
3.3	Depictions of (a) an asymmetric unit of $\mathbf{2Ga}$ drawn using 50% thermal ellipsoid and (b,c) coordination modes adopted by <i>di</i> -nitro- BPDC^{2-} and nitrite anions. Symmetry codes: (i) 1-x, 1-y, z; (ii) -0.5+x, -y, 0.75-z; (iii) -0.5+x, 1+y, 0.25+z; (iv) 1-x, -y, z; (v) 0.5-x, 0.5+y, 0.5-z; (vi) 0.5+x, 1.5-y, 0.5-z; (vii) 0.5-x, y, 0.75-z; (viii) 0.5-x, 1-y, 0.25+z).	54
3.4	Variation in coordination environment of Gd1 due to substitutional disorder <i>di</i> -nitro- BPDC^{2-} with nitrites and water molecules in $\mathbf{2Ga}$	56
3.5	Variation in coordination environment of Gd2 due to substitutional disorder <i>di</i> -nitro- BPDC^{2-} with nitrites and water molecules in $\mathbf{2Ga}$	57
3.6	Variation in coordination environment of Gd3 due to substitutional disorder <i>di</i> -nitro- BPDC^{2-} with nitrites and water molecules in $\mathbf{2Ga}$.	58

LIST OF FIGURES (Cont.)

Figure		Page
3.7	(a, b) the arrangement of the three unique Gd ^{III} in the zigzag chains along a and b directions within (c) the three-dimensional framework	58
3.8	Views of different possibilities of window openings arose from the crystallographic disorder. (a) with nitrite (N1 and N2) and water (O10, O25, O28, and O34), but not <i>di</i> -nitro-BPDC ²⁻ , (b) with a <i>di</i> -nitro-BPDC ²⁻ and water, but not nitrite (N1 and N2) (c) with nitrite (N1 and N2) and a <i>di</i> -nitro-BPDC ²⁻ , and (d) with <i>di</i> -nitro-BPDC ²⁻ , but not water and nitrite. Symmetry operation: (i) 0.5-x, y, 0.75-z, (ii) 2-x, 1-y, z, (iii) 1-x, 1-y, z.	59
3.9	(a) PXRD patterns of 2L_n compared with the simulated pattern generating from single crystal data of 2Ga , and (b) FT-IR spectra of 2L_n with corresponding band assignments	60
3.10	Element mappings of 2L_n crystals with corresponding elemental mappings	61
3.11	TGA profiles of 2L_n under heating from room temperature to 1000 °C under N ₂ flow with a list of the initial weight losses	62
3.12	PXRD of (a) simulated pattern from single crystal data of 2Ga compared with (b) as-synthesized 2Ga , (c) immersed in water at room temperature for a week, (d) immersed in hot water (80 °C) for 72 h, (e) heated at 250 °C for 3 h, and (f) heated at 1000 °C for 3 h	63
3.13	(a, c) The humidity-dependent Nyquist plots and (b, d) the corresponding conductivities of 2Ga at 0.1 and 1V applied voltages, respectively	65
3.14	(a, c) The temperature-dependent Nyquist plots and (b, d) the corresponding conductivities of 2Ga at 0.1 and 1 V applied voltages, respectively	66

LIST OF FIGURES (Cont.)

Figure		Page
3.15	The Nyquist plots of the pelletized polycrystalline sample of 2Ga prepared from ground crystals 1 V applied voltages	66
3.16	Arrhenius plot of the proton conductivity of 2Ga (25 to 55 °C and 99 RH%)	67
3.17	Calibration curves (red dashed-line) and the read-out data points (black) of humidity dependence with the expected values shown in brackets	69
3.18	Calibration curves (red dashed-line) and the read-out data points (black) of temperature dependence with the expected values shown in brackets	69
3.19	Ten successive measurements of (a) relative humidity (55 and 99 RH%, 25 °C) and (b) temperature (25 to 40 °C, 99 RH%) at 1V applied voltage	70
3.20	Gas adsorption/desorption isotherms of 2Ga for CO ₂ , N ₂ , H ₂ , and O ₂ (a) at 77 K, (b) at 195 K, (c) at 298 K, (d) water adsorption/desorption isotherms of 2Ga at 298 K, (e) the isosteric adsorption enthalpy of CO ₂ for 2Ga , and (f) comparison of CO ₂ adsorption/desorption of 2Pr to 2Eu at 298 K	73
3.21	(a) NH ₃ -TPD and (b) CO ₂ -TPD profiles of 2Pr (solid lines), 2Eu (dotted lines), and 2Ga (dashed lines)	75
3.22	Exemplary ¹ H NMR spectrum of the CO ₂ cycloaddition reaction with ECH catalyzed by 2Eu	76
3.23	(a) Percentage conversion (dark gray) and selectivity (light gray) for the recycling experiments of 2Eu , (b) the observed PXRD, (c) FT-IR spectra, and (d) SEM image with elemental mappings of 2Eu (selected element only Eu, Cl, and Br) after the eighth successive measurements	79

LIST OF FIGURES (Cont.)

Figure		Page
3.24	Diagram showing a possible mechanism of the CO ₂ cycloaddition reactions with epoxides (ECH as a model epoxide)	82
4.1	¹ H NMR spectrum of the as-synthesized K ₆ [L ^{Ir}] ₆ ·48H ₂ O in D ₂ O	101
4.2	FT-IR spectrum of K ₆ [L ^{Ir}] ₆ ·48H ₂ O	101
4.3	Crystal structures of K ₆ [L ^{Ir}] ₆ ·48H ₂ O. (a) [L ^{Ir}] ₆ ⁶⁻ metalloligand, (b) surrounded by six adjacent [L ^{Ir}] ₆ ⁶⁻ through N—H···O hydrogen bonds (black dash line), (c) the packing framework through hydrogen bonding, (d) window opening decorated with COO ⁻ functional groups from five [L ^{Ir}] ₆ ⁶⁻ metalloligands, and (e) O···O distance at pore space (site A) for available creating lanthanide cubanes; H atoms were omitted for clarity. Ir (brown), Zn (olive-green), S (yellow), N (blue), C (light grey), O (red), and [L ^{Ir}] ₆ ⁶⁻ (light blue)	102
4.4	Perspective views of disordered (a) K1, K2 occupied at site A and K6, (b) K3 and K4 occupied at site B, and (d) K5 coordinated with carboxylate groups in K ₆ [L ^{Ir}] ₆ ·48H ₂ O. H atoms were omitted for clarity. Ir (brown), Zn (olive-green), S (yellow), N (blue), C (light grey), and O (red)	103
4.5	FT-IR spectra of 3 _{Ln} (red line) and 4 _{Ln} (black line).	106
4.6	Perspective views of the disordered La1A, La1B, La2A, and La2B ions located at the (a) pore site A and (b) pore site B in 3 _{La} , and (c) packing framework of 3 _{La} with Ln ^{III} ions occupied (space-filling) at the sites A and B; H atoms were omitted for clarity. La (dark blue), Ir (brown), Zn (olive-green), S (yellow), N (blue), C (light grey), O (red), and [L ^{Ir}] ₆ ⁶⁻ (light blue); symmetry code (i) 0.5+x, 1.5-y, 1-z, (ii) 1-x, -0.5+y, 1.5-z, (iii) 0.5+x, 0.5-y, 1-z, (iv) 0.5-x, 1-y, -0.5+z	107

LIST OF FIGURES (Cont.)

Figure		Page
4.7	Perspective views of the Ln ^{III} ions occupied (space-filling) at the sites A and B in (a) 3_{Sc} , (b) 3_{Ce} , (c) 3_{Pr} , and (d) 3_{Nd} ; Sc (orange), Ce (pink), Pr (green), Nd (purple), and H atoms of [L ^{Ir}] ⁶⁻ (light blue) were omitted for clarity	108
4.8	Perspective views of (a) [Lu ₄ (OH) ₄ (OAc) ₃ (H ₂ O) ₇] ⁵⁺ cluster, (b) three [L ^{Ir}] ⁶⁻ coordinated with the cluster, (c) the connectivity of three adjacent cubanes through [L ^{Ir}] ⁶⁻ , and (d) packing framework showing the pore size ca. 5.6 × 9.9 Å ² in 4_{Lu} ; H atoms were omitted for clarity. Lu (orange), Ir (brown), Zn (olive-green), S (yellow), N (light blue), C (light grey), and O (red); symmetry code (i) x, y, z	111
4.9	Packing structures of (a) 4_{Sm} , (b) 4_{Gd} , (c) 4_{Tb} , (d) 4_{Dy} , (e) 4_{Ho} , (f) 4_{Er} , (g) 4_{Tm} , (h) 4_{Yb} , and (j) 4_Y ; H atoms were omitted for clarity. [L ^{Ir}] ⁶⁻ (light gray)	112
4.10	Perspective views of the [Ln ₄ (OH) ₄ (OAc) ₃ (H ₂ O) ₇] ⁵⁺ clusters in (a) 4_{Sm} , (b) 4_{Eu} , (c) 4_{Gd} , (d) 4_{Tb} , (e) 4_{Dy} , (f) 4_{Ho} , (g) 4_{Er} , (h) 4_{Tm} , (i) 4_{Yb} , and (j) 4_Y	113
4.11	Simulated (red solid line) and observed (black solid line) PXRD patterns of 3_{Ln} (λ = 0.8 Å)	114
4.12	Simulated (red solid line) and observed (black solid line) PXRD patterns of 4_{Ln} (λ = 0.8 Å)	115
4.13	Excitation (λ _{em} 620 nm; black dot line) and emission (λ _{ex} 370 nm) (black solid line) spectra of K ₆ [L ^{Ir}] ⁶⁻ ·48H ₂ O at 77 K compared to the excitation (λ _{em} 515 nm; red dot line) and emission (λ _{ex} 360 nm; red dot line) spectra of ZnO	120
4.14	Absorption spectra in water of K ₆ [L ^{Rh}] ⁶⁻ ·nH ₂ O (black line) and K ₆ [L ^{Ir}] ⁶⁻ ·48H ₂ O (red line)	120

LIST OF FIGURES (Cont.)

Figure		Page
4.15	Solid-state excitation (black line) and emission spectra of (a) $4E_u$ at room temperature, (b) $4T_b$ at room temperature, (c) $4E_u$ at 77 K, and (d) $4T_b$ at 77 K	121
4.16	Diffused reflectance spectra of $K_6[L^{Ir}]\cdot 48H_2O$ (black line), $4E_u$ (solid red), and $4T_b$ (solid green)	122
4.17	The $\chi_m T$ vs T plots for $3L_n$ and $4L_n$	123
5.1	Diagrams summarizing all reported LnCPs in this thesis.	132

LIST OF ABBREVIATIONS AND SYMBOLS

%	Percent
<i>RSD</i>	Relative Standard Deviation
<i>SD</i>	Standard Deviation
h^{-1}	Per hour
TON	Turnover number
TOF	Turnover frequency
CPs	Coordination polymers
<i>e.g.</i>	<i>example gratia</i> (for example)
<i>i.e.</i>	<i>id est (that is)</i>
Ln^{III}	Lanthanide ions
LnCPs	Lanthanide Coordination Polymers
pH	<i>pouvoir hydrogène</i>
<i>ca.</i>	Approximately
S	Siemens
RH	Relative Humidity
AC	Alternating Current
Hz	Hertz
ν	stretching
δ	Chemical shift
Ω	Ohm
<i>via</i>	Through
χ_{m}	Molar magnetic susceptibility
θ	theta

ข้อความแห่งการริเริ่ม

ข้าพเจ้า นางสาวสุภาพร ธรรมชั้น ขอยืนยันว่าเนื้อหาในคุษฎีนิพนธ์หัวข้อ “วิศวกรรมผลึกของแลนทาไนด์โคออร์ดิเนชันพอลิเมอร์แบบมีรูพรุนด้วยมัลติคาร์บอกซิเลตลิแกนด์” เล่มนี้เป็นผลงานต้นฉบับของข้าพเจ้าภายใต้คำแนะนำและการชี้แนะจาก รศ.ดร. อภินิภัต รุจิวัตร์ และ Prof. Dr. Takashi Yoshimura (อาจารย์ที่ปรึกษาหลัก)

ข้าพเจ้าขอรับรองว่าคุษฎีนิพนธ์เล่มนี้เป็นผลงานของข้าพเจ้า รวมถึงฉบับแก้ไขสุดท้าย ซึ่งได้รับความเห็นชอบจากคณะกรรมการสอบวิทยานิพนธ์และบัณฑิตวิทยาลัย มหาวิทยาลัยเชียงใหม่แล้ว และคุษฎีนิพนธ์เล่มนี้ยังไม่เคยถูกใช้ยื่นสำหรับขอปริญญา หรือคุณวุฒิจากมหาวิทยาลัย หรือสถาบันใดมาก่อน

STATEMENTS OF ORIGINALITY

I, Supaphorn Thammakan, hereby declare that the material presented in my dissertation entitled “Crystal Engineering of Porous Lanthanide Coordination Polymers with Multicarboxylate Ligands” is an original work performed by me under the guidance and advice of my advisors, Assoc. Prof. Dr. Apinpus Rujiwatra and Prof. Dr. Takashi Yoshimura.

I declare that this is a true copy of my dissertation, including any final revisions, as approved by my thesis committee and the Graduate School, Chiang Mai University. To the best of my knowledge, this dissertation has not been previously submitted for a degree to any other university or institution.

CHAPTER 1

General Introduction

Porous frameworks, particularly in the class of coordination polymers (CPs), have emerged as a new platform for the development of multifunctional materials owing to their tunable functionality through pore surface and pore size engineering [1,2]. Motivated by the outstanding properties of lanthanide ions (Ln^{III}) arising from the presence of $4f$ electrons, *e.g.* unique magnetic, electronic, and optical properties [2-5], porous lanthanide coordination polymers (LnCPs) have gained an earnest interest recently. A wide range of applications, *e.g.* magnetism, luminescence, and catalysis [2-5], have been realized. However, the implementation of crystal engineering with porous LnCPs is challenging due to the flexible geometries and high coordination numbers of Ln^{III} as well as their exceptional susceptibilities to water and small solvent molecules [7,8]. Contrary to transition metal ions, the versatile and sentient coordination chemistry of Ln^{III} is directed mainly by organic ligands [7,8]. Choices of organic ligands are thus critical for designing structures with desired properties.

In accordance with the hard-soft acid-base principle [9], the carboxyl groups should promote strong $\text{Ln}^{\text{III}}\text{—O}$ bonding and therefore robust frameworks. The commonly used ligands in the design of porous LnCPs are multicarboxylate ligands, which have been modified through the addition of various functional groups or the use of mixed ligands (Fig. 1.1). To yield porous LnCPs, the relative arrangement and number of donor atoms, length, rigidity and steric effect of the employed ligands must be considered with great care [10-12]. According to the literature, the divergent ligands processing two carboxylate groups are one of the important ligands promoting porous LnCPs. For example, monobenzene or pyridine-dicarboxylate could provide microporous LnCPs, *e.g.* $[\text{Ln}(\text{nitro-BDC})(\text{L})_{0.5}(\text{H}_2\text{O})] \cdot 3\text{H}_2\text{O}$ ($\text{Ln} = \text{Pr}^{\text{III}}, \text{Nd}^{\text{III}}, \text{Sm}^{\text{III}}$ and Gd^{III} , and $\text{L} = \text{BDC}^{2-}$ or $\text{BDC}^{2-}/\text{nitro-BDC}^{2-}$) [13], $[\text{Tb}(\text{L})_{1.5}(\text{H}_2\text{O})] \cdot 3\text{H}_2\text{O}$ ($\text{L} = 2\text{-(2-Hydroxy-propionylamino)-}$

terephthalate) [14], $[\text{Ce}_2(2,5\text{-pydc})_2(2,5\text{-Hpydc})(\text{H}_2\text{O})_2]\text{Cl}\cdot n\text{H}_2\text{O}$ [15], $[\text{Nd}(2,5\text{-pydc})(\text{OAc})(\text{H}_2\text{O})]_n\cdot 2n\text{H}_2\text{O}$ [16], $[\text{Ln}_6(\text{BDC})_9(\text{DMF})_6(\text{H}_2\text{O})_3]\cdot 3\text{DMF}$ ($\text{Ln} = \text{La}^{\text{III}}, \text{Ce}^{\text{III}},$ and Nd^{III}) [17], $[\text{Ce}_6\text{O}_4(\text{OH})_4(\text{F-BDC})_6]$ [18], and $\text{Ln}_4(\mu_3\text{-OH})_4(\text{NH}_2\text{-BDC})_3(\text{H}_2\text{O})_{7.5}(\mu_1\text{-OH})_{0.5}\cdot 1.5\text{Cl}, 10\text{DMF}$ and ($\text{Ln} = \text{Y}^{\text{III}}, \text{Eu}^{\text{III}}, \text{Gd}^{\text{III}}, \text{Tb}^{\text{III}}, \text{Dy}^{\text{III}}, \text{Er}^{\text{III}}, \text{Ho}^{\text{III}}, \text{Tm}^{\text{III}},$ and Yb^{III}) [19]

To yield larger porosity of LnCPs, lengthy ligands have been employed rendering open frameworks with large windows, *e.g.* $[\text{Gd}_2\text{L}_3(\text{DMF})_4]\cdot 4\text{DMF}, 3\text{H}_2\text{O}$ ($\text{L} = \text{tetra-nitro-BPDC}^{2-}$) [20], $[\text{LnK}(\text{DSBPDC})(\text{DMF})(\text{H}_2\text{O})]\cdot x(\text{solvent})$ ($\text{Ln} = \text{Pr}^{\text{III}}, \text{Sm}^{\text{III}},$ and Eu^{III}) [21], $[\text{Ln}_4(\mu_3\text{-OH})_4(\text{NH}_2\text{-BPDC})_4(\text{DMF})_3(\text{H}_2\text{O})]\cdot 8\text{H}_2\text{O}, 4.2\text{DMF}$, $[\text{Ln}_4(\mu_3\text{-OH})_4(\text{NH}_2\text{-TPDC})_4(\text{DMF})(\text{H}_2\text{O})_3]\cdot 16.6\text{H}_2\text{O}, 15.2\text{DMF}$ ($\text{Ln} = \text{Y}^{\text{III}}, \text{Eu}^{\text{III}}, \text{Gd}^{\text{III}}, \text{Tb}^{\text{III}}, \text{Dy}^{\text{III}}, \text{Er}^{\text{III}}, \text{Ho}^{\text{III}}, \text{Tm}^{\text{III}},$ and Yb^{III}) [19], and $[(\text{CH}_3)_2\text{NH}_2]_2[\text{Tb}_6(\mu_3\text{-OH})_8(\text{DFBPDC})_6(\text{H}_2\text{O})_6]\cdot x(\text{solvent})$ [22]. Most of these ligands are notably decorated with pending groups, especially those of the electron-rich moieties such as $-\text{SO}_3\text{H}$, $-\text{NH}_2$, $-\text{F}$, and $-\text{NO}_2$. The effect of steric groups should be carefully considered as they can be useful in disrupting the dense frameworks and allowing a larger pore size.

Apart from judicious choices of ligands, the synthesis of porous framework depends also on the number of lanthanide centers [23]. High-nuclearity of lanthanide centers can lead to large porosity [18,19,22]. Based on the common synthetic approach of ligand-controlled hydrolysis, the synthesis of the lanthanide clusters is still challenging for chemists due to the highly flexible chemistry of Ln^{III} [23]. Multicarboxylate ligands, *e.g.* hexa-, octa-, and dodecacarboxylate ligands, are great candidates to provide high-nuclearity lanthanide clusters with high stability and dimensionality [24]. In addition, multicarboxylate ligands could also decorate the internal pore spaces of the frameworks with free carboxylate groups, which should promote the potential functions of the derived frameworks [25,26]. Furthermore, there can be free carboxylate groups available for the establishment of hydrogen-bonding interactions, which can improve porosity through supramolecular assembly [27]. However, the synthesis procedure and structural arrangement based on organic multicarboxylate ligands might limit the development of the synthesis of desired structures. Multicarboxylates provided by discrete metal complexes or metalloligands have become more attractive owing to their stabilities,

solubilities, tunable structures and functionalities [25]. Known examples of LnCPs derived through this strategy are nonetheless limited, *e.g.* $\{\text{Ln}_7(\text{OH})_5[\text{Ru}(\text{dcbpy})]_4 \cdot n\text{H}_2\text{O}\}$ [28], $[\{\text{Gd}(\text{OAc})(\text{H}_2\text{O})\}\{\text{Gd}_4(\text{OH})(\text{OH})_4(\text{H}_2\text{O})_{11}\}\{(m\text{-L}_{\text{Ru}})_4(\text{HCOO})\}]\{\text{SiW}_{12}\text{O}_{40}\}_2 \cdot x\text{DMF} \cdot y\text{H}_2\text{O}$ [29], and $[\text{Ln}\{\text{Ln}_4(\mu_3\text{-OH})_4(\text{H}_2\text{O})_{10}\}\{(m\text{-L}_{\text{Ru}})_4(\text{HCOO})_2\}]\{\text{SiW}_{12}\text{O}_{40}\}_2 \cdot x\text{DMF} \cdot y\text{H}_2\text{O}$ ($m\text{-L}_{\text{Ru}} = \text{Ru}^{\text{II}}(\text{bpy})_2(4,4'\text{-dcbpy})$, $\text{Ln} = \text{Dy}^{\text{III}}$ and Er^{III}) [29].

In this thesis, the design and synthesis of porous LnCPs were examined through the use of multicarboxylate ligands with diverse rigidity, length, number of coordinating groups, and functional groups. All the ligands chosen herein are designed by slight structural modification of conventional ligand systems, *i.e.* the introduction of small ligands, the addition of pendant groups, and the substitution of the metal center. The results and discussion are presented in three chapters classified in accordance with different crystal structures (Fig.1.2). Properties and potential functions of the derived frameworks are also included.

Chapter 2: $[\text{Ln}(\text{poa})(2,5\text{-pydc})(\text{H}_2\text{O})_2] \cdot 3\text{H}_2\text{O}$ ($\mathbf{1}_{\text{Ln}}$) ($\text{Ln} = \text{Eu}^{\text{III}}$, Gd^{III} , Tb^{III} , and Sm^{III} , $\text{poa}^- = \text{phenoxy acetate}$, and $2,5\text{-pydc}^{2-} = 2,5\text{-pyridine dicarboxylate}$)

Chapter 3: $[\text{Ln}_4(\text{di-nitro-BPDC})_4(\text{NO}_2)_3(\text{OH})(\text{H}_2\text{O})_5] \cdot (\text{solvent})$ ($\mathbf{2}_{\text{Ln}}$) ($\text{di-nitro-BPDC}^{2-} = 2,2'\text{-dinitrobiphenyl-4,4'}\text{-dicarboxylate}$ and $\text{Ln} = \text{Pr}^{\text{III}}$, Nd^{III} , Sm^{III} , Eu^{III} , and Gd^{III})

Chapter 4: $\text{Ln}_2[\text{L}^{\text{Ir}}] \cdot n\text{H}_2\text{O}$ ($\mathbf{3}_{\text{Ln}}$) ($[\text{L}^{\text{Ir}}] = [\text{Zn}_4\text{O}\{\text{Ir}(\text{L-cys})_3\}_4]^{6-}$, $\text{L-cys} = \text{L-cysteinate}$, $\text{Ln} = \text{Sc}^{\text{III}}$, La^{III} , Ce^{III} , Pr^{III} , and Nd^{III}) and $\text{Ln}_{0.33}[\text{Ln}_4(\mu_3\text{-OH})_4(\mu_2\text{-OAc})_3(\text{H}_2\text{O})_7][\text{L}^{\text{Ir}}] \cdot n\text{H}_2\text{O}$ ($\mathbf{4}_{\text{Ln}}$) ($\text{Ln} = \text{Sm}^{\text{III}}$, Eu^{III} , Gd^{III} , Tb^{III} , Dy^{III} , Ho^{III} , Er^{III} , Tm^{III} , Yb^{III} , Lu^{III} , and Y^{III})

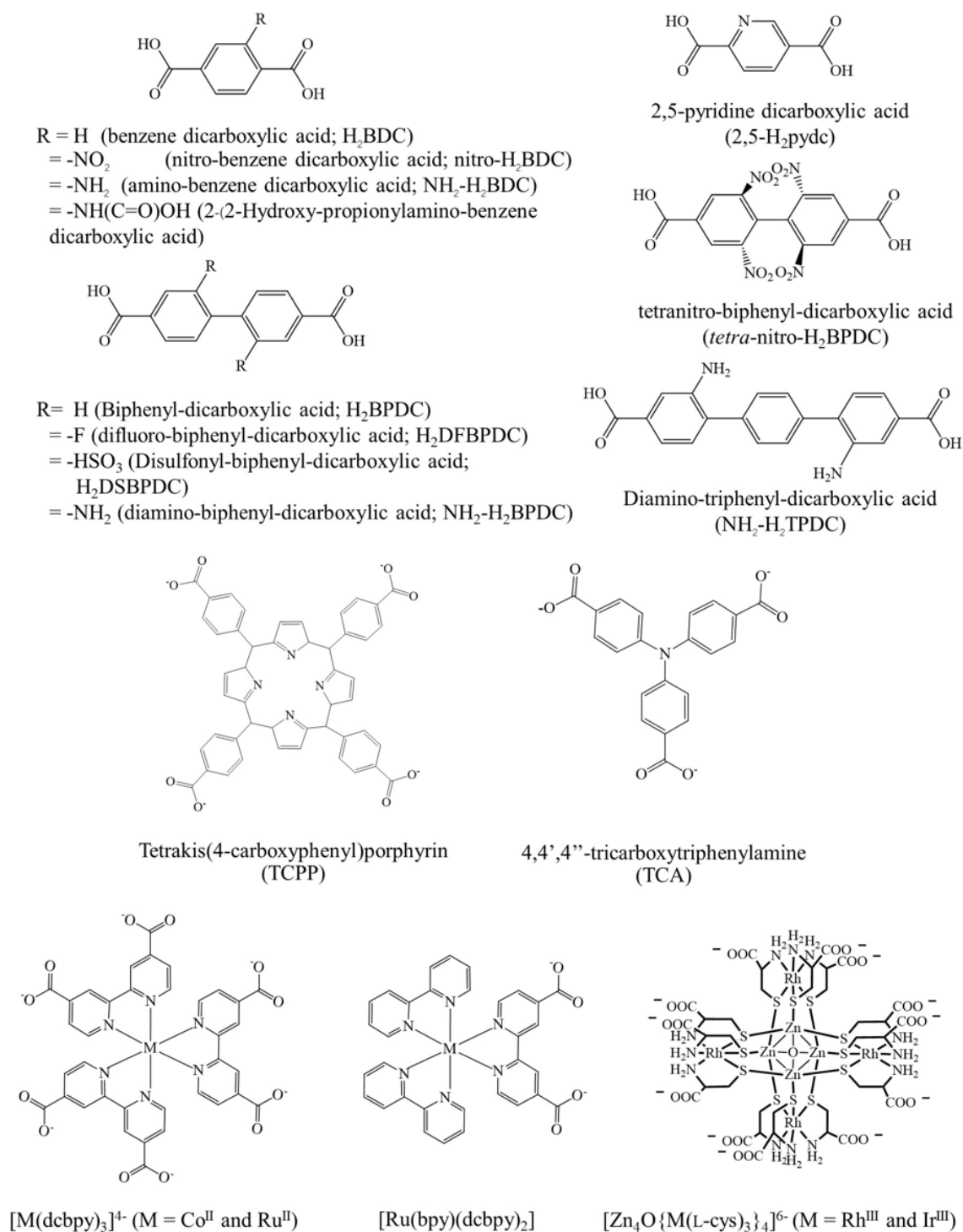


Fig. 1.1 Examples of ligands employed in the synthesis of porous LnCPs.

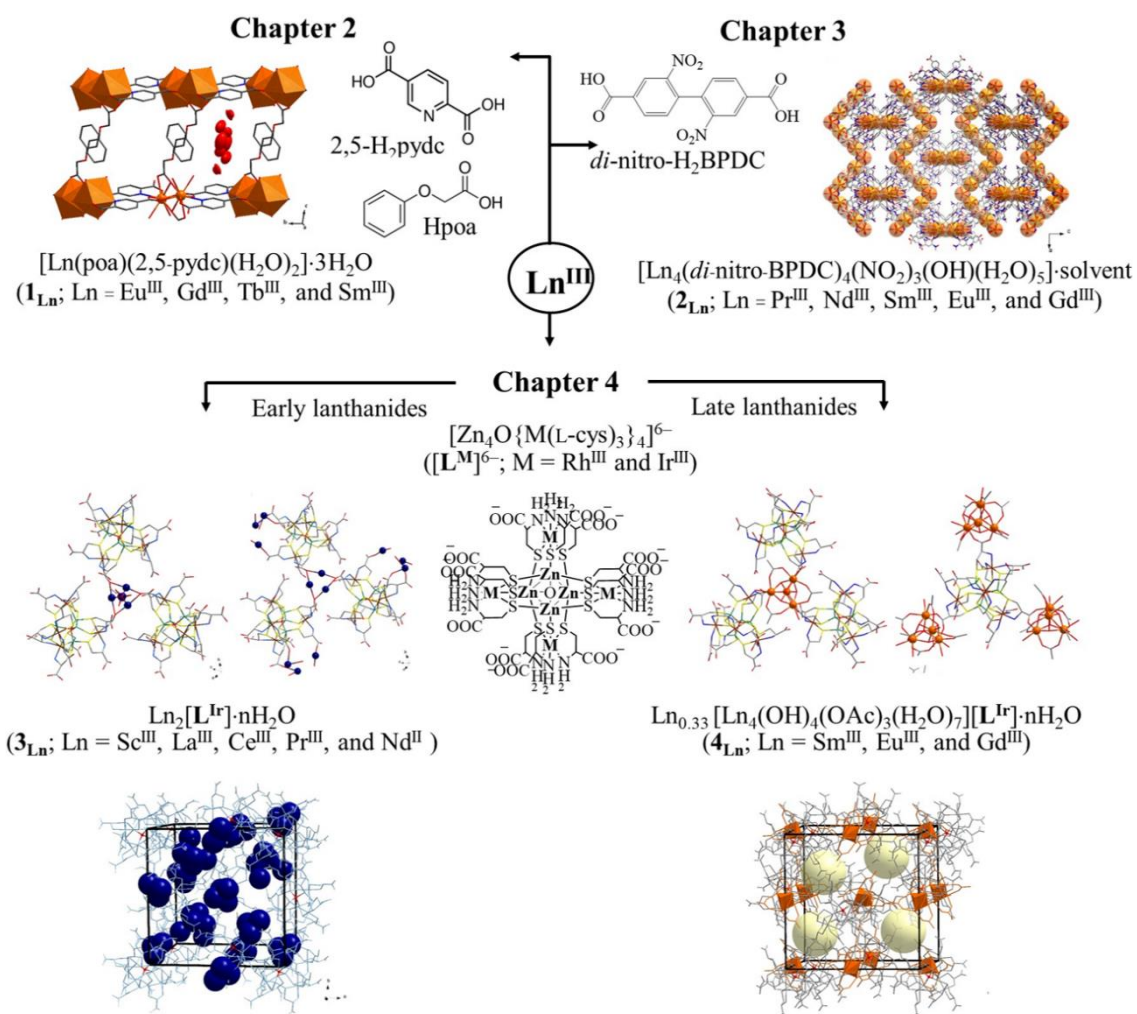


Fig. 1.2 Diagrams summarizing all reported LnCPs in this thesis.

References

- [1] Kitagawa, S.; Kitaura, R.; Noro, S. *Angew. Chem. Int. Ed.* **2004**, *43*, 2334–2375.
- [2] Du, M.; Li, C.-P.; Liu C.-S.; Fang, S.-M. *Coord. Chem. Rev.* **2013**, *257*, 1282–1305.
- [3] Li, B.; Wen, H.-M.; Cui, Y.; Qian, G.; Chen, B. *Prog. Polym. Sci.* **2015**, *48*, 40–84.
- [4] Roy, S.; Chakraborty, A.; Maji, T.-K. *Coord. Chem. Rev.* **2014**, *273-274*, 139-164.
- [5] Cui, Y.; Chen, B.; Qian, G. *Coord. Chem. Rev.* **2014**, *273–274*, 76–86.
- [6] Desiraju, G. R. *J. Chem. Sci.* **2010**, *122*, 667–675.

- [7] Robin, A. Y.; Fromm, K.M. *Coord. Chem. Rev.* **2006**, *250*, 2127–2157.
- [8] Bünzli, J.-C. G. *J. Coord. Chem.* **2014**, *67*, 3706–3733.
- [9] Hasegawa, Y.; Kitagawa, Y. *J. Photochem. Photobiol. C Photochem. Rev.* **2022**, *51*, 100485.
- [10] Eddaoudi, M.; Kim, J.; Rosi, N.; Vodak, D.; Wachter, J.; O’Keeffe, M.; Yaghi, O.M.; *Science* **2002**, *295*, 469–472.
- [11] Lee, J.; Farha, O. K.; Roberts, J.; Scheidt, K. A.; Nguyen, S. T.; Hupp, J. T.; *Chem. Soc. Rev.* **2009**, *38*, 1450–1459.
- [12] He, Y.; Chen, F.; Li, B.; Qian, G.; Zhou, W.; Chen, B.; *Coord. Chem. Rev.* **2018**, *373*, 167–198.
- [13] Panyarat, K.; Prior, T. J.; Rujiwatra, A. *Polyhedron* **2014**, *81*, 74–80.
- [14] Cao, L.-H.; Shi, F.; Zhang, W.-M.; Zang, S.-Q.; Mak, T. C. W. *Chem. Eur. J.* **2015**, *21*, 15705–15712.
- [15] Silva, P.; Valente, A. A.; Rocha, J.; Paz, F. A. A. *Cryst. Growth Des.* **2010**, *10*, 2025–2028.
- [16] Huang, Y.-G.; Jiang, F.-L.; Yuan, D.-Q.; Wu, M.-Y.; Gao, Q.; Wei, W.; Hong, M.-C. *Cryst. Growth Des.* **2008**, *8*, 166–168.
- [17] Han, Y.; Li, X.; Li, L.; Ma, C.; Shen, Z.; Song, Y.; You, X. *Inorg. Chem.* **2010**, *49*, 10781–10787.
- [18] Lammert, M.; Wharmby, M. T.; Smolders, S.; Bueken, B.; Lieb, A.; Lomachenko, K. A.; Vos, D. D.; Stock, N. *Chem. Commun.* **2015**, *51*, 12578–12581.
- [19] Luo, T.-Y., Liu, C., Eliseeva, S. V., Muldoon, P. F., Petoud, S., Rosi, N. L. *J. Am. Chem. Soc.* **2017**, *139*, 9333–9340.
- [20] Das, R. K.; Aijaz, A.; Sharma, M. K.; Lama, P.; Bharadwaj, P. K.; *Chem. A Eur. J.* **2012**, *18*, 6866–6872.

- [21] Zhou, L.-J.; Deng, W.-H.; Wang, Y.-L.; Xu, G.; Yin, S.-G.; Liu, Q.-Y.; *Inorg. Chem.* **2016**, *55*, 6271–6277.
- [22] Xue, D.-X.; Cairns, A. J.; Belmabkhout, Y.; Wojtas, L.; Liu, Y.; Alkordi, M. H.; Eddaoudi, M. *J. Am. Chem. Soc.* **2013**, *135*, 7660–7667.
- [23] Zheng, X. Y.; Xie, J.; Kong, X. J.; Long, L. S.; Zheng, L. S. *Coord. Chem. Rev.* **2019**, *378*, 222–236.
- [24] Wu, H.; Zhang, S.; Li, M.; Qiao, C.; Sun, L.; Wei, Q.; Xie, G.; Chen, S.; Gao, S. *ChemistrySelect* **2016**, *1*, 3335 – 3342.
- [25] Yoshinari, N.; Konno, T. *Coord. Chem. Rev.* **2023**, *474*, 214850.
- [26] Bhadra, B. N.; Ahmed, I.; Lee, H. J.; Jhung, S. H. *Coord. Chem. Rev.* **2022**, *450*, 214237.
- [27] Ivasenko, O.; Perepichka, D. F. *Chem. Soc. Rev.* **2011**, *40*, 191–206.
- [28] Watanabe, A.; Kobayashi, A.; Saitoh, E.; Nagao, Y.; Omagari, S.; Nakanishi, T.; Hasegawa, Y.; Sameera, W. M. C.; Yoshida, M.; Kato, M. *Inorg. Chem.* **2017**, *56*, 3005–3013.
- [29] Wang, L.; Yang, W.; Yi, F.-Y.; Wang, H.; Xie, Z.; Tang, J.; Sun, Z.-M. *Chem. Commun.* **2013**, *49*, 7911–7913.

CHAPTER 2

Microporous Frameworks of Lanthanide-2,5-Pyridine-Dicarboxylate-Phenoxy Acetate and Selective Ammonia Sensing

2.1 Introduction

In this chapter, new series of porous $[\text{Ln}(\text{poa})(2,5\text{-pydc})(\text{H}_2\text{O})_2]\cdot 3\text{H}_2\text{O}$ ($\mathbf{1}_{\text{Ln}}$) coordination polymers, where $\text{Ln} = \text{Eu}^{\text{III}}$, Gd^{III} , Tb^{III} , and Sm^{III} , were synthesized and characterized. 2,5-pyridine-dicarboxylic acid (2,5- H_2pydc) and phenoxy acetic acid (Hpoa) were chosen as organic building motifs. With respect to framework design, 2,5- H_2pydc containing two divergent carboxylates, was expected to provide infinite framework structures through various coordination modes, particularly $\mu_4\text{-}\eta_1:\eta_1:\eta_1:\eta_1$ (Fig. 2.1). However, both porous and dense frameworks are possible (Table 2.1). To disrupt dense framework formation, Hpoa with only one carboxylate was concurrently used. Regarding the promotion of the $f\text{-}f$ emissions, both 2,5- H_2pydc and Hpoa are acknowledged as effective sensitizers according to the antenna model [1,2]. The existence of pyridine ring of 2,5- H_2pydc as well as the O atom and phenyl ring of Hpoa should additionally encourage sufficient interactions with some small molecules, especially ammonia, to induce perturbation in $f\text{-}f$ emission profile through weak interactions, *e.g.* hydrogen bonding. Through these interactions with ammonia-responsive functional groups, the frameworks have been expected to exhibit sensing ability toward ammonia [3,4]. Single crystal structures, thermal stability and solid-state photoluminescent properties at room temperature of the synthesized frameworks were investigated. On the basis of room-temperature photoluminescent results, $\mathbf{1}_{\text{Eu}}$ was chosen for the study of ammonia gas sensing. The results are described and discussed in relation to the deduced single crystal structures and spectroscopy. Encouraged by the efficient photoluminescence for further practical uses, the $\mathbf{1}_{\text{Eu}}$ /PVA composite film was also fabricated *via* a facile drop-casting method providing exceptional performance as

selective, robust, and reusable ammonia gas sensors. The film can potentially be used for on-site monitoring due to its fast response and portability.

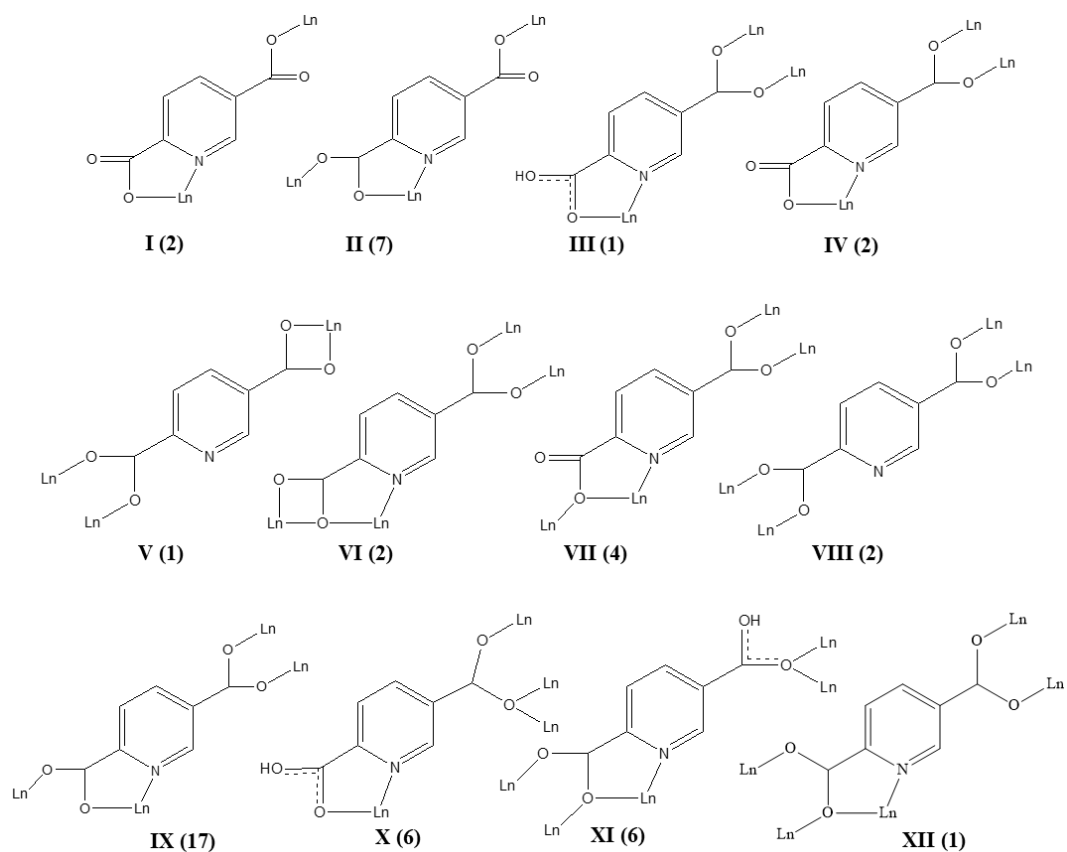
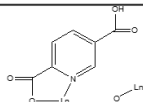
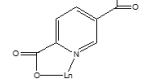
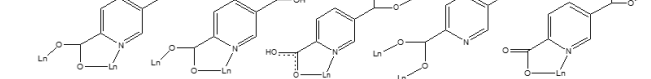
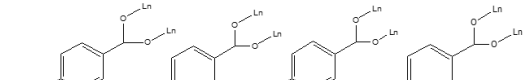
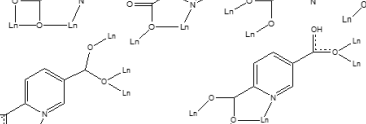


Fig. 2.1 Coordination modes of 2,5-pydc²⁻ found in LnCPs deposited to the Cambridge Structural Database [5] (frequency of appearance shown in brackets).

Table 2.1 Coordination modes of 2,5-pydc²⁻ or 2,5Hpydc⁻ and dimensionality of LnCPs deposited to the Cambridge Structural Database [5]

Coordination modes	Number of structures in various dimensions of framework			
	1D	2D	3D Dense	3D Porous
μ_1 	2	3	-	-
μ_2 	2	-	-	-
μ_3 	2	3	8	1
μ_4 	1	7	13	4
μ_5 	-	-	7	-

*1D = one-dimension, 2D = two-dimension, and 3D = three-dimension

2.2 Experimental

2.2.1 Synthesis of 1_{Ln} ($Ln = Eu^{III}, Gd^{III}, Tb^{III},$ and Sm^{III})

[Eu(poa)(2,5-pydc)(H₂O)₂] \cdot 3H₂O (1_{Eu}**).** First, EuCl₃ \cdot 6H₂O (73.3 mg, 0.20 mmol), 2,5-H₂pydc (33.4 mg, 0.20 mmol), and Hpoa (91.3 mg, 0.6 mmol) were dissolved in a mixed solvent of EtOH (10.00 mL) and water (5.00 mL), which was adjusted pH of the solution to 6 using TEA. The solution was then transferred into a 30 mL vial, which was sealed tightly and placed in an 80 °C oven. After 24 h, the vial was opened and heated at 60 °C for 72 h and then cooled down to room temperature. The colorless block-shaped crystals were then recovered through filtration (63% yield based on Eu^{III}).

[Gd(poa)(2,5-pydc)(H₂O)₂] \cdot 3H₂O (1_{Gd}**).** The colorless block-shaped crystals of **1_{Gd}** were synthesized following the same procedure as **1_{Eu}**, but with GdCl₃ \cdot 6H₂O (74.3 mg, 0.20 mmol; 67% yield based on Gd^{III}).

[Tb(poa)(2,5-pydc)(H₂O)₂·3H₂O (1_{Tb}). The colorless block-shaped crystals of **1_{Tb}** were synthesized following the same procedure as **1_{Eu}**, but with TbCl₃·6H₂O (74.7 mg, 0.20 mmol; 61% yield based on Tb^{III}).

[Sm(poa)(2,5-pydc)(H₂O)₂·3H₂O (1_{Sm}). The colorless block-shaped crystals of **1_{Sm}** were synthesized following the same procedure as **1_{Eu}**, but with SmCl₃·6H₂O (73.0 mg, 0.20 mmol; 62% yield based on Sm^{III}).

2.2.2 X-ray crystallography

The single crystal data of **1_{Ln}** (Ln = Eu^{III}, Gd^{III}, and Tb^{III}) were collected using a Rigaku-Oxford XtalLab Supernova diffractometer equipped with a micro-focus sealed X-ray tube of Mo K α radiation ($\lambda = 0.71073 \text{ \AA}$) and direct photon counting HyPix3000 detector at 293 K. The intensity data sets were carried out using the CrysAlisPro program [6]. SADABS program was applied for the empirical absorption corrections [7]. The crystal structures were solved using the SHELXT program [8] and refined on F^2 by the full-matrix least-squares technique using the SHELXL program [9] *via* the Olex² interface [10]. All hydrogen atoms were calculated using riding mode. Details on the crystallographic and refinement are summarized in Table 2.2. The hydrogen bond distances and angles of **1_{Eu}** were summarized in Table 2.3. The crystals of **1_{Sm}** were too small and not appropriate for full data collection. The structure of **1_{Sm}** is isostructure to **1_{Eu}**, **1_{Gd}**, and **1_{Tb}**. Their purity was evaluated based on the PXRD experiment and elemental analysis (Table 2.4).

Table 2.2 Crystallographic and refinement data of **1Eu**, **1Gd**, and **1Tb**

	1Eu	1Gd	1Tb
CCDC NO.	2206221	2206226	2206229
Crystal formula	EuC ₁₅ O ₁₂ NH ₂₀	GdC ₁₅ O ₁₂ NH ₂₀	TbC ₁₅ O ₁₂ NH ₂₀
Formula weight	554.25	559.54	561.21
Space group	Triclinic <i>P</i> -1	Triclinic <i>P</i> -1	Triclinic <i>P</i> -1
<i>a</i> (Å)	8.8731(1)	8.8712(2)	8.8591(3)
<i>b</i> (Å)	9.3731(4)	9.3698(10)	9.3380(3)
<i>c</i> (Å)	11.8367(6)	11.8432(2)	11.8545(4)
α (°)	99.632(4)	99.00(100)	99.424(3)
β (°)	95.378(3)	95.258(2)	95.130(2)
λ (°)	92.476(7)	92.4960(10)	92.509(2)
<i>V</i> (Å ³)	964.55(7)	964.76(3)	961.86(6)
<i>Z</i>	2	2	2
ρ /g·cm ⁻³	1.908	1.926	1.938
Radiation λ (Å)	Mo K α (0.71073)	Mo K α (0.71073)	Mo K α (0.71073)
Temperature (K)	293(2)	293(2)	293(2)
Crystal size (mm ³)	0.1×0.1×0.2	0.2×0.1×0.05	0.1×0.1×0.05
F(000)	544	546	548
Data/parameters/ restraints	4119/296/12	4125/289/0	4111/283/0
$R_1(I > 2\sigma(I))$ [†]	0.0289	0.0315	0.0353
wR_2 (all data) ^{††}	0.0628	0.0672	0.0819

$$^{\dagger}R_1 = \sum(|F_o| - |F_c|) / \sum(|F_o|), \quad ^{\dagger\dagger}wR = [\sum w(F_o^2 - F_c^2)^2 / \sum w(F_o^2)^2]^{1/2}$$

Table 2.3 Hydrogen bonding distance (d , Å) and angles (\angle , °) found in **1Eu**

D—H...A	$d(\text{D—H})$	$d(\text{H...A})$	$d(\text{D...A})$	$\angle(\text{D—H...A})$
O9 _w —H9WA...O7 ⁱ	0.89	2.16	2.9002	140
O9 _w —H9WB...O10A ⁱⁱ	0.89	1.96	2.7559	148
O8 _w —H8WB...O7 ⁱ	0.86	2.13	2.8845	145
O10A—H10A...O6	0.85	2.50	3.3154	160
C4—H4...O8W ^{iv}	0.93	2.47	3.3223	152
C6—H6...O3	0.93	2.44	2.7688	101
O8W ⁱⁱⁱ —H8WA ⁱⁱⁱ ...O1	0.86	1.85	2.7090	173
O8W ⁱⁱⁱ —H8WB ⁱⁱⁱ ...O1	0.86	2.90	2.7090	69
O8W ⁱⁱⁱ —H8WA ⁱⁱⁱ ...O2	0.86	2.63	3.1180	117
O8W ⁱⁱⁱ —H8WB ⁱⁱⁱ ...O2	0.86	2.68	3.1180	113
O8W ^{iv} —H8WA ^{iv} ...O4	0.86	3.06	3.5560	118
O8 _w —H8WA...O1 ⁱⁱⁱ	0.86	1.85	2.7090	173
O8 _w —H8WA...O2 ⁱⁱⁱ	0.86	2.63	3.1180	117
O8 _w —H8WA...O4 ^{iv}	0.86	3.06	3.5540	118
O8 _w —H8WB...O1 ⁱⁱⁱ	0.86	2.90	2.7090	69
O8 _w —H8WB...O2 ⁱⁱⁱ	0.86	2.68	3.1180	113
C4 ^{iv} —H4 ^{iv} ...O8W	0.93	2.47	3.3220	152
C3 ^{iv} —H3 ^{iv} ...O9W	0.93	2.83	3.4810	128
O10B ^{iv} —H10C ^{iv} ...O2	0.85	3.05	2.9056	72
O10B ^{iv} —H10D ^{iv} ...O2	0.85	2.09	2.9056	162
O9 _w —H9WA...O10A	0.89	2.92	2.7565	71
O9 _w —H9WA...O10B	0.89	3.03	2.7218	62
O9 _w —H9WB...O10A	0.89	1.96	2.7565	148
O9 _w —H9WB...O10B	0.89	2.05	2.7218	131

Symmetry: (i) 1-x, 2-y, 1-z (ii) 1-x, 1-y, 1-z (iii) -x, 2-y, 1-z (iv) -x, 1-y, 1-z (v) x, 1+y, Z (vi) x, -1+y, z (vii) 1-x, 1-y, 2-z (viii) -x, 1-y, 2-z (ix) -1+x, y, z

Table 2.3 Hydrogen bonding distance (d , Å) and angles (\angle , °) found in **1Eu** (Cont.)

D—H····A	$d(\text{D—H})$	$d(\text{H}····\text{A})$	$d(\text{D}····\text{A})$	$\angle(\text{D—H}····\text{A})$
O10A—H10B····O9W	0.85	3.06	2.7565	62
O10B—H10C····O9W	0.85	2.60	2.7218	89
O10B—H10D····O9W	0.85	3.00	2.7218	49
O10A—H10A····O12	0.85	2.54	2.6945	91
O10A—H10B····O12	0.85	2.58	2.6945	88
O10A—H10A····O6 ^{vi}	0.85	2.50	3.3150	160
O10A—H10A····O11A	0.85	3.10	2.7533	58
O10A—H10B····O11A	0.85	1.99	2.7533	149
O10B—H10C····O11A	0.85	1.53	2.1167	123
O10B—H10D····O11A	0.85	2.08	2.1167	81
O10B—H10C····O2 ^{iv}	0.85	3.05	2.9056	72
O10B—H10D····O2 ^{iv}	0.85	2.09	2.9056	162
C3 ^{iv} —H3 ^{iv} ····O1B	0.93	2.86	2.6933	150
C12 ^{viii} —H12 ^{viii} ····O11B	0.93	3.12	4.0364	170
O11A····O2 ^{iv}	-	-	2.7730	-
O11B····O2 ^{iv}	-	-	3.2390	-
O11A····O12	-	-	3.9820	-
O11A····O12 ^{vii}	-	-	2.6940	-
O11B····O12 ^{vii}	-	-	2.2530	-
O11B····O11B ^{viii}	-	-	1.9670	-
O11B····O12 ^{ix}	-	-	3.3550	-
O12····O11A ^{vii}	-	-	2.6970	-
O12····O11B ^{vii}	-	-	2.2530	-

Symmetry: (i) 1-x, 2-y, 1-z (ii) 1-x, 1-y, 1-z (iii) -x, 2-y, 1-z (iv) -x, 1-y, 1-z (v) x, 1+y, Z
(vi) x, -1+y, z (vii) 1-x, 1-y, 2-z (viii) -x, 1-y, 2-z (ix) -1+x, y, z

2.2.3 Preparation of 1_{Eu} /PVA composite film using a drop-cast method

Composite films of 1_{Eu} and PVA were prepared using a simple drop-casting method (Fig. 2.2). A suspension of finely ground 1_{Eu} (20 mg, 0.036 mmol) in PVA solution (50 mg of PVA in 2.00 mL of hot water) was first prepared and dropped into a $2 \times 2 \text{ cm}^2$ well excavated on a glass slide. It was then dried at $40 \text{ }^\circ\text{C}$ for 4 to 6 h. The yielded films were characterized by PXRD, scanning electron microscopy (SEM), and energy dispersive X-ray (EDX) spectroscopy.

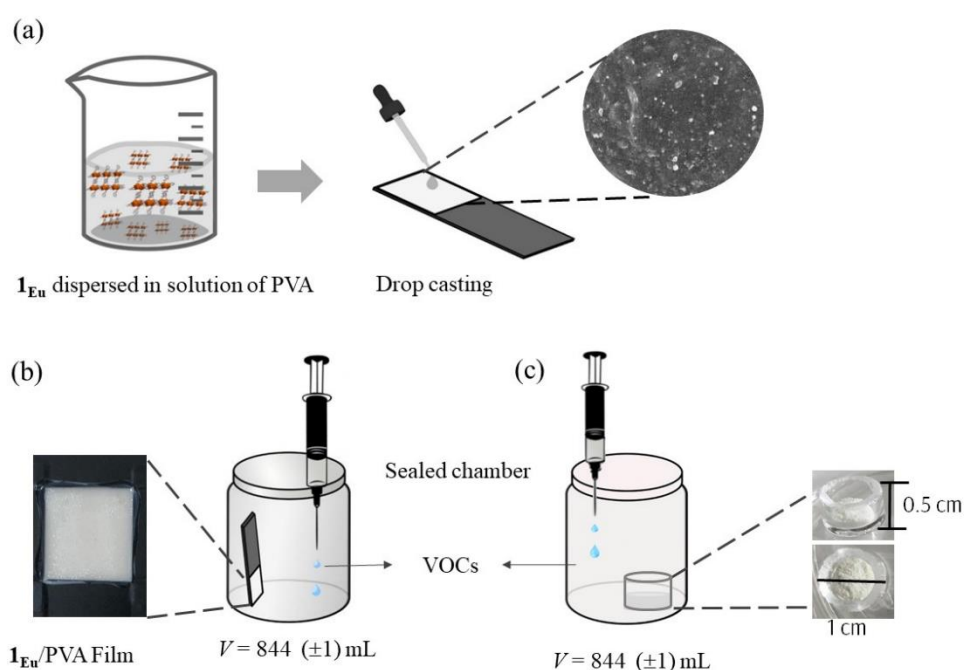


Fig. 2.2 Schematic illustration of the setup for VOCs sensing experiments using (a) the finely ground 1_{Eu} and (b) the 1_{Eu} /PVA composite film.

2.2.4 Photoluminescent study and ammonia sensing experiments

Room-temperature emission spectra of the as-synthesized 1_{Eu} , 1_{Gd} , 1_{Tb} , and 1_{Sm} were first collected and analyzed, from which 1_{Eu} was selected for the study of ammonia gas sensing (Fig. 2.10). First, the study was carried out using the finely ground crystals of 1_{Eu} (10 mg) was added into a small glass cylinder (1 cm in diameter and 0.5 cm tall), which was then placed separately in a tightly closed glass chamber (volume of the

container = 844 (± 1) mL). An ammonia solution was then injected into the chamber without touching the sample, using a 10.00 μL syringe. The volume of the introduced ammonia solution was varied from 0.95 to 38.00 μL in order to generate ammonia vapor concentrations of 0.25 to 10.0 ppm. To accelerate the vaporization of ammonia within the chamber, the vial was gently warmed at *ca.* 45 $^{\circ}\text{C}$. After exposure to the vapor for a designed duration, photoluminescent spectrum of $\mathbf{1Eu}$ was collected immediately using the excitation wavelength of 370 nm. The response (R) of $\mathbf{1Eu}$ was evaluated based on the change in the integral area under the most intense ${}^5\text{D}_0 \rightarrow {}^7\text{F}_2$ emission at 615 nm (A_{exp}) with respect to that of the pristine $\mathbf{1Eu}$ (used as a reference, A_0). All the experiments were carried out in triplicate.

$$R (\%) = \left[\frac{A_{\text{exp}} - A_0}{A_0} \right] \times 100 \quad \text{eq. (2.1)}$$

The same procedure was adopted for the experiments using the composite films. The concentration of the ammonia vapor and contact time varied from 0.50 to 15.0 ppm, and 1 to 120 min contact time. Both the ground crystal and film experiments should be noted that all the measurements were carried out at room temperature and pressure. The value of A_0 was measured before every measurement of A_{exp} , which was proved to promote reliability of the acquired data.

The responses of the ground crystals of $\mathbf{1Eu}$ (*ca.* 10 mg) and the $\mathbf{1Eu}$ /PVA films to the other common volatile organic compounds, including chloroform (CHCl_3), dichloromethane (CH_2Cl_2), benzene, *n*-hexane (*n*-hex), tetrahydrofuran (THF), acetonitrile (MeCN), ethanol (EtOH), methanol (MeOH) and acetone, were also investigated, which evaluated selectivity of the sensing. All experiments were also performed at ambient temperature and pressure. The long contact time and high concentrations of these analysts were studied; 17h under 4000 ppm for ground crystals and 30 min under 15.0 ppm for $\mathbf{1Eu}$ /PVA films. The emission spectra were collected instantly after the exposure. It should be noted that all the ammonia vapor sensing experiments were carried out in triplicate.

To investigate the robustness and reusability of the $\mathbf{1Eu}$ /PVA film, the ammonia concentration of 3.50 and 7.50 ppm with 30 min contracting time were chosen. The used

film was left under an ambient atmosphere overnight to regenerate the **1_{Eu}**/PVA films for the next cycles. The restoration of the emission spectra to approximately the original intensity was assured before every cycle.

2.3 Results and discussions

2.3.1 Crystal structure description of **1_{Ln}**

The crystal structure of **1_{Eu}** is described here as a representative of **1_{Gd}**, **1_{Tb}**, and **1_{Sm}** since they are all isostructural with the same crystal formula of $[\text{Ln}(\text{poa})(2,5\text{-pydc})(\text{H}_2\text{O})_2]\cdot 3\text{H}_2\text{O}$ ($\text{Ln} = \text{Eu}^{\text{III}}$, Gd^{III} , Tb^{III} , and Sm^{III}). The structure of **1_{Eu}** features a one-dimensional ladder-like framework (Fig. 2.4), which is constructed from a nine-fold tricapped trigonal prismatic Eu^{III} building motif, *i.e.* $\text{TPRS}\{-\text{EuNO}_8\}$ (Fig. 2.3c). Each $\text{TPRS}\{-\text{EuNO}_8\}$ motif is delineated by N and O atoms from 2,5-pydc²⁻, poa⁻, and water molecules. The neighboring $\text{TPRS}\{-\text{EuNO}_8\}$ motifs are connected by two oxo-bridges of poa⁻ and two carboxylate-bridges of 2,5-pydc²⁻ to form an edge-shared $\text{TPRS}\{-\text{EuNO}_8\}_2$ dimers. To establish the polymeric ladder-like structure, these dimers are further fastened by 2,5-pydc²⁻ in the direction of the *b* axis (Fig. 2.4a). Coordination modes of poa⁻ is $\mu_2\text{-}\eta^2\text{:}\eta^1$ and 2,5-pydc²⁻ is $\mu_3\text{-}\eta^0\text{:}\eta^1\text{:}\eta^1\text{:}\eta^1$ (Fig. 2.3b). Through these coordination modes, 2,5-pydc²⁻ plays an important role as a divergent linker in the construction of the framework whereas poa⁻ fulfills the coordination of Eu^{III} and limits dimensionality of the framework to be one-dimension. In the crystal structure, the established ladders are assembled into a three-dimensional supramolecular assembly *via* hydrogen bonding and $\pi\text{-}\pi$ interactions (Table 2.3). The assembly of these ladders leads to the establishment of the one-dimensional channels running along *a* axis (Fig. 2.4b), which account for *ca.* 21% of solvent accessible void calculated by PLATON [11]. The effective window opening to these channels is *ca.* $4.2 \times 5.5 \text{ \AA}^2$. Within the channels, the crystallizing water molecules are accommodated. They show site disordering, which is consistent with their involvement with the hydrogen bonding interactions. Noticeably, size of the opening should allow the entry of small molecules, *e.g.* ammonia (3.26 Å), carbon dioxide (3.33 Å), and

hydrogen sulfide (3.60 Å) [12,13]. In addition, the internal surface of these channels is decorated by potential functional groups of the organic ligands, *i.e.* O atoms of both 2,5-pydc²⁻ and phenyl ring of poa⁻. These should be available for interactions with these molecules, especially ammonia.

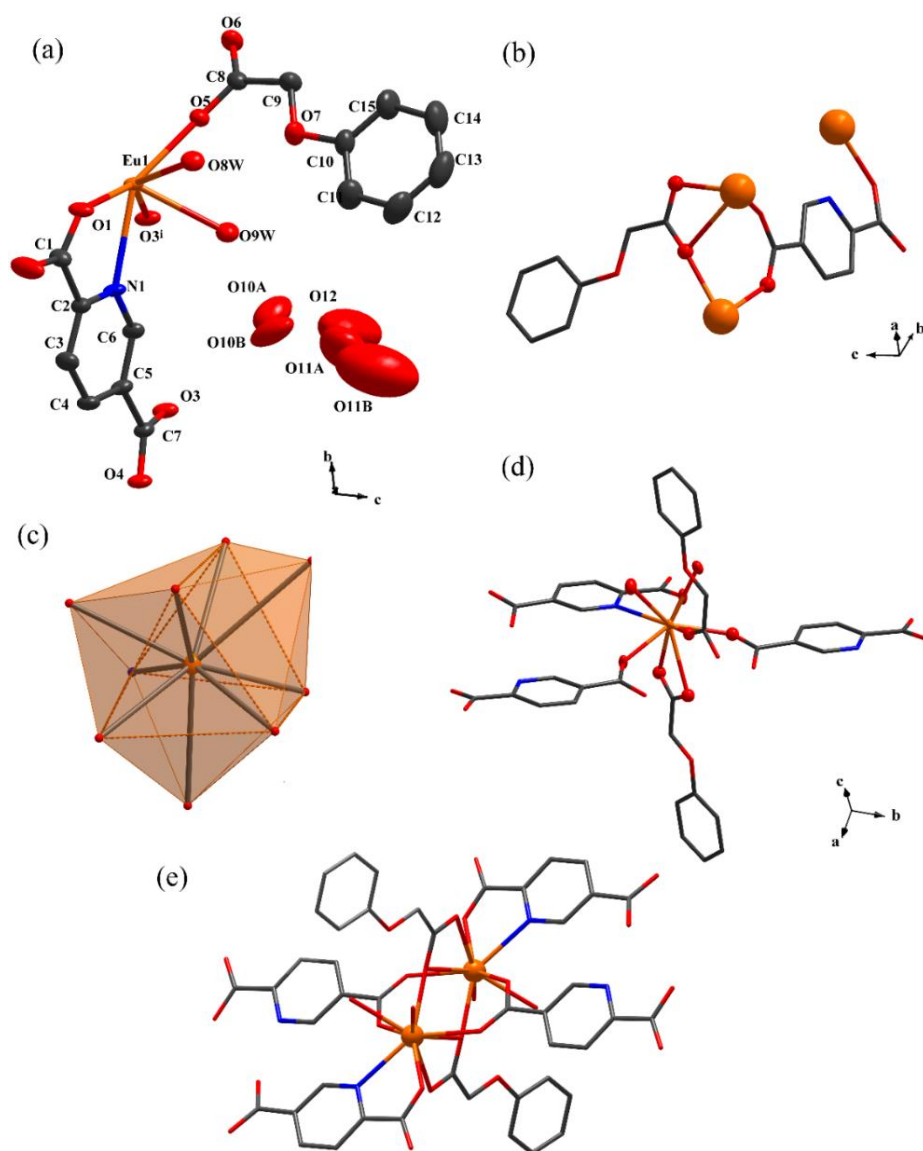


Fig. 2.3 Crystallographic illustrations of **1Eu**: (a) asymmetric unit (drawn using 50% thermal ellipsoids), (b) modes of the coordination adopted by poa⁻ and 2,5-pydc²⁻, (c) the TPRS-{EuNO₈} structural building motif, (d) the coordination environment of Eu^{III} and (e) the formation of the edge-shared TPRS-{Eu₂N₂O₆} dimer.

Compared to the previous reported LnCPs showing only 2,5-pydc²⁻ ligand of [Ln_{1.375}(pydc)₂(H₂O)₄] (Ln = Sm^{III}, Eu^{III}, Gd^{III}, Tb^{III}, Dy^{III}, Ho^{III}, and Er^{III}) [1], non-porous LnCPs was observed. This might be due to the crowned coordination, which might reduce the available space and led to be non-porosity. The introduction of auxiliary poa⁻ ligand into the framework is thus an important role to disrupt dense framework as we expected. To yield porous LnCPs, the influence of small auxiliary ligands to fulfill the coordination sphere of Ln^{III} might be a potential approach for further development.

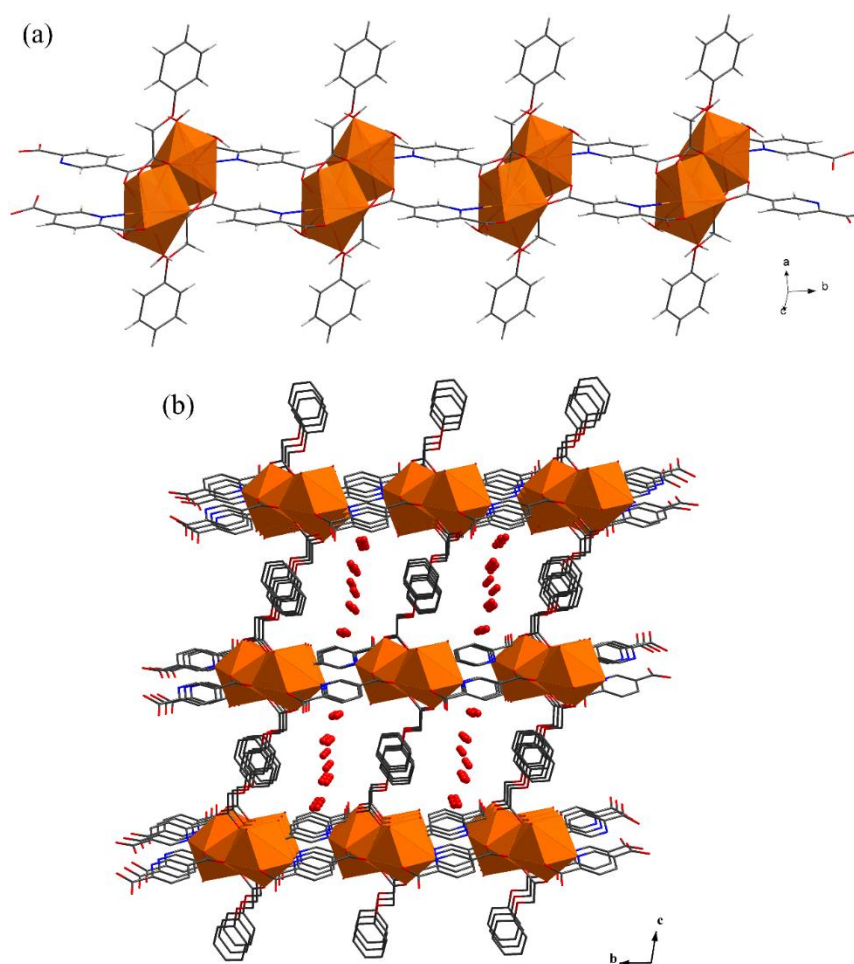


Fig. 2.4 Illustrations of (a) the *TPRS*-{EuNO₈}₂ dimer and a one-dimensional ladder in **1**_{Eu}, and their assembly viewed along (b) *a* axis.

2.3.2 Purity and thermal stability of **1Ln**

The isostructure **1Ln** and their purity were confirmed by PXRD experiments, which showed the consistency of all the diffraction peaks (Fig. 2.5), and elemental analysis (Table 2.5). A slight discrepancy in the intensity of a few diffraction peaks at low 2θ range from the patterns simulated from the single crystal data is commonly observed after the grinding of the crystals. The presence of their expected functional groups was affirmed based on FT-IR spectroscopy. The band assignments are shown in Fig. 2.6 and Table 2.4.

Thermal stability of **1Eu** as a representative of **1Ga**, **1Tb**, and **1Sm** was evaluated by TG/DTA analysis (Fig. 2.7). Evidently, the framework was retained even after the endothermic liberation of the crystallizing water molecules, which occurred at *ca.* 90 °C. The retained framework structure of **1Eu** after heating up to 90 °C for 30 min was also confirmed by PXRD (Fig. 2.8). On the other hand, the loss of the coordinating water molecules at *ca.* 200 °C led to the disruption of the framework. The substantial weight drop commenced at *ca.* 400 °C should attribute to the decomposition of the organic molecules. Therefore, the stability of the framework and the application at room temperature up to *ca.* 90 °C is verified.

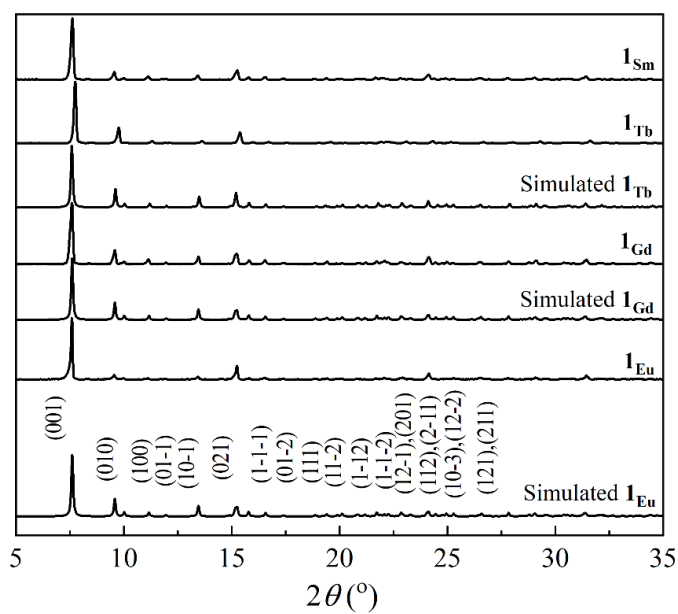


Fig. 2.5 PXRD patterns of 1_{Ln} compared with the patterns simulated from the corresponding single crystal data in the cases of 1_{Eu} , 1_{Gd} , and 1_{Tb} .

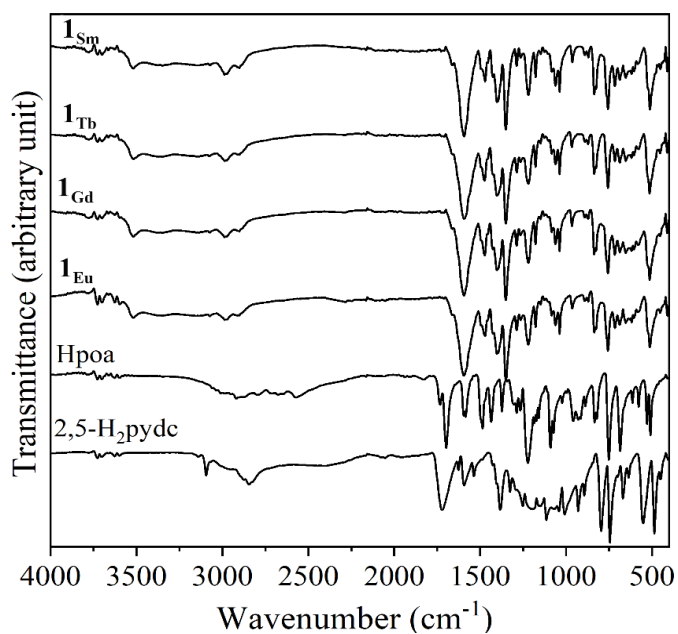


Fig. 2.6 FT-IR spectra of 1_{Ln} compared with those of H₂poa and 2,5-H₂pydc.

Table 2.4 Band assignments of FT-IR spectra of **1_{Ln}** compared with Hpoa and 2,5-H₂pydc

Band assignment	1_{Eu} (cm⁻¹)	1_{Gd} (cm⁻¹)	1_{Tb} (cm⁻¹)	1_{Sm} (cm⁻¹)
ν(O-H)	3520–3080	3519–2982	3519–2982	3520–2985
ν(COO), phenyl ether	1660	1660	1660	1663
ν(COO)	1593	1593	1593	1593
ν(C=N), aromatic	1495	1495	1493	1500
ν(C=C), aromatic	1473	1473	1473	1473
δ(C-H), alkyl	1422–1400	1422–1400	1422–1400	1422–1400
ν(C-O), COO ⁻	1350	1350	1350	1350
δ(C-H), aromatic	1288–1036	1285–1036	1285–1036	1288–1036
δ(C=C), mono-substituted	966	966	964	966
δ(C=C), di-substituted	891	891	891	891
δ(C-H), di-substituted	756	756	756	756
δ(C-H), mono-substituted	717	717	717	717
Ln ^{III} —O	513	511	511	514

Table 2.5 CHN analyses of **1_{Ln}**

		C (%)	H (%)	N (%)
1_{Eu}	Anal. Calcd for EuC ₁₅ O ₁₂ NH ₂₀	32.37	3.61	2.51
	Found	32.27	3.40	2.56
1_{Gd}	Anal. Calcd for GdC ₁₅ O ₁₂ NH ₂₀	31.97	3.58	2.49
	Found	31.79	3.08	2.94
1_{Tb}	Anal. Calcd for TbC ₁₅ O ₁₂ NH ₂₀	31.87	3.57	2.78
	Found	31.71	3.11	2.86
1_{Sm}	Anal. Calcd for SmC ₁₅ O ₁₂ NH ₂₀	32.36	3.62	2.52
	Found	32.51	3.39	2.67

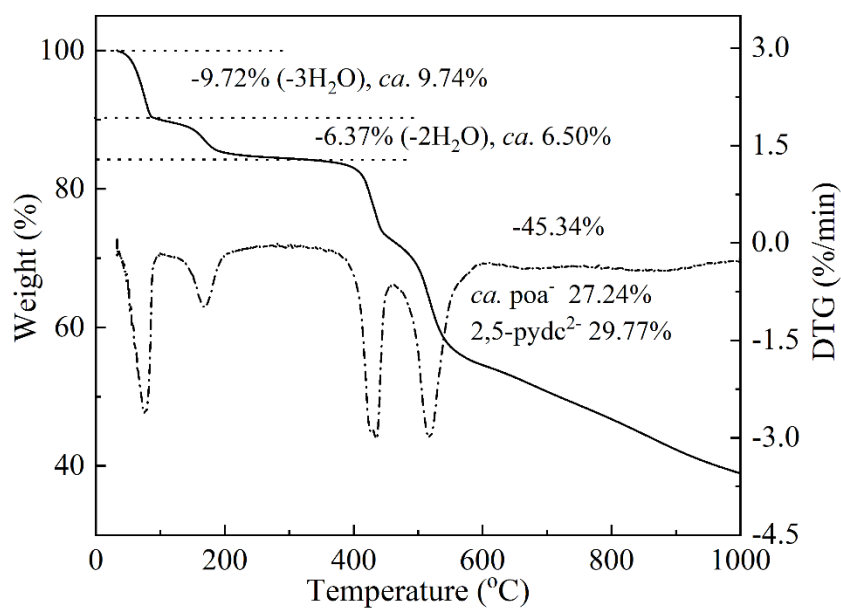


Fig. 2.7 TG/DTA curves of **1Eu**.

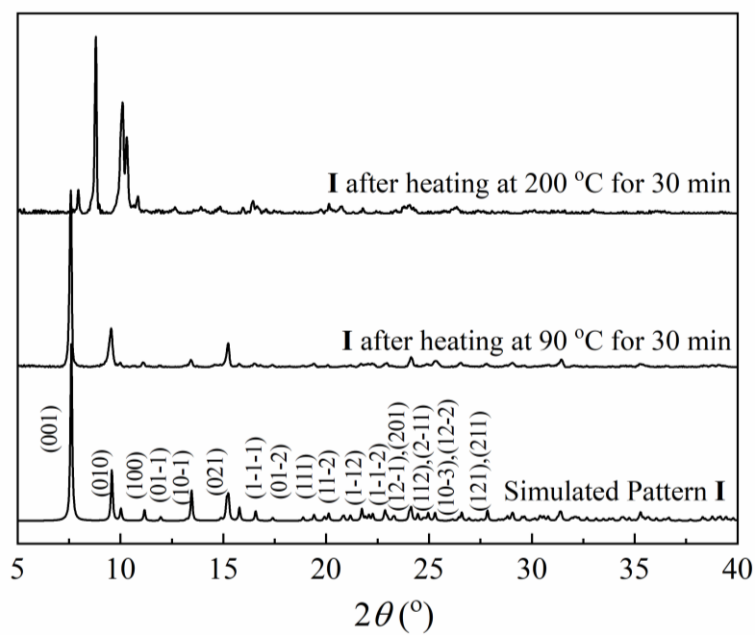


Fig. 2.8 PXRD patterns of **1Eu** before and after the treatment at 90 and 200 °C for 30 min compared with the patterns simulated from the single crystal data.

2.3.3 UV-Vis and photoluminescent properties of 1_{Ln}

The UV-Vis spectra of 1_{Ln} are demonstrating the ligand centered $\pi \rightarrow \pi^*$ absorption at 219 nm and $n \rightarrow \pi^*$ absorption at 268, 274, and 281 nm (Fig. 2.9). Compared to the $\pi \rightarrow \pi^*$ absorption of Hpoa (217 nm) and 2,5- H_2 pydc (222 nm), the $\pi \rightarrow \pi^*$ absorption of 1_{Ln} is red shifted from Hpoa but blue shifted from 2,5- H_2 pydc. Similar fashion was also observed in the $n \rightarrow \pi^*$ absorption of Hpoa (268 and 275 nm) and 2,5- H_2 pydc (270 nm). This feature corresponds to the increased molecular rigidity of organic ligands upon the coordinating to Ln^{III} metal centers of both terminations of 2,5-pydc²⁻ and π - π stacking between neighbored pyridyl groups. In the poa⁻ ligand case, the contrarily enhanced disarray in poa⁻ molecular due to the influences of both the O—H \cdots O and C—H \cdots O hydrogen bonding at phenyl rings, leading to more flexibility and distortion in poa⁻ ligand. This is consistent with the shifting of the transition features and consistently manifested through the significantly larger thermal ellipsoids of O and C atoms of poa⁻.

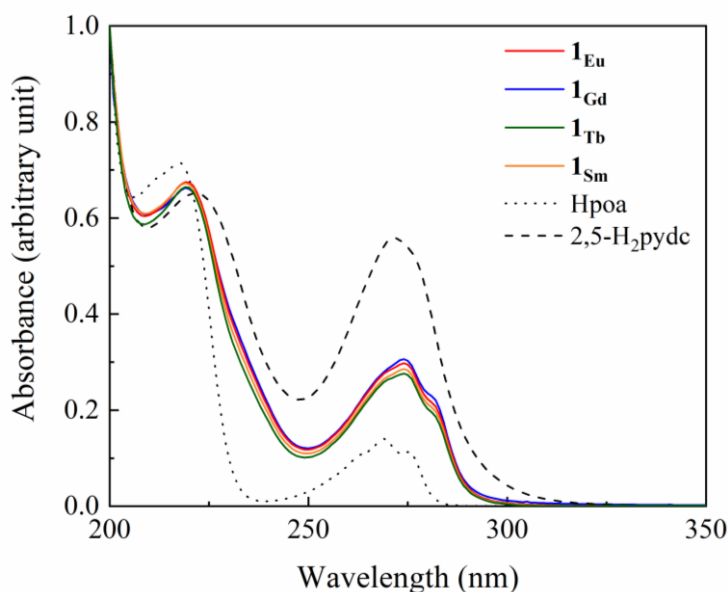


Fig. 2.9 UV-Vis spectra of 1_{Ln} (solid line) compared to the Hpoa (dash line) and 2,5- H_2 pydc (dash-dot line) ligands.

2.3.4 Room-temperature photoluminescent spectra of 1_{Ln}

The room-temperature emission spectra of 1_{Ln} were carried out under the excitation at 370 nm (Fig. 2.10), which revealed the effective sensitization of the characteristic $f-f$ emissions from 1_{Eu} ($^5D_0 \rightarrow ^7F_J$, $J = 1 - 4$), 1_{Tb} ($^5D_4 \rightarrow ^7F_J$, $J = 6 - 3$) and 1_{Sm} ($^4G_{5/2} \rightarrow ^6H_J$, $J = 5/2 - 11/2$). Based on the emission spectra of 1_{Ga} , the triplet state energies of the sensitizers were estimated [14], which showed a broad energy range of *ca.* 15,000 – 25,000 cm^{-1} . Compared with the emission spectra of 2,5- H_2 pydc and Hpoa, this energy range encloses the combined range of the ligand-centered emissions, which could be taken as the range of triplet state energies of the co-existing sensitizers without considering the interactions between the triplet state energies of the two sensitizers [15]. According to the literatures [16,17], the energy gap between the sensitizer's triplet state energy and the Ln^{III} accepting level should be approximately *ca.* 2500 – 3500 cm^{-1} , leading to the high efficiency of the sensitization of the $f-f$ emissions. With respect to the common accepting energy levels of Eu^{III} ($^5D_0 = 17,270\text{ cm}^{-1}$, $^5D_1 = 19,030\text{ cm}^{-1}$) and Tb^{III} ($^5D_4 = 20,470\text{ cm}^{-1}$), the sensitization of 1_{Eu} and 1_{Tb} should be effective. This corresponds excellently with the absence of the ligand-centered emission in the spectra of 1_{Eu} and 1_{Tb} [14].

Regarding the emission spectra of 1_{Sm} , the intensity and broad emission in the emission range of 2,5- H_2 pydc were decreased. While the intense and broad emission of Hpoa was still present. Based on our assumption on the non-interacting triplet states of the two co-existing sensitizers, the sensitization of Sm^{III} can be from only 2,5-pydc²⁻. On the other hand, the poor emission profile may ascribe to the competitive non-radiative emissions caused by the excessive number of the low-lying energy multiplex of Sm^{III} , each of which is divided by small energy gaps [1,18].

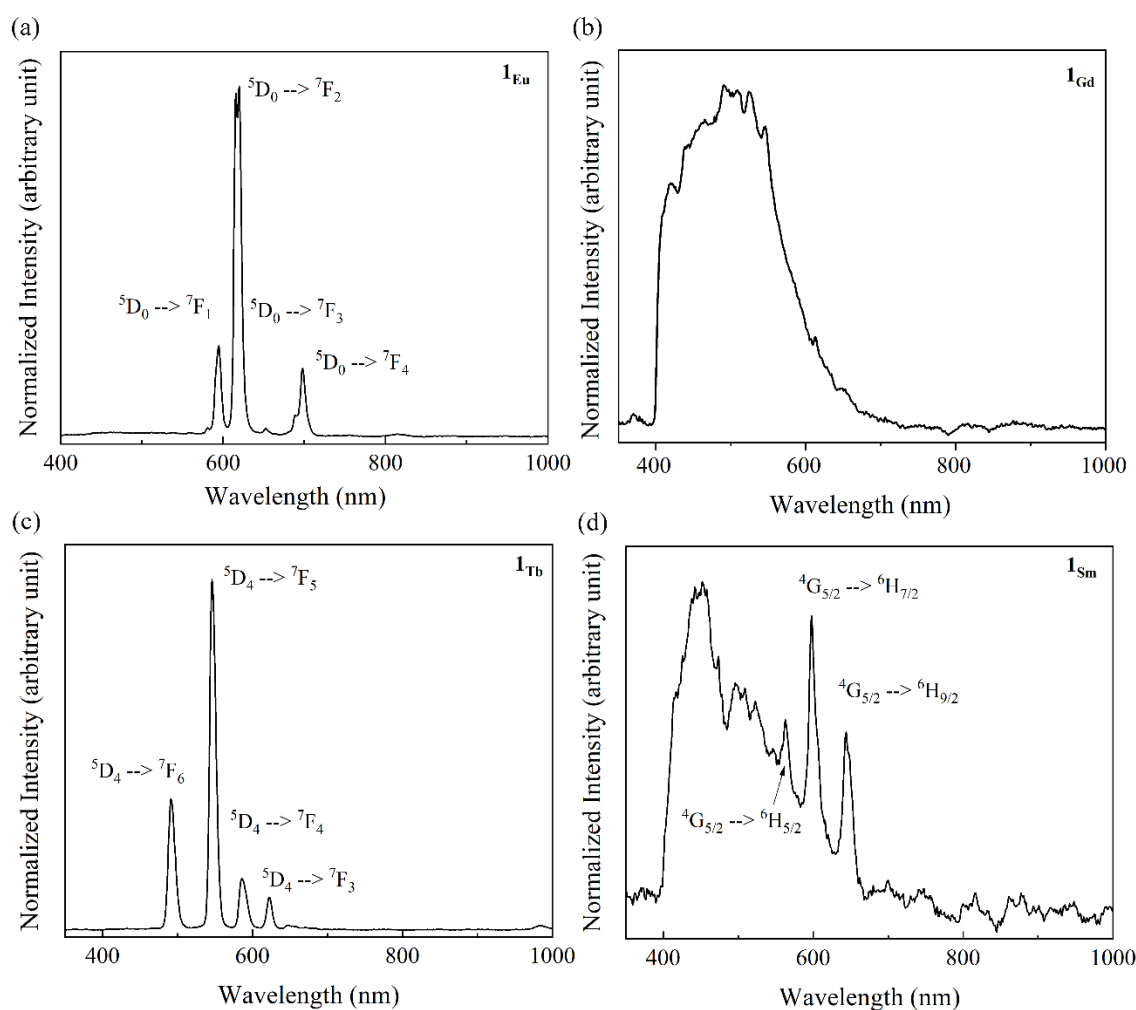


Fig. 2.10 Room-temperature emission spectra (solid line) of (a) **1Eu** (b) **1Gd** (c) **1Tb**, and (d) **1Sm**.

2.3.5 Chemical robustness of **1Eu** and its selective sensing of ammonia gas

Inspired by its opened supramolecular structure, specific porosity, availability of potentially functional groups on the ligands, and the intense red emission of Eu^{III} , **1Eu** was chosen for further experiments on ammonia gas sensing. The robustness of **1Eu** upon exposure to different volatile organic compounds (VOCs) in gaseous state including ammonia, MeOH, EtOH, acetone, MeCN, THF, *n*-hex, benzene, CHCl_3 , and CH_2Cl_2 , was first examined. Regarding the PXRD results (Fig. 2.11), **1Eu** was substantially robust with respect to every experimented VOCs even after the prolonged contact. Following the confirmation of its stability, the photoluminescent responses of **1Eu** upon being exposed

to these VOCs were then explored. Intriguingly, only ammonia caused the significant and reliable quenching of the most intense $\text{Eu}^{\text{III}}:5\text{D}_0 \rightarrow 7\text{F}_2$ emission. It is therefore conclusive that the quenching of $\mathbf{1Eu}$ by ammonia is selective (Fig. 2.12), which is not due to the collapse of the framework. This obvious selectivity corresponds well with the small molecular-sized window of the framework structure of $\mathbf{1Eu}$, which prohibits the other VOCs possessing larger molecular structures from accessing into the framework. The extremely high vapor concentration of 4000 ppm and the lengthy exposure time of 17 h were decided for these experiments to ensure the selectivity to ammonia and the robustness of $\mathbf{1Eu}$. It should be noted that the quenching of the $\text{Eu}^{\text{III}}:5\text{D}_0 \rightarrow 7\text{F}_2$ emission by ammonia gas at this concentration could be apparent within only a few minutes.

Considering the framework structure of $\mathbf{1Eu}$, there are several functional groups showing potential to form hydrogen bonding interactions with ammonia gas, *i.e.* the uncoordinated O atom of carboxylate and the pyridine ring of 2,5-pydc²⁻ as well as the O atom and the phenyl ring of poa⁻ (Fig. 2.3). These functional groups notably aligned along the internal surface of the framework's one-dimensional channel and therefore should be susceptible to the incoming ammonia gas. This type of host-guest interactions may induce the change in molecular rigidity and consequently the energy levels involving with the sensitization process [19]. This assumption is well supported by the additional $\pi \rightarrow \pi^*$ transitions at 202 nm, the blue shift of the $n \rightarrow \pi^*$ transitions from 268, 274, and 281 nm to 263, 269 and 276 nm, respectively, after being exposed to ammonia (Fig. 2.13). These changes agree well based on the assumption of the interactions with ammonia to be on the organic motifs in the framework structure of $\mathbf{1Eu}$ to a change in the triplet state energies [19]. This assumption has been evident through the DFT calculation, which suggests the formation of hydrogen bonding interaction between the analyte and the framework (Fig. A-1 and Table A-1). Based on the calculation, the plausible active sites have been disclosed. Regarding the TG/DTA results, the crystallizing and coordinated water still occurred until *ca.* 90 °C and 200 °C, all those water molecules including coordination about Eu^{III} thus remained. Therefore, Eu^{III} should not be any direct interaction between ammonia.

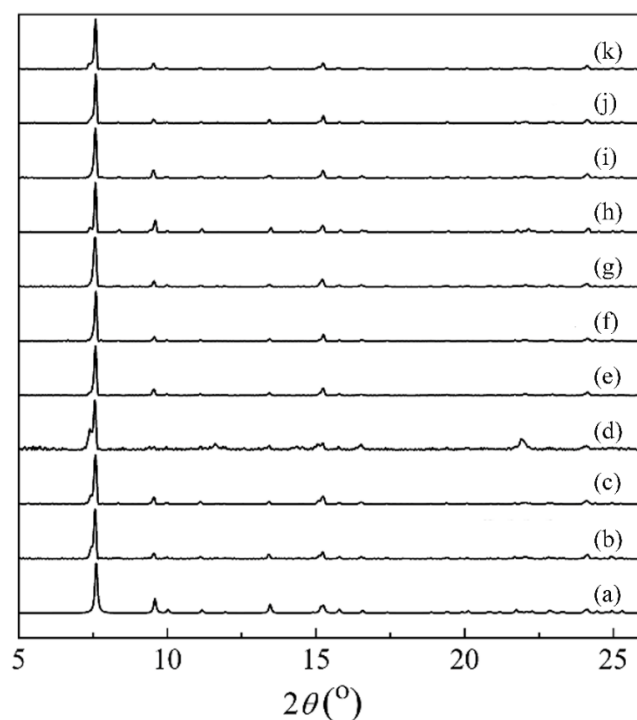


Fig. 2.11 Simulated PXRD patterns of **1Eu** (a) compared with the PXRD patterns after exposed to MeOH, EtOH, ammonia, acetone, MeCN, THF, *n*-hex, benzene, CHCl₃, and CH₂Cl₂ (b-k), respectively.

To study the triplet state energies of the poa^- and 2,5-pydc²⁻ sensitizers after contact with ammonia, photoluminescent spectrum of **1Ga** after being exposed to ammonia gas was collected to ensure the non-sensitization effect of Gd^{III} (Fig. 2.14). The change in the emission profile of **1Ga** was certain with a drastic drop in intensity of the emission in the 400 to 480 nm range, which indicated the inefficacy of poa^- as a sensitizer. The shift of the broad and intense band centering at *ca.* 550 nm (18,200 cm⁻¹), which clearly reflected the lowered energy range of 2,5-pydc²⁻. These altered features indicate the modulation of the triplet state energies of both sensitizers to be more prominent in the lowered energy range implying the shrinkage of the energy gap with respect to the accepting energy levels of Eu^{III} in the case of **1Eu**. It can therefore be assumed that the interactions between ammonia and **1Eu** disturb the energy gap between the triplet state energies of the sensitizers, which in turn inefficiency of the sensitization process, leading to the quenching of the Eu^{III}:⁵D₀→⁷F₂ emission. It is worth noted that the emission profile of **1Eu** was restored after being left under ambient air or warmed at low temperatures. The

reversible interactions between 1_{Eu} and ammonia gas are certainly suggested as hydrogen bonding, which can be easily released from the framework. These features are essential to encourage the possibility in recovering of 1_{Eu} and its reusability in sensing.

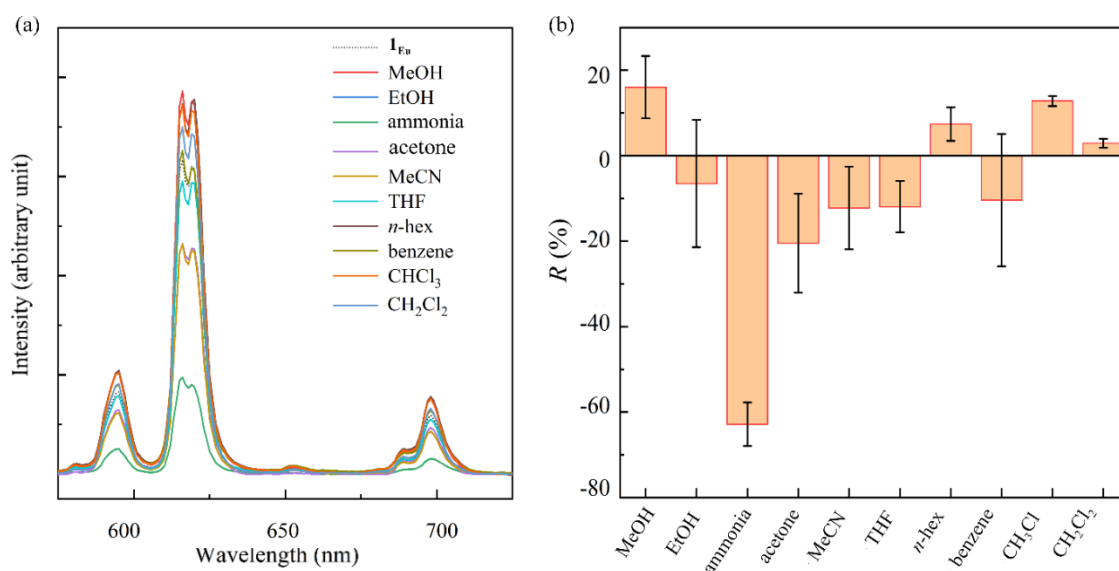


Fig. 2.12 (a) Emission spectra of 1_{Eu} after being exposed to VOCs and (b) the corresponding R values.

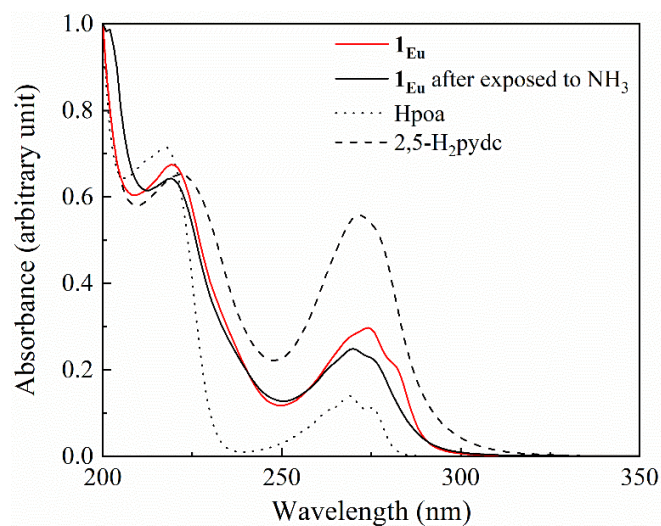


Fig. 2.13 UV-Vis spectra of 1_{Eu} (solid-red line) and after being exposed to ammonia gas (solid-blank line) compared to the Hpoa (dash line) and 2,5- H_2 pydc (dash-dot line) ligands.

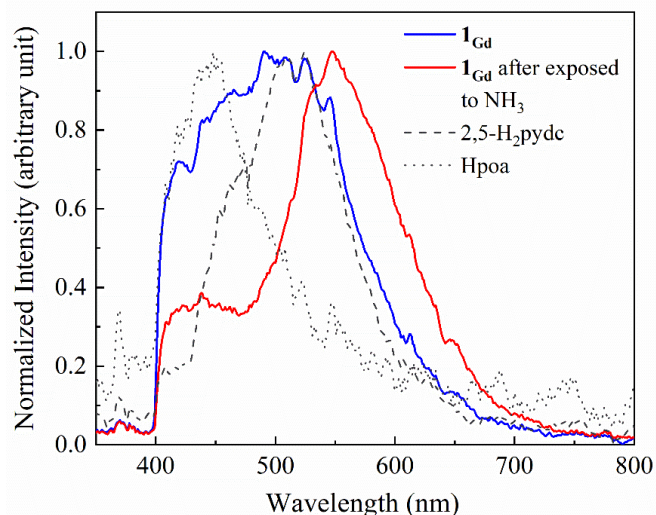


Fig. 2.14 Emission spectrum of **1_{Gd}** before and after being exposed to ammonia compared with those of 2,5-H₂pydc and Hpoa.

2.3.6 Characterization of **1_{Eu}**/PVA composite film and its photoluminescence

To fabricate film of **1_{Eu}**/PVA was chosen as a matrix because of (i) its hydrophilic nature, which allows the incorporation of a variety of aqueous-based guest molecules; (ii) its ready formulation as a film, which naturally produced folds during drying and demolding; (iii) its inertness towards guest molecules [20]. A drop-cast method was employed due to its simple handling and inexpensive instrumentation [21]. After attempting various **1_{Eu}**-to-PVA mole ratios, a film with a smooth and crack-free surface could be obtained only when it was fixed at 1:60 mole ratio (Fig. 2.15a). The thickness of the film was estimated from the SEM images and found to be *ca.* 100 μm . The mappings of the composing elements of both the surface and the cross-section area of the fabricated film displayed a good dispersion of **1_{Eu}** in the casted film (Fig. 2.15). Despite the smooth surface, the cracking and the existence of holes were apparent inside which should own to the drying condition. These defects were apparently insignificant to the photoluminescent profile of **1_{Eu}** (Fig. 2.16). The emission spectrum of the **1_{Eu}**/PVA film was identical to **1_{Eu}** displaying the characteristic emissions of $^5\text{D}_0 \rightarrow ^7\text{F}_J$ ($J = 1 - 4$) of Eu^{III} . In addition, the remained structure of **1_{Eu}** in the **1_{Eu}**/PVA film was also confirmed by the PXRD result displaying well matching with the pristine **1_{Eu}**.

To further evaluate the stability of the film after long storage, it was stored under ambient conditions for a month. The photoluminescent profile of the $1_{Eu}/PVA$ film after the long storage was also collected (Fig. 2.16), which showed the remained profile $^5D_0 \rightarrow ^7F_J$ ($J = 1 - 4$) of Eu^{III} compared with the freshly prepared one. This feature should indicate excellent stability in long-term storage and promising application as ammonia sensor. In addition, the film did not show any physical deterioration.

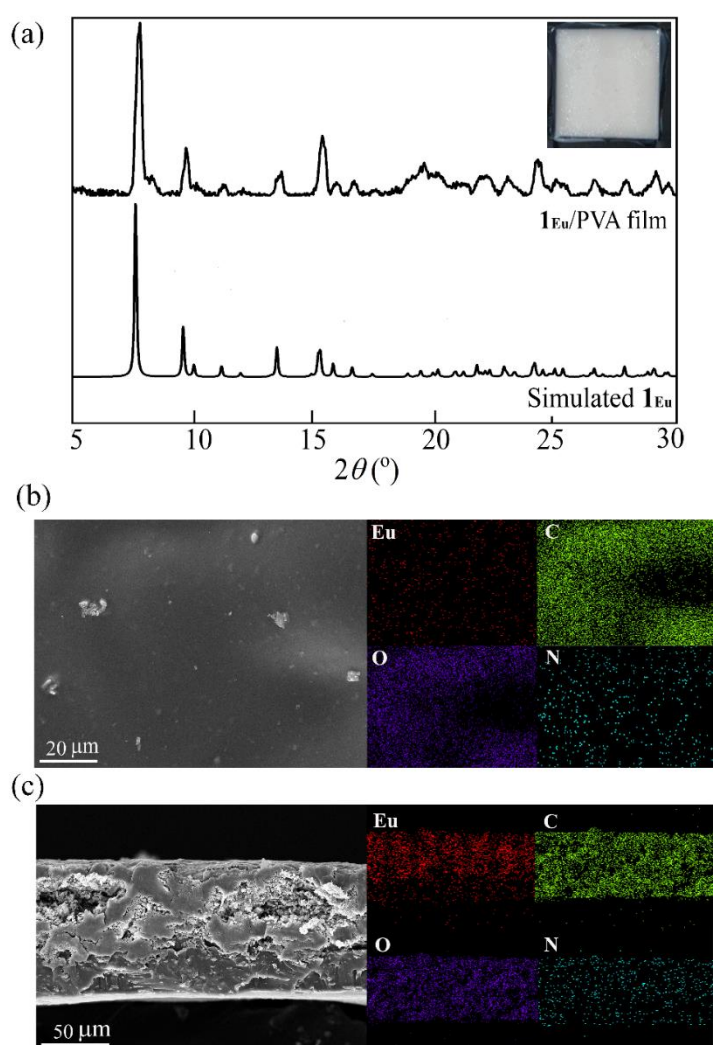


Fig. 2.15 (a) PXRD pattern of $1_{Eu}/PVA$ film (with a photo of the film in the inset) (b) SEM images with the corresponding elemental mappings showing (b) the top surface) and (c) the cross-sectional area of the film.

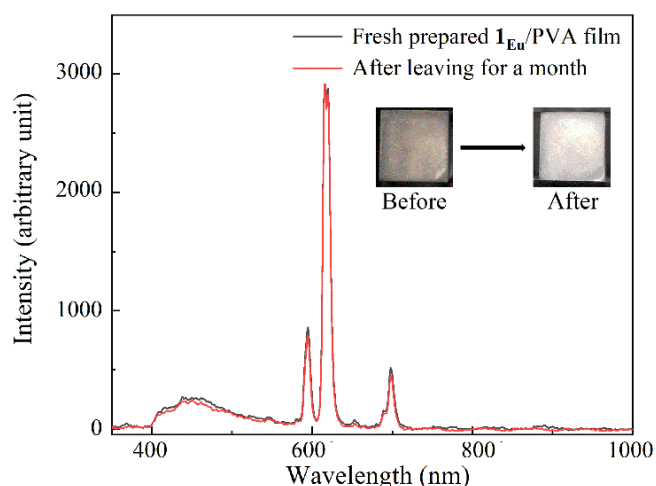


Fig. 2.16 Photoluminescent spectra of the freshly prepared $1\text{Eu}/\text{PVA}$ film compared with that left at ambient condition for a month (photos of the films shown in insets).

2.3.7 Determination of ammonia gas concentration using $1\text{Eu}/\text{PVA}$ film

The exposure of $1\text{Eu}/\text{PVA}$ film to different VOCs provided almost identical responses to those of 1Eu (Fig. 2.17). Selective quenching to ammonia gas in photoluminescence of $1\text{Eu}/\text{PVA}$ film was clearly observed with substantially lower vapor concentration of 15.0 ppm and shorter exposure time of 30 min. Photoluminescent signals of the film have been demonstrated to be reliable with smaller values of standard deviation (SD) than the ground crystals sample on the basis of the triplicate data, especially on ammonia gas. The impregnation of 1Eu within the PVA film apparently did not cause the deviation in responses of 1Eu to ammonia and the other VOCs. Therefore, the fabrication of $1\text{Eu}/\text{PVA}$ film could be successfully achieved without any adverse effect on the sensing.

To optimize the ammonia gas sensing by $1\text{Eu}/\text{PVA}$ film, exposure time, which is one of the important parameters in real practice, was studied using the ammonia gas concentration of 10.0 ppm (Fig. 2.18a and b). The quenching of the $\text{Eu}^{\text{III}}: {}^5\text{D}_0 \rightarrow {}^7\text{F}_2$ emission was apparently rapid and could be observed since the first minute of contact. The substantial turn-off of *ca.* 50% could nonetheless be yielded at *ca.* 30 min, which was decided for further study on the sensing conditions. Stability of the photoluminescent signal reflected through the preserved emission profile of $1\text{Eu}/\text{PVA}$ film throughout the experiments even after 120 min of exposure time should be noted.

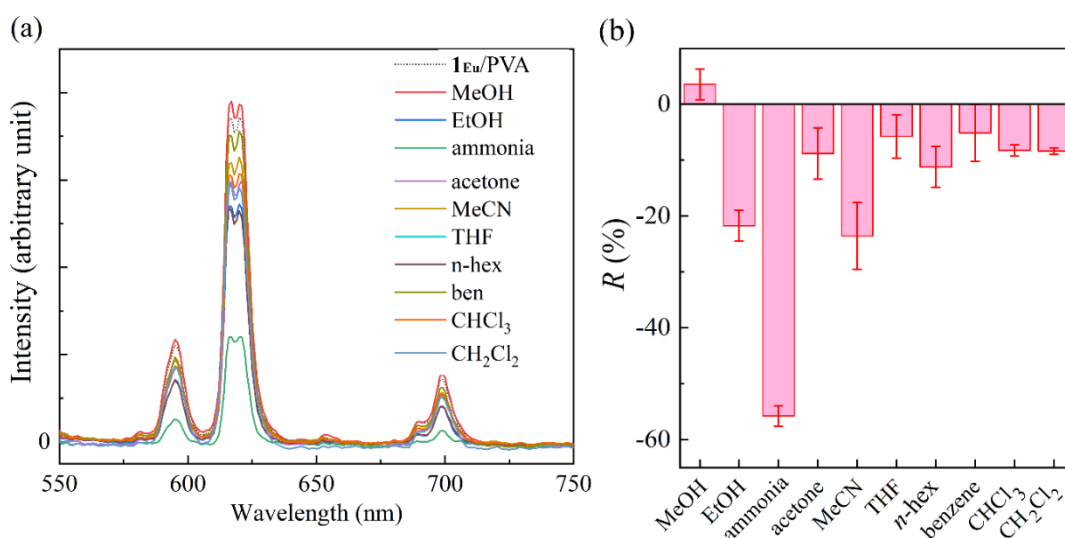


Fig. 2.17 Responses of $1_{Eu}/PVA$ film in terms of (a) emission spectra and (b) the corresponding R values after contact with different VOCs vapors (15.0 ppm and 30 min).

At the constant exposure time of 30 min, the gradual quenching in the intensity of the $^5D_0 \rightarrow ^7F_J$ ($J = 1 - 4$) of Eu^{III} was revealed with increased concentration of ammonia gas from 0.20 to 15.0 ppm, without any shift in position of every emission (Fig. 2.18c). Founded on the change of the $^5D_0 \rightarrow ^7F_2$ emission with the pristine $1_{Eu}/PVA$ film, the R values were calculated and plotted against the ammonia vapor concentration over the range of 0.50 to 10.0 ppm with excellent linear correlation (Fig. 2.18d). Based on the slope of the linear plot and the SD of the triplicate data of the reference (A_0), the sensitivity and limit of detection (LOD) of 4.04 % and 0.14 ppm were calculated, respectively. Compared with the other photoluminescent sensing probes based CPs-films (Table 2.6), *e.g.* Tb-BTC inkjet printed patterns (LOD = 0.3 ppm, sensitivity = $0.0586 \text{ \%} \cdot \text{ppm}^{-1}$) [22], Eu@UMOF-Eu-LA (LOD = 9 ppm, sensitivity = $0.016 \text{ \%} \cdot \text{ppm}^{-1}$) [23], $Eu^{3+}@Ga(OH)bpydc$ (LOD = 2.4 ppm, sensitivity = $0.015 \text{ \%} \cdot \text{ppm}^{-1}$) [19], Phen-Eu-IM@BMOF (LOD = 12.750 ppm, sensitivity = $0.0006 \text{ \%} \cdot \text{ppm}^{-1}$) [24], TMOF-6 (Cl) (LOD = 12 ppm, sensitivity = $0.045 \text{ \%} \cdot \text{ppm}^{-1}$) [25], and 1-PVDF membranes (LOD = 22 ppm, sensitivity = $0.0243 \text{ \%} \cdot \text{ppm}^{-1}$) [26], the $1_{Eu}/PVA$ film provided a remarkably low LOD and high sensitivity. It is worth noted that the yielded working range of concentration and precision provided by $1_{Eu}/PVA$ are comparable to those materials

applied for breath ammonia sensors, which is a useful biomarker predicting chronic kidney disease (0.4 – 1.8 ppm) and lung diseases (0.8 – 14.7 ppm) [27,28], *e.g.* SnO¹⁺ (0.5 – 5 ppm) [29], Fc@ZIF-8 (0.4 – 20 ppm) [30]. With respect to the established linear calibration, the accuracy and precision of the three known ammonia vapor concentrations, *i.e.* 3.50, 6.50, and 7.50 ppm, were evaluated (Fig. 2.18d). The read-out concentrations from the calibration curve were closely similar to the expected values, which are summarized in Table 2.7. The corresponding statistical data are also listed in Table 2.7.

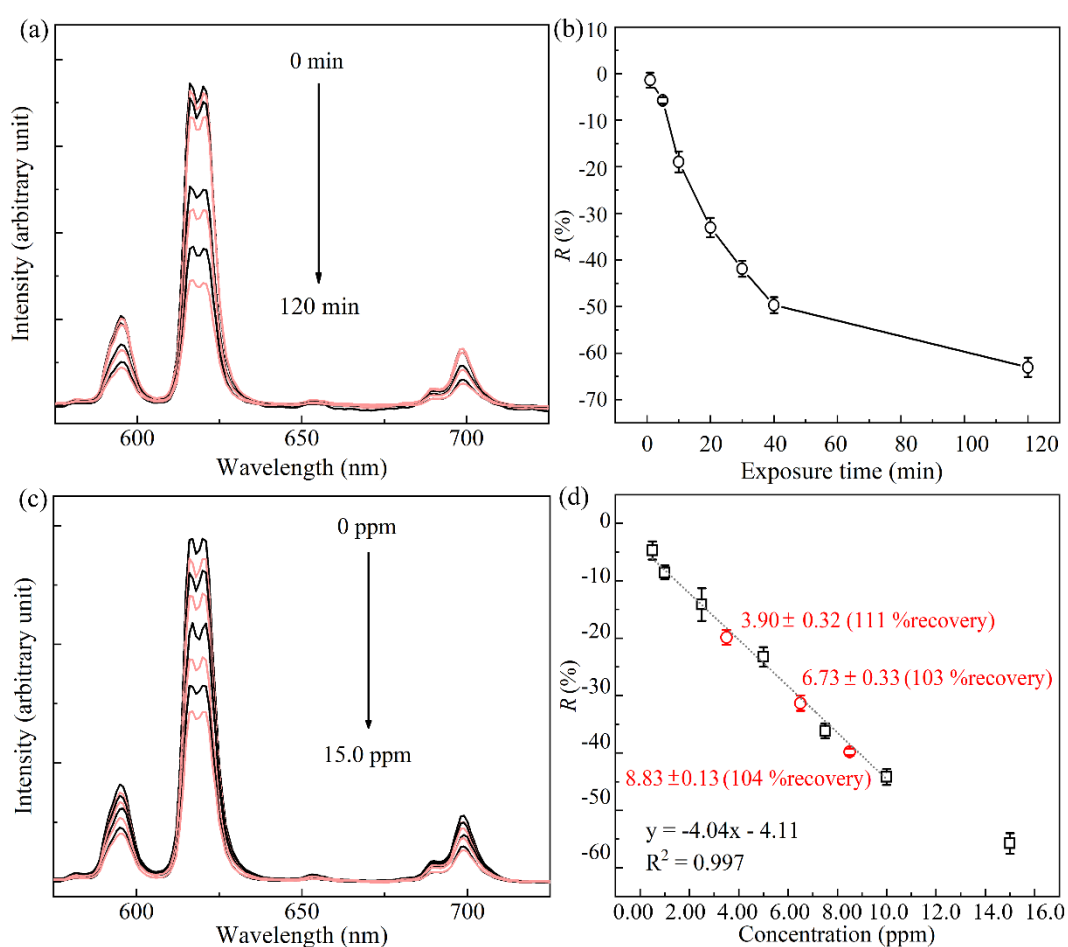


Fig. 2.18 (a, c) Emission spectra of 1Eu/PVA film for time-dependence at 10 ppm of ammonia vapor concentration and concentration-dependence at 30 min contact time and (b, d) the consisted R values calculated from triplicate data.

Table 2.6 Performances of exemplified photoluminescent CP-films used for ammonia sensing^ξ

Sensor	Concentration range (ppm)	Detection limit (ppm)	Contact time (min)	Sensitivity (% · ppm ⁻¹)	Repeatability	%Recovery	RSD (%)	Ref
Eu ^{III} @Ga(OH)bpydc	10-500	2.4	4	0.015	<i>na</i>	<i>na</i>	<4	[19]
Tb-BTC	5-80	0.3	2	0.0586	<i>na</i>	<i>na</i>	<i>na</i>	[22]
Eu@UMOF-Eu-LA	25-400	9	5	0.016	<i>na</i>	<i>na</i>	<i>na</i>	[23]
Phen-Eu-IM@BMOF	0- 000	<i>ca.</i> 13	60	0.0006	<i>na</i>	<i>na</i>	<i>na</i>	[24]
TMOF-6 (Cl)	25-400	12	<i>ca.</i> 1.8	0.045	<i>na</i>	<i>na</i>	<i>na</i>	[25]
1-PVDF	0-3000	22	<i>na</i>	0.0243	<i>na</i>	<i>na</i>	<i>na</i>	[26]
MIL-124@Eu ^{III}	100-1350	26.2	5	0.0002	<i>na</i>	<i>na</i>	<i>na</i>	[31]
MR-MOF-RE	0-300	<i>ca.</i> 11	-	0.005	<i>na</i>	<i>na</i>	<i>na</i>	[32]
ZA-MPTMS-Eu-UiO-67	0-200	<i>ca.</i> 8.4	60	0.009	<i>na</i>	<i>na</i>	<i>na</i>	[33]
SNNU-88	3-100	<i>na</i>	>10	<i>na</i>	<i>na</i>	<i>na</i>	<i>na</i>	[34]
1Eu/PVA	1.00-15.0	0.61	30	4.04	95% (at 3.50 ppm)	111 (at 3.50 ppm)	3.3 (at 3.50 ppm)	This work
					<i>na</i>	103 (at 6.50 ppm)	<i>na</i>	
					97% (at 8.50 ppm)	104 (at 8.50 ppm)	1.5 (at 8.50 ppm)	

^ξ*na* = not available

Table 2.7 The read-out ammonia concentrations and statistical data

Expected Conc. (ppm)	Read-out conc. ($\pm SD$) (ppm)	%recovery	%RSD
3.50	3.90 (± 0.32)	111	8.2
6.50	6.73 (± 0.33)	103	4.9
8.50	8.83 (± 0.13)	104	1.5

2.2.8 Recyclability of $\mathbf{1}_{Eu}/PVA$ film

Recyclability and robustness over several cycles of the measurements and restorations of the film are highly essential for practical sensing probes. This aspect of $\mathbf{1}_{Eu}/PVA$ film was evaluated using two different ammonia gas concentrations of 3.50 and 8.50 ppm at 30 min of exposure time. To regenerate the used film, it was simply left under ambient pressure and temperature overnight. The emission spectra of the regenerated films were checked before the re-use to ensure complete restoration of all the $Eu^{III}:^5D_0 \rightarrow ^7F_J$ ($J = 1 - 4$) emissions. Ten successive cycles of the measurements and regenerations were explored (Fig. 2.19 and 2.20), disclosing excellent repeatability of 95% and 97% and small value of the variation of 3.3 and 1.5 %RSD for the expected concentration of 3.50 ppm and 8.50 ppm, respectively. These values indicate the excellent reliability and reusability of the film. Among the ammonia sensors based on CPs-films, *e.g.* $Eu^{III}@Ga(OH)(bpydc)$ (%RSD <4%) [19], the values obtained for the $\mathbf{1}_{Eu}/PVA$ film are exceptional.

The SEM images with the corresponding mappings of the comprising elements of the $\mathbf{1}_{Eu}/PVA$ film after ten cycles were carried out (Fig. 2.21). The reused film appeared to remain approximately the same although a slight increase in surface roughness was apparent. The mappings of the comprising elements accordingly exhibited an insignificant change in the distribution of the elements on both the surface and the cross-section of the film. The emission profile of $Eu^{III}:^5D_0 \rightarrow ^7F_J$ ($J = 1 - 4$) was apparently the same as those freshly prepared. It is therefore conclusive

that the long storage of at least a month did not result in any deterioration of the film. Therefore, it should be concluded that the film is significantly stable and robust during several cycles of the measurement-and-regeneration process.

Table 2.8 Read-out concentration (ppm) from the calibration curve for tenth measurements compared with the expected concentration of 3.50 and 8.50 ppm

Cycle number	Read-out conc. (ppm)	Read-out conc. (ppm)
1	3.44	8.70
2	3.71	8.71
3	3.47	8.83
4	3.79	8.61
5	3.52	8.50
6	3.66	8.50
7	3.57	8.83
8	3.93	8.67
9	3.75	8.97
10	3.71	8.70

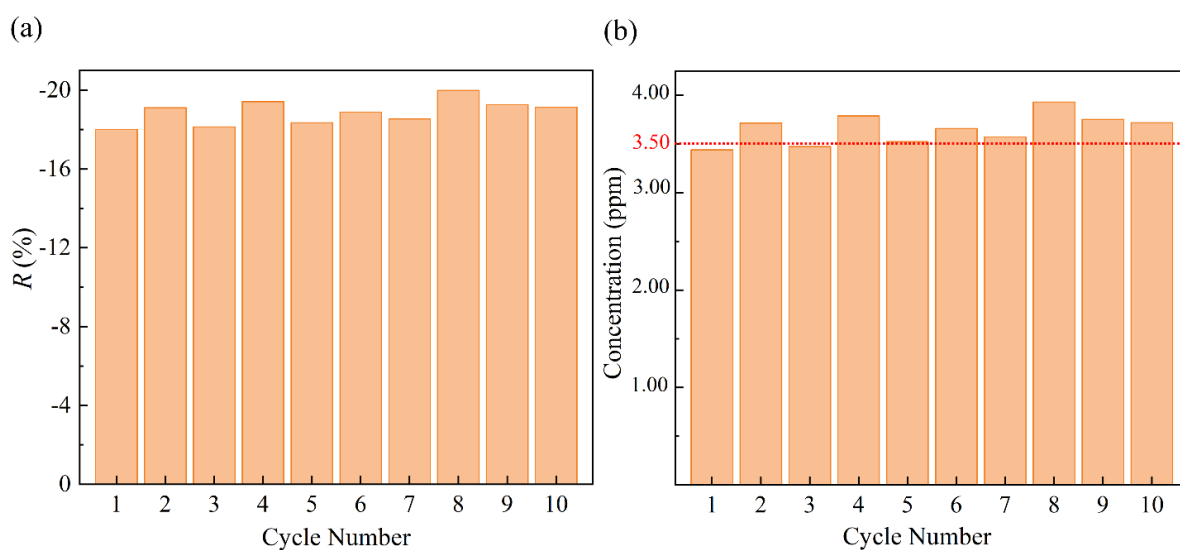


Fig. 2.19 (a) The R values of the $1E_u$ /PVA films over ten cycles of the measurement-and-regeneration and the (b) corresponding concentrations of ammonia vapor determined using the standard calibration method for the expected concentrations of 3.50 ppm.

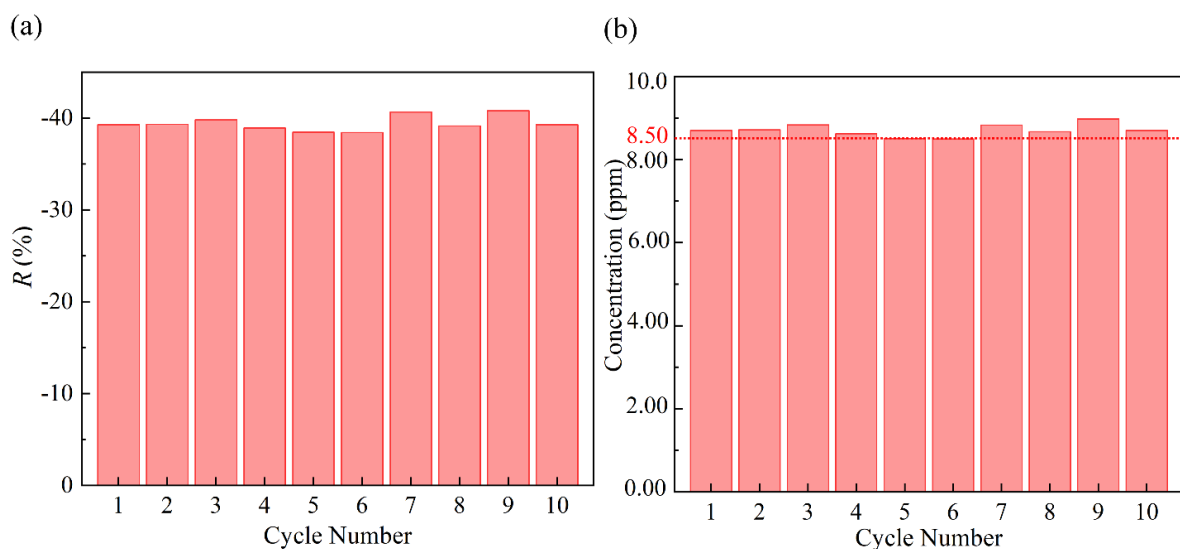


Fig. 2.20 (a) R values of the $1E_u$ /PVA films over ten cycles of the measurement-and-regeneration and (b) the corresponding concentrations of ammonia vapor determined using the standard calibration method for the expected concentrations of 8.50 ppm.

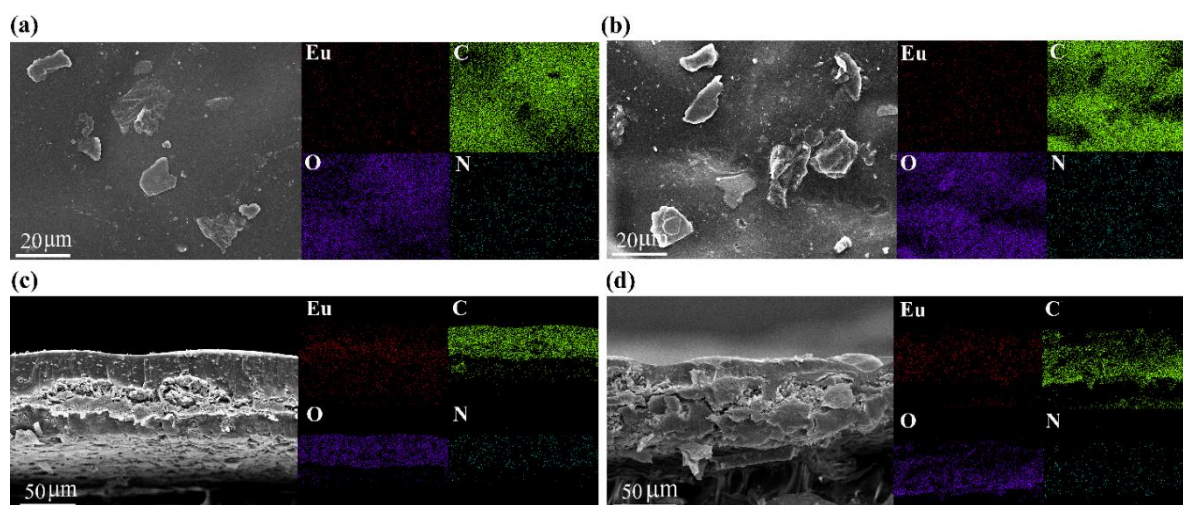


Fig. 2.21 SEM images and the elemental mapping analysis of the $\mathbf{1}_{Eu}$ /PVA-film after ten successive measurements of ammonia vapor sensing in (a, b) top-view and (c, d) cross-section for 3.50 ppm and 7.50 ppm, respectively.

2.4 Conclusions

Aiming at the design of porous LnCPs using dicarboxylate ligand, *i.e.* 2,5-pydc²⁻ as the linker to extend the framework and poa⁻ as the fulfilled ligand of the coordination sphere of Ln^{III} to avoid dense framework, a new series of isostructural [Ln(poa)(2,5-pydc)(H₂O)₂] \cdot 3H₂O ($\mathbf{1}_{Ln}$), where Ln = Eu^{III}, Gd^{III}, Tb^{III} and Sm^{III}, were synthesized and characterized. The single crystal data revealed the open framework structure with *ca.* 21% void and $4.2 \times 5.5 \text{ \AA}^2$ opening. The efficient sensitization of the *f-f* emissions of Eu^{III} ($\mathbf{1}_{Eu}$) and Tb^{III} ($\mathbf{1}_{Tb}$) by poa⁻ and 2,5-pydc²⁻ were disclosed. Found on the specific open window and photoluminescent property, the ammonia sensing probe of $\mathbf{1}_{Eu}$ was evaluated with high selectivity among the common organic vapors. For practical use, the composite $\mathbf{1}_{Eu}$ /PVA films were then successfully prepared without deteriorating the photoluminescent profile of $\mathbf{1}_{Eu}$ using a simple drop-casting method. The robustness and selectivity of $\mathbf{1}_{Eu}$ /PVA film toward different VOCs in gaseous state were also examined leading to the conclusions on their exceptional stability toward every experimented VOCs and obviously selective quenching to ammonia gas. Based on both experimental and calculated results, the selectivity quenching to ammonia is evidenced through the

molecular sieve property of the framework and the change in triplet state energies of the sensitizers *via* the hydrogen bonding formation. The calculation findings are in line with experimentally perceived electronic transitions of the ligands in **1Eu** from the $n \rightarrow \pi^*$ features and $\pi \rightarrow \pi^*$ after being exposed to ammonia from the UV-Vis and photoluminescent measurement. Ammonia gas sensing performance of **1Eu**/PVA was then examined. With respect to the linear calibration established within 0.50 – 10.0 ppm range, the ammonia gas sensing by **1Eu**/PVA displayed excellent sensitivity ($4.04 \% \cdot \text{ppm}^{-1}$) and detection limit (0.14 ppm). The determination of three ammonia gas concentrations, *i.e.* 3.50, 6.50, and 7.50 ppm, were calculated from the calibration providing excellent accuracy and precision manifested through the percentage recoveries of 103 – 111% and %RSD of 1.5 – 8.2%. Additionally, the regeneration of the used films was easily achieved by being exposed to ambient air and reusable for at least ten cycles (95 – 97% repeatability) without changes in the film structure and photoluminescent profile.

2.5 References

- [1] Yotnoi, B.; Sinchow, M.; Ngamjarrojana, A.; Rujiwatra, A. *Inorg. Chim. Acta.* **2020**, *500*, 119236.
- [2] Fang, X.-N.; Yi, X.-G.; Tang, B.-X.; Kuang, R.-Y.; Xu, Y.-P. *Rev. Roum. Chim.* **2019**, *64*, 529–534.
- [3] Zhang, X.; Li, B.; Chen, Z. H.; Chen, Z. N. *J. Mater. Chem.* **2012**, *22*, 11427–11441.
- [4] Hasegawa, Y.; Kitagawa, Y. *J. Photochem. Photobiol. C Photochem. Rev.* **2022**, *51*, 100485.
- [5] Groom, C. R.; Bruno, I. J.; Lightfoot, M. P.; Ward, S. C.; IUCr. The Cambridge Structural Database, *Acta Cryst.* **2016**, *B72*, 171–179.
- [6] CrysAlisPRO software system (ver.71.39.46); Rigaku Corporation: Oxford, U.K., **2018**.
- [7] Sheldrick, G. M. SADABS; University of Göttingen: Göttingen, Germany, **1996**.

- [8] Sheldrick, G. M. *Acta Cryst.* **2008**, *A64*, 112–122.
- [9] Sheldrick, G. M. *Acta Cryst.* **2015**, *C71*, 3–8.
- [10] Dolomanov, O. V.; Bourhis, L. J.; Gildea, R. J.; Howard, J. A. K.; Puschmann, H. *J. J. Appl. Cryst.* **2009**, *42*, 339–341.
- [11] Spek, A. L. *Acta Cryst. D.* **2009**, *65*, 148–155.
- [12] Wales, D. J.; Grand, J.; Ting, V. P.; Burke, R. D.; Edler, K. J.; Bowen, C. R.; Mintova, S.; Burrows, A. D. *Chem. Soc. Rev.* **2015**, *44*, 4290–4321.
- [13] Li, H.-Y.; Zhao, S.-N.; Zang, S.-Q.; Li, J. *Chem. Soc. Rev.* **2020**, *49*, 6364–6401.
- [14] Chuasaard, T.; Ngamjarurojana, A.; Surinwong, S.; Konno, T.; Bureekaew, S.; Rujiwatra, A. *Inorg. Chem.* **2018**, *57*, 2620–2630.
- [15] Elliott, L. D.; Kayal, S.; George, M. W.; Booker-Milburn, K. *J. Am. Chem. Soc.* **2020**, *142*, 14947–14956
- [16] Heffern, M. C.; Matosziuk, L. M.; Meade T. J. *Chem. Rev.* **2014**, *114*, 4496–4539.
- [17] Bünzli, J.-C. G. *Chem. Rev.* **2010**, *110*, 2729–2755.
- [18] Huang, Y.-G.; Wu, B.-L.; Yuan, D.-Q.; Xu, Y.-G.; Jiang, F.-L.; Hong, M.-C. *Inorg. Chem.* **2007**, *46*, 1171–1176.
- [19] Hao, J. N.; Yan, B. *Nanoscale* **2016**, *8*, 2881–2886.
- [20] Kim, J. M.; Lee, Y. B.; Chae, S. K.; Ahn, D. J. *Adv. Funct. Mater.* **2006**, *16*, 2103–2109.
- [21] Ellis, J. E.; Crawford, S. E.; Kim, K. J. *Mater. Adv.* **2021**, *2*, 6169–6196.
- [22] Goel, P.; Singh, S.; Kaur, H.; Mishra, S.; Deep, A. *Sens. Actuators B Chem.* **2021**, *329*, 129157.
- [23] Ma, W. P.; Yan, B. *Dalton Trans.* **2020**, *49*, 15663–15671.
- [24] Ma, J.; Yan, B. *J. Colloid Interface Sci.* **2018**, *513*, 133–140.

- [25] Chen, X.; Yu, Y.; Yang, C.; Yin, J.; Song, X.; Li, J.; Fei, H. *ACS Appl. Mater. Interfaces* **2021**, *13*, 52765–52774.
- [26] Li, G.; Yang, S. L.; Liu, W. S.; Guo, M. Y.; Liu, X. Y.; Bu, R.; Gao, E. Q. *Inorg. Chem. Front.* **2021**, *8*, 4828–4837.
- [27] Hermawan, A.; Amrillah, T.; Riapanitra, A.; Ong, W.-J.; Yin, S. *Adv. Healthcare Mater.* **2021**, 2100970;
- [28] Chan, M.-J.; Li, Y.-J.; Wu, C.-C.; Lee, Y.-C.; Zan, H.-W.; Meng, H.-F.; Hsieh, M.-H.; Lai, C.-S.; Tian, Y.-C. *Biomedicines* **2020**, *8*, 468.
- [29] Ricci, P. P.; Gregory, O. J. *Sci. Rep.* **2021**, *11*, 7185.
- [30] Banga, I.; Paul, A.; Muthukumar, S.; Prasad, S. *ACS Appl. Mater. Interfaces* **2021**, *13*, 16155–16165.
- [31] Zhang, J.; Yue, D.; Xia, T.; Cui, Y.; Yang, Y.; Qian, G. *Microporous Mesoporous Mater.* **2017**, *253*, 146–150.
- [32] Ma, J.; Zhao, L. M.; Jin, C. Y.; Yan, B. *Dyes Pigm.* **2020**, *173*, 107883.
- [33] Ma, J.; Yan, B. *Spectrochim. Acta A Mol. Biomol. Spectrosc.* **2019**, *220*, 117107.
- [34] Li, Y. P.; Li, S. N.; Jiang, Y. C.; Hu, M. C.; Zhai, Q. G. *Chem. Commun.* **2018**, *54*, 9789–9792.

CHAPTER 3

Nanoporous Frameworks of Lanthanide-2,2'-Dinitrobiphenyl-4,4'-Dicarboxylates as Multifunctional Materials

3.1 Introduction

Contrary to microporous LnCPs, the fabrication of nanoporous LnCPs is more complicated owing to the flexible coordination geometry and high coordination number of Ln^{III}, which tend to render the crowded coordination and therefore microporosity. To yield nanoporous LnCPs, number and relative arrangement of donor atoms, length, rigidity, and steric effect of ligands must be carefully considered [1-3]. According to literatures (Table 3.1), a linear and rigid biphenyl-4,4'-dicarboxylic acid (H₂BPDC) and its derivatives can lead to large porous frameworks. The steric effect introduced by additional functional groups, *e.g.* -SO₃H, -NH₂, -F, and -NO₂, on the backbone can hinder the formation of dense frameworks [4-6]. In this chapter, the synthesis and characterization of nanoporous [Ln₄(*di*-nitro-BPDC)₄(NO₂)₃(OH)(H₂O)₅] · (solvent) (**2**_{Ln}) when *di*-nitro-H₂BPDC = 2,2'-dinitrobiphenyl-4,4'-dicarboxylic acid and Ln = Pr^{III}, Nd^{III}, Sm^{III}, Eu^{III}, and Gd^{III} are reported. Their potential applications in superprotonic conductivities, humidity and temperature sensing, and catalysis of CO₂ capture and conversion are presented and discussed in relevant to the single crystal structures.

Table 3.1 Selected examples of LnCPs of BPDC²⁻ and its derivatives possessing large pores

Organic linker	Chemical formula	Pore size (nm ²)	Surface area (m ² g ⁻¹)	Ref
	[Gd ₂ L ₃ (DMF) ₄]·4DMF,3H ₂ O	0.33 × 0.86	NA	[4]
	[Ln ₄ (μ ₃ -OH)(L) ₃ (BPDAC) _{0.5} (H ₂ O) ₆] (Ln = Gd ^{III} and Tb ^{III})	0.30 × 0.70 and 0.45 × 0.55	NA	[7]
	(DMA) ₂ [Ln ₆ (μ ₃ -OH) ₈ (L) ₆]·x(Solvent) (Ln = Eu ^{III} and Tb ^{III})	1.2 × 1.2 and 1.8 × 1.8	NA	[8]
	[Ln ₄ (μ ₃ -OH) ₄ (L) ₄ (DMF) ₃ (H ₂ O)] ·8H ₂ O,4.2DMF (Ln = Sm ^{III} , Eu ^{III} , Gd ^{III} , Tb ^{III} , Dy ^{III} , Ho ^{III} , Er ^{III} , Tm ^{III} , and Yb ^{III})	0.90 × 1.1	NA	[9]
	[Ln ₂ (L) ₃ (DMF) ₄]·3DMF,2H ₂ O (Ln = Nd ^{III} , Eu ^{III} , and Gd ^{III})	0.80 × 1.2	NA	[10]
	[LnK(L)(DMF)(H ₂ O)]·x(solvent) (Ln = Sm ^{III} , Eu ^{III} , and Pr ^{III})	1.3 × 1.3 and 2.8 × 2.8	738	[11]
	[(CH ₃) ₂ NH ₂] ₂ [Tb ₆ (μ ₃ - OH) ₈ (L) ₆ (H ₂ O) ₆]·x(solvent)	1.2 × 1.2 and 1.6 × 1.6	1854	[12]
	[(CH ₃) ₂ NH ₂] ₂ [Tb ₆ (μ ₃ - OH) ₈ (L) ₆ (H ₂ O) ₆]·x(solvent)	1.2 × 1.2 and 1.6 × 1.6	1940	[12]

3.2. Experimental

3.2.2 Synthesis of *di*-nitro- H_2 BPDC

The synthesis of *di*-nitro- H_2 BPDC was modified following the reported procedure [13]. A suspension of 0.1200 g of biphenyl-4,4-dicarboxylic acid (H_2 BPDC) in 12.50 mL of concentrated sulfuric acid was prepared and kept at temperatures below 50 °C using an ice bath. With continuous stirring, 3.00 mL of fuming nitric acid was added. The reaction mixture was refluxed at 80 °C for 4 h. The reaction was then subsequently cooled down using an ice bath after complete the consumption of H_2 BPDC. The yellowish precipitate was collected by filtration. The precipitate was washed with a large amount of cold water and dried at 60 °C (84% yield). Thin-layer chromatography was used to follow up the reaction. The visualization was prompted under the UV light (254 nm). The crude product was dissolved in DMSO- d_6 and then the 1H NMR spectra were recorded at room temperature.

The yielded *di*-nitro- H_2 BPDC was notably sufficient (over 90%) for further use without any purification (Fig. 3.1). The purity of the crude product was indicated as 1H NMR (500 MHz, DMSO- d_6): δ 8.68 (*d*, $J = 1.6$ Hz, 1H), 8.37 – 8.35 (*m*, 1H), 7.70 (*dd*, $J = 21.7, 8.0$ Hz, 1H).

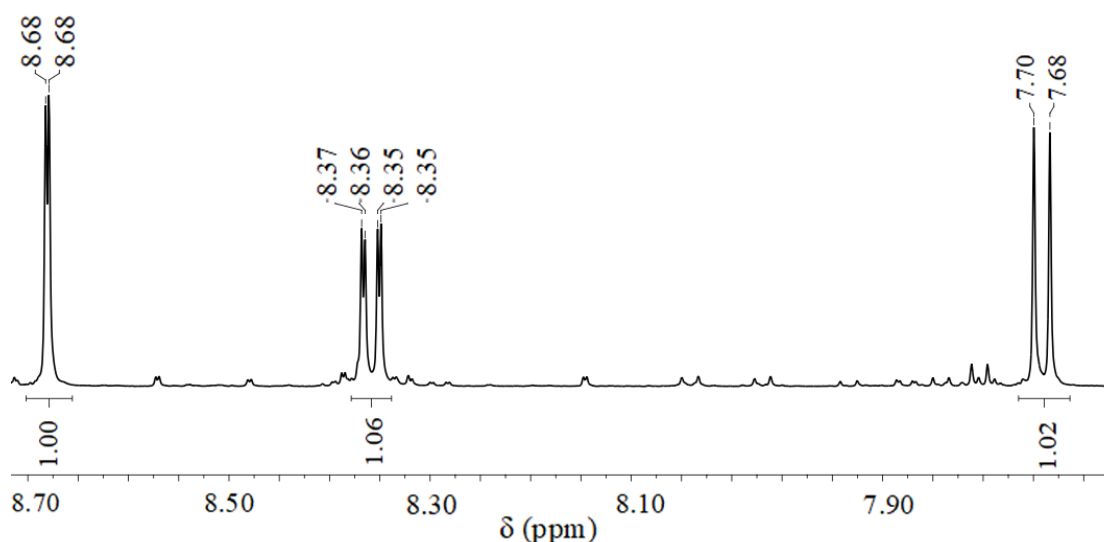


Fig. 3.1 1H NMR spectrum of the as-synthesized *di*-nitro- H_2 BPDC.

3.2.3 Synthesis 2_{Ln} ($Ln = Pr^{III}, Nd^{III}, Sm^{III}, Eu^{III},$ and Gd^{III})

[Pr₄(*di*-nitro-BPDC)₄(NO₂)₃(OH)(H₂O)₅] · (solvent) (2_{Pr}). Pr(NO₃)₃·6H₂O (0.20 mmol) and *di*-nitro-H₂BPDC (0.50 mmol) were dissolved in 12.5 mL of a mixed solvent of dimethylformamide/water (4/1). The mixture was then transferred into a 25 mL Teflon-lined hydrothermal, closed and placed under autogenous pressure generated at 140 °C for 12 h (84% yield). Based on the TGA data, 6 molecules of methanol solvent, which occupied in the void space, were calculated after soaking the crystals in MeOH for overnight.

[Nd₄(*di*-nitro-BPDC)₄(NO₂)₃(OH)(H₂O)₅] · (solvent) (2_{Nd}). Following the same synthesis procedure as **2_{Pr}**, **2_{Nd}** was synthesized using Nd(NO₃)₃·6H₂O instead of Pr(NO₃)₃·6H₂O and the reaction duration of 24 h (78% yield). Based on the TGA data, 4 molecules of methanol solvent, which occupied in the void space, were calculated after soaking the crystals in MeOH for overnight.

[Sm₄(*di*-nitro-BPDC)₄(NO₂)₃(OH)(H₂O)₅] · (solvent) (2_{Sm}). Following the same synthesis procedure as **2_{Pr}**, **2_{Sm}** was synthesized using Sm(NO₃)₃·6H₂O instead of Pr(NO₃)₃·6H₂O and the reaction duration of 48 h (81% yield). Based on the TGA data, 4 molecules of methanol solvent, which occupied in the void space, were calculated.

[Eu₄(*di*-nitro-BPDC)₄(NO₂)₃(OH)(H₂O)₅] · (solvent) (2_{Eu}). Following the same synthesis procedure as **2_{Pr}**, **2_{Eu}** was synthesized using Eu(NO₃)₃·6H₂O instead of Pr(NO₃)₃·6H₂O and the reaction duration of 72 h (84% yield). Based on the TGA data, 5 molecules of methanol solvent, which occupied in the void space, were calculated after soaking the crystals in MeOH for overnight.

[Gd₄(*di*-nitro-BPDC)₄(NO₂)₃(OH)(H₂O)₅] · (solvent) (2_{Gd}). Following the same synthesis procedure as **2_{Pr}**, **2_{Gd}** was synthesized using Gd(NO₃)₃·6H₂O instead of Pr(NO₃)₃·6H₂O and the reaction duration of 72 h (70% yield). Based on the TGA data, 4 molecules of methanol solvent, which occupied in the void space, were calculated after soaking the crystals in MeOH for overnight.

The bimetallic frameworks of Pr^{III}/Gd^{III} (**2Pr/Gd**) and Pr^{III}/Eu^{III} (**2Pr/Eu**) were synthesized following the same synthesis procedure as the monometallic **2Ln** (Ln = Pr^{III}, Nd^{III}, Sm^{III}, Eu^{III}, and Gd^{III}) but using an equimolar ratio of the corresponding Ln(NO₃)₃·6H₂O; Pr(NO₃)₃·6H₂O (0.10 mmol) and Gd(NO₃)₃·6H₂O (0.10 mmol) for **2Pr/Gd** with 76% yield, and Pr(NO₃)₃·6H₂O (0.10 mmol) and Eu(NO₃)₃·6H₂O (0.10 mmol) for **2Pr/Eu** with 80% yield. Contents of Ln^{III} in the bimetallic **2Pr/Gd** and **2Pr/Eu** were indicated by an energy dispersive X-ray (EDX) spectroscopy provided on a scanning electron microscope (SEM).

3.2.4 X-ray crystallography

The single crystal data of **2Ga** were collected using a Rigaku-Oxford XtalLab Supernova diffractometer equipped with a micro-focus sealed X-ray tube of Mo K α radiation ($\lambda = 0.71073 \text{ \AA}$) and direct photon counting HyPix3000 detector at 293 K. The intensity data set were carried out using the CrysAlisPro program [14]. SADABS program was applied for the empirical absorption corrections [15]. The crystal structure was solved using the SHELXS program [16] and refined on F^2 by the full-matrix least-squares technique using the SHELXL program [17] *via* the Olex² interface [18]. The data set were treated using the SQUEEZE routine [19] because of the problem with diffusing guest species in the void, which could not be identified with precision by the X-ray diffraction technique. A number of diffused electrons could be determined *ca.* 13,464 per unit cell. Details on the crystallographic and refinement are summarized in Table 3.2. The crystal qualities of others **2Ln** (Ln = Pr^{III}, Nd^{III}, Sm^{III}, Eu^{III}, Pr^{III}/Gd^{III}, and Pr^{III}/Eu^{III}) were not appropriate to collect full data. Their purities were evaluated based on the PXRD experiment and elemental analysis (Table 3.3).

Table 3.2 Crystallographic and refinement data of **2Ga**

CCDC No.	1919470
Crystal formula	Gd ₄ C ₅₆ N ₁₁ O ₄₄
Formula weight	2183.86
Space group	Tetragonal $I\bar{4}_2d$
a (Å)	25.2376(2)
c (Å)	46.3754(4)
V (Å ³)	29,538.4(5)
Z	8
ρ (g·cm ⁻³)	0.982
Radiation λ (Å)	Mo K α (0.71073)
Temperature (K)	293(2)
Crystal size (mm ³)	0.5 × 0.4 × 0.3
F(000)	13505
Data/ parameters/restraints	10640/536/16
R_1 ($I > 2\sigma(I)$) [†]	0.0633
wR_2 (all data) ^{† †}	0.2035

$$^{\dagger}R_1 = \frac{\sum(|F_o| - |F_c|)}{\sum(|F_o|)}, \quad ^{\dagger\dagger}wR = \left[\frac{\sum w(F_o^2 - F_c^2)^2}{\sum w(F_o^2)^2} \right]^{1/2}$$

Table 3.3 Elemental analysis of **2Ln**

		C (%)	H (%)	N (%)
2Pr	Anal. Calcd for Pr ₄ C ₆₂ H ₅₉ N ₁₁ O ₅₀	32.07	2.56	6.64
	Found	36.45	2.33	6.25
2Nd	Anal. Calcd for Nd ₄ C ₆₀ H ₅₁ N ₁₁ O ₄₈	31.73	2.26	6.78
	Found	35.82	2.28	6.21
2Sm	Anal. Calcd for Sm ₄ C ₆₀ H ₅₁ N ₁₁ O ₄₈	31.39	2.24	6.71
	Found	36.39	2.28	6.64
2Eu	Anal. Calcd for Eu ₄ C ₆₁ H ₅₅ N ₁₁ O ₄₉	31.39	2.38	6.60
	Found	36.91	2.35	6.61
2Gd	Anal. Calcd for Gd ₄ C ₆₀ H ₅₁ N ₁₁ O ₄₈	31.02	2.21	6.63
	Found	36.06	2.28	6.36

3.2.5 Proton conductivity measurements

Proton conductivity experiments were measured using single crystal samples under the customized chamber (Fig. 3.2). A TH2827 precision LCR meter with frequency operation from 1000 Hz to 1 MHz and an amplitude of 1 V AC voltage was used as impedance analyzer. The humidity, which was generated by vapor generator with setting target values as 55 to 99 RH%, was measured using a digital Thermo-Hygrometer O-271BK. A THORLabs TED3 temperature controller was used to control temperature, which was varied from 25 to 55 °C. To ensure the contact with electrodes, the crystals were painted with a conductive silver paint on the trigonal faces.

The proton conductivities (σ , S·cm⁻¹) could be calculated based on the impedance data following equations:

$$\sigma = \frac{1}{\rho} \quad \text{eq. (3.1)}$$

$$\rho = \frac{zS}{d} \quad \text{eq. (3.2)}$$

$$\sigma = \frac{d}{zS} \quad \text{eq. (3.3)}$$

where d is the thickness (cm) of the single crystal, S is cross-sectional area (cm²) of the single crystal, and Z is the total resistance of the sample (Ω), which was yielded from the fit of the semicircle of the Nyquist plots (using ZView software). Dimensions of the single crystals were measured using the scale equipped with the optical microscope. Values of the thickness (d) and the surface area (S) of the single crystal samples used for all the measurements were listed in Table 3.4.

From the data collected at 99 RH% and 25 to 55 °C, an Arrhenius plot was established between $\ln(\sigma/S \cdot \text{cm}^{-1})$ and $1000/T$ from which the activation energy of the proton conduction (E_a) was calculated;

$$\sigma_T = \sigma_0 [e^{(-E_a/RT)}] \quad \text{eq. (3.4)}$$

$$\ln(\sigma_T) = \ln\sigma_0 - \frac{E_a}{RT} \quad \text{eq. (3.5)}$$

$$\ln(\sigma_T) = \ln\sigma_0 - \frac{1000E_a}{1000RT} \quad \text{eq. (3.6)}$$

where σ = proton conductivity of the sample; E_a = activation energy, R = ideal gas constant, and T = temperature in Kelvin (K). And from the plot between $\ln(\sigma_T)$ versus $\frac{1000}{T}$, the value of E_a can be calculated from slope of the plot.

Table 3.4 Thickness (d/cm) and surface areas (S/cm^2) of **2Ga** used in proton conductivity experiments

Single Crystal Experiments	d	S
Humidity- and temperature-dependence	0.077	0.0020
Ten successive measurements between 55 and 99 RH%	0.077	0.0020
Ten successive measurements between 25 and 40 °C	0.059	0.0015
Humidity sensing	0.095	0.0079
Temperature sensing	0.061	0.0016
Pellet of Grinding Crystal Experiments		
Temperature dependence of proton conductivity (25 and 55 °C)	0.055	0.7663

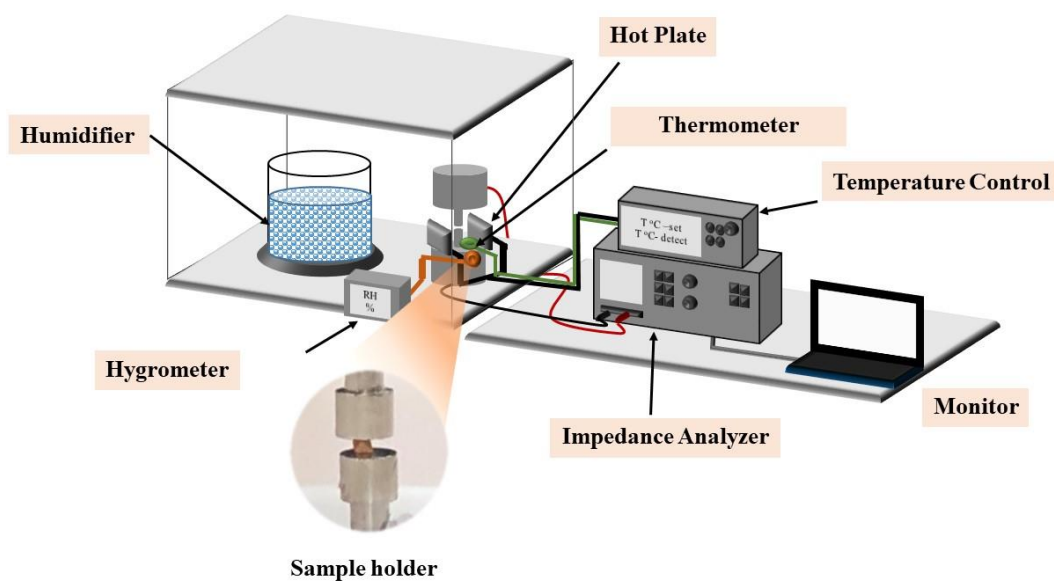


Fig. 3.2 Diagram showing the experimental setting and the measurement chamber used in proton conductivity experiments.

3.2.6 Gas adsorption experiments

A BELSORP-mini II instrument was used for gas adsorption/desorption experiments, which were performed in a range of 0 - 1 bar pressures with ultra-pure grade N_2 , H_2 , O_2 , and CO_2 . Before the measurements, the samples were immersed in methanol for overnight and then heated at 80 °C for 4 h under vacuum. The experiments were carried out at 77 K for N_2 and H_2 , 195 K for CO_2 , N_2 and O_2 , and 298 K for CO_2 and N_2 . Water sorption/desorption measurement was conducted using a BELSORP-max volumetric adsorption instrument at 298 K.

The enthalpy of CO_2 adsorption (Q_{st}) onto the framework was calculated using the Clausius-Clapeyron equation at near-zero CO_2 coverage [20].

$$\frac{d \ln(P)}{d(1/T)} = \frac{Q_{st}}{R} \quad \text{eq. (3.7)}$$

$$\ln \left(\frac{P_1}{P_2} \right) = Q_{st} \frac{T_1 - T_2}{R \times T_1 \times T_2} \quad \text{eq. (3.8)}$$

where P_i = pressure for isotherm i ; T_i = temperature in Kelvin for isotherm I (K), R = ideal gas constant ($8.315 \text{ J} \cdot \text{mol}^{-1} \cdot \text{K}^{-1}$) and Q_{st} = enthalpy of CO_2 adsorption.

3.2.7 Catalytic activities for CO₂ cycloaddition reactions with epoxides

The ground samples were soaked in MeOH for overnight and then was dried at 80 °C for 4 h under the N₂ flow to allow the vacant coordination sites. Tetrabutylammonium bromide (*n*-Bu₄NBr) and epoxyhydrin (ECH) were subsequently added into the pretreated sample in a 10 mL round bottom flask, which was then equipped with a CO₂ balloon. The experiments were performed under ambient CO₂ pressure and solvent-free conditions. The reaction was then cooled to room temperature. The reactions were progressed by using ¹H NMR spectroscopy. The performance of catalysts was indicated based on percentage conversion, selectivity, turnover number (TON), and turnover frequency (TOF), which were calculated following these equations when integral areas of a single proton derived from the epoxide substrate (*I*_{ep}) and the products (*I*_p)

$$\%conversion = \frac{I_p}{I_{ep}} \times 100 \quad \text{eq. (3.9)}$$

$$\%selectivity = \frac{I_c}{I_p} \times 100 \quad \text{eq. (3.10)}$$

$$TON = \left(\frac{\%conversion}{100} \times \frac{\%selectivity}{100} \right) \times \frac{mmol \text{ of epoxides}}{mmol \text{ of cat.}} \quad \text{eq. (3.11)}$$

$$TOF = \frac{TON}{reaction \text{ time}} \quad \text{eq. (3.12)}$$

when *I*_{ep} is integral areas of a single proton derived from the epoxide substrate, *I*_c is the integral area of the desired product (cyclic carbonate).

To make certain that the negligible diversity in structural subtleties effect, which might obtain from different batches of the syntheses, triplicate data were produced for every experiment. Influences of type of catalysts, (**2Pr**, **2Nd**, **2Sm**, **2Eu**, **2Gd**, **2Pr/Gd**, and **2Pr/Eu**), mole percentage of the catalysts, type of co-catalysts (tetraethylammonium bromide or Et₄NBr, tetrapropylammonium bromide or *n*-Pr₄NBr, and *n*-Bu₄NBr), reaction temperature, and reaction time were studied. A scope of other epoxides was also attempted. To study recyclibilities, the catalysts were filtrated, washed with CHCl₃ several times, and then dried under ambient temperature for using in the next cycle. The retaining of the framework structures was affirmed by PXRD after the recycling experiments.

3.3 Results and discussions

3.3.1 Crystal structure description of 2Ga

2Ga crystallized in the tetragonal space group $I\bar{4}2d$ with the refined unit cell parameters $a = 25.0247(3)$ Å, $c = 46.3377(5)$ Å, $V = 29,018.32(76)$ Å³ (Table 3.2). The framework features a nanoporous framework with high disorder. Its structure consists of three unique Gd^{III} ions (Gd1, Gd2, and Gd3) and three independent *di*-nitro-BPDC²⁻. One of *di*-nitro-BPDC²⁻ is presented with fully occupied crystallographic sites. The other two *di*-nitro-BPDC²⁻ exhibit however 50% possibility of site occupancy due to the substitutional disorder (Fig. 3.3a). Nitrites were generated *in situ* under the highly acidic solvothermal condition [5,21]. Atoms O8, O9, O13, and O19 can attribute to both carboxylates of O8–C27–O19 and O9–C3–O13 in the same *di*-nitro-BPDC²⁻ and two crystallographically unique nitrites of O8–N2–O19 and O9–N1–O13. The other disordering *di*-nitro-BPDC²⁻ exhibits similar substitutional disorder with coordinating water instead nitrites at O10, O25, O28, and O34 atoms, which can form to be both carboxylates in the same *di*-nitro-BPDC²⁻ of O25–C28–O28 and O10–C41–O34 and four independent coordinating water. Noticeably, there also is one of the –NO₂ group of the fully occupied *di*-nitro-BPDC²⁻ showing the disorder between two crystallographic sites with site occupying ratio of 50%, *i.e.* O1–N10–O2 and O5–N9–O6. Due to the relatively shorter Gd^{III}–O28 distance of 2.292(17) Å compared to the other Gd^{III}–O distance and the statistical data from the Cambridge Structural Database [22], it was identified as hydroxide rather than water molecule resulting in the charge neutralization of the framework.

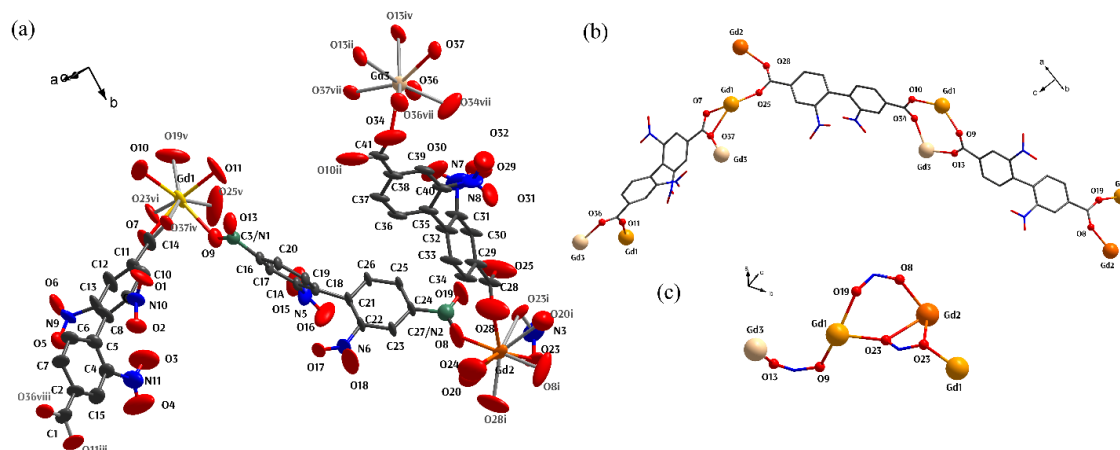


Fig. 3.3 Depictions of (a) an asymmetric unit of **2Ga** drawn using 50% thermal ellipsoid and (b,c) coordination modes adopted by *di*-nitro-BPDC²⁻ and nitrite anions. Symmetry codes: (i) 1-x, 1-y, z; (ii) -0.5+x, -y, 0.75-z; (iii) -0.5+x, 1+y, 0.25+z; (iv) 1-x, -y, z; (v) 0.5-x, 0.5+y, 0.5-z; (vi) 0.5+x, 1.5-y, 0.5-z; (vii) 0.5-x, y, 0.75-z; (viii) 0.5-x, 1-y, 0.25+z).

Owing to the substitutional disorder accompanying the coordinating ligands, it leads to significant variation in the coordination environment of all three unique Gd^{III} ions in the asymmetric unit of **2Ga**. Although they are eight-fold coordinated alike, the number of the coordinating *di*-nitro-BPDC²⁻ ligand around the Gd^{III} ions ranges from eight to two (Fig. 3.4-3.6). The *di*-nitro-BPDC²⁻ ligands exhibit two different coordination modes, *i.e.* μ₄-η²:η¹:η¹:η¹ for the fully occupied *di*-nitro-BPDC²⁻ μ₄-η¹:η¹:η¹:η¹ for the substitutional disordering *di*-nitro-BPDC²⁻ (Fig. 3.3b). The commonly found bridging μ₂-η¹:η¹ (N1, N2) and μ₃-η²:η² (N3) coordination modes of the nitrite ligand are adopted (Fig. 3.3c). Based on the coordination modes of *di*-nitro-BPDC²⁻ and nitrite linkers, the Gd^{III} ions were bridged to form one-dimensional chains extending along the *a* and *b* axes (Fig. 3.7a and b). The derived chains feature a zigzag pattern performed by the μ₄-η²:η¹:η¹:η¹ *di*-nitro-BPDC²⁻ and the μ₃-η²:η² nitrite coordinating to the Gd2 position.

The three-dimensional framework of **2Ga** can be regarded as being built up of these Gd^{III} zigzag chains (Fig. 3.7) containing two disconnected channels aligning also along the *a* and *b* directions. Due to the disordering of *di*-nitro-BPDC²⁻ and nitrate ligands, the effective window opening size could be varied in the range from 2.0 × 1.1 nm² to 1.5 × 1.1 nm² which

can be accounted for *ca.* 45% void or $0.46 \text{ cm}^3 \cdot \text{g}^{-1}$ (Fig. 3.8). If there is no *di*-nitro-BPDC²⁻ involving in the window opening site, the window opening size of $2.0 \times 1.1 \text{ nm}^2$ should be observed. But if *di*-nitro-BPDC²⁻ ligands appear in the window opening site, then the smallest window opening size of $1.5 \times 1.1 \text{ nm}^2$ should be responsible. These values are in good agreement with the BET active surface area, the void volume, and the average pore size of $770.84 \text{ m}^2 \cdot \text{g}^{-1}$, $0.49 \text{ cm}^3 \cdot \text{g}^{-1}$, and 1.7 nm , respectively. They are also consistent with those nanoporous frameworks fabricated using H₂BPDC and its derivatives (Table 3.1).

With reference to the Cambridge Structural Database [22], the nanoporous LnCPs frameworks based on BPDC²⁻ and their derivatives linkers are limited, and noticeably they all contain secondary linkers and functional groups on the organic linkers. In the case of **2Ga**, the nitrite functions as the secondary linker and fulfilled the Ln^{III} coordination sphere introducing the zigzag character to the Gd^{III}-carboxylate chains. To confirm the effect of the electron-withdrawing -NO₂ pendants on the organic linkers, the same synthesis condition was controlled resulting in [Tb(BPDC)₂](CH₃)₂NH₂] with a smaller opening size of $5.6 \times 8.3 \text{ \AA}^2$ [23]. This smaller porosity might be due to the more crowded environment around Ln^{III} center, which could reduce the pore spaces in the framework. The decorated -NO₂ moieties of BPDC²⁻ are the important steric groups to disrupt the shrinkage porosity and then provide the larger pore size to be nanoporous frameworks as expected.

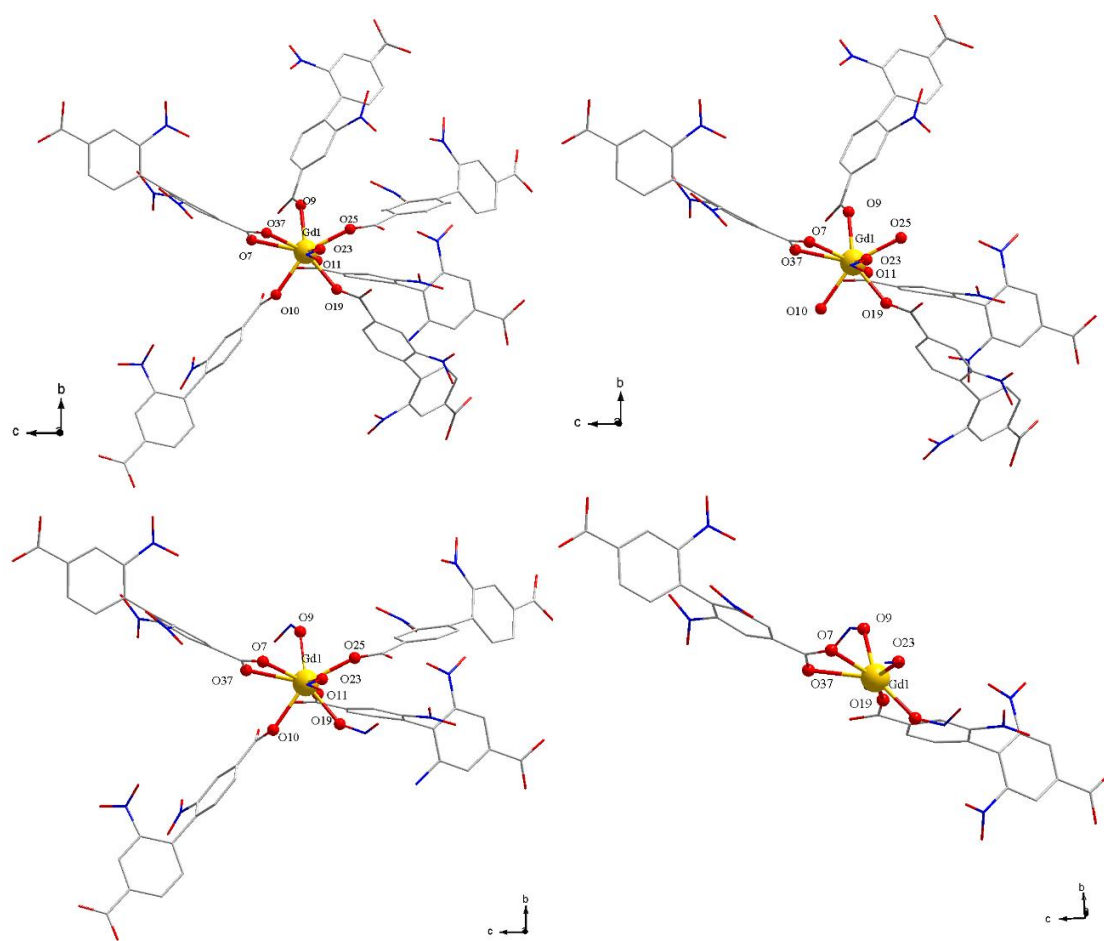


Fig. 3.4 Variation in coordination environment of Gd1 due to substitutional disorder *di*-nitro-BPDC²⁻ with nitrites and water molecules in **2Ga**.

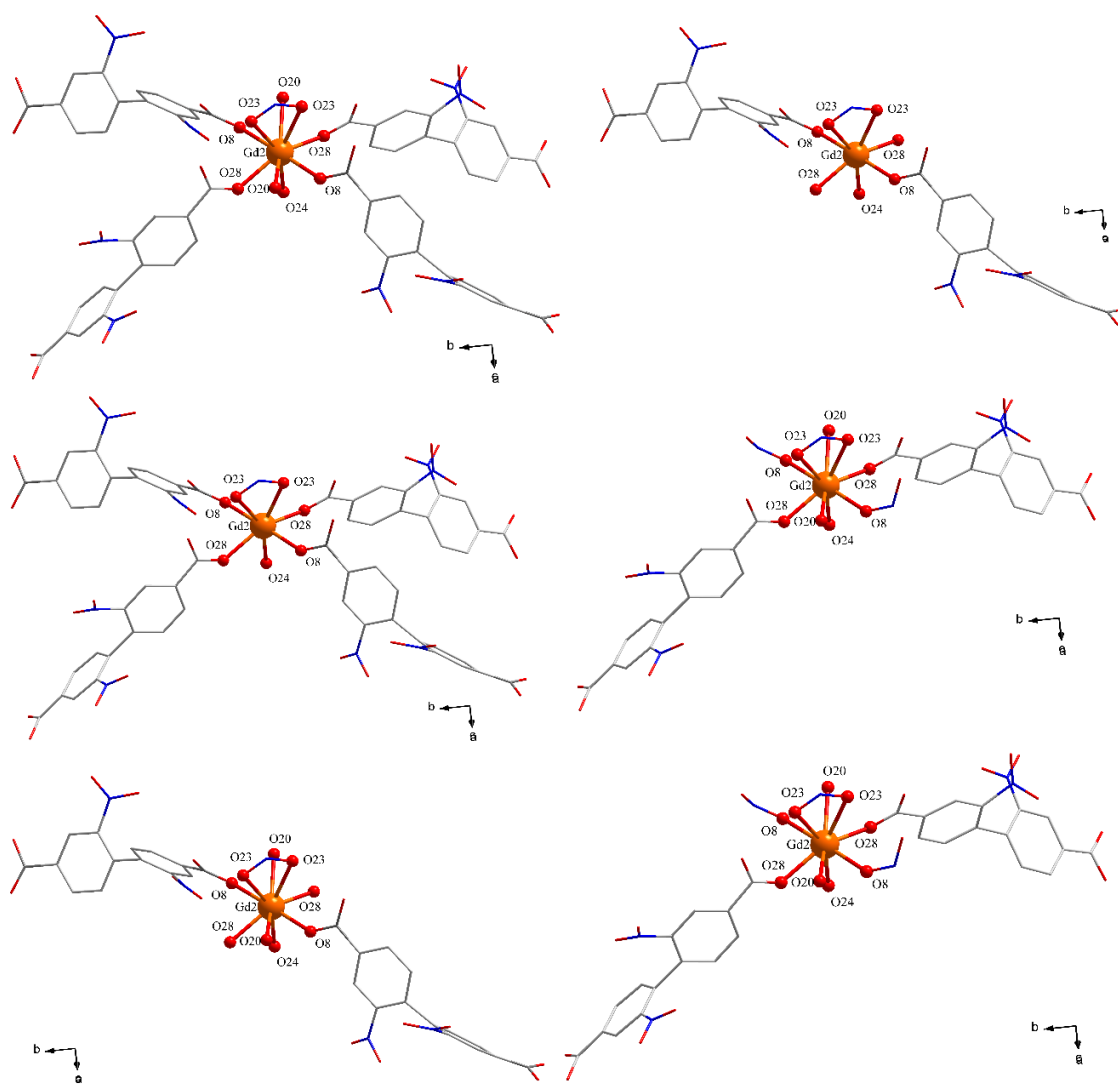


Fig. 3.5 Variation in coordination environment of Gd₂ due to substitutional disorder *di*-nitro-BPDC²⁻ with nitrites and water molecules in **2Ga**.

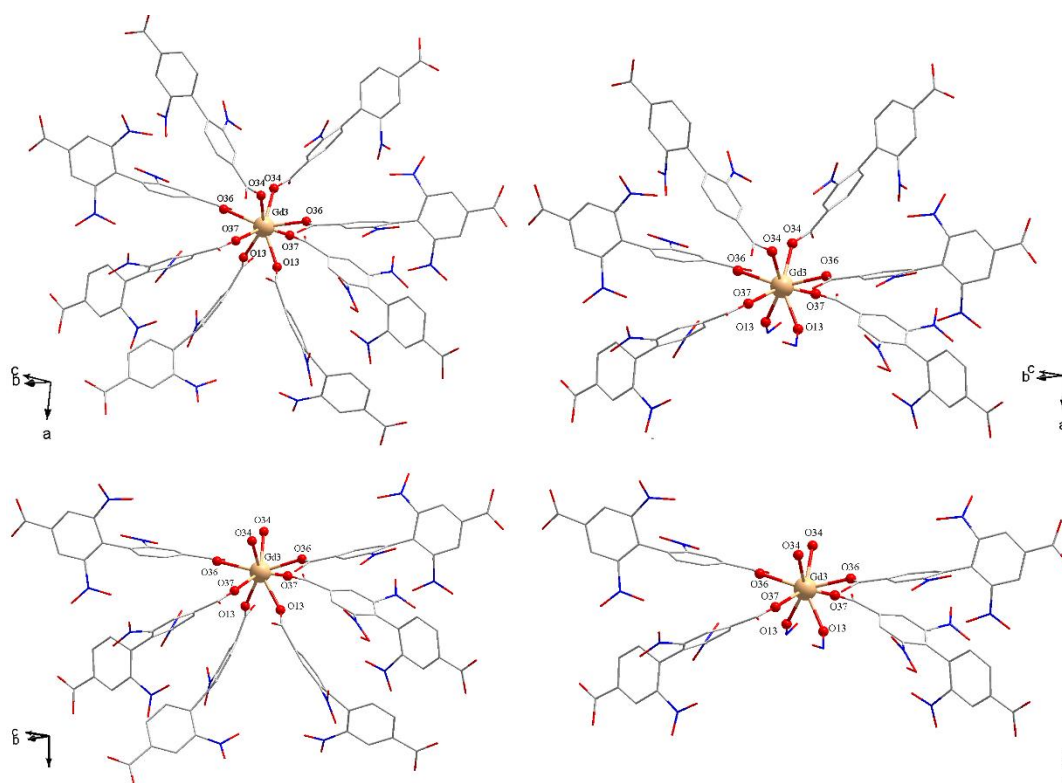


Fig. 3.6 Variation in coordination environment of Gd³⁺ due to substitutional disorder *di*-nitro-BPDC²⁻ with nitrites and water molecules in **2Ga**.

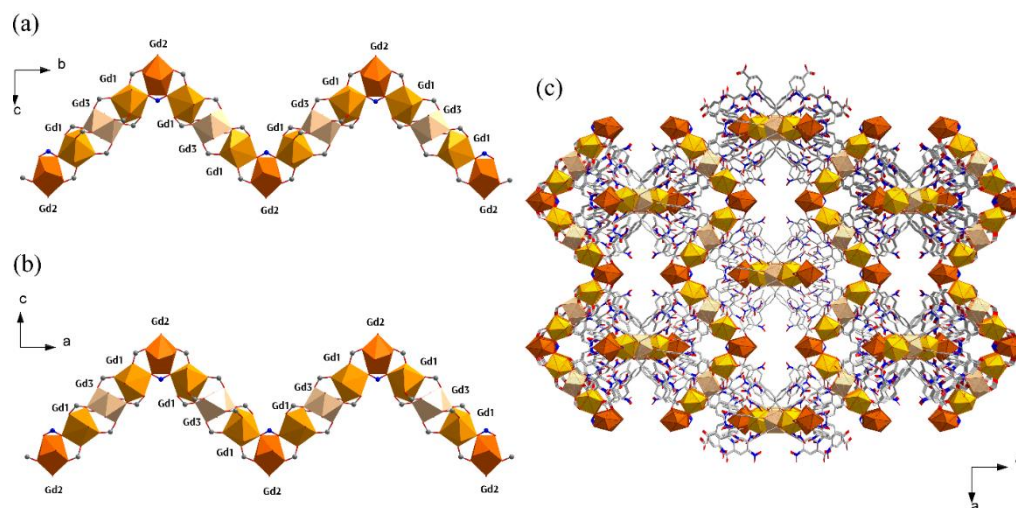


Fig 3.7 (a, b) the arrangement of the three unique Gd^{III} in the zigzag chains along a and b directions within (c) the three-dimensional framework.

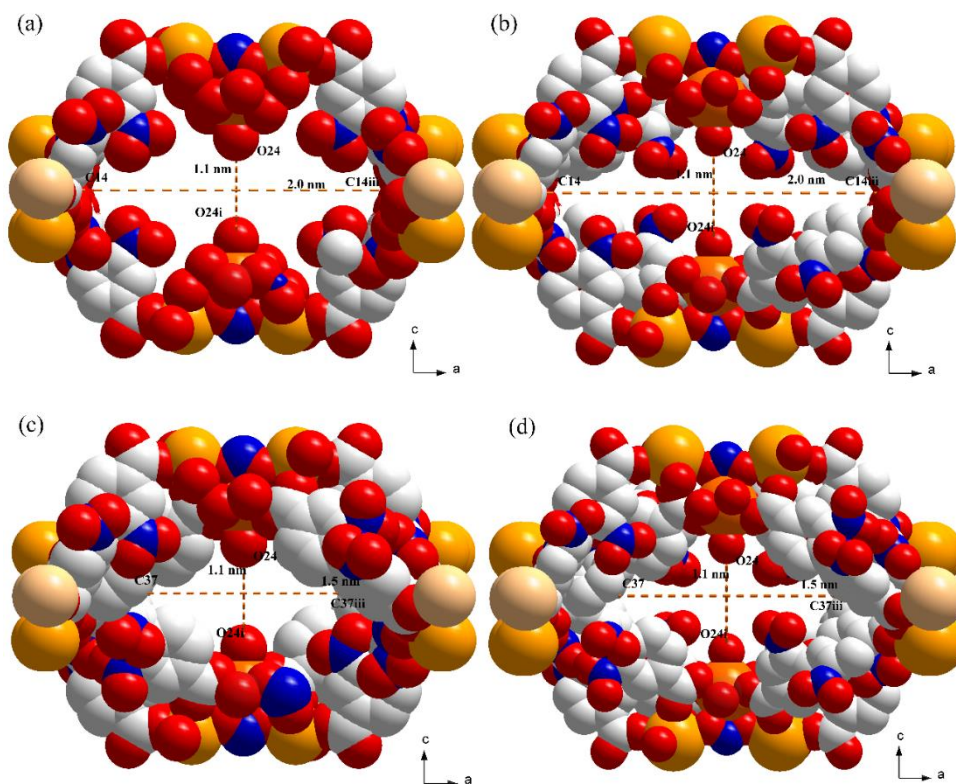


Fig. 3.8 Views of different possibilities of window openings arose from the crystallographic disorder. (a) with nitrite (N1 and N2) and water (O10, O25, O28, and O34), but not *di*-nitro-BPDC²⁻, (b) with a *di*-nitro-BPDC²⁻ and water, but not nitrite (N1 and N2) (c) with nitrite (N1 and N2) and a *di*-nitro-BPDC²⁻, and (d) with *di*-nitro-BPDC²⁻, but not water and nitrite. Symmetry operation: (i) 0.5-x, y, 0.75-z, (ii) 2-x, 1-y, z, (iii) 1-x, 1-y, z.

3.3.2 Phase and purity of **2_{Ln}**

Based on the PXRD results (Fig. 3.9a), pure phases of **2_{Ln}**, which are isostructural, were successfully synthesized. The FT-IR spectra of **2_{Ln}** showed also similar profiles (Fig. 3.9b). The phase and purity of **2_{Ln}** could be confirmed based on PXRD diffraction patterns, which were well matched with simulated patterns gerating from the single crystal data of **2_{Ga}**. Due to the grinding effect, the intensity of a few diffraction peaks in the low 2θ range were different. Elecmetal mapping analysis confirms the regular distribution of the corresponding elements (Fig. 3.10). Based on the EDX spectroscopic results, the

equimolar ratio of the composing Ln^{III} in the bimetallic $\mathbf{2}_{\text{Pr}/\text{Gd}}$ and $\mathbf{2}_{\text{Pr}/\text{Eu}}$ frameworks can be ensured. On the basis of these characterization, phase and purity of $\mathbf{2}_{\text{Ln}}$ could be certain.

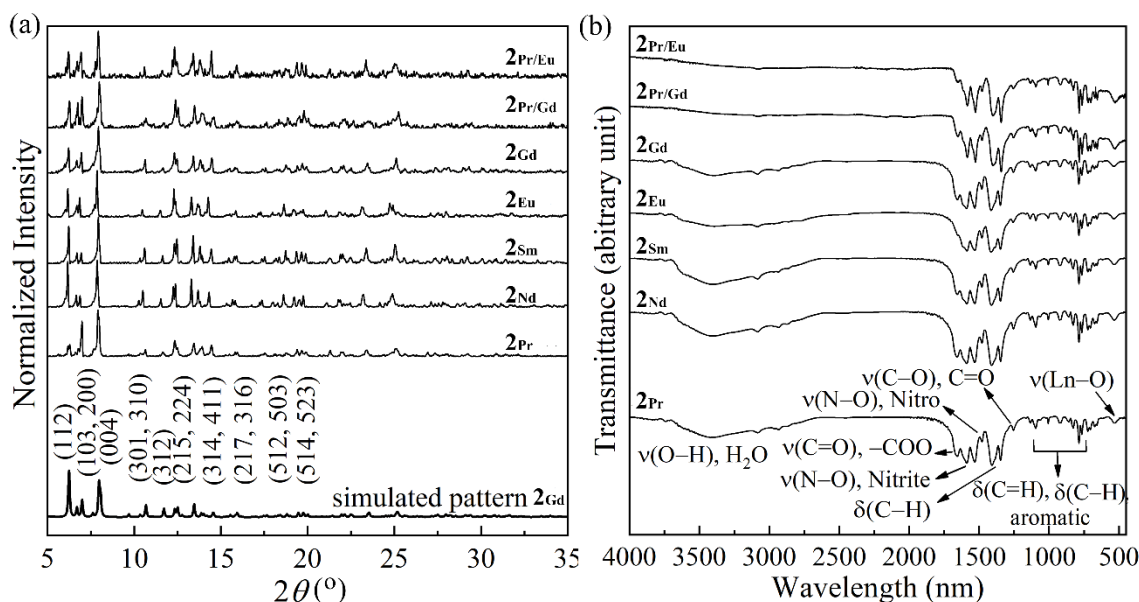


Fig. 3.9 (a) PXRD patterns of $\mathbf{2}_{\text{Ln}}$ compared with the simulated pattern generating from single crystal data of $\mathbf{2}_{\text{Gd}}$, and (b) FT-IR spectra of $\mathbf{2}_{\text{Ln}}$ with corresponding band assignments.

3.3.3 Thermogravimetric behavior and stability

The occluded solvents are readily lost even at room temperature under the flow of N_2 gas, suggesting the remarkably weak intermolecular interactions, which are consistent with their diffusing character in the single crystal data. They can be substituted with methanol through a simple immersion overnight. After being soaked, the thermogravimetric behaviors of $\mathbf{2}_{\text{Ln}}$ were carried out under the N_2 flow, which exhibited the same fashion (Fig. 3.11). The difference in type of Ln^{III} in $\mathbf{2}_{\text{Ln}}$ did not cause any significant variation in their thermogravimetric profiles, which could ensure their isostructures.

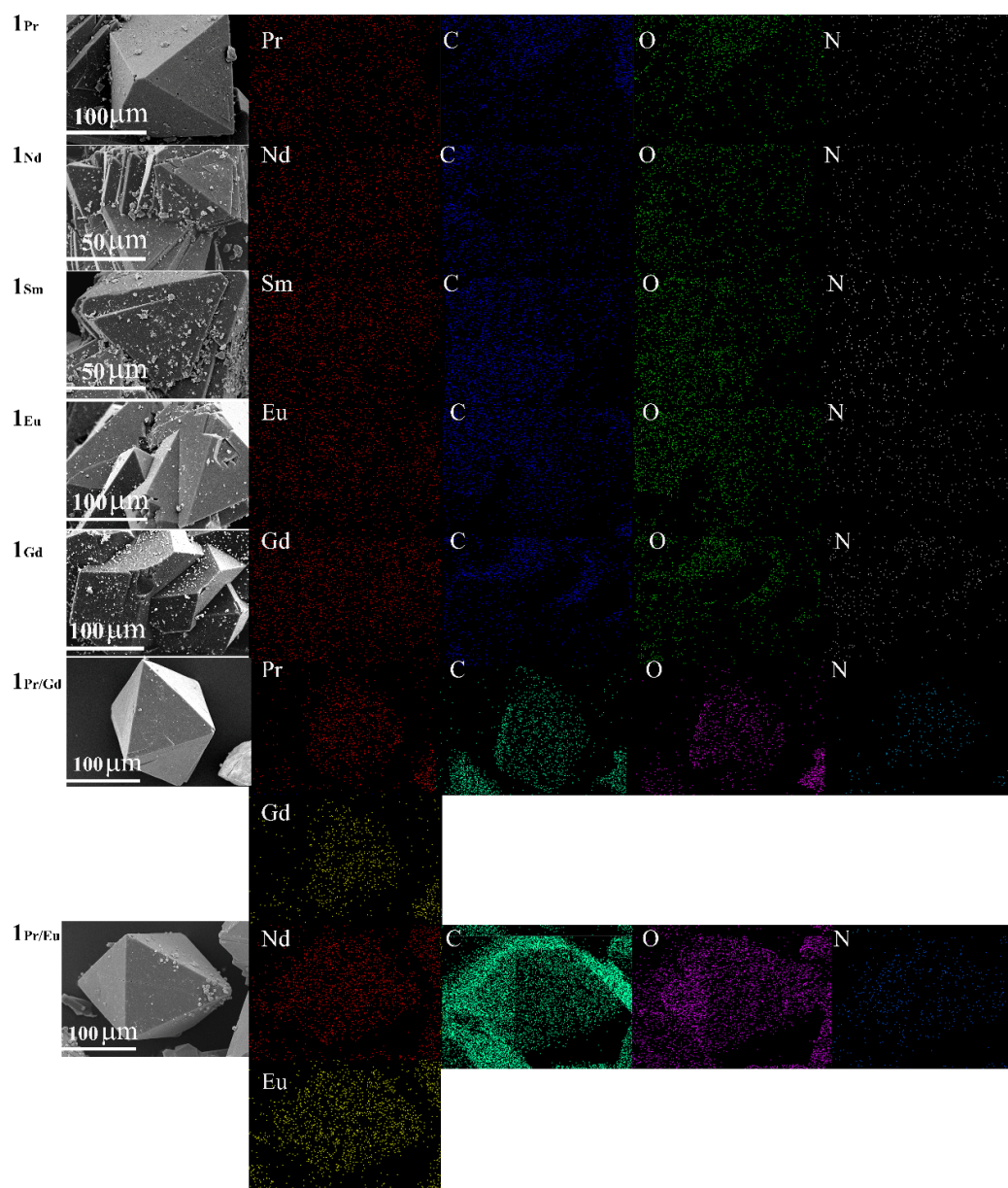


Fig. 3.10 Element mappings of $2L_n$ crystals with corresponding elemental mappings.

Based on the TGA curves, the methanol was also readily liberated under the N_2 gas flow due to showing endothermic behavior even at room temperature. The continual weight loss due to the desolvation was then observed until *ca.* 100 °C. The multiple endothermic behaviors during the loss (up to *ca.* 250 °C) imply disparity in intermolecular interactions involving these guest species. A partial disruption of the framework would be displayed after heating at 250 °C. It might be due to the decomposition of the organic

moieties, which was affirmed by the loss of a long-range order in PXRD patterns of **2Ga** (Fig. 3.12e). The collapse of the framework leading to the additional 64% weight loss was evident after heating higher than 250 °C, which provided a white powder of Gd_2O_3 as a product (Fig. 3.12f). The generation of vacant coordination sites on Ln^{III} could be, therefore, expected at temperatures lower than *ca.* 100 °C, which could be appropriated for the pretreatment for further pretreatment of other experiments was considered.

To study the water stability, the diffraction patterns of **2Ga** after being immersed in the water at room temperature for a week and 80 °C for 72 h were collected (Fig. 3.12c and e). The maintained structures were affirmed through the unchanged diffraction patterns compared with the as-synthesized sample. Due to the strong $\text{Ln}^{\text{III}}\text{—O}$ bond in the frameworks, it may lead to robustness with excellent water stability.

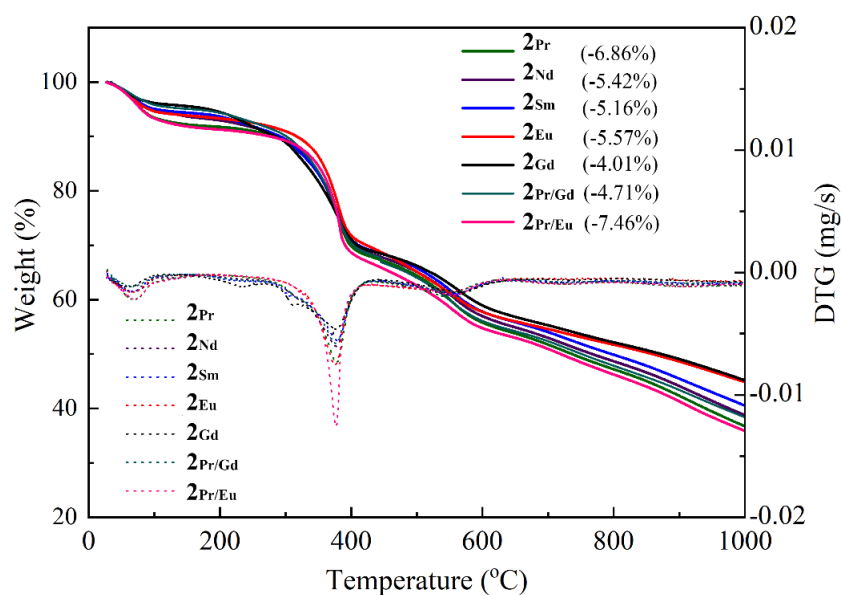


Fig. 3.11 TGA profiles of **2Ln** under heating from room temperature to 1000 °C under N_2 flow with a list of the initial weight losses.

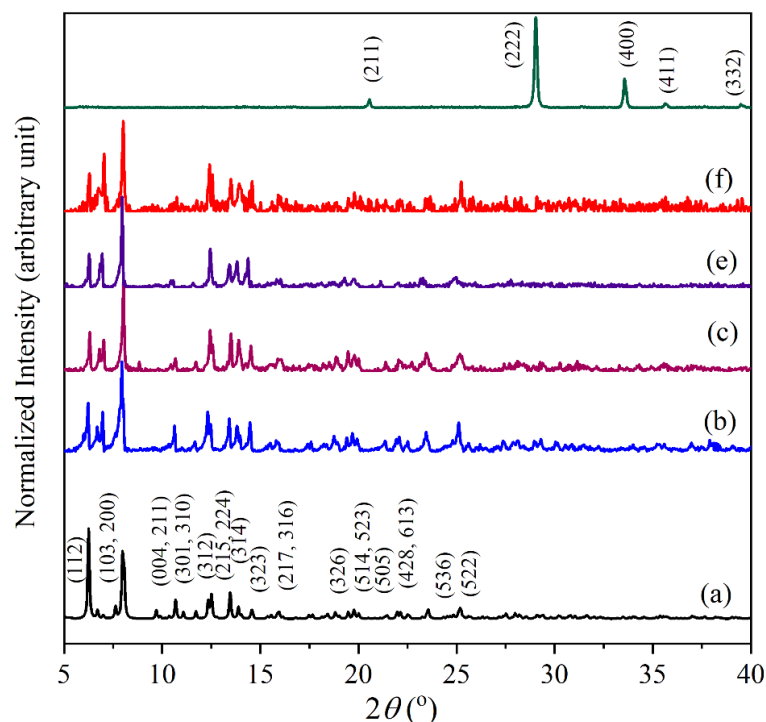


Fig. 3.12 PXRD of (a) simulated pattern from single crystal data of **2Ga** compared with (b) as-synthesized **2Ga**, (c) immersed in water at room temperature for a week, (d) immersed in hot water (80 °C) for 72 h, (e) heated at 250 °C for 3 h, and (f) heated at 1000 °C for 3 h.

3.3.4 Proton conductivity of **2Ga**

3.3.4.1 Superprotonic conductivity

Inspired by the specific direction of the one-dimensional channels in the nanoporous framework structure of **2Ga**, the introduction of mobile proton carriers into the large void and the transportation promoters into the framework could be enhanced [24-26]. Additionally, introducing the electron-withdrawing $-\text{NO}_2$ groups can also improve the ability of proton carriers in the framework structures through the enhancing the hydrogen bonding interactions and increasing the hydrophilicity along the surface channel [6]. To avoid the effects of the grain boundary and nondirectional proton conduction, the proton conductivities of **2Ga** based on single crystal data are revealed to be substantial using applied AC voltage of 0.1V and 1V. Both voltages provided a similar

fashion of the dependence conductivity on humidity temperature (Fig. 3.13 and 3.14). Based on the impedance data, the lower applied voltage however resulted in slightly lower proton conductivity values under the same conditions. With increasing humidity from 55 RH% to 99 RH% (fixed 25 °C), the conductivities were enhanced from $7.28 \times 10^{-5} \text{ S}\cdot\text{cm}^{-1}$ to $1.18 \times 10^{-2} \text{ S}\cdot\text{cm}^{-1}$ at 0.1V and $9.08 \times 10^{-5} \text{ S}\cdot\text{cm}^{-1}$ to $1.42 \times 10^{-2} \text{ S}\cdot\text{cm}^{-1}$ at 1V. While the temperature-dependence conductivities from 25 °C to 55 °C (fixed 99 RH%) results also could improve values as high as $5.76 \times 10^{-2} \text{ S}\cdot\text{cm}^{-1}$ at 0.1V applied voltage and 55 °C and $6.17 \times 10^{-2} \text{ S}\cdot\text{cm}^{-1}$ at 1V applied voltage and 55 °C.

According to the literature (Table 3.5), the proton conductivities with both maximum values of $5.76 \times 10^{-2} \text{ S}\cdot\text{cm}^{-1}$ (0.1V) and $6.17 \times 10^{-2} \text{ S}\cdot\text{cm}^{-1}$ (1V) under 99 RH% and 55 °C are very high value among those reported for the single crystals. The room temperature conductivity of **2Ga** ($1.42 \times 10^{-2} \text{ S}\cdot\text{cm}^{-1}$; 99 RH% and 25 °C) is also leading high value among proton-conducting CPs. These results could be clarified as superprotonic conducting LnCPs, which could be rationalized by the large content of diffused mobile proton carriers and the existence of the pending $-\text{NO}_2$ moieties of BPDC²⁻ along the channels [27]. To verify the assumption, the conductivities of the polycrystalline sample were investigated (Fig. 3.15). The proton conductivities of the pellet samples were 4.64×10^{-7} and $7.40 \times 10^{-7} \text{ S}\cdot\text{cm}^{-1}$ under 99 RH% at 25 and 55 °C, respectively. The disconnection of the channels could therefore disrupt the proton conduction. The water sorption ability of **2Ga** was therefore evident (Fig. 3.18d), providing a maximum value of $6.66 \text{ mmol}\cdot\text{g}^{-1}$ at 1 bar and 298 K.

Regarding the temperature-dependence conductivities at the highest humidity (99 RH%), the activation energy (E_a) of the single crystal sample was calculated as 0.43 eV (Fig. 3.16), which could estimate the proton conducting mechanism pathway. This calculated E_a value is in the borderline between the proton-carrier pathway ($> 0.4 \text{ eV}$) and the proton-hopping pathway ($< 0.4 \text{ eV}$) suggesting the possibility of both pathways to be responsible for the superprotonic conduction in **2Ga** [39]. Both transportation pathways in **2Ga** could be attributed due to the interaction between proton and polar groups on the internal surface of the channel in the framework and only the interaction of the water carrier, which is further away from the surface into the large void in the channel. This

phenomenon is not unexpected for nanoporous frameworks, *e.g.* MFM-500(Ni) (average pore size = 1.2 nm, $E_a = 0.43$ eV) [40] and $(\text{H}_3\text{O})[\text{Y}_2(\text{H}_5\text{btp})(\text{H}_4\text{btp})]\cdot\text{H}_2\text{O}$ (average pore size = 1.07 nm, $E_a = 0.40$ eV) [41].

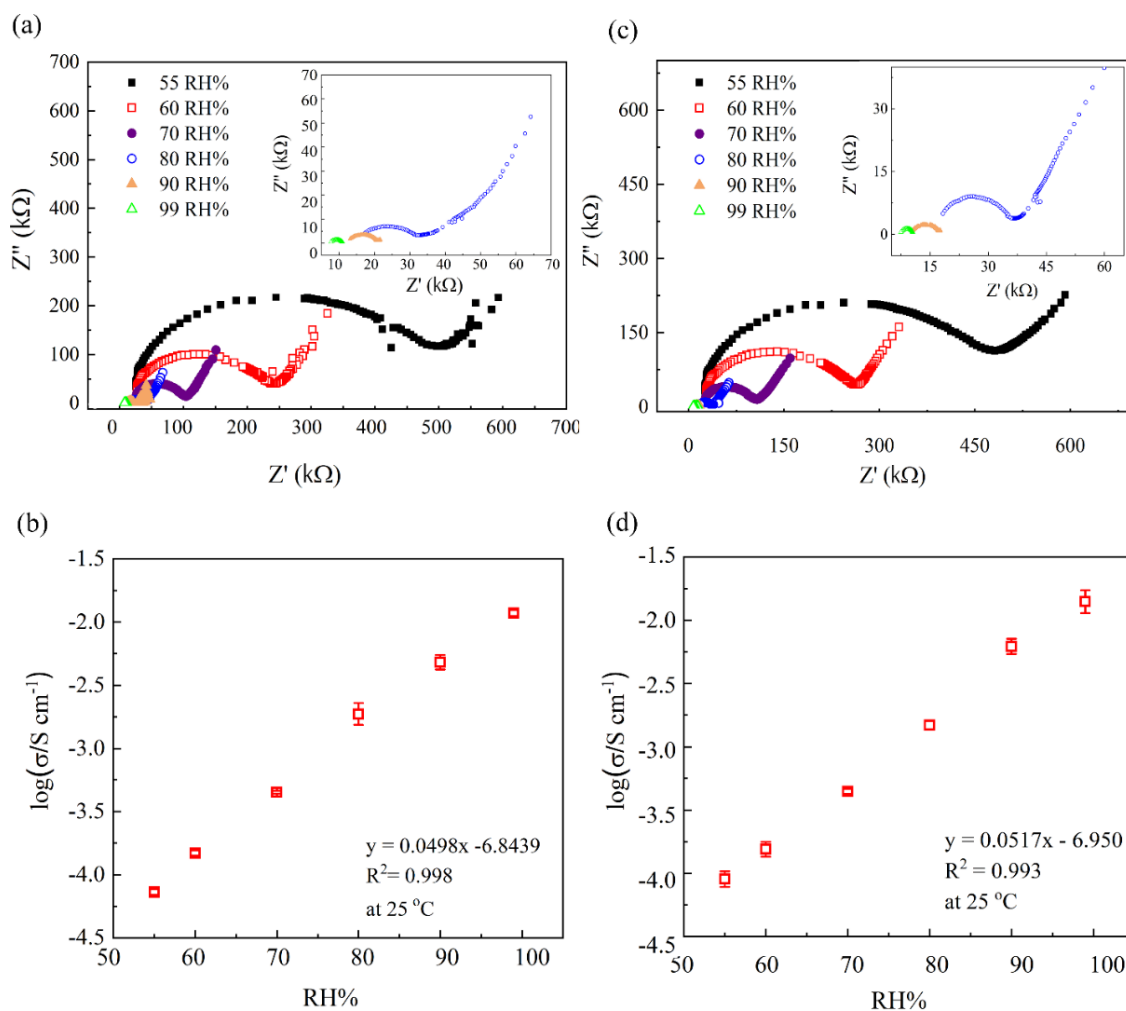


Fig. 3.13 (a, c) The humidity-dependent Nyquist plots and (b, d) the corresponding conductivities of 2Ga at 0.1 and 1V applied voltages, respectively.

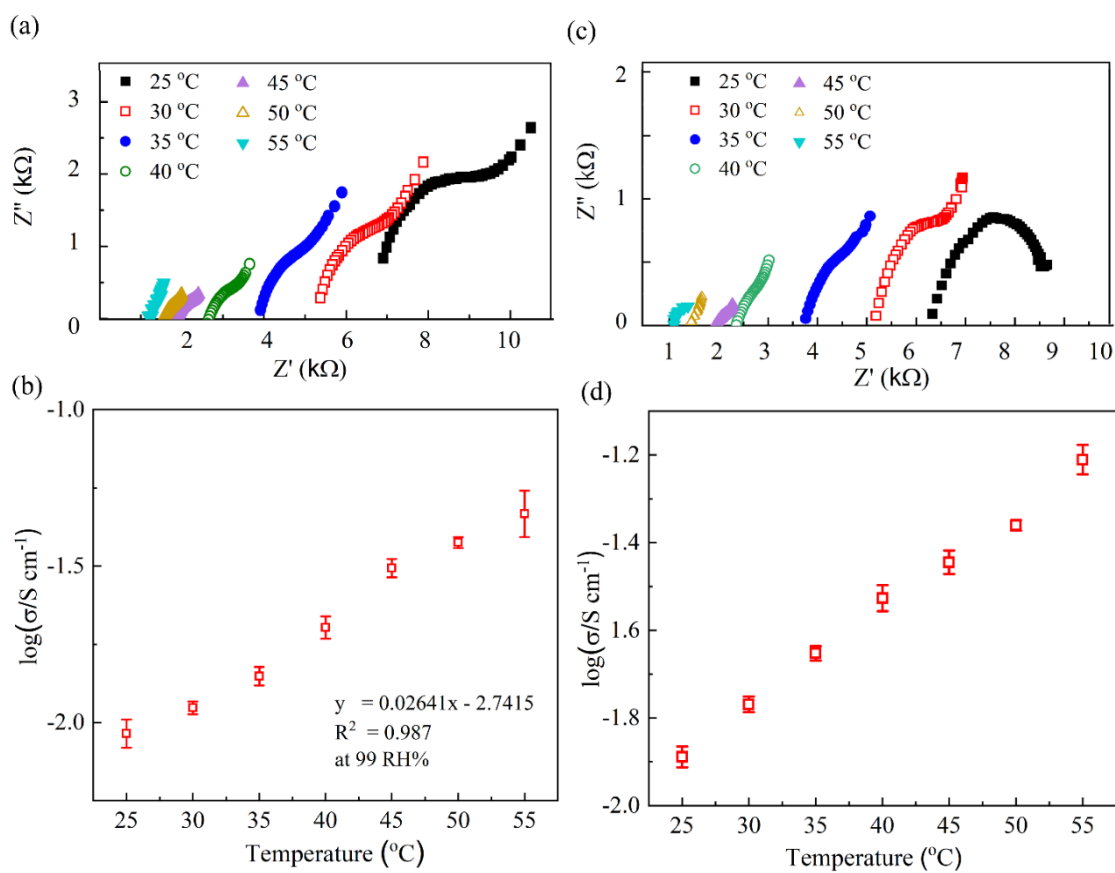


Fig. 3.14 (a, c) The temperature-dependent Nyquist plots and (b, d) the corresponding conductivities of 2Ga at 0.1 and 1 V applied voltages, respectively.

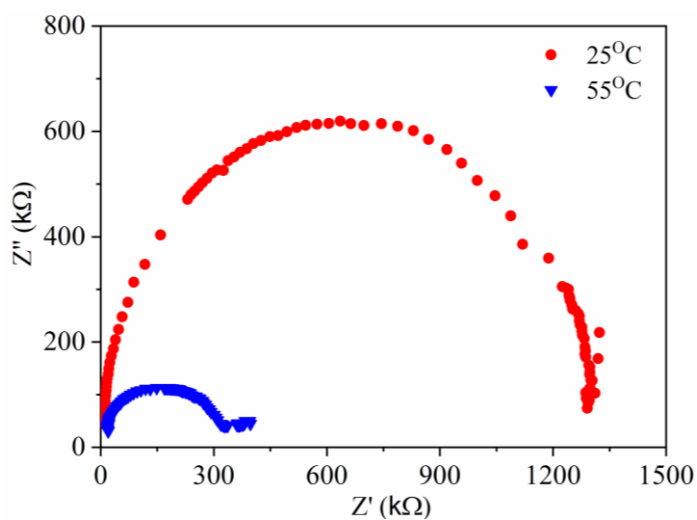


Fig. 3.15 The Nyquist plots of the pelletized polycrystalline sample of 2Ga prepared from ground crystals at 1 V applied voltages.

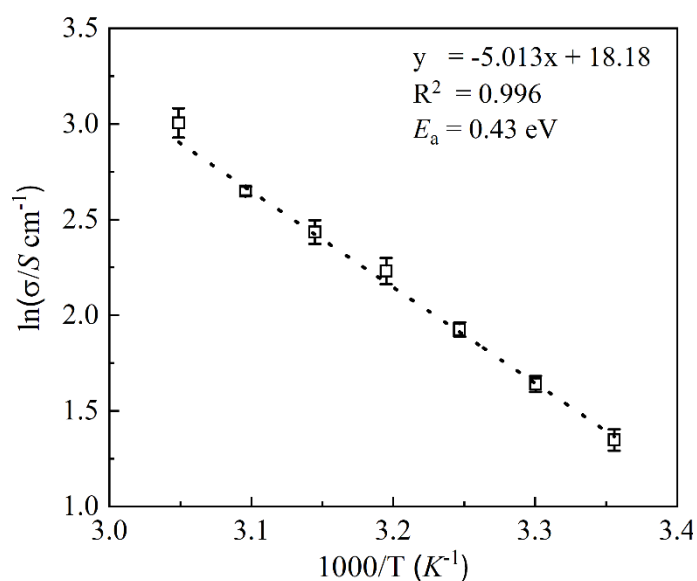


Fig. 3.16 Arrhenius plot of the proton conductivity of **2Ga** (25 to 55 °C and 99 RH%).

3.3.4.2 Humidity- and temperature-dependent proton conductivities

As the proton conductivities of **2Ga** in terms of $\log \sigma (\text{S} \cdot \text{cm}^{-1})$ exhibit excellent linear correlation for both humidity and temperature with $R^2 > 0.99$ for 55-99 RH% at 25 °C and $R^2 > 0.99$ for 25 to 55 °C at 99 RH% at 1V applied voltage (Fig. 3.17 and 3.18). With reference to the calibration curve, excellent accuracy and precision have been revealed for the humidity measurements; 64 ± 1 , 74 ± 1 , and 95 ± 1 RH% for the expected values of 65, 75, and 95 RH%, respectively. This is comparable to the commercialized humidity sensors. The temperature sensing performance of **2Ga** was also studied for the 25 to 40 °C at 99 RH% and 1V applied voltage, *i.e.* 27.61 ± 0.19 , 32.04 ± 0.64 , and 36.98 ± 0.73 °C for the expected value of 28.00, 32.00, and 36.50 °C, respectively. Regarding these temperature and humidity sensing ranges, **2Ga** is a significant candidate to use in a wide range of industries applications, *e.g.* storage and logistics of agricultural products as well as electronic devices.

Founded on ten successive measurements (Fig. 3.19), the excellent $\delta(\text{RH})$ (*ca.* 1 % at both 55 and 99 RH%, $R > 97\%$) and δT (0.42 °C at 25 and 40 °C, $R > 97\%$) were investigated. Note that R is the repeatability of the measurements and δ is the standard deviations of the read-outs values. Based on the R values of the measurements provided

by **2Ga**, the highest among the sensing materials based on conducting CPs [42,43] could be reported, which could be essentially comparable to those of conducting ceramics, *e.g.* SnO₂ nanowires ($R < 90\%$) [44] and graphite oxide ($R = 90\%$) [45]. The robustness of **2Ga** is notable through ten successive measurements for both humidity and temperature experiments. The high stability of **2Ga** is also evident *via* the remained PXRD patterns after immersion in water at both room temperature and 80 °C (Fig. 3.12c and d).

Table 3.5 Proton conductivities and activation energies of **2Ga** compared with previously reported superprotonic conducting CPs and single crystal samples

Samples	σ (S·cm ⁻¹)	Temp. (°C)	Humidity (RH%)	E_a (eV)	Ref
UiO-66-SO ₃ H ^{††}	1.64×10^{-1}	80	95	0.107	[28]
BUT-8(Cr)A ^{††}	1.27×10^{-1}	80	100	0.11	[27]
PCMOF2 ^{1/2} (Tz) ^{††}	1.17×10^{-1}	85	100	0.22	[29]
PCMOF2 ^{1/2} (Pz) ^{††}	1.1×10^{-1}	85	90	0.16	[29]
UiO-66-(SO ₃ H) ₂ ^{††}	8.4×10^{-2}	80	90	0.32	[30]
{H[(N(CH ₃) ₄) ₂][Gd ₃ (NIPA) ₆]}·3H ₂ O [†]	7.17×10^{-2}	75	98	0.13	[6]
2Ga This work[†]	6.17×10^{-2}	55	99	0.43	
Fe-CAT-5 ^{††}	5×10^{-2}	25	98	0.24	[31]
[(Me ₂ NH ₂) ₃ (SO ₄) ₂][Zn ₂ (ox) ₃] ^{††}	4.2×10^{-2}	25	98	0.13	[32]
PCC-72 [†]	3.4×10^{-3}	25	99	0.23	[33]
CFA-17	2.1×10^{-3}	22	95	0.3	[34]
[Cu ₂ (Htzehp) ₂ (4,4-bipy)]·3H ₂ O [†]	1.43×10^{-3}	80	95	0.48	[35]
PCMOF-17 [†]	1.25×10^{-3}	25	40	0.31	[36]
(Me ₂ NH ₂)[Eu(L)] [†]	1.25×10^{-3}	150	0	0.21	[37]
CoLa-II [†]	3.1×10^{-4}	25	95	0.34	[38]

[†]The values were from single crystal samples.

^{††}The values were from pellet samples.

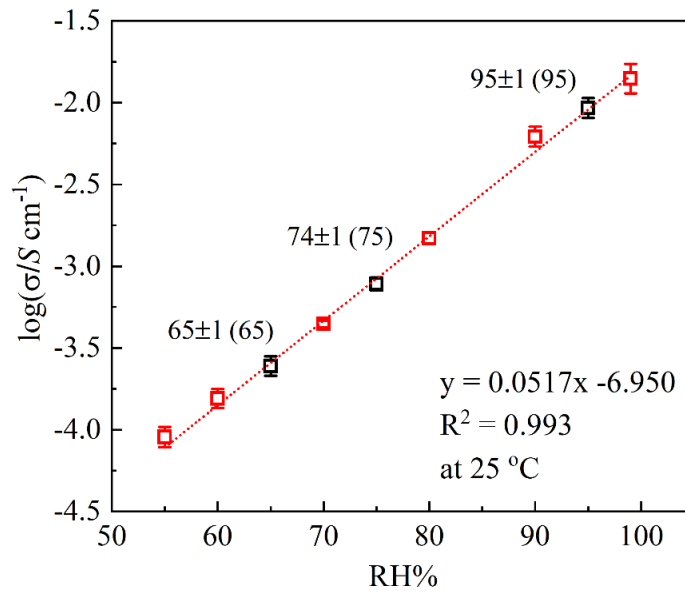


Fig. 3.17 Calibration curves (red dashed-line) and the read-out data points (black) of humidity dependence with the expected values shown in brackets.

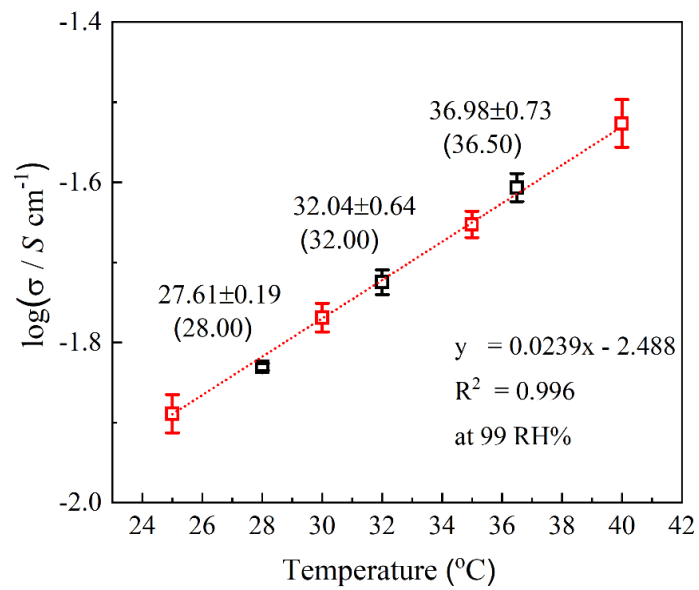


Fig. 3.18 Calibration curves (red dashed-line) and the read-out data points (black) of temperature dependence with the expected values shown in brackets.

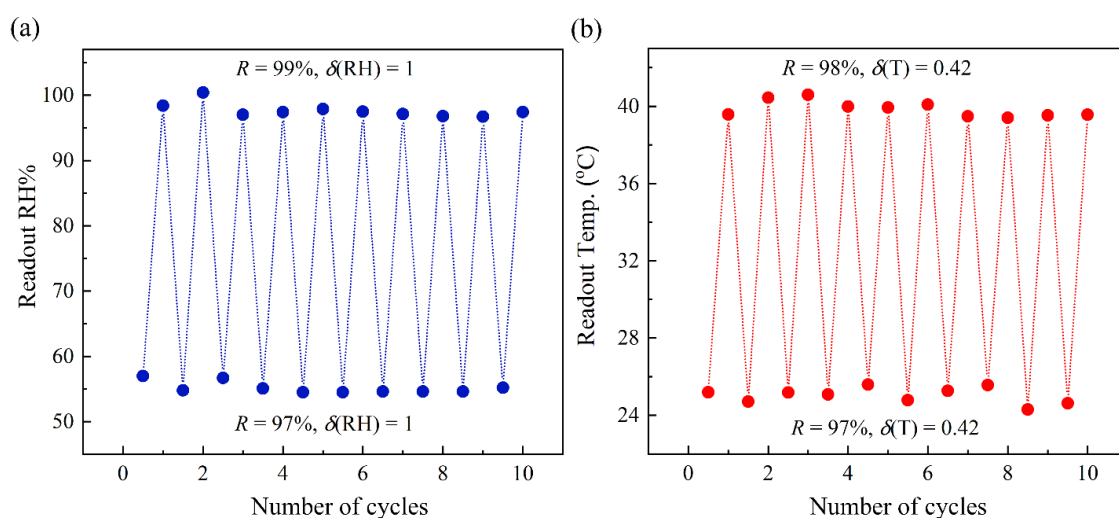


Fig. 3.19 Ten successive measurements of (a) relative humidity (55 and 99 RH%, 25 °C) and (b) temperature (25 to 40 °C, 99 RH%) at 1V applied voltage.

3.3.5 Gas adsorption and selectivity

As we expected that the larger pore may promote the gas adsorption capacity and the decorated polar $-\text{NO}_2$ groups may enhance the selectivity. The gas adsorption behaviors of $\mathbf{2}_{\text{Ga}}$ were evaluated for several gases, *i.e.* H_2 , N_2 , O_2 , and CO_2 at different temperatures of 77 K, 195 K, and 298 K. The typical type I adsorption isotherm was observed for all the tested gases, exhibiting sudden uptake at the initial experiments before approaching the saturation plateau (Fig. 3.20). The intriguing characteristic of $\mathbf{2}_{\text{Ga}}$ is its temperature-dependent adsorption selectivity (Table 3.6).

At 77 K (Fig. 3.20a), the adsorption of the H_2 was significantly poorer than the N_2 gas, which showed a sudden uptake to the saturation of $7.33 \text{ mmol}\cdot\text{g}^{-1}$ ($164.22 \text{ cm}^3\cdot\text{g}^{-1}$) at 1 bar. On the other hand, H_2 gas showed a gradual uptake with the rising pressure and reached $2.95 \text{ mmol}\cdot\text{g}^{-1}$ ($66.06 \text{ cm}^3\cdot\text{g}^{-1}$) at 1 bar. At 195 K (Fig. 3.20b), the highly selective adsorption of CO_2 was significantly evident compared with N_2 and O_2 gases. Whilst the adsorption of the two gases was extremely poor, the CO_2 uptake capacity of $\mathbf{2}_{\text{Ga}}$ was $4.87 \text{ mmol}\cdot\text{g}^{-1}$ ($109.1 \text{ cm}^3\cdot\text{g}^{-1}$) at 1 bar. At 298 K (Fig. 3.20c), the CO_2 uptake capacity at 1 bar fell drastically to $0.80 \text{ mmol}\cdot\text{g}^{-1}$ ($18 \text{ cm}^3\cdot\text{g}^{-1}$), whereas the N_2 gas was negligible. The abrupt adsorption was not observed at this temperature. Intriguingly, the uptake capacities

of CO₂ for all temperatures are much higher than N₂ and O₂, indicating significant gas selectivity behavior for CO₂.

To study the adsorption selectivity for CO₂ over O₂ and N₂, the initial uptake capacity ratios at 0.1 bar were determined. The selectivity of **2Ga** toward CO₂ over O₂ and N₂ were investigated, i.e. 39:1 for CO₂/O₂ at 195 K, 46:1 for CO₂/N₂ at 195 K and 21:1 CO₂/N₂ 298 K, respectively. The values of selectivity are relatively high which are comparable to those previous reported MOFs under similar conditions. The high CO₂ adsorption properties and outstanding selectivity of **2Ga** could be due to the interactions between the polar –NO₂ groups on the *di*-nitro-BPDC²⁻. The interaction between CO₂ and the frameworks could be also evident *via* the isosteric adsorption enthalpies (Q_{st}) using the Clausius-Clapeyron equation [46,47]. Based on the adsorption isotherms at 195 K and 298 K, the Q_{st} for CO₂ was calculated to be the average value of *ca* 20.7±4 kJ·mol⁻¹ (Fig. 3.20e) suggesting the strong physical interactions between the CO₂ molecules and the framework, *e.g.* open metal site and polar –NO₂ functional group.

In comparison to the CO₂ uptake capacity for those **2Ln** (Ln = Pr^{III}, Nd^{III}, Sm^{III}, and Eu^{III}), the adsorption/desorption behaviors were measured at 195 K (Fig. 3.20f). The sudden rise in CO₂ adsorption could confirm the presence of vacant coordination sites on Ln^{III}. The CO₂ adsorption capacity of those **2Ln** (Ln = Pr^{III}, Nd^{III}, Sm^{III}, and Eu^{III}) was 1.81 mmol·g⁻¹ (40.5 cm³·g⁻¹) for **2Pr**, 2.00 mmol·g⁻¹ (44.8 cm³·g⁻¹) for **2Nd**, 2.98 mmol·g⁻¹ (66.6 cm³·g⁻¹) for **2Sm**, and 5.97 mmol·g⁻¹ (133.8 cm³·g⁻¹) for **2Eu**, respectively. The corresponding surface areas and average pore sizes of the framework were also determined as 107 m²·g⁻¹ and 1.90 nm for **2Pr**, 120 m²·g⁻¹ and 1.87 nm for **2Nd**, 194 m²·g⁻¹ and 1.72 nm for **2Sm**, 408 m²·g⁻¹ and 1.65 nm for **2Eu**, and 407 m²·g⁻¹ and 1.35 nm for **2Ga**, respectively. These values consist of the effect of lanthanide contraction resulting in different interactions between CO₂ and Ln^{III} vacant coordination sites as well as the other active sites within the frameworks. On the other hand, the slightly smaller CO₂ capacity of **2Ga** than **2Eu** was observed due to the substantial shrinkage of the opening of framework **2Ga**, which might limit the entering of CO₂.

Table 3.6 The gas uptake capacities at 1 atm for 77 K, 195 K, and 298 K

Temperature (K)	Sample	Gas	Gas uptake capacities at 1 bar	
			V (cm ³ ·g ⁻¹)	mmol·g ⁻¹
77	2Gd	N ₂	164.2	7.33
	2Gd	H ₂	66.06	2.95
195	2Pr	CO ₂	40.51	1.81
	2Nd	CO ₂	44.75	2.00
	2Sm	CO ₂	66.56	2.98
	2Eu	CO ₂	133.79	5.97
	2Gd	CO ₂	109.07	4.87
	2Gd	N ₂	15.34	0.68
	2Gd	O ₂	14.25	0.64
298	2Gd	CO ₂	17.82	0.80
	2Gd	N ₂	1.33	0.059
	2Gd	H ₂ O	149.16	6.66

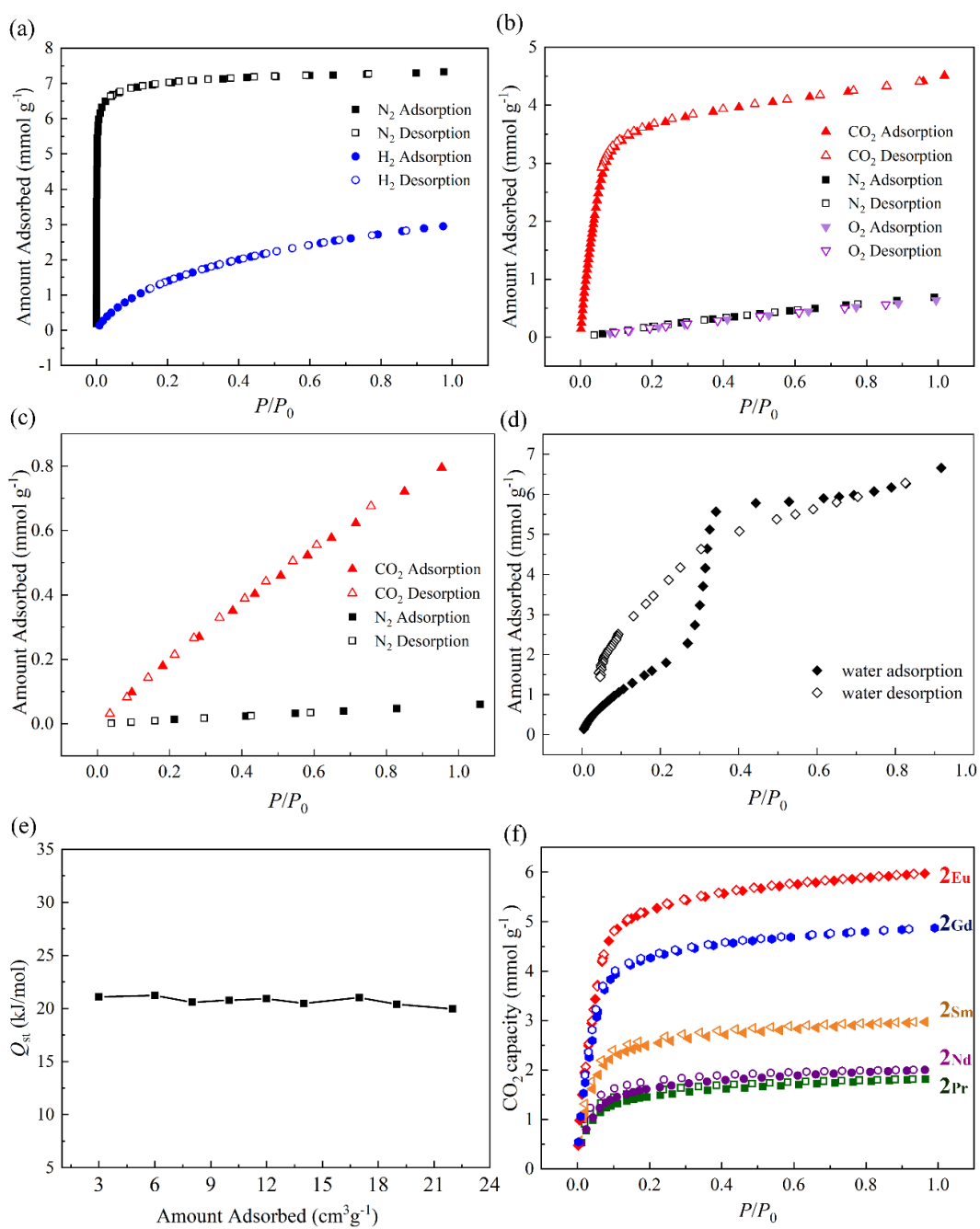


Fig. 3.20 Gas adsorption/desorption isotherms of 2Gd for CO_2 , N_2 , H_2 , and O_2 (a) at 77 K, (b) at 195 K, (c) at 298 K, (d) water adsorption/desorption isotherms of 2Gd at 298 K, (e) the isosteric adsorption enthalpy of CO_2 for 2Gd , and (f) comparison of CO_2 adsorption/desorption of 2Ln at 298 K.

3.3.6 Acidity and basicity of **2Pr**, **2Eu**, and **2Gd**

To study content of acidic and basic sites and acidic and basic strength in the frameworks, the NH₃-TPD and the CO₂-TPD profiles of the supposedly weakest Lewis acidic Pr^{III} (**2Pr**) and the two strongest Lewis acidic Eu^{III} (**2Eu**) and Gd^{III} (**2Gd**) were evaluated (Fig. 3.21). According to the NH₃ desorptions, a range of acidic sites possessing different strengths from weak to medium can be assumed, occurring in the 90 to 170 °C temperature range and at temperatures >200 °C. Based on the integral area at the lower temperature range of **2Pr** was obviously larger than both **2Eu** and **2Gd**, which required the higher temperature. The presence of weaker acidic sites in **2Pr** can therefore be presumed. On the other hand, the profile of **2Eu** exhibited a tendency of large integral area at high temperature. This might suggest the strong interaction with NH₃ in the framework resulting in stronger acidic strength. The profile of **2Gd** presented a small peak at low temperature, which was unexpectedly poorer than **2Eu**. Since the major desorption of **2Gd** was still required at the higher temperature, a large amount of strong acidic sites could, however, be assumed. Regarding the results, the increasing acidity from **2Pr** to **2Eu** and **2Gd** could be concluded, corresponding to the lanthanide contraction effect. Concerning the CO₂-TPD profiles, the desorption of CO₂ was observed with similar profiles of NH₃. In the case of **2Pr**, the desorption peak was clearly observed at the temperature range of 70 to 190 °C with a rising trend at higher temperatures. In contrast, the predominant desorption profile of **2Eu** and **2Gd** required temperatures >180 °C. The stronger attractions of CO₂ in **2Eu** and **2Gd** than **2Pr** were therefore conclusive.

It should be noted nonetheless that all of the present functional groups in the frameworks such as the electron withdrawing –NO₂, the electron rich phenyl rings, the lone-paired electron of O atoms of carboxylates on the organic ligand, and the vacant coordination sites on Ln^{III} can interact with both NH₃ and CO₂ through different strength of interactions. As **2Pr**, **2Eu**, and **2Gd** are isostructural and contain the same functional groups, dissimilarities in strength and content of both acidity and basicity the frameworks are clearly attributable to type of Ln^{III}, *i.e.* Pr^{III} (**2Pr**), Eu^{III} (**2Eu**), and Gd^{III} (**2Gd**). The smaller Gd^{III} should in principle interact with both NH₃ and CO₂ with better strength than the larger Pr^{III}.

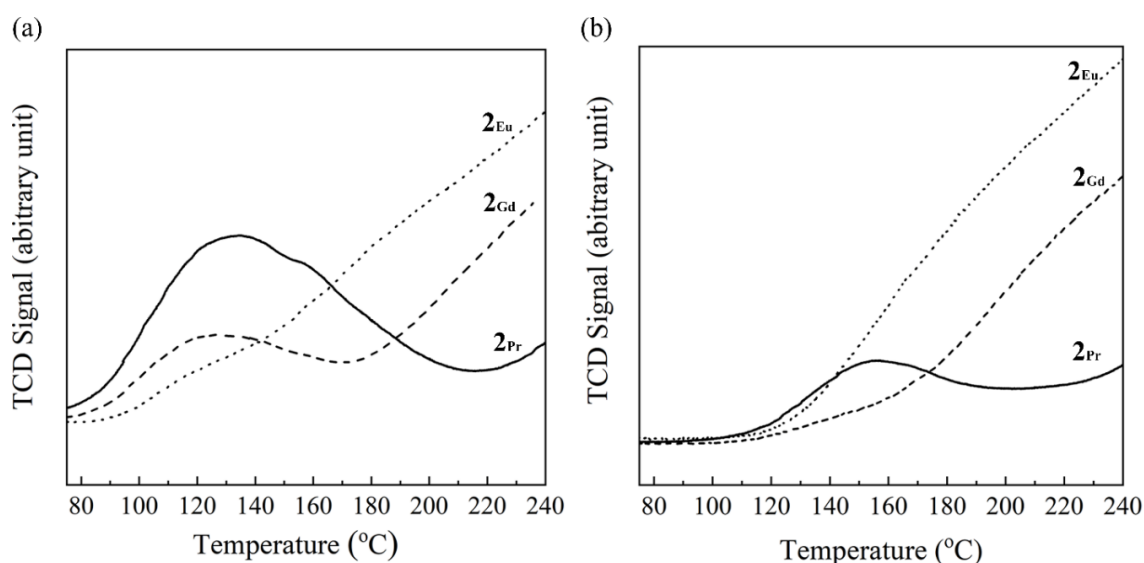


Fig. 3.21 (a) NH₃-TPD and (b) CO₂-TPD profiles of **2Pr** (solid lines), **2Eu** (dotted lines), and **2Ga** (dashed lines).

3.3.7 Catalytic activities

3.3.7.1 CO₂ cycloaddition reactions with epoxides

Inspired by the highest CO₂ sorption capacity, **2Eu** was selected as a representative of others **2Ln** to evaluate the catalytic performance based on the CO₂ cycloaddition reaction with ECH as a catalytic model. The reaction was carried out with ECH in the presence of *n*-Bu₄NBr co-catalyst and optimized out under solven-free and ambient CO₂ pressure conditions (Table 3.7). The percentage conversion, selectivity, TON, and TOF were calculated based on the ¹H NMR spectra. These parameters reflect only the performance of the catalyst and not the other processing factors. The common by-product of 1-chloro-3-bromo-2-propanol was also slightly observed in ¹H NMR spectra (Fig 3.22). The selectivity of the reaction was thus additionally included for accuracy of the evaluation. The catalyzed reactions with only either *n*-Bu₄NBr or **2Eu** were also conducted (Table 3.7; entry 1 and 2) to illustrate the essence of the co-catalyst and its synergy with **2Eu**. Intriguingly, this synergistic effect was pronounced through the percentage conversion.

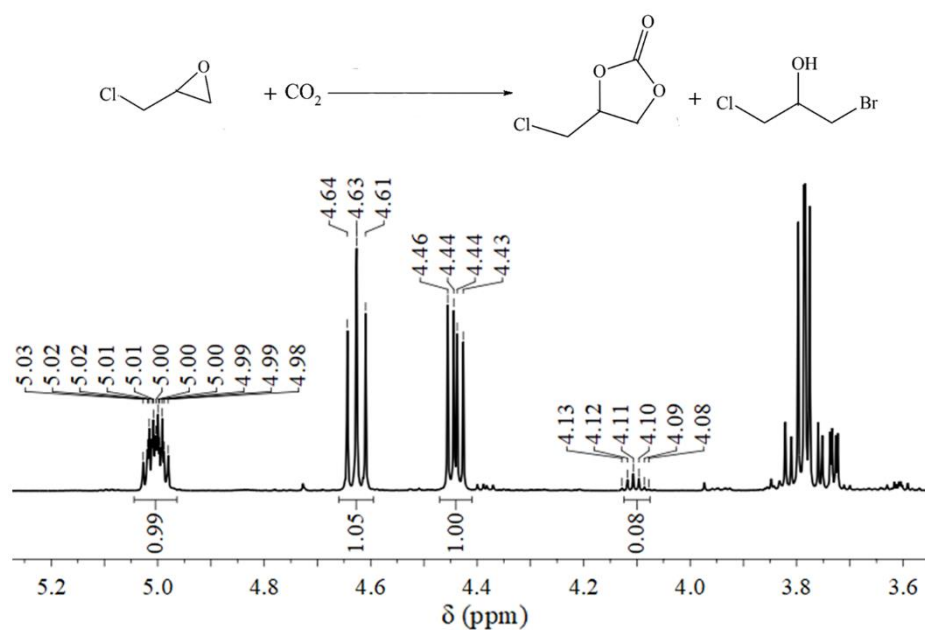
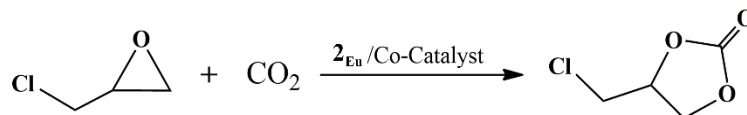


Fig. 3.22 Exemplary ¹H NMR spectrum of the CO₂ cycloaddition reaction with ECH catalyzed by **2Eu**.

The influences of reaction temperature and time were investigated from 80 to 60 °C (Table 3.7; entry 3-6) and 4 to 2 h (Table 3.7; entry 3, 7, and 8), respectively under controlled other catalytic conditions (20 mmol of ECH, 2.5 mol% of *n*-Bu₄NBr and 0.25 mol% of **2Eu**). At low reaction temperature and short reaction time revealed low conversion due to the restriction of transportation and accessibility to the catalytic sites in the framework [48]. Based on these results, the reaction temperature of 80 °C and reaction time of 4 h were chosen for the other experiments with the fixed 20 mmol of ECH. With an increasing amount of *n*-Bu₄NBr from 2.5 mol% to 5.0 mol% (Table 3.7; entry 3 and 9) under the specified condition, the conversion of ECH did not improve. In contrast, the selectivity of the reaction was reduced by approximately 10%. This suggests that the large amount of *n*-Bu₄NBr apparently favors the formation of by-product, which can occur in the presence of any acid [49-51]. In addition, the influences of different co-catalyst were also investigated.

Table 3.7 Catalytic activities of **2_{Eu}** in CO₂ cycloaddition reactions with ECH under solvent-free and ambient CO₂ pressure conditions



Entry	Co-catalyst (mol%)	IV (mol%)	Temp (°C)	Time (h)	%Conversion ($\pm SD$)	% selectivity ($\pm SD$)	TON ‡	TOF ‡
1	<i>n</i> -Bu ₄ NBr (2.5)	-	80	4	58 [†]	85 [†]	20	5
2	-	0.25	80	4	19 [†]	58 [†]	44	11
3	<i>n</i> -Bu ₄ NBr (2.5)	0.25	80	4	98(± 2)	91(± 1)	356	89
4	<i>n</i> -Bu ₄ NBr (2.5)	0.25	75	4	94(± 2)	93(± 1)	351	88
5	<i>n</i> -Bu ₄ NBr (2.5)	0.25	70	4	88(± 10)	86(± 4)	303	76
6	<i>n</i> -Bu ₄ NBr (2.5)	0.25	60	4	68(± 12)	90(± 1)	244	61
7	<i>n</i> -Bu ₄ NBr (2.5)	0.25	80	3	95(± 5)	92(± 1)	349	116
8	<i>n</i> -Bu ₄ NBr (2.5)	0.25	80	2	74(± 6)	86(± 1)	254	127
9	<i>n</i> -Bu ₄ NBr (5.0)	0.25	80	4	98(± 1)	82(± 2)	318	79
10	<i>n</i> -Bu ₄ NBr (2.5)	0.12	80	4	89(± 1)	87(± 1)	623	156
11	<i>n</i> -Bu ₄ NBr (2.5)	0.062	80	4	79(± 4)	87(± 1)	1106	276
12	<i>n</i> -Pr ₄ NBr (2.5)	0.25	80	4	99(± 2)	91(± 1)	360	90
13	Et ₄ NBr (2.5)	0.25	80	4	91(± 3)	91(± 1)	330	83

[†]Data from one experiment [‡]Determined from average conversion and selectivity

Compared with the other co-catalysts showing different hydrocarbon chain lengths *i.e.* *n*-Pr₄NBr and Et₄NBr (Table 3.7; entry 12 and 13), the comparable performances to *n*-Bu₄NBr suggested the flexibility in choices of the co-catalysts in this reaction. Moreover, the attempt to decrease amount of the catalyst (Table 3.7; entry 3, 10, and 11) from 0.25 to 0.12 and 0.062 mol% brought down the conversion from 98(± 2)% to 89(± 1)

and 79(±4)%, respectively under controlling the other catalytic conditions. Nonetheless, the selectivity was slightly dropped from 91(±1)% to 87(±1)%. TON and TOF factors were also evaluated to indicate the performance of different catalysts. Under the maximum values of conversion and selectivity of 98(±2)% and 91(±1)%, respectively (Table 3.7; entry 3), the satisfying values of TON of 356 and TOF of 89 h⁻¹ were displayed. These values are comparable to those previous reported transition metal- and Ln^{III}- based CPs under the ambient CO₂ pressure (Table 3.10). The TON and TOF values of **2Eu** could be raised to 1,106 and 276 h⁻¹ under diminished catalyst to 0.062 mol% with satisfiable conversions and selectivity of of ≥79(±4)% and 87(±1)%, respectively. Compared with the other nanoporous MOFs catalysts (Table 3.10), these catalytic conditions of **2Eu** are considerably milder with notable TON and TOF values, especially for the ambient CO₂ pressure.

One of the significant features of **2Eu** is its robustness, which illustrated through the recyclability and the retaining framework even after eight successive measurements (Fig. 3.23b). The conversions were approxilately unchanged from the first to the last cycle, varying between 91 and 100% (Fig. 3.23a). However, the selectivity slightly dropped from 91% in the first cycle to 76% in the eighth cycle. This may be due to the framework blockage and the resticted transportation within the framework. The constant catalytic conversion throughout the measurement could be meant the completely abstracted of ECH substrate in the reaction and capted within the framework. Therefore, the selectivity should be poisoned as the formation of the by-product, which could be occurred outside the framework. To prove the assumption, the FT-IR and the EDX results of **2Eu** after the eighth measurements were conducted (Fig. 3.23c and d). There were characteristics of $\nu(\text{C}-\text{Cl})$ and remaining of Br and Cl elements, which were evident in the elemental mappings. The remaining ECH substrate, by-product (1-chloro-3-bromo-2-propanol), and chloropropene carbonate product in **2Eu** were considered. The trapping of these molecules within the framework could be resulted in the diminished selectivity values of the reaction, affirming the assumption. Therefore, the occlusion of these molecules in the framework is a critical issue for the dropped performance of the re-used catalyst, which may need more attention.

To extend the scope of epoxides in this reaction, $\mathbf{2}_{\text{Eu}}$ and $n\text{-Bu}_4\text{NBr}$ were used as the representative catalyst and co-catalyst (Table 3.8). The smaller size of substrates, *i.e.* propylene oxide (1a) and 1,2-epoxybutane (1b), could exhibit exceptional conversion to cyclic carbonates, but the selectivity was apparently low. On the other hand, the longer and the bulky substrates obviously showed ineffective performance with very low conversion. Therefore, nanoporous framework $\mathbf{2}_{\text{Eu}}$ can provide potential molecular sieve properties for the diffusion of bulky epoxides.

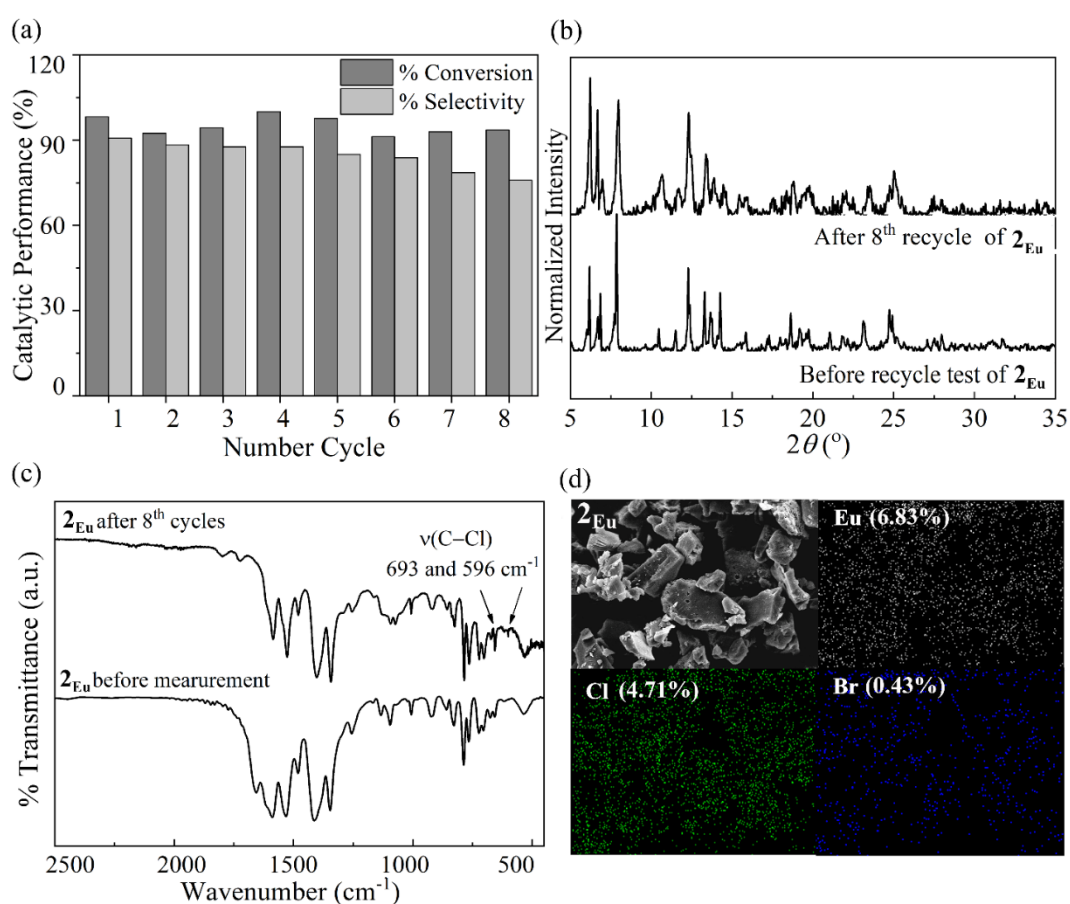


Fig. 3.23 (a) Percentage conversion (dark gray) and selectivity (light gray) for the recycling experiments of $\mathbf{2}_{\text{Eu}}$, (b) the observed PXRD, (c) FT-IR spectra, and (d) SEM image with elemental mappings of $\mathbf{2}_{\text{Eu}}$ (selected element only Eu, Cl, and Br) after the eighth successive measurements.

Table 3.8 Catalytic activities of **2_{Eu}** in CO₂ cycloaddition reactions with several epoxides under solvent-free and ambient CO₂ pressure conditions

	Substrate	% conversion (SD)	% selectivity (SD)	TON	TOF
1a		100 [†]	NA ^{††}	NA ^{††}	NA ^{††}
1b		99(±2)	58(±14)	214	54
1c		75(±3)	100	300	75
1d		72(±14)	100	288	72
1e		40(±8)	100	160	40
1f		39(±5)	100	155	39

[†]Data from one experiment

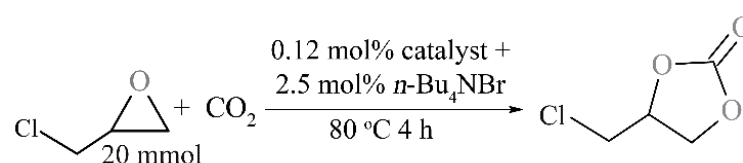
^{††}Unidentified by-product

3.3.7.2 Influence of lanthanide contraction on the catalytic performance

To investigate the effect of diverse Lewis acidic strength introduced by the diminishing in ionic radii of Ln^{III} through the lanthanide contraction, the catalysis performances of **2_{Ln}** (Ln = Pr^{III}, Nd^{III}, Sm^{III}, Eu^{III}, and Gd^{III}) were evaluated (Table 3.9). The increasing conversion, TON, and TOF values from **2_{Pr}** to **2_{Gd}** was observed (Table 3.9; entry 1-5). Through the effect of lanthanide contraction with the gradual diminishing in ionic radii from Pr^{III} to Gd^{III}, the enhanced catalysis tendency should be ascribed to the improved acidic strength of Ln^{III}. The highest performance catalyst of **2_{Gd}** provided the

TON and TOF of 695 and 174 h⁻¹, respectively. On the basis of these results, the significance of Lewis acidic Ln^{III} in the catalysis by the nanoporous **2Pr** to **2Ga** has nonetheless been emphasized. Interestingly, the selectivity of difference in Lewis acidity strength of the reactions was not as vividly modulated as the conversion suggesting the formation of the by-product outside the framework.

Table 3.9 Catalytic activities of **2Ln** in CO₂ cycloaddition reactions with ECH under solvent-free and ambient CO₂ pressure conditions



Entry	2Ln catalyst	%Conversion (<i>SD</i>)	% selectivity (<i>SD</i>)	TON [‡]	TOF [‡]
1	2Pr	77 (±1)	82 (±4)	504	125
2	2Nd	84 (±5)	86 (±4)	580	145
3	2Sm	86 (±3)	88 (±2)	604	150
4	2Eu	89 (±1)	87 (±1)	623	156
5	2Gd	98 (±1)	89 (±4)	695	174
6	2Pr/Gd	94 (±4)	86 (±6)	692	173
7	2Pr/Eu	95 (±1)	87 (±5)	698	174

[‡]Calculated from the average conversion and selectivity

Compared to the homometallic framework, the dilution of the stronger Lewis acidic Ln^{III} (Eu^{III} and Gd^{III}) in the framework by weaker acidic Pr^{III}, *i.e.* **2Pr/Gd** (Table 3.9; entry 6) and **2Pr/Eu** (Table 3.9; entry 7), significantly promoted the conversion about *ca.* 17% and 18%, respectively. The synergistic effect of the fluctuation in Lewis acidic strength within the framework could be thus essential to the catalyst. With mixing different Ln^{III} within the coordination framework, the creation of framework defects should also be

considered. It could be concluded that introducing different Ln^{III} into the same coordination framework without the disruption of the structure may be beneficial for their coordination chemistry and can be an additional route to regard in designing new catalysts.

Referring to the mechanism of the CO_2 cycloaddition reactions with epoxides as depicted in Fig. 3.24, the ring-opening process the determining step to indicate the performance of the catalysts [52,53]. Therefore, the strong interaction between catalyst and substrate should provide high catalytic performance. In addition, the accessibility of the substrate and available Lewis acidic sites are also critical. These factors might depend on the number of vacant coordination sites on Ln^{III} . To affirm this assumption, the computational calculation were supported [54], which suggested the less crowded environments of Ln^{III} centers as effective catalytic sites.

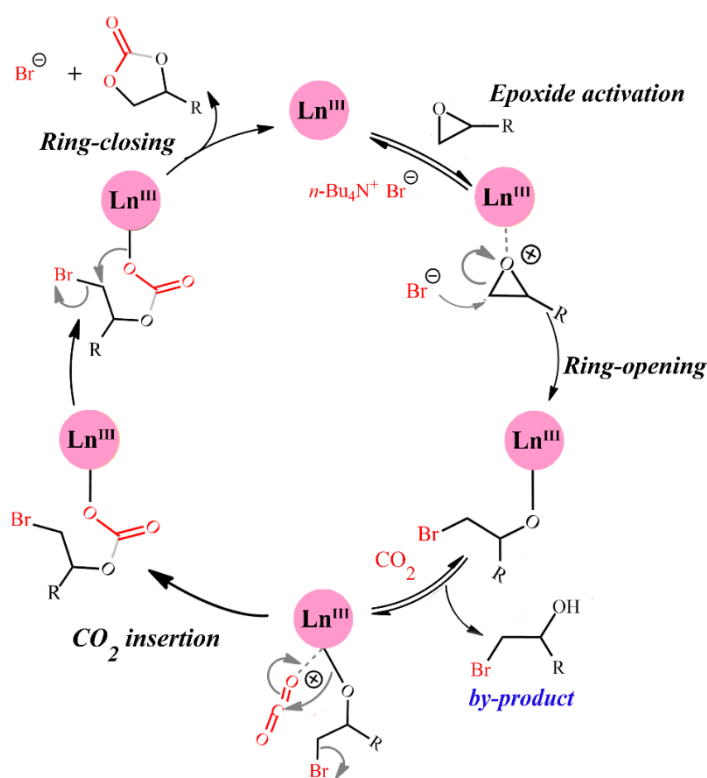


Fig. 3.24 Diagram showing a possible mechanism of the CO_2 cycloaddition reactions with epoxides (ECH as a model epoxide).

Table 3.10 Conversion, selectivity (if available), and the corresponding TON and TOF values reported for nanoporous CPs catalysts employed in the CO₂ cycloaddition with ECH under various conditions

Catalyst	Catalyst (mol%)	Co-Cat. (mol%)	Temp. (°C)	Time (h)	P (atm)	Conversion (%)	Selectivity (%)	TON	TOF (h ⁻¹)	Pore Size (nm)	Ref.
Ce ₂ NDC ₃	2.4	1.8	RT	8	1	92	NA	372	47	1.3	[55]
PCN-900(Eu)-CoTCPP-CoBPYDC	0.12	4.32	50	12	1	74	NA	617	31	1.3	[56]
1·Gd	7.5	2.5	60	12	1	97	NA	13	1	1	[57]
[TbL(H ₂ O) ₂]·H ₂ O] _n	3.5	3.5	70	12	1	>99	NA	29	2	0.78×1.21	[58]
NUC-25	2.5	5	75	8	1	99	NA	40	5	0.54 – 1.04	[59]
[Me ₂ NH ₂][Cd(dtztp) _{0.5} (HCOO)] · 1.5DMF·H ₂ O	0.2	2	80	4	1	97	NA	485	121	1 – 1.59	[60]
Mn ₄ (L) ₂ (H ₂ O) ₄] _n ·4DMF·H ₂ O	0.5	10	80	8	1	99	NA	198	25	1.13×0.88 1.07×0.87	[61]
{[Co(TCPB) _{0.5} (H ₂ O)]·DMF} _n	0.10	2.5	80	9	1	99	NA	990	110	1.14	[62]
NUC-7	0.2	5	80	24	1	98	98	632	23	1.18 & 1.26	[63]
(I-)Meim-UiO-66	0.52	-	120	24	1	100	93	179	7.5	0.6, 1.1, 3.4	[64]
Zn(Bmic)(AT)	0.54	1.45	80	6	5	98	98	180	30	0.59,0.73,1.18	[65]
[Zn ₃ (L) ₃ (H ₂ L)·2DMF·H ₂ O]	0.27	0.9	80	5	10	97	98	360	72	0.98×1.1	[66]
Zn-MOF	0.2	2	80	4	20	97	NA	485	121	0.6 & 1.2	[67]
Cr-MIL-101-[BuPh ₃ P]Br	0.045	-	120	2	20	98.3	99.3	2184	1092	2.4	[68]
gea-MOF-1	0.15	0.15	120	6	20	89	NA	593	99	1.12×0.56 2.48×1.46 2.24×2.24	[69]

3.4 Conclusion

To enlarge porosity of LnCPs, *di*-nitro-BPDC²⁻ was used to fabricate a new series of [Ln₄(*di*-nitro-BPDC)₄(NO₂)₃(OH)(H₂O)₅] · (solvent) (**2**_{Ln}; Ln = Pr^{III}, Nd^{III}, Sm^{III}, Eu^{III}, and Gd^{III}). The effective one-dimensional window openings varying in sizes from 2.0 × 1.1 nm² to 1.5 × 1.1 nm² have been achieved. Owing to the large porosity and the accessible –NO₂ groups, the framework exhibited capacity in proton conduction, temperature and humidity sensing, CO₂ gas adsorption and selectivity, and catalytic properties.

Regarding the proton conductivity, **2**_{Gd} exhibited superprotonic conduction with a maximum value of 6.17 × 10⁻² S·cm⁻¹ at 1V applied voltage, 55 °C, and 99 RH%. Based on proton conduction, the sensing of humidity and temperature were shown to be excellent within a working range of 55 to 99 RH% at fixed 25°C and 25 to 40 °C at fixed 99 RH%, respectively. Its outstanding reusability was indicated with 97% repeatability and the standard deviations of 1 RH% and 0.42 °C. The fabricated LnCPs also showed excellent selectivity with CO₂ over other gases (N₂, O₂, and H₂), which could motivate the study of catalytic activities with CO₂, *i.e.* CO₂ cycloaddition reaction with epoxides. The excellent performances with high selectivity under ambient CO₂ pressure and 80 °C manifested through the maximum TON of 1,106 and TOF of 276 h⁻¹ for **2**_{Eu}. The effect of lanthanide contraction was also investigated providing the increased performance with the gradual diminishing in ionic radii from Pr^{III} to Gd^{III}. These could suggest a further design to achieve effective catalysts.

3.5 References

- [1] Eddaoudi, M.; Kim, J.; Rosi, N.; Vodak, D.; Wachter, J.; O’Keeffe, M.; Yaghi, O. M. *Science* **2002**, 295, 469–472.
- [2] Lee, J.; Farha, O. K.; Roberts, J.; Scheidt, K. A.; Nguyen, S. T.; Hupp, J. T. *Chem. Soc. Rev.* **2009**, 38, 1450–1459.

- [3] He, Y.; Chen, F.; Li, B.; Qian, G.; Zhou, W.; Chen, B. *Coord. Chem. Rev.* **2018**, *373*, 167–198.
- [4] Das, R. K.; Aijaz, A.; Sharma, M. K.; Lama, P.; Bharadwaj, P. K. *Chem. A Eur. J.* **2012**, *18*, 6866–6872.
- [5] Panyarat, K.; Prior, T.J.; Rujiwattra, A. *Polyhedron* **2014**, *81*, 74–80.
- [6] Xing, X.-S.; Fu, Z.-H.; Zhang, N.-N.; Yu, X.-Q.; Wang, M.-S.; Guo, G.-C. *Chem. Commun.* **2019**, *55*, 1241–1244.
- [7] Zhou, J.-M.; Shi, W.; Li, H.-M.; Li, H.; Cheng, P. *J. Phys. Chem. C* **2014**, *118*, 416–426.
- [8] Gao, M.-L.; Wang, W.-J.; Liu, L.; Han, Z.-B.; Wei, N.; Cao, X.-M.; Yuan, D.-Q. *Inorg. Chem.* **2017**, *56*, 511–517.
- [9] Luo, T.-Y.; Liu, C.; Eliseeva, S. V.; Muldoon, P. F.; Petoud, S.; Rosi, N. L. *J. Am. Chem. Soc.* **2017**, *139*, 9333–9340.
- [10] Yan, L.; Yue, Q.; Jia, Q.-X.; Lemercier, G.; Gao, E.-Q. *Cryst. Growth Des.* **2009**, *9*, 2984–2987.
- [11] Zhou, L.-J.; Deng, W.-H.; Wang, Y.-L.; Xu, G.; Yin, S.-G.; Liu, Q.-Y. *Inorg. Chem.* **2016**, *55*, 6271–6277.
- [12] Xue, D.-X.; Cairns, A. J.; Belmabkhout, Y.; Wojtas, L.; Liu, Y.; Alkordi, M. H.; Eddaoudi, M. *J. Am. Chem. Soc.* **2013**, *135*, 7660–7667.
- [13] McDonald, K. A.; Ko, N.; Noh, K.; Bennion, J. C.; Kim, J. A.; Matzger, J. *Chem. Commun.* **2017**, *53*, 7808–7811.
- [14] CrysAlisPRO software system (ver.71.39.46); Rigaku Corporation: Oxford, U.K., **2018**.
- [15] Sheldrick, G. M. SADABS; University of Göttingen: Göttingen, Germany, **1996**.
- [16] Sheldrick, G. M. *Acta Cryst.* **2008**, *A64*, 112–122.
- [17] Sheldrick, G. M. *Acta Cryst.* **2015**, *C71*, 3–8.

- [18] Dolomanov, O. V.; Bourhis, L. J.; Gildea, R. J.; Howard, J. A. K.; Puschmann, H. *J. J. Appl. Cryst.* **2009**, *42*, 339–341.
- [19] Spek, A. *J. Appl. Cryst.* **2003**, *36*, 7–13.
- [20] Dinca, M.; Long, J. R. *J. Am. Chem. Soc.* **2005**, *127*, 9376–9377.
- [21] Pouessel, J.; Thuéry, P.; Berthet, J.-C.; Cantat, T. *Dalton Trans.* **2014**, *43*, 4415–4425.
- [22] Groom, C. R.; Bruno, I. J.; Lightfoot, M. P.; Ward, S. C. IUCr. The Cambridge Structural Database, *Acta Cryst.* **2016**, *B72*, 171–179.
- [23] Ye, J.; Bogale, R. F.; Shi, Y.; Chen, Y.; Liu, X.; Zhang, S.; Yang, Y.; Zhao, J.; Ning, G. *Chem. Eur. J.* **2017**, *23*, 7657–7662.
- [24] Li, A. L.; Gao, Q.; Xu, J.; Bu, X. H. *Coord. Chem. Rev.* **2017**, *344*, 54–82.
- [25] Yoon, M.; Suh, K.; Natarajan, S.; Kim, K. *Angew. Chem. Int. Ed.* **2013**, *52*, 2688–2700.
- [26] Jeong, N. C.; Samanta, B.; Lee, C. Y.; Farha, O. K.; Hupp, J. T. *J. Am. Chem. Soc.* **2012**, *134*, 51–54.
- [27] Yang, F.; Xu, G.; Dou, Y.; Wang, B.; Zhang, H.; Wu, H.; Zhou, W.; Li, J.-R.; Chen, B. A. *Nat. Energy* **2017**, *2*, 877–883.
- [28] Mukhopadhyay, S.; Debgupta, J.; Singh, C.; Sarkar, R.; Basu, O.; Das, S. K. *ACS Appl. Mater. Interfaces* **2019**, *11*, 13423–13432.
- [29] Kim, S.; Joarder, B.; Hurd, J. A.; Zhang, J.; Dawson, K. W.; Gelfand, B. S.; Wong, N. E.; Shimizu, G. K. H. *J. Am. Chem. Soc.* **2018**, *140*, 1077–1082.
- [30] Phang, W. J.; Jo, H.; Lee, W. R.; Song, J. H.; Yoo, K.; Kim, B. S.; Hong, C. S. *Angew. Chem. Int. Ed.* **2015**, *54*, 5142–5146. DOI: 10.1002/anie.201411703
- [31] Nguyen, N. T. T.; Furukawa, H.; Gándara, F.; Trickett, C. A.; Jeong, H. M.; Cordova, K. E.; Yaghi, O. M. *J. Am. Chem. Soc.* **2015**, *137*, 15394–15397.

- [32] Nagarkar, S. S.; Unni, S. M.; Sharma, A.; Kurungot, S.; Ghosh, S. K. *Angew. Chem. Int. Ed.* **2014**, *53*, 2638–2642.
- [33] Qin, L.; Yu, Y.-Z.; Liao, P.-Q.; Xue, W.; Zheng, Z.; Chen, X.-M.; Zheng, Y.-Z. *Adv. Mater.* **2016**, *28*, 10772–10779.
- [34] Bunzen, H.; Javed, A.; Klawinski, D.; Lamp, A.; Grzywa, M.; Kalytta-Mewes, A.; Tiemann, M.; Krug von Nidda, H.-A.; Wagner, T.; Volkmer, D. *ACS Appl. Nano Mater.* **2019**, *2*, 291–298.
- [35] Li, R.; Wang, S.-H.; Chen, X.-X.; Lu, J.; Fu, Z.-H.; Li, Y.; Xu, G.; Zheng, F.-K.; Guo, G.-C. *Chem. Mater.* **2017**, *29*, 2321–2331.
- [36] Joarder, B.; Lin, J.-B.; Romero, Z.; Shimizu, G. K. H. *J. Am. Chem. Soc.* **2017**, *139*, 7176–7179.
- [37] Wei, Y.-S.; Hu, X.-P.; Han, Z.; Dong, X.-Y.; Zang, S.-Q.; Mak, T. C. W. *J. Am. Chem. Soc.* **2017**, *139*, 3505–3512.
- [38] Bao, S.-S.; Otsubo, K.; Taylor, J. M.; Jiang, Z.; Zheng, L.-M.; Kitagawa, H. *J. Am. Chem. Soc.* **2014**, *136*, 9292–9295.
- [39] Mueller, M.; Schubert, M.; Puetter, H.; Schierle-Arndt, K.; Pastre, J. *Mater. Chem.* **2006**, *16*, 626–636.
- [40] Pili, S.; Argent, S. P.; Morris, C. G.; Rought, P.; García-Sakai, V.; Silverwood, I. P.; Easun, T. L.; Li, M.; Warren, M. R.; Murray, C. A.; Tang, C. C.; Yang, S.; Schröder, M. *J. Am. Chem. Soc.* **2016**, *138*, 6352–6355.
- [41] Firmino, A. D. G.; Mendes, R. F.; Antunes, M. M.; Barbosa, P. C.; Vilela, S. M. F.; Valente, A. A.; Figueiredo, F. M. L.; Tomé, J. P. C.; Paz, F. A. A. *Inorg. Chem.* **2017**, *56*, 1193–1208.
- [42] Su, P.-G.; Lee, X.-H. *Sens. Actuators B chem.* **2018**, *269*, 110–117.
- [43] Zhang, J.; Sun, L.; Chen, C.; Liu, M.; Dong, W.; Guo, W.; Ruan, S. *J. Alloys Compd.* **2017**, *695*, 520–525.

- [44] Kuang, Q.; Lao, C.-S.; Wang, Z.-L.; Xie, Z.-X.; Zheng, L.-S. *J. Am. Chem. Soc.* **2007**, *129*, 6070–6071.
- [45] Borini, S.; White, R.; Wei, D.; Astley, M.; Haque, S.; Spigone, E.; Harris, N.; Kivioja, J.; Ryhänen, T. *ACS Nano* **2013**, *7*, 11166–11173.
- [46] Angeli, G. K.; Sartsidou, C.; Vlachaki, S.; Spanopoulos, I.; Tsangarakis, C.; Kourtellaris, A.; Klontzas, E.; Froudakis, G. E.; Tasiopoulos, A.; Trikalitis, P. N. *ACS Appl. Mater. Interfaces* **2017**, *9*, 44560–44566.
- [47] Du, L.; Lu, Z.; Zheng, K.; Wang, J.; Zheng, X.; Pan, Y.; You, X.; Bai, J. *J. Am. Chem. Soc.* **2013**, *135*, 562–565.
- [48] Johnson, B. A.; Beiler, A. M.; McCarthy, B. D.; Ott, S. *J. Am. Chem. Soc.* **2022**, *142*, 11941–11956.
- [49] Anjali, K.; Christopher, J.; Sakthivel, A. *ACS Omega* **2019**, *4*, 13454–13464.
- [50] Vagnoni, M.; Samorì, C.; Galletti, P. *J. CO₂ Util.* **2020**, *42*, 101302.
- [51] Martín, C.; Fiorani, G.; Kleij, A. W. *ACS Catal.* **2015**, *5*, 1353–1370.
- [52] Shaikh, R. R.; Pornpraprom, S.; D’Elia, V., *ACS Catal.* **2018**, *8*, 419–450.
- [53] Hu, T.-D.; Jiang Y.; Ding, Y.-H., *J. Mater. Chem. A*, **2019**, *7*, 14825–14834.
- [54] Thammakan, S.; Kuwamura, N.; Chiangraeng, N.; Nimmanpipug, P.; Konno, T.; Rujiwatra, *J. Solid State Chem.* **2021**, *303*, 122464.
- [55] Das, S.; Chatterjee, S.; Bhunia, S.; Mondal, A.; Mitra, P.; Kumari, V.; Pradhan, A.; Bhaumik, A. *Dalton Trans.* **2017**, *46*, 13783–13792.
- [56] Zhang, L.; Yuan, S.; Feng, L.; Guo, B.; Qin, J.; Xu, B.; Lollar, C.; Sun, D.; Zhou, H. *Angew. Chem. Int. Ed.* **2018**, *57*, 5095–5099.
- [57] Dong, J.; Cui, P.; Shi, P.; Cheng, P.; Zhao, B. *J. Am. Chem. Soc.* **2015**, *137*, 15988–15991.
- [58] Jing, T.; Chen, L.; Jiang, F.; Yang, Y.; Zhou, K.; Yu, M.; Cao, Z.; Li, S.; Hong, M. *Cryst. Growth Des.* **2018**, *18*, 2956–2963.

- [59] Chen, H.; Hu, T.; Fan, L.; Zhang, X. *Inorg. Chem.* **2021**, *60*, 1028–1036.
- [60] Wang, G.-D.; Li, Y.-Z.; Shi, W.-J.; Hou, L.; Zhu, Z.; Wang, Y.-Y. *Inorg. Chem. Front.* **2020**, *7*, 1957–1964.
- [61] Cheng, S.; Wu, Y.; Jin, J.; Liu, J.; Wu, D.; Yang, G.; Wang, Y.-Y. *Dalton Trans.* **2019**, *48*, 7612–7618.
- [62] Dhankhar, S. S.; Nagaraja, C. M. *New J. Chem.* **2019**, *43*, 2163–2170.
- [63] Chen, H.; Fan, L.; Zhang, X. *ACS Appl. Nano Mater.* **2020**, *3*, 7201–7210.
- [64] Liang, J.; Chen, R.-P.; Wang, X.-Y.; Liu, T.-T.; Wang, X.-S.; Huang, Y.-B.; Cao, R. *Chem. Sci.* **2017**, *8*, 1570–1575
- [65] Li, Y.; Zhang, X.; Lan, J.; Xu, P.; Sun, J. *Inorg. Chem.* **2019**, *58*, 13917–13926.
- [66] Gao, Z.; Zhang, X.; Xu, P.; Sun, J. *Inorg. Chem. Front.* **2020**, *7*, 1995–2005.
- [67] Li, Y. Z.; Wang, G. D.; Yang, H. Y.; Hou, L.; Wang, Y. Y.; Zhu, Z. *Inorg. Chem. Front.* **2020**, *7*, 746–755.
- [68] Dai, W.; Mao, P.; Liu, Y.; Zhang, S.; Li, B.; Yang, L.; Luo, X.; Zou, J. *J. CO₂ Util.* **2020**, *36*, 295–305.
- [69] Guillerm, V.; Weseliński, Ł. J.; Belmabkhout, Y.; Cairns, A. J.; D’Elia, V.; Wojtas, Ł.; Adil, K.; Eddaoudi, M. *Nat. Chem.* **2014**, *6*, 673–680.

CHAPTER 4

Tunable Installation of Lanthanide Cubane Clusters in Porous Supramolecular Frameworks Based on Multicarboxylate Metalloligands

4.1 Introduction

In recent years, the high-nuclearity lanthanide clusters in LnCPs becomes the most interesting research frontier because of their unique properties and fantastic architectures. In some cases, the combination of lanthanide clusters with bridging ligands provides porous LnCPs [1,2]. Among a variety of lanthanide clusters, lanthanide clusters with bridging hydroxide groups, *i.e.* $\text{Ln}_x(\text{OH})_y$, have attracted much attention in various fields owing to their intriguing chemical, physical, and magnetic properties as well as their potential applications [3-5]. A variety of $\text{Ln}_x(\text{OH})_y$ clusters with different compositions have been rationalized by a ligand-controlled hydrolytic approach. Using suitable ligands can limit and control the degree of hydrolysis of Ln^{III} ions leading to the formation $\text{Ln}_x(\text{OH})_y$ clusters ability [6-9]. The available literature indicated that carboxylate ligands, amino acids, Schiff base ligands, and other polydentate ligands are reasonable options for supporting the $\text{Ln}_x(\text{OH})_y$ clusters formation [9].

Regarding the ligand-control approach for constructing tetranuclear clusters, *i.e.* $\text{Ln}_4(\text{OH})_4$ cubanes, the contributions of the ligands, *e.g.* their identity, charge, polarity, polarizability, and binding ability, are critical [10]. Known examples of the ligands are limited, *e.g.* amino acid; L-aspartic acid, L-glutamic acid, DL-cysteine, L-valine, proline, [6,11-13], Schiff-base complexes [14,15], and aromatic carboxylic acid; nicotinic acid (Hnic) [16], isonicotinic acid (HIN) [7], 4-(4-carboxyphenyl)-1,2,4-triazole ligand (Hcpt) [17], and 4,4',4''-tricarboxytriphenylamine (H_3TCA) [18]. However, the synthetic approach for controlling the number of lanthanide ions in the clusters is still challenging

due to the large pH dependency of lanthanides and their exceptional flexibility of coordination spheres and geometries.

The study on the template effects, *e.g.* anions and pores, to control the generating $\text{Ln}_4(\text{OH})_4$ cubane clusters would be an alternative pathway for overcoming the limitations of conventional methods [19,20]. Concerning pore as a template, the discrete metallosupramolecular complexes could be regarded as an effective candidate to control the $\text{Ln}_4(\text{OH})_4$ cubane formation through the tunable porosity by modification of weak interactions, *e.g.* hydrogen bonding [21]. Literature examples of such pores as a template in discrete metallosupramolecular systems are, however, quite rare. To the best of our knowledge, there is only one example published by Konno's group, *i.e.* $\text{Ln}_{0.33}[\text{Ln}_4(\mu_3\text{-OH})_4(\mu_2\text{-OAc})_3(\text{H}_2\text{O})_7][\text{L}^{\text{Rh}}] \cdot n\text{H}_2\text{O}$ (**6_{Ln}**) when $[\text{L}^{\text{Rh}}]^{6-} = [\text{Zn}_4\text{O}\{\text{Rh}(\text{L-cys})_3\}_4]^{6-}$, $\text{Ln} = \text{Gd}^{\text{III}}$, Tb^{III} , Dy^{III} , Er^{III} , Ho^{III} , Tm^{III} , Yb^{III} , and Lu^{III} [22]. In this system, the lanthanide cubane clusters are formed in specific spaces surrounded by free carboxylate groups belonging to the metalloligand $\text{K}_6[\text{Zn}_4\text{O}\{\text{Rh}(\text{L-cys})_3\}_4] \cdot n\text{H}_2\text{O}$ (**K₆[L^{Rh}]·nH₂O**). Nevertheless, lanthanide cubane clusters were formed only for the late lanthanide ions. While cluster formation was not observed for the early lanthanide ions, *i.e.* La^{III} , Ce^{III} , Pr^{III} , Nd^{III} , Sm^{III} , and Eu^{III} , which had formula as $\text{Ln}_2[\text{L}^{\text{Rh}}] \cdot n\text{H}_2\text{O}$ (**5_{Ln}**).

To expand the range of the cubane cluster formation in the lanthanide series, in this chapter, a new discrete anionic metalloligand $\text{K}_6[\text{Zn}_4\text{O}\{\text{Ir}(\text{L-cys})_3\}_4] \cdot 48\text{H}_2\text{O}$ (**K₆[L^{Ir}]·48H₂O**) (Fig. 4.3a) was designed. The heavier Ir^{III} centers would differently direct the interactions for the packing structure, particularly hydrogen bonding, allowing a different porosity. Moreover, the higher energy of the *d-d* excited state of Ir^{III} compared to Rh^{III} may diminish the emission quenching due to the energy transfer to the *d-d* excited state [23]. The enhancement of photoluminescent properties in **K₆[L^{Ir}]·48H₂O** and the lanthanide cubane clusters in the frameworks was thus investigated. The study of the interaction between Ln^{III} in the cubane clusters was also presented through magnetic measurements.

4.2 Experimental

4.2.1 Synthesis (Δ_{LLL})₄-K₆[Zn₄O{Ir(L-cys)₃}]₄·48H₂O (K₆[L^{Ir}]₄·48H₂O)

A suspension of 0.25 g (0.44 mmol) of Δ_{LLL} -H₃[Ir(L-cys)₃], which was synthesized following the literature [24], in 10 mL of DI. water was prepared at room temperature. With continuous stirring, 0.38 g (4.6 mmol) of ZnO and 0.23 g (1.0 mmol) of ZnBr₂ were added. The pH of the mixture was adjusted to *ca.* 8 to 9 using 0.5 M of KOH aqueous solution. The mixture was stirred at room temperature for 2 h and then filtered to remove insoluble ZnO. The colorless filtrate was concentrated to a small volume with a rotary evaporator, followed by adding a large amount of ethanol to precipitate the product. The resulting pale-white-yellow solid was filtrated and dried at room temperature (65% yield). The crude product was dissolved in 0.1 M of KOAc aqueous solution and then recrystallized *via* diffusing ethanol vapor for 3 days. ¹H NMR (500 MHz, D₂O): δ (ppm) 2.62 – 2.65 (*dd*, 1H) and 2.77 – 2.82 (*t*, 1H) (methylene signals) and 3.26 – 3.29 (*dd*, 1H) (methine signal). Anal. Calcd for K₆[L^{Ir}]₄·48H₂O = K₆C₃₆Zn₄Ir₄O₇₃H₁₅₆S₁₂N₁₂: C, 12.09; H, 4.23; N, 4.71. Found: C, 12.09; H, 4.40; N, 4.70.

4.2.2 Synthesis of Ln₂[L^{Ir}]_n·nH₂O (**3**_{Ln}; Ln = Sc^{III}, La^{III}, Ce^{III}, Pr^{III}, and Nd^{III}) and Ln_{0.33}[Ln₄(OH)₄(OAc)₃(H₂O)₇][L^{Ir}]_n·nH₂O (**4**_{Ln}; Ln = Sm^{III}, Eu^{III}, Gd^{III}, Tb^{III}, Dy^{III}, Er^{III}, Ho^{III}, Tm^{III}, Yb^{III}, Lu^{III}, and Y^{III})

50 mg (14.0 μ mol) of freshly prepared single crystals of K₆[L^{Ir}]₄·48H₂O were immersed in 10 mL of a 0.02 M of Ln(OAc)₃ in ethanol:water (3:1) solution in a sealed glass vessel and allowed to stand at room temperature for a week. The solution was then changed to 5 mL of a 0.1 M Ln(OAc)₃ aqueous solution while keeping the crystals in the vessel for 2 days to complete the reaction. The resulting block crystals of **3**_{Ln} or **4**_{Ln} were then collected by filtration and then washed with DI. water.

Anal. Calcd for Sc₂[L^{Ir}]₂·23H₂O (**3**_{Sc}) = C₃₆H₁₀₆Sc₂N₁₂O₄₈Ir₄S₁₂Zn₄: C, 14.51; H, 3.58; N, 5.63%. Found: C, 14.53; H, 3.41; N, 5.30%.

Anal. Calcd for La₂[L^{Ir}]₂·30H₂O (**3**_{La}) = C₃₆H₁₂₀La₂N₁₂O₅₅Ir₄S₁₂Zn₄: C, 13.12; H, 3.67; N, 5.10%. Found: C, 13.09; H, 3.57; N, 4.98%.

Anal. Calcd for Ce₂[L^{Ir}] \cdot 29H₂O (**3Ce**) = C₃₆H₁₁₈Ce₂N₁₂O₅₄Ir₄S₁₂Zn₄: C, 13.18; H, 3.63; N, 5.13%. Found: C, 13.05; H, 3.52; N, 5.00%.

Anal. Calcd for Pr₂[L^{Ir}] \cdot 26H₂O (**3Pr**) = C₃₆H₁₁₂Pr₂N₁₂O₅₁Ir₄S₁₂Zn₄: C, 13.42; H, 3.49; N, 5.20%. Found: C, 13.44; H, 3.39; N, 4.97%.

Anal. Calcd for Nd₂[L^{Ir}] \cdot 35H₂O (**3Nd**) = C₃₆H₁₃₀Nd₂N₁₂O₆₀Ir₄S₁₂Zn₄: C, 12.73; H, 3.85; N, 4.95%. Found: C, 12.66; H, 3.67; N, 4.79%.

Anal. Calcd for Sm_{0.33}[Sm₄(OH)₄(OAc)₃][L^{Ir}] \cdot 22H₂O (**4Sm**) = C₄₂H₁₁₇Sm_{4.33}N₁₂O₅₇Ir₄S₁₂Zn₄: C, 13.39; H, 3.13; N, 4.46%. Found: C, 13.43; H, 3.27; N, 4.43%.

Anal. Calcd for Eu_{0.33}[Eu₄(OH)₄(OAc)₃][L^{Ir}] \cdot 21H₂O (**4Eu**) = C₄₂H₁₁₅Eu_{4.33}N₁₂O₅₆Ir₄S₁₂Zn₄: C, 13.42; H, 3.03; N, 4.47%. Found: C, 13.58; H, 3.18; N, 4.46%.

Anal. Calcd for Gd_{0.33}[Gd₄(OH)₄(OAc)₃][L^{Ir}] \cdot 28H₂O (**4Gd**) = C₄₂H₁₂₉Gd_{4.33}N₁₂O₆₃Ir₄S₁₂Zn₄: C, 12.91; H, 3.33; N, 4.30%. Found: C, 12.94; H, 3.35; N, 4.27%.

Anal. Calcd for Tb_{0.33}[Tb₄(OH)₄(OAc)₃][L^{Ir}] \cdot 32H₂O (**4Tb**) = C₄₂H₁₃₇Tb_{4.33}N₁₂O₆₇Ir₄S₁₂Zn₄: C, 12.66; H, 3.46; N, 4.22%. Found: C, 12.59; H, 3.33; N, 4.32%.

Anal. Calcd for Dy_{0.33}[Dy₄(OH)₄(OAc)₃][L^{Ir}] \cdot 21H₂O (**4Dy**) = C₄₂H₁₁₅Dy_{4.33}N₁₂O₅₆Ir₄S₁₂Zn₄: C, 13.26; H, 3.05; N, 4.42%. Found: C, 13.26; H, 3.11; N, 4.44%.

Anal. Calcd for Ho_{0.33}[Ho₄(OH)₄(OAc)₃][L^{Ir}] \cdot 23H₂O (**4Ho**) = C₄₂H₁₁₉Ho_{4.33}N₁₂O₅₈Ir₄S₁₂Zn₄: C, 13.10; H, 3.12; N, 4.37%. Found: C, 13.03; H, 3.10; N, 4.44%.

Anal. Calcd for Er_{0.33}[Er₄(OH)₄(OAc)₃][L^{Ir}] \cdot 29H₂O (**4Er**) = C₄₂H₁₃₁Er_{4.33}N₁₂O₆₄Ir₄S₁₂Zn₄: C, 12.71; H, 3.33; N, 4.24%. Found: C, 12.59; H, 3.24; N, 4.38%.

Anal. Calcd for Tm_{0.33}[Tm₄(OH)₄(OAc)₃][L^{Ir}] \cdot 25H₂O (**4Tm**) = C₄₂H₁₂₃Tm_{4.33}N₁₂O₆₀Ir₄S₁₂Zn₄: C, 12.92; H, 3.18; N, 4.31%. Found: C, 12.96; H, 3.21; N, 4.49%.

Anal. Calcd for Yb_{0.33}[Yb₄(OH)₄(OAc)₃][L^{Ir}] \cdot 25H₂O (**4Yb**) = C₄₂H₁₂₃Yb_{4.33}N₁₂O₆₀Ir₄S₁₂Zn₄: C, 12.86; H, 3.16; N, 4.29%. Found: C, 12.79; H, 3.16; N, 4.50%.

Anal. Calcd for $\text{Lu}_{0.33}[\text{Lu}_4(\text{OH})_4(\text{OAc})_3][\text{L}^{\text{Ir}}]\cdot 24\text{H}_2\text{O}$ (**4Lu**) = $\text{C}_{42}\text{H}_{121}\text{Lu}_{4.33}\text{N}_{12}\text{O}_{59}$
 $\text{Ir}_4\text{S}_{12}\text{Zn}_4$: C, 12.90; H, 3.12; N, 4.30%. Found: C, 12.80; H, 3.10; N, 4.39%.

Anal. Calcd for $\text{Y}_{0.33}[\text{Y}_4(\text{OH})_4(\text{OAc})_3][\text{L}^{\text{Ir}}]\cdot 28\text{H}_2\text{O}$ (**4Y**) = $\text{C}_{42}\text{H}_{129}\text{Y}_{4.33}\text{N}_{12}\text{O}_{63}$
 $\text{Ir}_4\text{S}_{12}\text{Zn}_4$: C, 13.97; H, 3.60; N, 4.66%. Found: C, 13.81; H, 3.43; N, 4.73%.

4.2.3 X-ray crystallography

Crystallographic data sets of $\text{K}_6[\text{L}^{\text{Ir}}]\cdot 48\text{H}_2\text{O}$, **3Ln** and **4Ln** were collected at 100(2) K using a Rigaku XtaLAB Synergy Custom X-ray Diffractometer equipped with a Hypix-6000HE hybrid pixel array detector ($\lambda = 0.71075 \text{ \AA}$) excepting **4Sm**, **4Dy**, and **4Er**, which were collected using a synchrotron X-ray source at the BL02B1 beamline in SPring-8 (Japan) ($\lambda = 0.7005 \text{ \AA}$). Data collection and reduction of $\text{K}_6[\text{L}^{\text{Ir}}]\cdot 48\text{H}_2\text{O}$, **3Ln** and **4Ln** were performed using CrysAlisPro 1.171.40.60a [25]. Empirical absorption corrections were applied using the SADABS program [26]. For **4Sm**, **4Dy**, and **4Er**, the absorption correction was applied using the Mulabs program [27]. All structures were solved by the intrinsic phasing method within the SHELXT program [28] and refined on F^2 by the full-matrix least-squares technique using the SHELXL program [29] *via* the Olex² interface [30]. Hydrogen atoms, except those of water molecules and hydroxides, were calculated and placed using riding models. Due to the high disordering at Sm3A and Sm3B in **4Sm**, three OAc^- molecules in the cubane cluster could not be assigned. However, the present OAc^- moieties in **4Sm** were confirmed by elemental analysis. The crystallographic and refinement data for $\text{K}_6[\text{L}^{\text{Ir}}]\cdot 48\text{H}_2\text{O}$, **3Ln**, and **4Ln** are summarized in Table 4.1, Table 4.2, and Table 4.3, respectively.

Table 4.1 Crystallographic and refinement data of $K_6[L^{Ir}]\cdot 48H_2O$

Crystal formula	$C_{36}H_{60}Ir_4K_6N_{12}O_{50}S_{12}Zn_4$
Formula weight	3110.59
Crystal System	Cubic
Space group	$P2_13$
a (Å)	23.4451(5)
V (Å ³)	12887.1(8)
Z	4
$\rho/g\cdot cm^{-3}$	1.603
Radiation λ (Å)	0.71073
Temperature (K)	100(2)
Crystal size (mm ³)	0.15×0.15×0.15
F(000)	5976.0
Data/ restraints/parameters	10633/16/295
Flack parameter	0.006(6)
R_{int}	0.0455
R_1 ($I > 2\sigma(I)$) [†]	0.0641
wR_2 (all data) ^{††}	0.1771

$$^{\dagger}R_1 = \Sigma(|F_o| - |F_c|) / \Sigma(|F_o|). \quad ^{\dagger\dagger}wR = [\Sigma w(F_o^2 - F_c^2)^2 / \Sigma w(F_o^2)^2]^{1/2}$$

Table 4.2 Crystallographic and refinement data of **3Ln**

	3Sc	3La	3Ce	3Pr	3Nd
Crystal formula	C ₃₆ H ₅₇ Ir ₄ N ₁₂ O ₃₉ S ₁₂ Sc ₂ Zn ₄	C ₃₆ H ₆₀ La ₂ Ir ₄ N ₁₂ O ₄₁ S ₁₂ Zn ₄	C ₃₆ H ₆₀ Ce ₂ Ir ₄ N ₁₂ O ₄₄ S ₁₂ Zn ₄	C ₃₆ H ₆₀ Pr ₂ Ir ₄ N ₁₂ O ₃₈ S ₁₂ Zn ₄	C ₃₆ H ₆₀ Nd ₂ Ir ₄ N ₁₂ O ₄₂ S ₁₂ Zn ₄
Formula weight	2786.85	3009.81	3060.20	2965.78	3036.44
Crystal System	Cubic	Cubic	Cubic	Cubic	Cubic
Space group	<i>P</i> 2 ₁ 3	<i>P</i> 2 ₁ 3	<i>P</i> 2 ₁ 3	<i>P</i> 2 ₁ 3	<i>P</i> 2 ₁ 3
<i>a</i> (Å)	23.2847(4)	23.4807(3)	23.3229(4)	23.4111(3)	23.6007(3)
<i>V</i> (Å ³)	12624.4(7)	12945.9(5)	12686.7(7)	12831.1(5)	13145.4(5)
<i>Z</i>	4	4	4	4	4
ρ /g·cm ⁻³	1.466	1.544	1.602	1.535	1.534
Radiation λ (Å)	0.71073	0.71073	0.71073	0.71073	0.71073
Temperature (K)	100(2)	100(2)	100(2)	100(2)	100(2)
Crystal size (mm ³)	0.04×0.04×0.04	0.09×0.12×0.12	0.12×0.12×0.12	0.15×0.15×0.12	0.09×0.09×0.09
F(000)	5301.0	5400.0	5792.0	5608.0	5744.0
Data/ restraints/parameters	8926/20/207	10545/11/287	9771/3/292	10193/8/279	10519/12/299
Flack parameter	0.002(10)	0.009(5)	0.004(6)	0.007(6)	0.030(5)
<i>R</i> _{int}	0.0526	0.0267	0.032 5	0.0342	0.0307
<i>R</i> ₁ (<i>I</i> >2σ(<i>I</i>)) [†]	0.0868	0.0689	0.0692	0.0721	0.0699
<i>wR</i> ₂ (all data) ^{† †}	0.2573	0.1972	0.2083	0.2217	0.1952

[†]*R*₁ = Σ(|*F*_o| - |*F*_c|) / Σ(|*F*_o|). ^{††}*wR* = [Σ*w*(*F*_o² - *F*_{c²})² / Σ*w*(*F*_o²)²]^{1/2}

Table 4.3 Crystallographic and refinement data of **4Ln**

	4Sm	4Eu	4Gd	4Tb
Crystal formula	C ₃₆ H ₆₀ Sm _{4.33} Ir ₄ N ₁₂ O ₇₃ S ₁₂ Zn ₄	C ₄₂ H ₆₉ Eu _{4.33} Ir ₄ N ₁₂ O ₆₄ S ₁₂ Zn ₄	C ₄₂ H ₆₉ Gd _{4.33} Ir ₄ N ₁₂ O ₆₉ S ₁₂ Zn ₄	C ₄₂ H ₆₉ Tb _{4.33} Ir ₄ N ₁₂ O ₇₃ S ₁₂ Zn ₄
Formula weight	3782.97	3839.07	3941.98	4013.21
Crystal System	Cubic	Cubic	Cubic	Cubic
Space group	<i>P</i> 2 ₁ 3	<i>P</i> 2 ₁ 3	<i>P</i> 2 ₁ 3	<i>P</i> 2 ₁ 3
<i>a</i> (Å)	23.748(3)	23.7101(2)	23.7624(2)	23.7712(2)
<i>V</i> (Å ³)	13392(5)	13329.1(3)	13417.5(3)	13432.4(3)
<i>Z</i>	4	4	4	4
ρ /g·cm ⁻³	1.876	1.910	1.951	1.984
Radiation λ (Å)	0.7005	0.71073	0.71073	0.71073
Temperature (K)	100(2)	100(2)	100(2)	100(2)
Crystal size (mm ³)	0.02×0.03×0.04	0.06×0.06×0.09	0.12×0.12×0.09	0.09×0.06×0.09
F(000)	7106.0	7239.0	7416.0	7514.0
Data/ restraints/parameters	10268/8/333	11149/18/327	10548/11/364	11079/17/369
Flack parameter	0.056(12)	0.012(6)	-0.006(5)	-0.005(5)
<i>R</i> _{int}	0.1194	0.0465	0.0305	0.0452
<i>R</i> ₁ (<i>I</i> >2σ(<i>I</i>)) [†]	0.0848	0.0785	0.0642	0.0568
<i>wR</i> ₂ (all data) ^{††}	0.2539	0.2377	0.1880	0.1610

[†]*R*₁ = Σ(|*F*_o|-|*F*_c|)/Σ(|*F*_o|). ^{††}*wR* = [Σ*w*(*F*_o²-*F*_c²)²/Σ*w*(*F*_o²)²]^{1/2}

Table 4.3 Crystallographic and refinement data of **4Ln** (cont.)

	4Dy	4Ho	4Er	4Tm
Crystal formula	C ₄₂ H ₆₀ Dy _{4.33} Ir ₄ N ₁₂ O ₅₇ S ₁ 2Zn ₄	C ₄₂ H _{68.67} Ho _{4.33} Ir ₄ N ₁₂ O ₇₃ S ₁ 2Zn ₄	C ₄₂ H ₆₉ Er _{4.33} Ir ₄ N ₁₂ O ₅₈ S ₁ 2Zn ₄	C ₄₂ H ₆₉ Tm _{4.33} Ir ₄ N ₁₂ O ₈ 1S ₁₂ Zn ₄
Formula weight	3811.62	4038.90	3809.32	4184.55
Crystal System	Cubic	Cubic	Cubic	Cubic
Space group	<i>P</i> 2 ₁ 3	<i>P</i> 2 ₁ 3	<i>P</i> 2 ₁ 3	<i>P</i> 2 ₁ 3
<i>a</i> (Å)	23.6018(14)	23.798(3)	23.5792(11)	23.6918(4)
<i>V</i> (Å ³)	13147(2)	13,478.2(5)	13109.5(18)	13298.2(7)
<i>Z</i>	4	4	4	4
ρ /g·cm ⁻³	1.926	1.990	1.930	2.090
Radiation λ (Å)	0.7005	0.71073	0.7005	0.71073
Temperature (K)	100(2)	100(2)	100(2)	100(2)
Crystal size (mm ³)	0.08×0.08×0.06	0.09×0.09×0.09	0.1×0.09×0.06	0.09×0.12×0.12
F(000)	7127.0	7595.0	7134.0	7887.0
Data/ restraints/parameters	10078/24/303	10887/11/343	6303/15/328	10341/11/402
Flack parameter	0.019(9)	-0.009(5)	0.012(8)	-0.005(5)
<i>R</i> _{int}	0.0742	0.0315	0.0525	0.0354
<i>R</i> ₁ (<i>I</i> >2σ(<i>I</i>)) [†]	0.0682	0.0525	0.0515	0.0504
<i>wR</i> ₂ (all data) ^{††}	0.1938	0.1455	0.1455	0.1312

[†]*R*₁ = Σ(|*F*_o|-|*F*_c|)/Σ(|*F*_o|). ^{††}*wR* = [Σ*w*(*F*_o²-*F*_{c²})²/Σ*w*(*F*_o²)²]^{1/2}

Table 4.3 Crystallographic and refinement data of **4Ln** (cont.)

	4Yb	4Lu	4Y
Crystal formula	C ₄₂ H ₆₉ Yb _{4.33} Ir ₄ N ₁₂ O ₇₂ S ₁₂ Zn ₄	C ₄₂ H ₆₉ Lu _{4.33} Ir ₄ N ₁₂ O ₇₈ S ₁₂ Zn ₄	C ₄₂ H ₆₉ Y _{4.33} Ir ₄ N ₁₂ O ₇₃ S ₁₂ Zn ₄
Formula weight	4058.35	4163.15	3710.07
Crystal System	Cubic	Cubic	Cubic
Space group	<i>P</i> 2 ₁ 3	<i>P</i> 2 ₁ 3	<i>P</i> 2 ₁ 3
<i>a</i> (Å)	23.5740(3)	23.7498(3)	23.7790(3)
<i>V</i> (Å ³)	13100.9(5)	13396.1(5)	13445.6(5)
<i>Z</i>	4	4	4
ρ /g·cm ⁻³	2.058	2.064	1.833
Radiation λ (Å)	0.71073	0.71073	0.71073
Temperature (K)	100(2)	100(2)	100(2)
Crystal size (mm ³)	0.1×0.1×0.08	0.06×0.06×0.04	0.09×0.09×0.06
F(000)	7616.0	7826.0	7111.0
Data/ restraints/parameters	10847/17/355	11266/2/405	10956/7/404
Flack parameter	0.009(5)	-0.001(5)	0.003(4)
<i>R</i> _{int}	0.0419	0.0381	0.0342
<i>R</i> ₁ (<i>I</i> >2σ(<i>I</i>)) [†]	0.0613	0.0467	0.0457
<i>wR</i> ₂ (all data) ^{††}	0.1643	0.1245	0.1233

$$^{\dagger}R_1 = \Sigma(|F_o| - |F_c|) / \Sigma(|F_o|), \quad ^{\dagger\dagger}wR = [\Sigma w(F_o^2 - F_c^2)^2 / \Sigma w(F_o^2)^2]^{1/2}$$

4.3 Results and discussions

4.3.1 Synthesis, characterizations, and crystal structures of $K_6[L^{Ir}]\cdot 48H_2O$

The colorless block crystals of $K_6[L^{Ir}]\cdot 48H_2O$ were yielded by the recrystallization process with ethanol vapor diffusion in a KOAc aqueous solution. The phase purity of the product could be affirmed by H-NMR spectra (Fig. 4.1). To confirm the presence of the ligands in $K_6[L^{Ir}]\cdot 48H_2O$, the IR spectrum of $K_6[L^{Ir}]\cdot 48H_2O$ was shown in Fig. 4.2. The characteristic C=O stretching band at 1610 cm^{-1} indicated fully deprotonated carboxylate groups on the L-cys ligand.

The single crystal X-ray analysis revealed that the complex crystallizes in the cubic $P2_13$ space group. The structure contained four $\Delta_{LLL}-[Ir(L-cys)_3]^{3-}$ units binding with tetrahedral $\{Zn_4O\}^{6+}$ core (Fig. 4.3a). Each Zn^{II} ion was coordinated with three S atoms from three different units of $\Delta_{LLL}-[Ir(L-cys)_3]^{3-}$ and one central O atom resulting in $[L^{Ir}]^{6-}$ anionic complex with a diameter size of *ca.* 15.32 \AA similar to that of $[L^{Ir}]^{6-}$ anionic complex (*ca.* 15.34 \AA) [31]. Through hydrogen bonding N—H \cdots O_{COO} (average N \cdots O distance of 2.90 \AA) with six adjacent $[L^{Ir}]^{6-}$ units (Fig. 4.3b), the three-dimensional supramolecular framework of $[L^{Ir}]^{6-}$ was built up (Fig. 4.3c). The framework showed the effective window opening with the approximate window opening size of *ca.* $6.0 \times 12.2\text{ \AA}^2$ and 53 % porosity. The pore's surface was decorated by free carboxylate groups from five $[L^{Ir}]^{6-}$ units (Fig. 4.3d).

To balance the charge of the framework, six disordered K^+ ions, *i.e.* K1, K2, K3, K4, K5, and K6, were located in different spaces. Site A was occupied by the K1 ion, which was surrounded by three positional disordered K2 ions (Fig. 4.4a). The disordered K3 ion was located at site B and was also surrounded by three positional disordered K4 ions as shown in Fig. 4.4b. Other K5 and K6 ions were coordinated with carboxylate groups as shown in Fig. 4.4a and 4.4c. Due to the high disordering of the water solvent molecules in the framework, the number of water solvents was affirmed by elemental analysis.

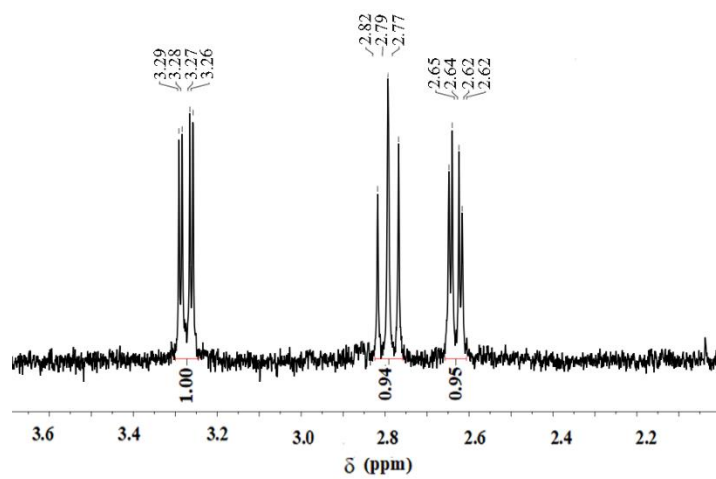


Fig. 4.1 ¹H NMR spectrum of the as-synthesized K₆[L^{Ir}] \cdot 48H₂O in D₂O.

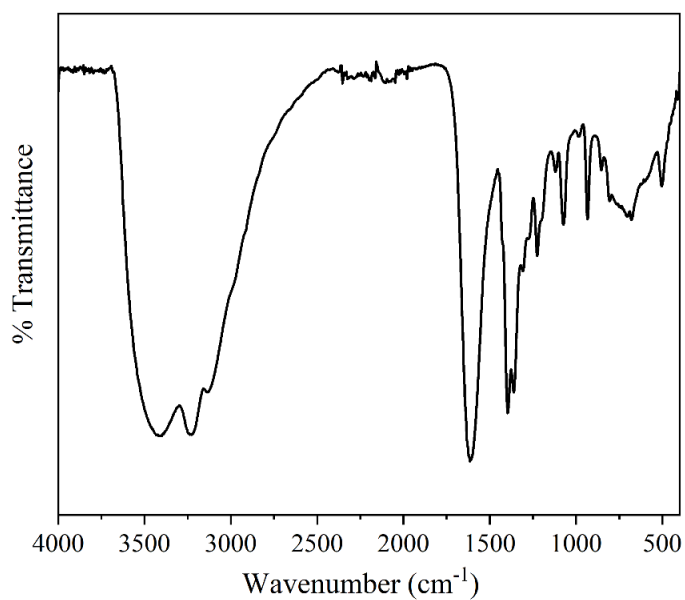


Fig. 4.2 FT-IR spectrum of K₆[L^{Ir}] \cdot 48H₂O.

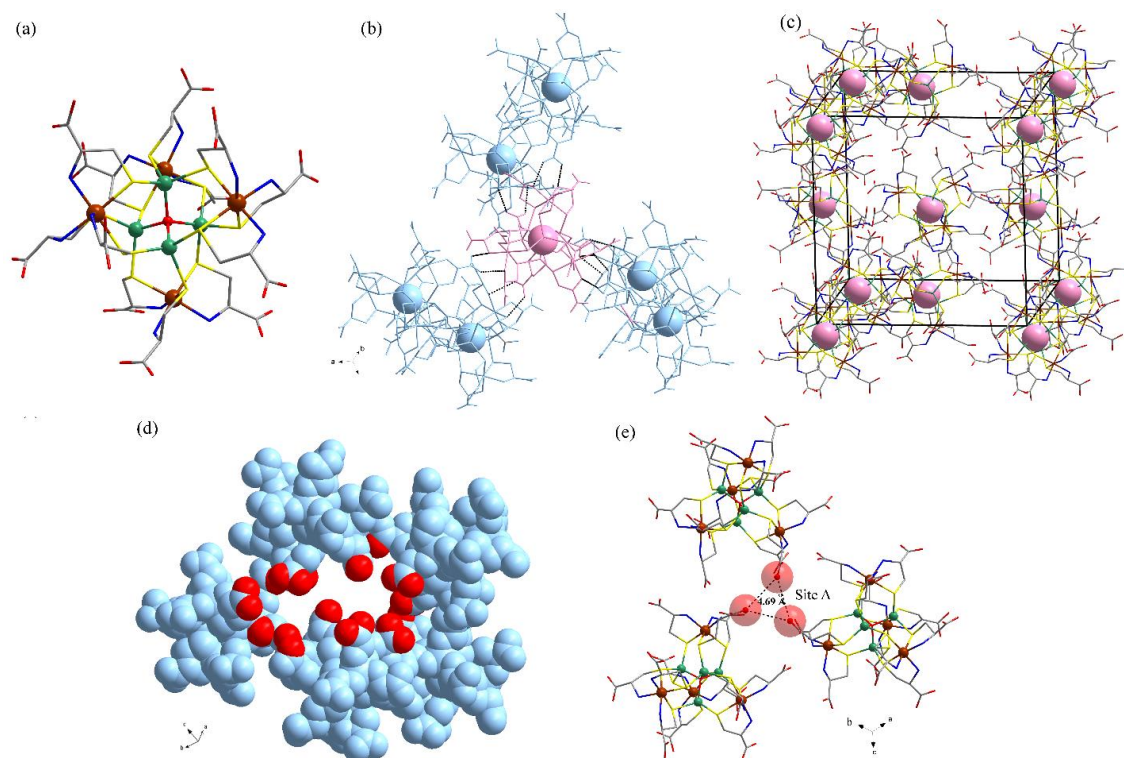


Fig. 4.3 Crystal structures of $K_6[L^{Ir}] \cdot 48H_2O$. (a) $[L^{Ir}]^{6-}$ metalloligand, (b) surrounded by six adjacent $[L^{Ir}]^{6-}$ through N—H...O hydrogen bonds (black dash line), (c) the packing framework through hydrogen bonding, (d) window opening decorated with COO^- functional groups from five $[L^{Ir}]^{6-}$ metalloligands, and (e) O...O distance at pore space (site A) for available creating lanthanide cubanes; H atoms were omitted for clarity. Ir (brown), Zn (olive-green), S (yellow), N (blue), C (light grey), O (red), and $[L^{Ir}]^{6-}$ (light blue).

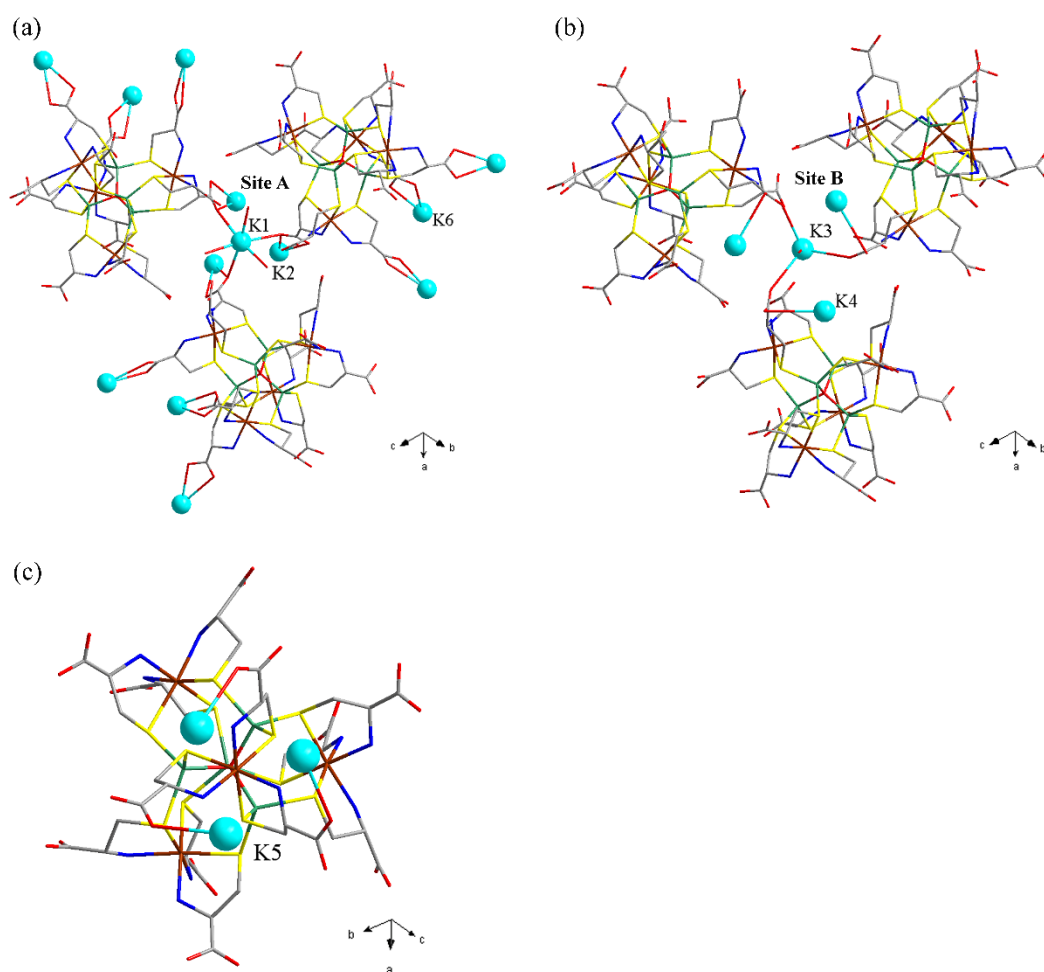


Fig. 4.4 Perspective views of disordered (a) K1, K2 occupied at site A and K6, (b) K3 and K4 occupied at site B, and (d) K5 coordinated with carboxylate groups in $\text{K}_6[\text{L}^{\text{Ir}}]\cdot 48\text{H}_2\text{O}$. H atoms were omitted for clarity. Ir (brown), Zn (olive-green), S (yellow), N (blue), C (light grey), and O (red).

A shorter averaged $\text{N}\cdots\text{O}$ distance of 2.86 Å was observed in the relating $[\text{L}^{\text{Rh}}]^{6-}$ framework, leading to the stronger $\text{N}-\text{H}\cdots\text{O}_{\text{COO}}$ hydrogen bonding in the packing structure. The stronger interaction in the $[\text{L}^{\text{Rh}}]^{6-}$ framework resulted in a smaller porosity of *ca.* 46 % and a smaller opening window of *ca.* $4.7 \times 11.5 \text{ \AA}^2$. The heavier metal center of the Ir^{III} ion might stabilize the $\text{Ir}^{\text{III}}-\text{N}$ bond rather than the Rh^{III} center [32,33], which is supported by the shorter $\text{Ir}^{\text{III}}-\text{N}$ distance *ca.* 2.101 to 2.112 Å in the $[\text{L}^{\text{Ir}}]^{6-}$ compared to the $[\text{L}^{\text{Rh}}]^{6-}$ ($\text{Rh}^{\text{III}}-\text{N} = 2.107$ to 2.113 Å in). Therefore, it is assumed that the hydrogen

bond donor ability of the NH₂ groups on the Ir^{III} center might be reduced leading to the weaker and longer N—H···O_{COO} interactions in the crystal packing of K₆[L^{Ir}] \cdot 48H₂O having the larger interstitial space *ca.* 4.69 Å (Fig. 4.3e). The available space might be significant for further developing the construction of lanthanide cubane clusters in a confined space.

4.3.2 Synthesis, crystal structures, and characterizations of **3_{Ln}**

Freshly prepared crystals of K₆[L^{Ir}] \cdot 48H₂O were soaked in 0.02 M Ln(OAc)₃ solutions in ethanol/H₂O 3:1 for a week (Ln = Sc^{III}, La^{III} – Nd^{III}). To complete the reaction, the mixture was then changed to 0.1 M aqueous solutions of Ln(OAc)₃. The retained shape of the crystals was shown after the treatment. The same profiles of FT-IR spectra suggested the unchanged structure and functional groups on the ligand (Fig. 4.5).

The crystal structure of **3_{La}** is described as a representative of those **3_{Ln}** since they are all isostructural with the same crystal formula of Ln₂[L^{Ir}] \cdot nH₂O. Based on the single crystal X-ray diffraction analysis, **3_{La}** revealed the cubic *P*2₁3 space groups featuring a high disorder at La^{III} centers in the framework. The structure of **3_{La}** contains two La^{III} ions, which disorder between four crystallographic sites of La1A, La1B, La2A, and La2B, and one [L^{Ir}]⁶⁻ metalloligand. As shown in Fig. 4.6a, the three disordered La1A ions were coordinated with three COO⁻ groups from three [L^{Ir}]⁶⁻ metalloligands at the space site A surrounded by one disordered La1B ion. The space site B was occupied by three La2A ions coordinated with three [L^{Ir}]⁶⁻ metalloligands. Whilst the La2B was only coordinated with other COO⁻ groups (Fig. 4.6b). Therefore, the disordered La^{III} ions only played a role to balance the charge of the anionic crystal framework. The framework structure of **3_{La}** could thus form a three-dimensional supramolecular framework (Fig. 4.6c), which was similar to the pristine framework of K₆[L^{Ir}] \cdot 48H₂O. The framework structures of other **3_{Ln}** were shown in Fig. 4.7. Quite similar PXRD profile of **3_{Ln}** compared with the pristine framework was also verified (Fig. 4.11). The diffraction peaks in the PXRD patterns of **3_{Ln}** could be indexed based on the generated patterns from their single crystal data. The number of Ln^{III} in **3_{Ln}** was affirmed *via* XRF results, which indicate the ratio of

2 to 1 for Zn to Ln (Table 4.4). The coordinating water and crystallizing water in the void were affirmed based on the elemental analysis.

Table 4.4 Comparisons of ratio Zn to Ln in XFA data and crystal structure data of **3_{Ln}** and **4_{Ln}**

Samples	Ratio Zn to Ln from XFA data	Ratio Zn to Ln from crystal structures
3_{Sc}	4 : 1.6	4 : 2
3_{La}	4 : 1.0	4 : 2
3_{Ce}	4 : 1.5	4 : 2
3_{Pr}	4 : 1.4	4 : 2
3_{Nd}	4 : 1.9	4 : 2
4_{Sm}	4 : 2.5	4 : 4.33
4_{Eu}	4 : 2.7	4 : 4.33
4_{Gd}	4 : 3.4	4 : 4.33
4_{Tb}	4 : 3.3	4 : 4.33
4_{Dy}	4 : 3.2	4 : 4.33
4_{Ho}	4 : 3.5	4 : 4.33
4_{Er}	4 : 3.9	4 : 4.33
4_{Tm}	4 : 3.8	4 : 4.33
4_{Yb}	4 : 4.3	4 : 4.33
4_{Lu}	4 : 3.6	4 : 4.33
4_Y	4 : 4.2	4 : 4.33

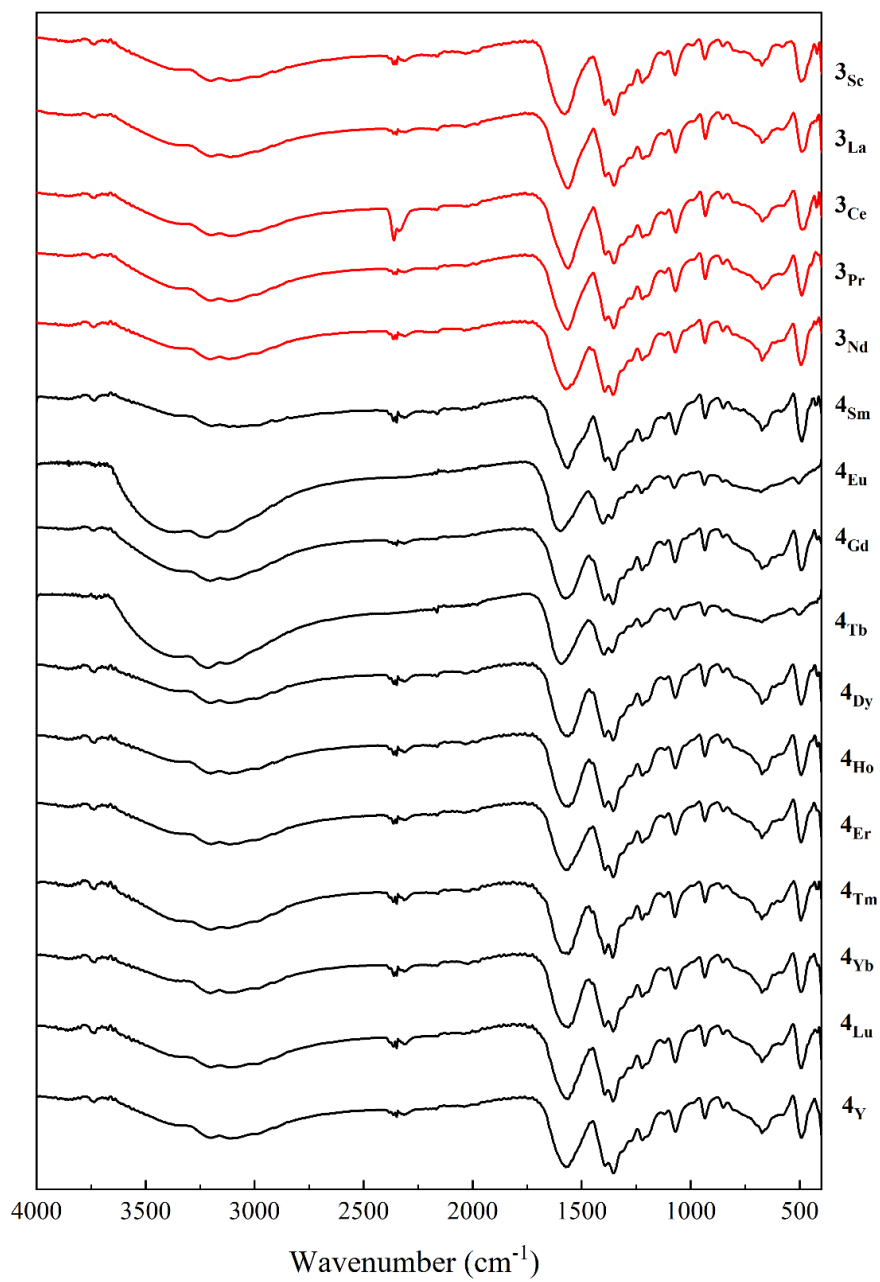


Fig. 4.5 FT-IR spectra of **3_{Ln}** (red line) and **4_{Ln}** (black line).

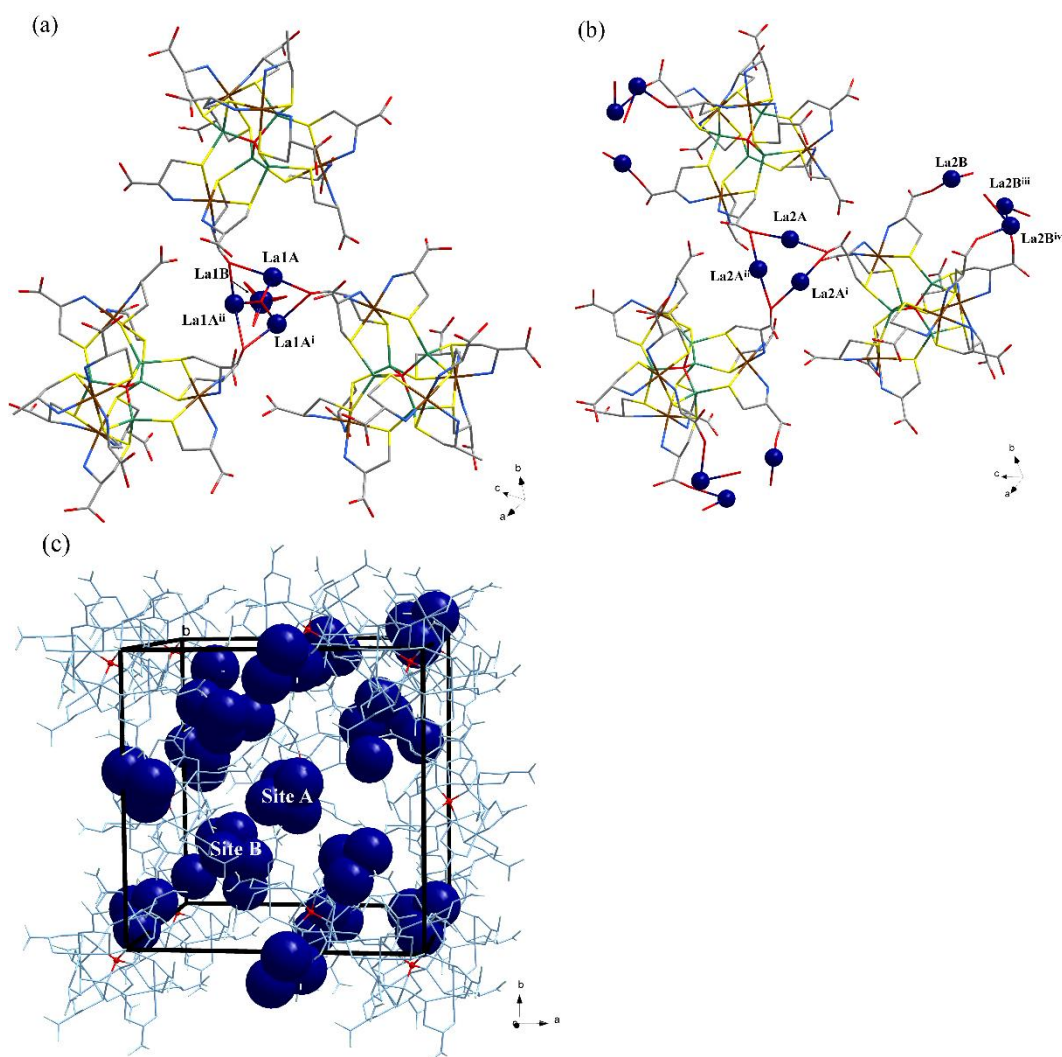


Fig. 4.6 Perspective views of the disordered La1A, La1B, La2A, and La2B ions occupied at the (a) pore site A and (b) pore site B in 3La , and (c) packing framework of 3La with Ln^{III} ions occupied (space-filling) at the sites A and B; H atoms were omitted for clarity. La (dark blue), Ir (brown), Zn (olive-green), S (yellow), N (blue), C (light grey), O (red), and $[\text{L}^{\text{Ir}}]^{6-}$ (light blue); symmetry code (i) $0.5+x, 1.5-y, 1-z$, (ii) $1-x, -0.5+y, 1.5-z$, (iii) $0.5+x, 0.5-y, 1-z$, (iv) $0.5-x, 1-y, -0.5+z$.

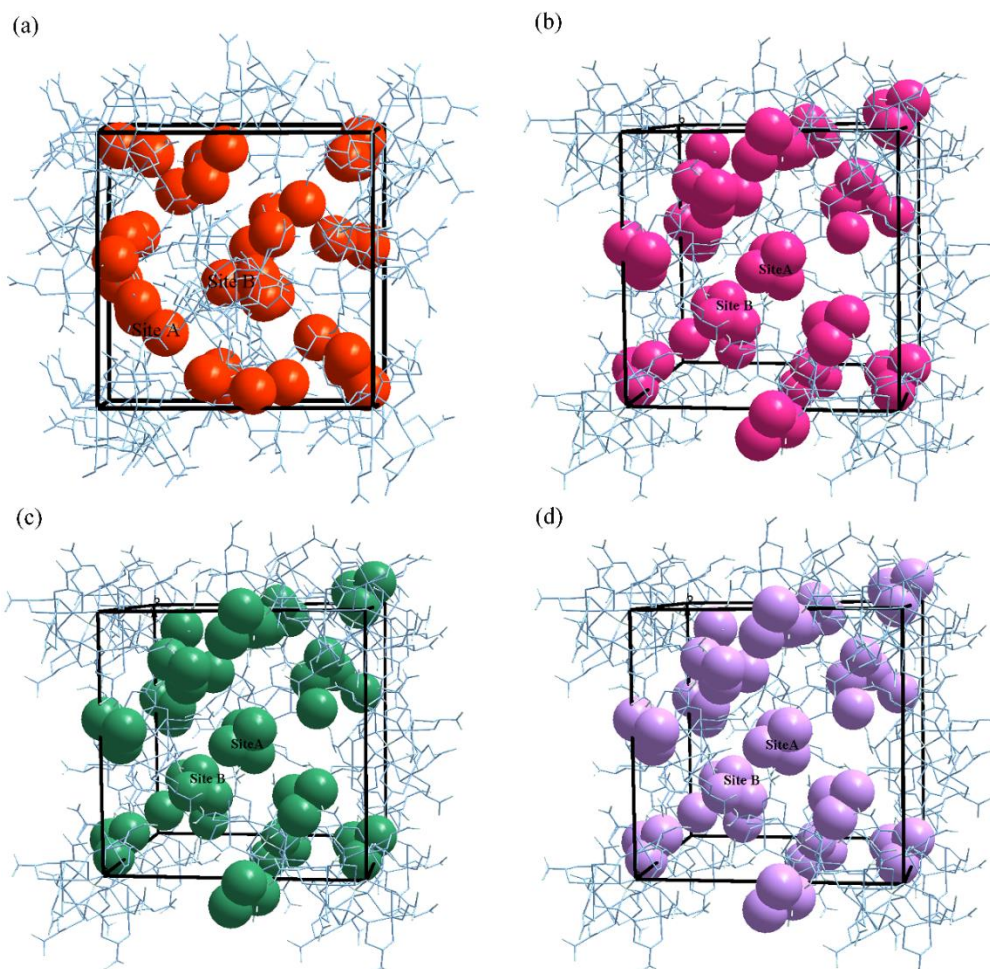


Fig. 4.7 Perspective views of the Ln^{III} ions occupied (space-filling) at the sites A and B in (a) **3**_{Sc}, (b) **3**_{Ce}, (c) **3**_{Pr}, and (d) **3**_{Nd}; Sc (orange), Ce (pink), Pr (green), Nd (purple), and H atoms of [L^{Ir}]⁶⁻ (light blue) were omitted for clarity.

4.3.3 Synthesis, crystal structures, and characterizations of **4**_{Ln}

The same treatment procedures as **3**_{Ln} were followed for **4**_{Ln} (Ln = Sm^{III} – Lu^{III}, Y^{III}). Their crystal shape remained intact after the reaction. The high stabilities in water were also observed indicating the formation of the exceptionally strong Ln^{III}—O bond. The same profiles of FT-IR spectra as those of **3**_{Ln} and K₆[L^{Ir}]⁶⁻·48H₂O were treasured (Fig. 4.5).

Based on the single crystal X-ray diffraction, the same cubic *P2₁3* space group of **4**_{Ln} was provided. However, cubane structures of Ln^{III} ions in a three-dimensional

framework were observed in $\mathbf{4}_{Ln}$, which is markedly different from the disordered Ln^{III} ions in $\mathbf{3}_{Ln}$. From PXRD profiles of $\mathbf{4}_{Ln}$, the intensity at (111) and (200) indices were however different from those $\mathbf{3}_{Ln}$ indicating the different packing structures. The crystal structure of $\mathbf{4}_{Lu}$ is selected to describe as a representative of those $\mathbf{4}_{Ln}$. The structure of $\mathbf{4}_{Lu}$ features a three-dimensional framework, which was constructed from the formation of $[Lu_4(OH)_4(OAc)_3(H_2O)_7]^{5+}$ cluster in the interstices of the host framework of $[L^{Ir}]^{6-}$. In each tetranuclear cubane cluster, four molecules of bridging μ_3 -OH⁻ were coordinated to form the $[Lu_4(OH)_4]^{8+}$ cubane structure showing the average Lu^{III}—O bond length of 2.26 Å and Lu···Lu distance of 3.67 Å. Based on the bond length of Lu^{III}—OH and in the Cambridge structural database [34] for tetranuclear $Lu_4(OH)_4$ cubanes compounds with hydroxide-bridging, the bridging species of each cubane in $\mathbf{4}_{Lu}$ should be assigned as OH⁻ rather than O²⁻ and H₂O. In each cubane cluster, three OAc⁻ molecules were bridged three pairs of Ln1 to form the $[Lu_4(OH)_4(OAc)_3]^{5+}$ structure. To fulfill the coordination sphere of Lu^{III} centers, seventh molecules of coordinating water were coordinated around the cluster resulting in $[Lu_4(OH)_4(OAc)_3(H_2O)_7]^{5+}$ formula (Fig. 4.8a). The derived cluster was transfixed by three coordinating carboxylate groups from three $[L^{Ir}]^{6-}$ anions showing averaged Lu^{III}—O_{COO} bond length of 2.28 Å (Fig. 4.8b).

As shown in Fig. 4.8e, the $[Lu_4(OH)_4(OAc)_3(H_2O)_7]^{5+}$ could function as a building block to construct a three-dimensional porous framework through the forming coordination bond with bridging COO⁻ groups in the $[L^{Ir}]^{6-}$ motif. The calculated 34% porosity and pore size *ca.* $5.6 \times 9.9 \text{ \AA}^2$ of $\mathbf{4}_{Lu}$ could be also estimated. The N—H···O_{COO} hydrogen bond in $\mathbf{4}_{Lu}$ was calculated *ca.* 2.96 Å. The average N—H···O_{COO} hydrogen bonds of other $\mathbf{4}_{Ln}$ were summarized in Table 4.6. Due to the highly disordered water solvents occupied in the void, the number of those water molecules was confirmed *via* elemental analysis. Another disordered Lu3 ion was occupied in other voids (Fig. 4.8d) with a total occupying ratio of 33% leading to a formula of $Lu_{0.33}[Lu_4(OH)_4(OAc)_3(H_2O)_7][L^{Ir}] \cdot nH_2O$. This formula corresponded well with elemental analysis data. Other $\mathbf{4}_{Ln}$ frameworks were shown in Fig. 4.9.

Concerning the space for creating the cubane cluster, which was surrounded by three $[L^{Ir}]^{6-}$ metalloligands as shown in Fig. 4.3e, the pore size might play an important

role to limit the border for tuning the lanthanide-hydroxide cluster formation. The averaged $\text{Ln}^{\text{III}}\text{—O}_{\text{COO}}$ bond lengths and $\text{Ln}\cdots\text{Ln}$ distances in the $[\text{Ln}_4(\text{OH})_4]^{8+}$ of those $\mathbf{4}_{\text{Ln}}$ (Fig. 4.10) were summarized in Table 4.5. The tendency of distances decreased in the order from $\mathbf{4}_{\text{Sm}}$ to $\mathbf{4}_{\text{Lu}}$ corresponding with the decreasing of the ionic radii of Ln^{III} , *i.e.* 0.96 Å (Sm^{III}), 0.95 Å (Eu^{III}), 0.94 Å (Gd^{III}), 0.92 Å (Tb^{III}), 0.91 Å (Dy^{III}), 0.90 Å (Ho^{III}), 0.89 Å (Er^{III}), 0.88 Å (Tm^{III}), 0.87 Å (Yb^{III}), and 0.86 Å (Lu^{III}) as well as 0.90 Å for Y^{III} [35]. The available space is, therefore, a critical factor to limit the size of lanthanide ions for tuning $[\text{Ln}_4(\text{OH})_4]^{8+}$ cubane formation. In the case of Sc^{III} ions, the ionic radii of 0.74 Å might be too small and not favor to form the cubane cluster in this confined space. To verify our assumption, the similar complex of $\text{K}_6[\text{L}^{\text{Rh}}]\cdot n\text{H}_2\text{O}$ processing smaller unit cell of $a = 22.99$ Å was compared. The bordering lanthanide cubane formation in the $[\text{L}^{\text{Rh}}]^{6-}$ framework was limited only between Eu^{III} and Gd^{III} ions. The forming $[\text{Ln}_4(\text{OH})_4]^{8+}$ cubane clusters for La^{III} , Ce^{III} , Pr^{III} , Nd^{III} , Sm^{III} , and Eu^{III} ions could thus not be observed.

Comparison of $\text{Ln}\cdots\text{Ln}$ in the $[\text{Ln}_4(\text{OH})_4]^{8+}$ and $\text{Ln}^{\text{III}}\text{—O}_{\text{COO}}$ bonds between both $\mathbf{4}_{\text{Ln}}$ and $\mathbf{6}_{\text{Ln}}$, the average $\text{Ln}\cdots\text{Ln}$ in $\mathbf{4}_{\text{Ln}}$ were slightly shorter, but the $\text{Ln}^{\text{III}}\text{—O}_{\text{COO}}$ bond lengths were significantly longer. These differences could be due to the larger pore size of $[\text{L}^{\text{Ir}}]^{6-}$, which was estimated from $\text{O}\cdots\text{O}$ distance between COO^- groups (Fig. 4.3e), were expanded from 4.05 Å to 4.69 Å for $[\text{L}^{\text{Rh}}]^{6-}$ and $[\text{L}^{\text{Ir}}]^{6-}$, respectively. This larger cavity size could be due to the weaker and longer $\text{N—H}\cdots\text{O}_{\text{COO}}$ hydrogen bonds, *i.e.* average ca. 2.91 Å and 2.86 Å for $[\text{L}^{\text{Ir}}]^{6-}$ and $[\text{L}^{\text{Rh}}]^{6-}$, respectively, resulting in the expanded cavities in the packing structures. In addition, the $\text{N—H}\cdots\text{O}_{\text{COO}}$ hydrogen bonds in $\mathbf{3}_{\text{Ln}}$ and $\mathbf{4}_{\text{Ln}}$ were also compared and summarized in Table 4.6, which supported our assumptions. By using the larger pore size of the $\text{K}_6[\text{L}^{\text{Ir}}]\cdot 48\text{H}_2\text{O}$, the bordering lanthanide cubane formation was shifted to larger ionic radii between Nd^{III} and Sm^{III} as we expected. To further design and tune the formation of lanthanide cubane clusters in other platforms, the pore space is critical. The tunable porosity through the controlling hydrogen bonding interaction by replacement of M^{III} centers in metalloligands is an effective approach for further developing and controlling the border of lanthanide cubane installation rather than the conventional method.

The phase purity of those $\mathbf{4}_{Ln}$ was confirmed *via* the PXRD patterns (Fig. 4.12), which showed the consistency of all the diffraction peaks with their single crystal data. To evident the number of Ln^{III} in the cubane clusters of $\mathbf{4}_{Ln}$, XRF analysis was also investigated. The results revealed the 1:1 ratio of $Ln:Zn$ except for $\mathbf{4}_{Sm}$ and $\mathbf{4}_{Eu}$, which were lower than expected. It might be due to the overlapped profiles of Sm and Eu with other elements. However, the formation of cubane in $\mathbf{4}_{Sm}$ and $\mathbf{4}_{Eu}$, which were isostructural with those $\mathbf{4}_{Ln}$, was affirmed *via* PXRD profiles. Therefore, the four lanthanide ions in the cubane cluster of $\mathbf{4}_{Ln}$ were verified.

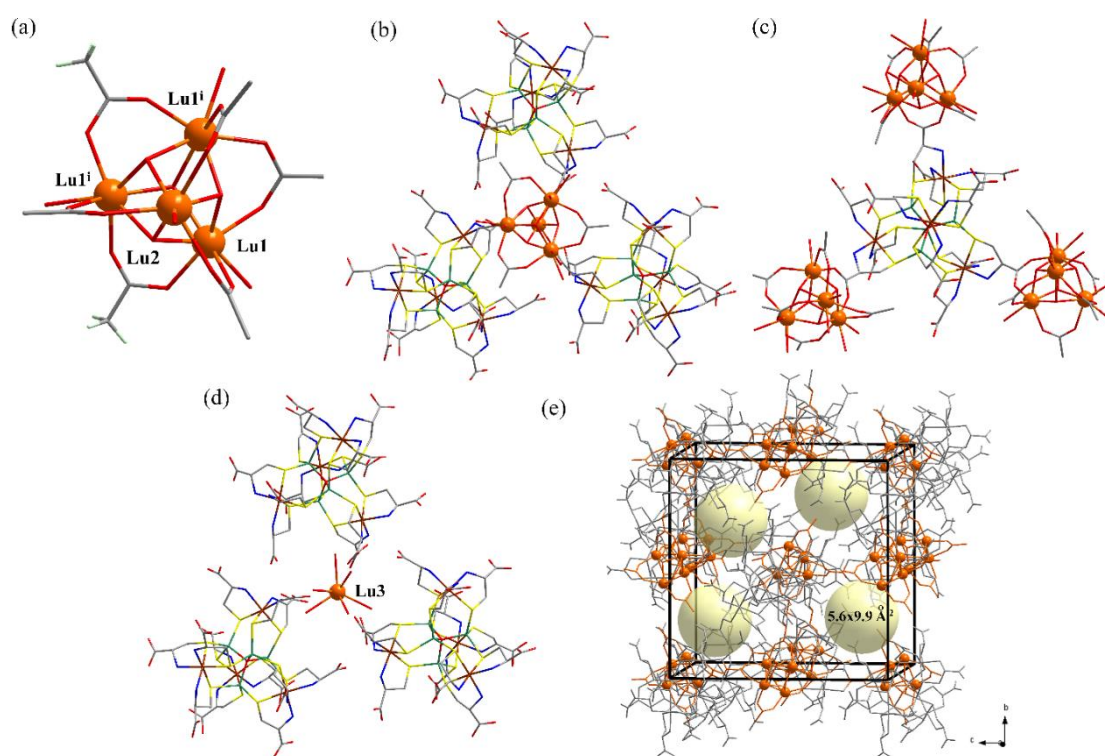


Fig. 4.8 Perspective views of (a) $[Lu_4(OH)_4(OAc)_3(H_2O)_7]^{5+}$ cluster, (b) three $[L^{Ir}]^{6-}$ coordinated with the cluster, (c) the connectivity of three adjacent cubanes through $[L^{Ir}]^{6-}$ (d) disordered Lu3 ion occupied at pore site B, and (e) packing framework showing the pore size *ca.* $5.6 \times 9.9 \text{ \AA}^2$ in $\mathbf{4}_{Lu}$; H atoms were omitted for clarity. Lu (orange), Ir (brown), Zn (olive-green), S (yellow), N (light blue), C (light grey), and O (red); symmetry code (i) x, y, z.

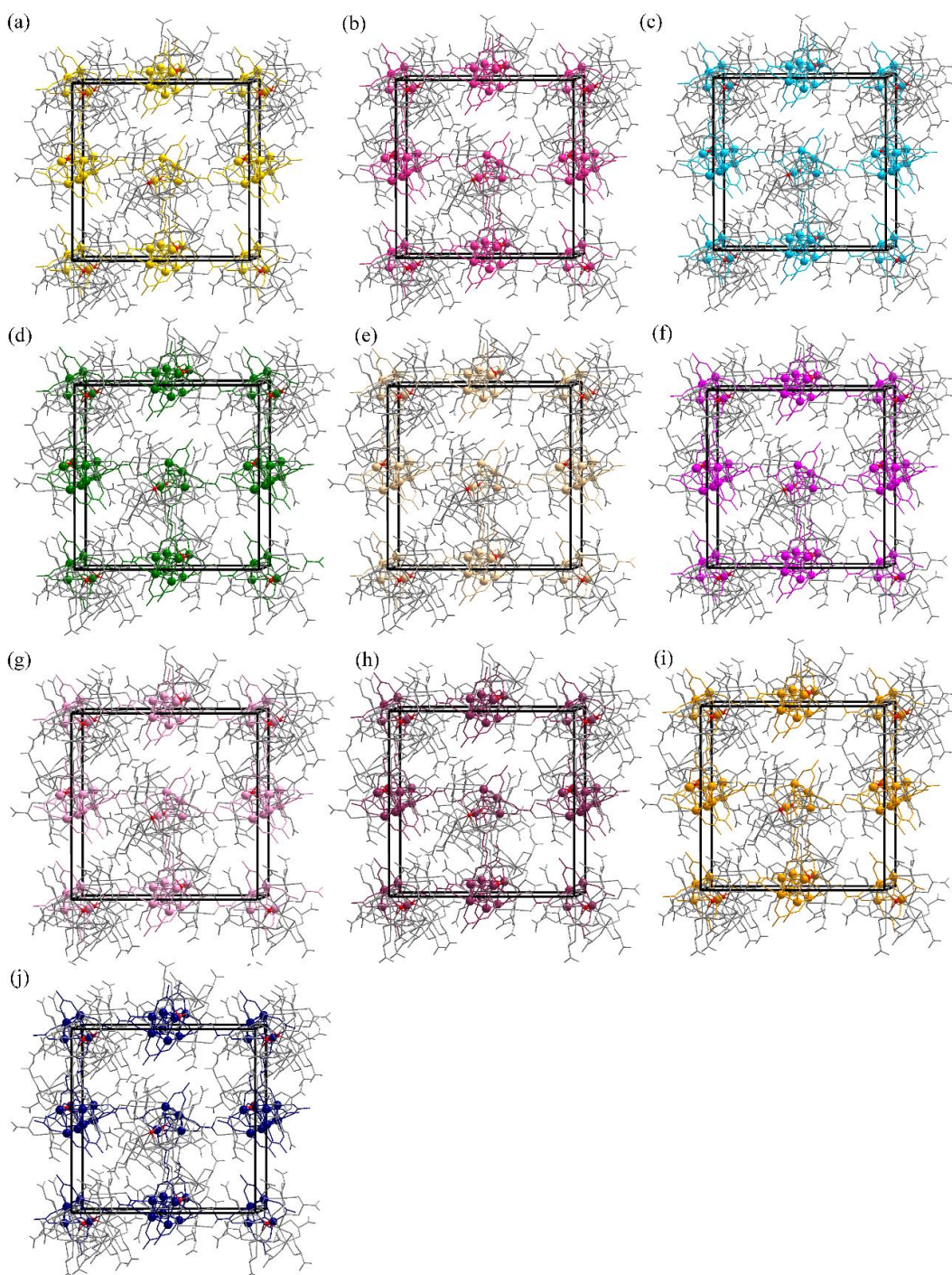


Fig. 4.9 Packing structures of (a) **4_{Sm}**, (b) **4_{Gd}**, (c) **4_{Tb}**, (d) **4_{Dy}**, (e) **4_{Ho}**, (f) **4_{Er}**, (g) **4_{Tm}**, (h) **4_{Yb}**, and (j) **4_Y**; H atoms were omitted for clarity. $[\text{L}^{\text{Ir}}]^{6-}$ (light gray).

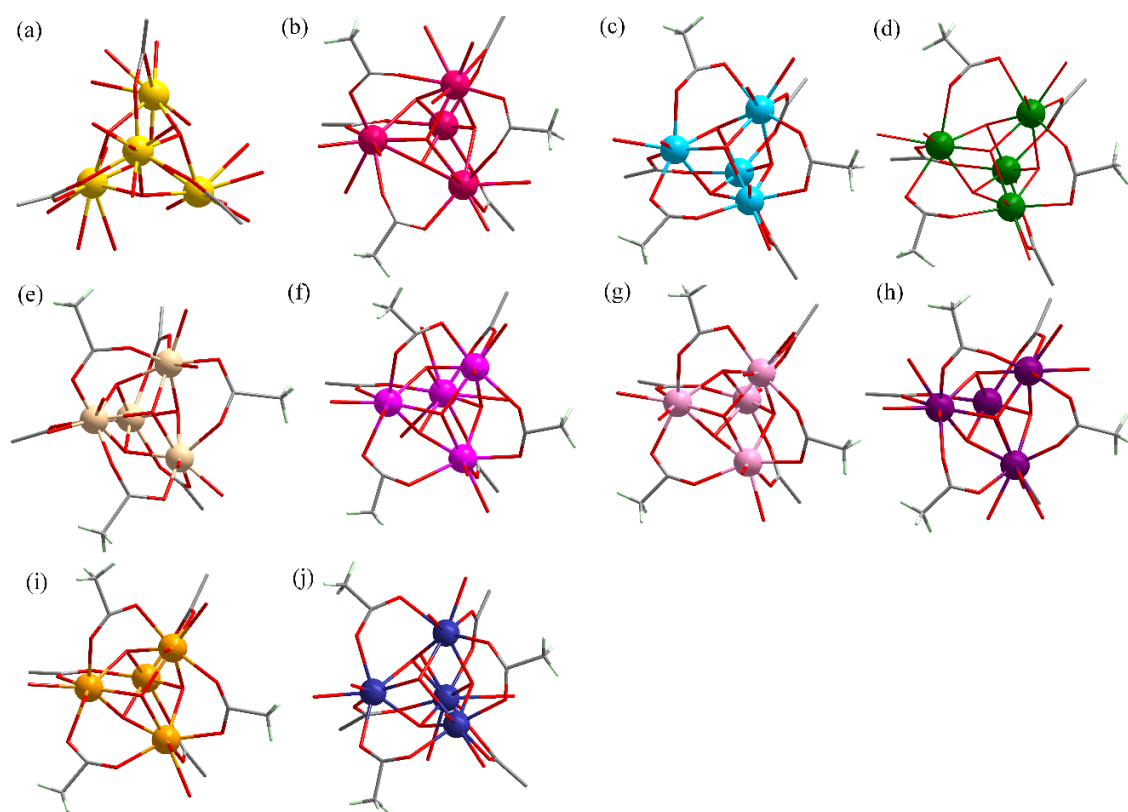


Fig. 4.10 Perspective views of the $[\text{Ln}_4(\text{OH})_4(\text{OAc})_3(\text{H}_2\text{O})_7]^{5+}$ clusters in (a) **4Sm**, (b) **4Eu**, (c) **4Ga**, (d) **4Tb**, (e) **4Dy**, (f) **4Ho**, (g) **4Er**, (h) **4Tm**, (i) **4Yb**, and (j) **4Y**.

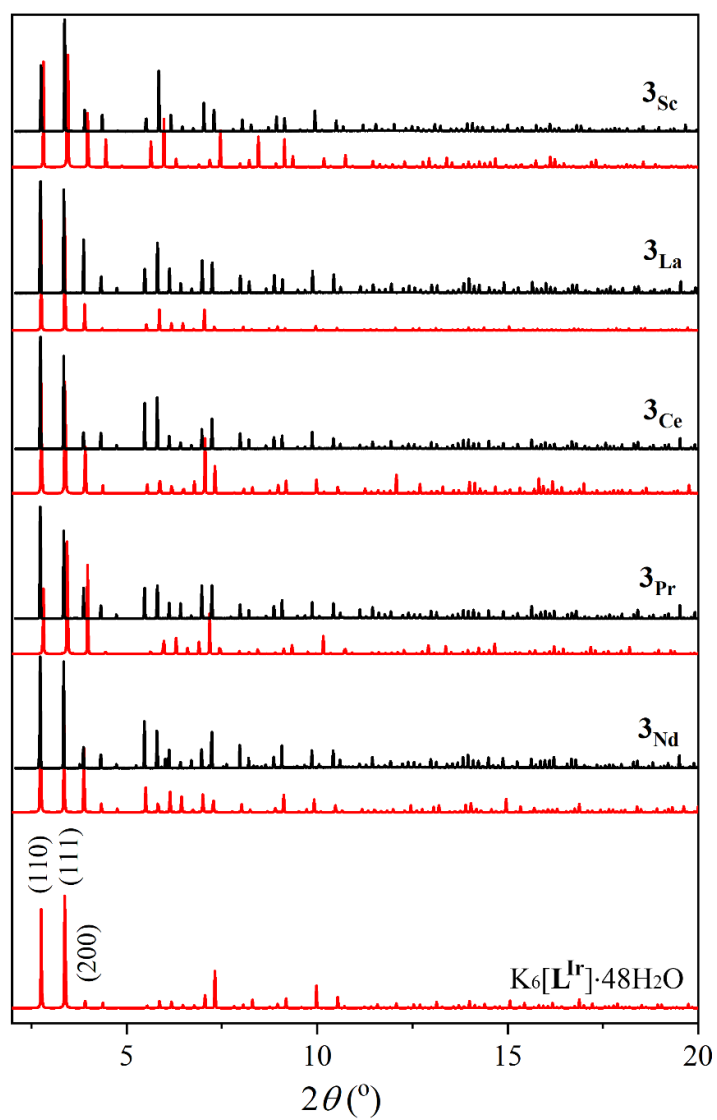


Fig. 4.11 Simulated (red solid line) and observed (black solid line) PXRD patterns of 3_{Ln} ($\lambda = 0.8 \text{ \AA}$).

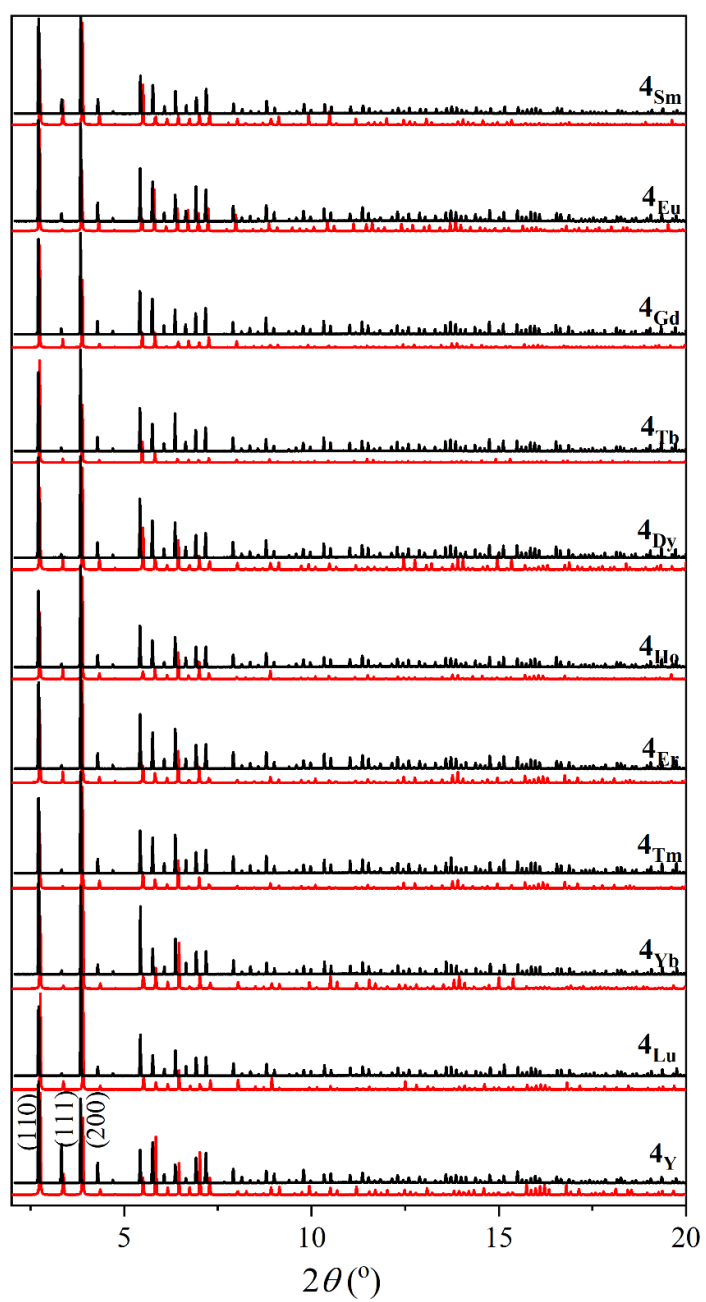


Fig. 4.12 Simulated (red solid line) and observed (black solid line) PXRD patterns of **4_{Ln}** ($\lambda = 0.8 \text{ \AA}$).

Table 4.5 The averaged distance of Ln^{III}—O_{COO} and Ln···Ln in the cubanes of **4**L_n compared to **6**L_n

Samples	Ln ^{III} —O _{COO} (Å) ^a	Ln ^{III} —O _{COO} (Å) ^b	Ln···Ln (Å) ^a	Ln···Ln (Å) ^b
4 Sm	2.43	<i>na</i>	3.94	<i>na</i>
4 Eu	2.42	<i>na</i>	3.83	<i>na</i>
4 Gd or 6 Gd	2.42	2.35	3.80	3.81
4 Tb or 6 Tb	2.41	2.35	3.80	3.79
4 Dy or 6 Dy	2.37	2.40 ^c	3.75	3.77
4 Ho or 6 Ho	2.31	2.31	3.74	3.75
4 Er or 6 Er	2.33	2.30	3.72	3.73
4 Tm or 6 Tm	2.30	2.31 ^c	3.70	3.73
4 Yb or 6 Yb	2.28	2.29 ^c	3.68	3.69
4 Lu or 6 Lu	2.28	2.26	3.67	3.68
4 Y	2.33	<i>na</i>	3.73	<i>na</i>

^aCalculated from **4**L_n

^bCalculated from **6**L_n

^cPositional disordering at Ln^{III} centers may lead to a large deviation in the distances

Table 4.6 The averaged N—H···O_{COO} hydrogen bond distances in **3_{Ln}** and **4_{Ln}** compared to **5_{Ln}** and **6_{Ln}**

Samples	N—H···O _{COO} (Å) ^a	N—H···O _{COO} (Å) ^b
3_{Sc}	2.93	<i>na</i>
3_{La} OR 5_{La}	2.89	2.88
3_{Ce} OR 5_{Ce}	2.97	2.88
3_{Pr} OR 5_{Pr}	2.86	2.88
3_{Nd} OR 5_{Nd}	2.95	2.87
4_{Sm} OR 5_{Sm}	2.97	2.87
4_{Eu} OR 5_{Eu}	2.92	2.84
4_{Gd} OR 6_{Gd}	2.97	2.93
4_{Tb} OR 6_{Tb}	2.94	2.94
4_{Dy} OR 6_{Dy}	2.94	2.93
4_{Ho} OR 6_{Ho}	2.93	2.91
4_{Er} OR 6_{Er}	2.91	2.91
4_{Tm} OR 6_{Tm}	2.93	2.90
4_{Yb} OR 6_{Yb}	2.85	2.70
4_{Lu} OR 6_{Lu}	2.96	2.88
4_Y	2.90	<i>na</i>

^aCalculated from **3_{Ln}** and **4_{Ln}**

^bCalculated from **5_{Ln}** and **6_{Ln}**

4.3.4 Photoluminescent properties of $K_6[L^{Ir}]\cdot 48H_2O$, $4Eu$ and $4Tb$

In addition to the tuning border of lanthanide cubane formation in the supramolecular frameworks, the solid-state photoluminescent properties of $K_6[L^{Ir}]\cdot 48H_2O$ and $4Ln$, *i.e.* $4Eu$ and $4Tb$, were enhanced by changing the Rh^{III} to Ir^{III} centers in the metalloligands. The emission spectra of the pristine framework $K_6[L^{Ir}]\cdot 48H_2O$ could not be observed at room temperature due to the high thermal vibration at a high temperature. At 77 K, a broad emission band with a maximum peak at 620 nm of $K_6[L^{Ir}]\cdot 48H_2O$ was then shown (Fig. 4.13). This emission spectrum is tentatively assigned to the emission from the Zn_4O core structure (O_{2p} to Zn_{4s}), which shows a similar profile with the emission spectra of ZnO with a maximum peak at 515 nm but a large difference in intensity and slightly shifting peak. The photoluminescence efficiency may be promoted by increasing energy transfer populations through the bonding with S atoms from L-cys ligand of $[Ir(L-cys)_3]^{3-}$ moieties (S_{3p} to Zn_{4s}) [36-38], resulting in the 4.4 % quantum yield at 77 K of $K_6[L^{Ir}]\cdot 48H_2O$. A slightly red-shifted excitation band from 360 to 370 nm for ZnO and $K_6[L^{Ir}]\cdot 48H_2O$, respectively, could be also contributed by the bonding with S atoms of L-cys ligands, which may reduce the band gap energy by mixing between S_{3p} and Zn_{4s} orbitals [36,37]. In addition, the shifted emission spectrum at 620 nm of $K_6[L^{Ir}]\cdot 48H_2O$ from 515 nm of ZnO might be due to a much larger of vibrational perturbation of the discrete supramolecular framework, leading to a larger Stokes shifts compared to the bulk ZnO structure [39].

For non-emissive character of $K_6[L^{Rh}]\cdot nH_2O$ even at low temperature, the $d-d$ transition band with maximum bands at 324 and 370 nm (Fig 4.14), which overlapped with the charge transfer band of the Zn_4O core structure. Therefore, the irradiation of excitation light at the ZnO charge transfer band promotes unfavorable energy transfer to the non-emissive $d-d$ excited state of Rh^{III} , rather than the photoluminescence from radiative ZnO excited state. This led to the silent of photoluminescence in $K_6[L^{Rh}]\cdot nH_2O$. Whereas, the $K_6[L^{Ir}]\cdot 48H_2O$ does not possess any absorption bands over 400 nm due to the higher energy of the $d-d$ excited state of Ir^{III} . This could account for the enhancement of photoluminescence in $K_6[L^{Ir}]\cdot 48H_2O$ [23]. In addition, the heavier Ir^{III} centers may also

help to improve the emission efficiency by promoting the intersystem crossing (ISC) from singlet state to triplet state charge transfer rather than Rh^{III} centers [40,41].

The room temperature emission was observed under the excitation at 395 and 370 nm for **4Eu** and **4Tb**, respectively. Their emission spectra revealed the characteristic *f-f* transitions of **4Eu** (⁵D₀→⁷F_J, J = 1 – 4), **4Tb** (⁵D₄→⁷F_J, J = 6 – 3) with calculated quantum yields of 0.22 and 0.21% for **4Eu** and **4Tb**, respectively (Fig. 4.15a and 4.15b). At 77 K, the broad emission band from the metalloligand [L^{Ir}]⁶⁻ overlapped with the *f-f* emissions of Eu^{III} and Tb^{III} with 3.57 and 3.96 % quantum yield for **4Eu** and **4Tb**, respectively (Fig. 4.15c and 4.15d). To clarify the interaction between both [L^{Ir}]⁶⁻ and Ln^{III}, the diffused reflectance spectra of **4Eu** and **4Tb** compared with K₆[L^{Ir}].48H₂O were investigated. The broad absorption band tails covering 200 to 400 nm with a maximum peak at 240 nm were observed (Fig. 4.16), indicating the absorption band of K₆[L^{Ir}].48H₂O, *i.e.* charge transfer and *d-d* transition in Ir^{III} centers. The similar profiles of **4Eu** and **4Tb** were confirmed with a slightly red shifting of the maximum peak from 240 to 250 nm, which contributed to the changes in rigidity due to coordinating to Ln^{III} centers. These adsorptions only slightly overlapped with the excitation and emission spectra of **4Eu** and **4Tb**, resulting in the independent emission of both emissions of [L^{Ir}]⁶⁻ metalloligand and *f-f* emissions of Eu^{III} and Tb^{III} in **4Eu** and **4Tb**. In other words, the energy transfer from the metalloligand to Ln^{III} is negligible. However, to further enhance the photoluminescent properties of **4Eu** and **4Tb**, the modified coordination sphere on Ln^{III} centers for introducing other antenna ligands should be proposed. Compared to the previous system of [L^{Rh}]⁶⁻ metalloligand, *i.e.* **5Eu** and **6Tb**, the characteristic *f-f* emissions could not be allowed due to the overlapping between its adsorption processing peaks at *ca.* 324 and 370 nm (Fig. 4.14) and excitation wavelength of *f-f* emissions Eu^{III} (λ_{ex} 395 nm) and Tb^{III} (λ_{ex} 370 nm). Thus, insufficient excitation to Ln^{III} centers had occurred for **5Eu** and **6Tb**. Whereas, the [L^{Ir}]⁶⁻ metalloligand showed negligible absorption at those wavelengths. Therefore, the characteristic *f-f* emissions of Eu^{III} and Tb^{III} in [L^{Ir}]⁶⁻ metalloligand could be enhanced.

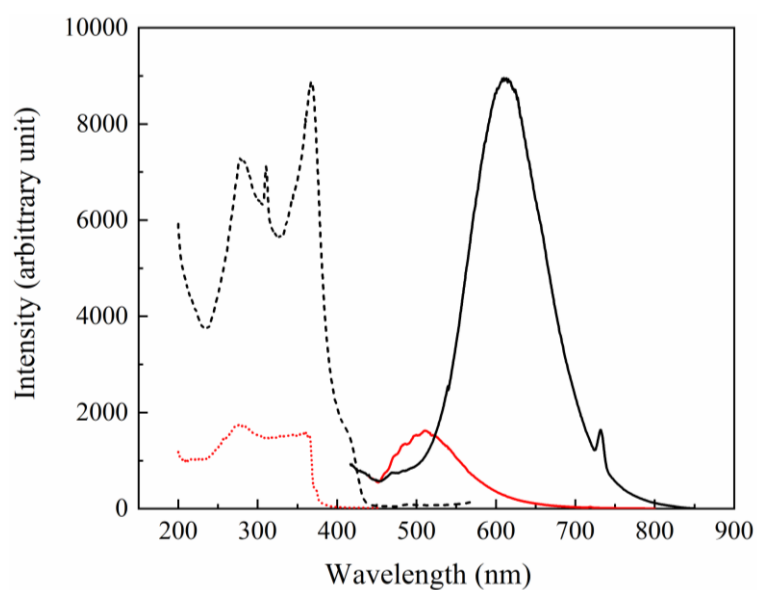


Fig. 4.13 Excitation (λ_{em} 620 nm; black dot line) and emission (λ_{ex} 370 nm) (black solid line) spectra of $K_6[L^{Ir}] \cdot 48H_2O$ at 77 K compared to the excitation (λ_{em} 515 nm; red dot line) and emission (λ_{ex} 360 nm; red dot line) spectra of ZnO.

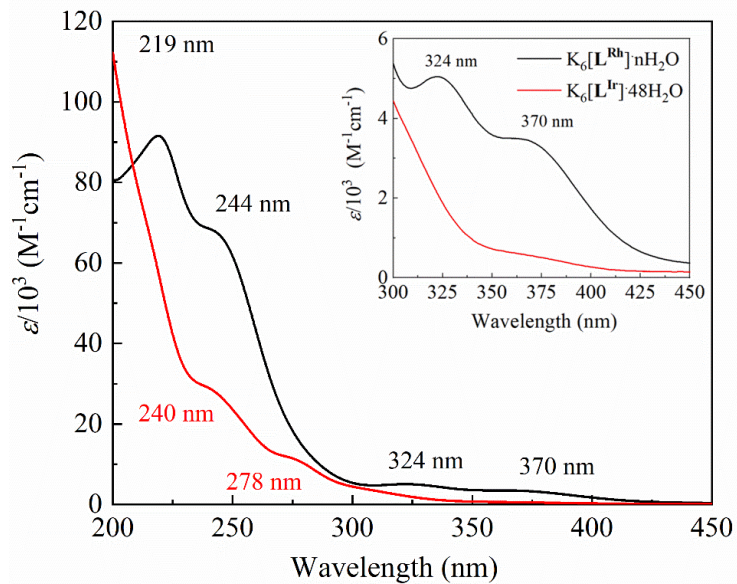


Fig. 4.14 Absorption spectra in water of $K_6[L^{Rh}] \cdot nH_2O$ (black line) and $K_6[L^{Ir}] \cdot 48H_2O$ (red line).

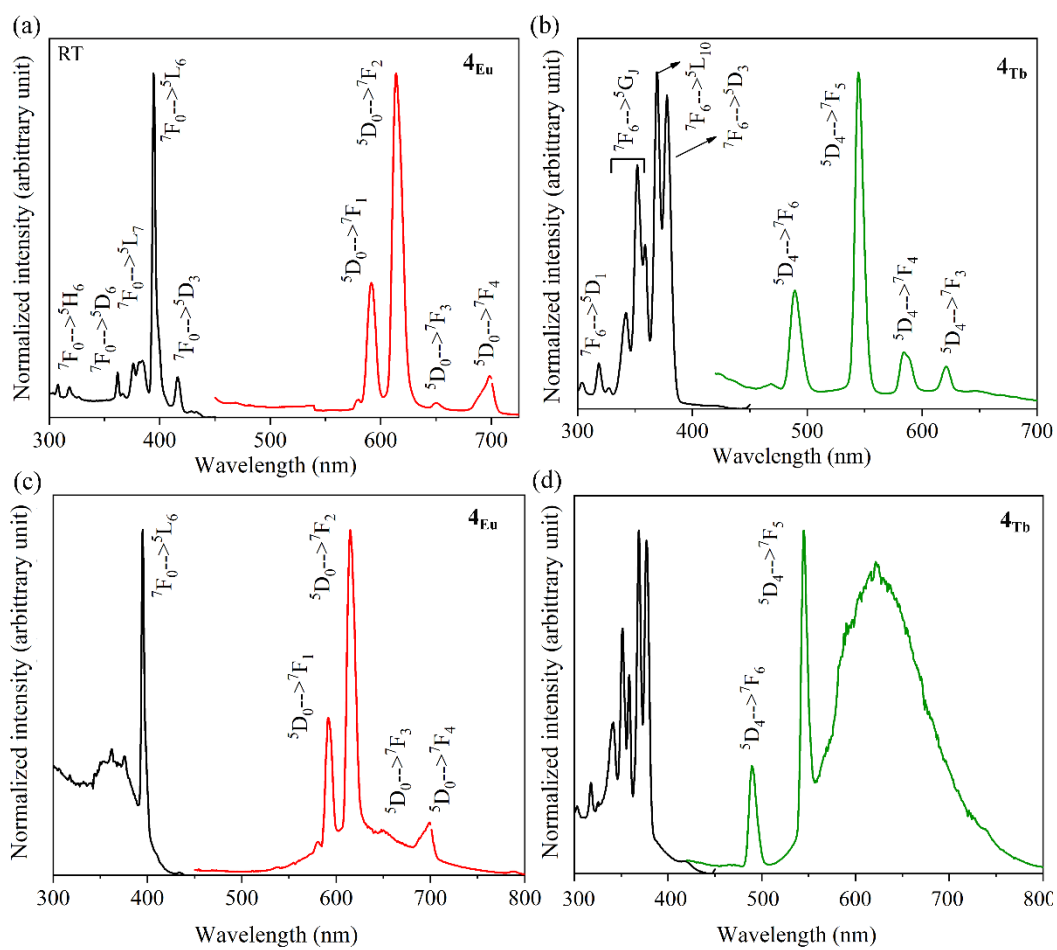


Fig. 4.15 Solid-state excitation (black line) and emission spectra of (a) 4Eu at room temperature, (b) 4Tb at room temperature, (c) 4Eu at 77 K, and (d) 4Tb at 77 K.

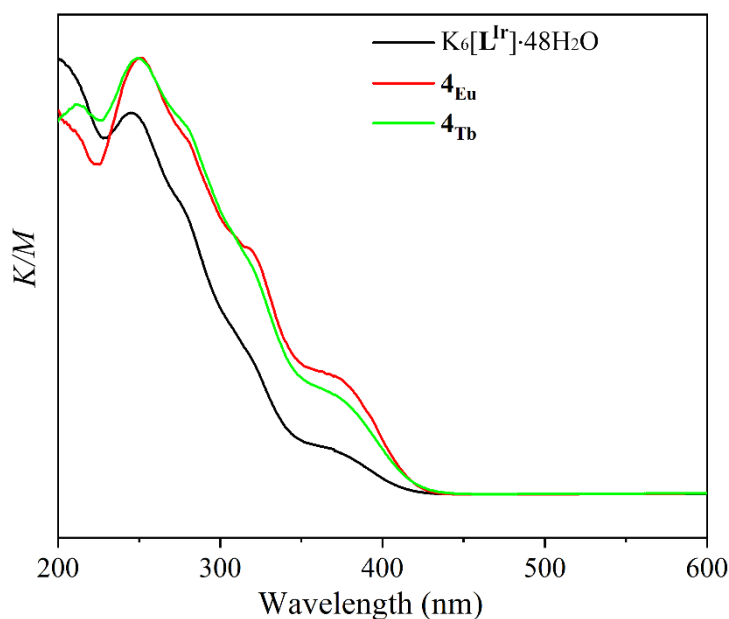


Fig. 4.16 Diffused reflectance spectra of $K_6[L^{III}] \cdot 48H_2O$ (black line), 4_{Eu} (solid red), and 4_{Tb} (solid green).

4.3.5 Magnetic properties of 3_{Ln} and 4_{Ln}

The temperature-dependent magnetic susceptibilities of 3_{Ln} and 4_{Ln} complexes were performed in the temperature range 2 – 300 K at 1000 Oe applied magnetic field. As shown in Fig. 4.17, the $\chi_m T$ values at 300 K of 3_{Ln} were 1.49 (3_{Ce}), 3.49 (3_{Pr}), and 4.00 (3_{Nd}) $cm^3 K \cdot mol^{-1}$ consisting of the expected values as 1.60, 3.20, and 3.28 $cm^3 K \cdot mol^{-1}$ [35], respectively. A similar fashion of 4_{Ln} was also observed. At 300 K, the $\chi_m T$ values were 1.05, 32.30, 42.10, 53.50, 53.60, 43.50, 24.30, and 9.63 $cm^3 K \cdot mol^{-1}$ for 4_{Sm} , 4_{Gd} , 4_{Tb} , 4_{Dy} , 4_{Ho} , 4_{Er} , 4_{Tm} , and 4_{Yb} , respectively. To study the interaction between each Ln^{III} in the cubane clusters, the typical $\chi_m T$ profiles and calculated $\chi_m T$ values from isolated Ln^{III} ions were considered. The calculated $\chi_m T$ values of those 4_{Ln} with isolated ions are following, *i.e.* 0.39 (Sm^{III}), 34.12 (Gd^{III}), 51.18 (Tb^{III}), 61.36 (Dy^{III}), 60.92 (Ho^{III}), 49.71 (Er^{III}), 30.96 (Tm^{III}), and 11.13 (Yb^{III}) $cm^3 K \cdot mol^{-1}$. As the result of these considerations, the interaction between each Ln^{III} center in the cubane clusters was found to be therefore almost silent, probably due to the cubic arrangement of the Ln^{III} ions. The absence of magnetic

interactions among the Ln^{III} centers is beneficial to the future application for the magnetic cooling materials.

As an exception, the magnetic properties of 4_{Sm} largely differ from the prediction. These contributions to the very low spin-orbit coupling make the lower gap between the ground state and the excited state, which allowed the thermal accessibility to other low-lying paramagnetic levels with higher magnetic moment than the ⁶H_{5/2} ground state, *e.g.* ⁶H_{7/2} state [35].

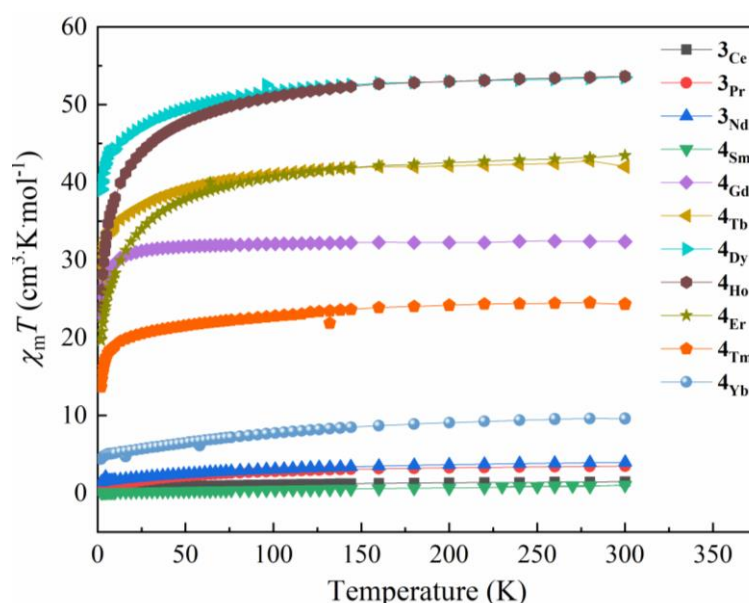


Fig. 4.17 The $\chi_m T$ vs T plots for 3_{Ln} and 4_{Ln}.

4.4 Conclusions

In this chapter, fine-tuning of the crystal porosity of the metallosupramolecular framework of K₆[L^M] \cdot nH₂O was achieved through the metal substitution of the metalloligand from Rh^{III} to Ir^{III}. By using the heavier Ir^{III} center, the Ir^{III}—N bonds were more stabilized rather than Rh^{III}—N bonds, leading to the longer N—H \cdots O_{COO} hydrogen bonding in K₆[L^{Ir}] \cdot 48H₂O. The enlarged pore size of 6.0 \times 12.2 Å² with larger porosity of 53% was achieved in K₆[L^{Ir}] \cdot 48H₂O. The extension of the space resulted in the expansion of the available space for the lanthanide cubane clusters formation. As a result,

a series of clusters $[\text{Ln}_4(\mu_3\text{-OH})_4(\mu_2\text{-OAc})_3(\text{H}_2\text{O})_7]^{5+}$ in $[\text{L}^{\text{Ir}}]^{6-}$ framework was obtained after the border between Nd^{III} and Sm^{III} ions, whilst the cubane formation in $[\text{L}^{\text{Rh}}]^{6-}$ framework could be synthesized after the border between Eu^{III} and Gd^{III} [22]. In the conventional approach, *i.e.* ligand-controlled hydrolysis, the creation of the lanthanide-hydroxide cubane clusters are achieved by (i) reducing the number of coordinating water or solvent on Ln^{III} coordination sphere by occupying organic ligands and (ii) controlling pH by using suitable ligands such as amino acids. On the other hand, in our system, the control of the cubane cluster formation was readily achieved through the tuning porosity by replacing only M^{III} centers of $\text{K}_6[\text{L}^{\text{M}}]\cdot n\text{H}_2\text{O}$ metalloligand. This concept is exceptionally beneficial for further design and synthesis of the lanthanide hydroxide clusters in other platforms.

Furthermore, the Ir^{III} could improve the photoluminescent properties by avoiding the quenching effect due to the *d-d* transition. The photoluminescence of $\mathbf{4}_{\text{Eu}}$ and $\mathbf{4}_{\text{Tb}}$ was also enhanced. For the development of photoluminescent properties of $\mathbf{4}_{\text{Eu}}$ and $\mathbf{4}_{\text{Tb}}$, the modified coordination sphere of Ln^{III} would be a potential approach for further work. The magnetic properties of $\mathbf{3}_{\text{Ln}}$ and $\mathbf{4}_{\text{Ln}}$ indicated almost silent interaction between Ln^{III} ions in the cubane structures, which would be significantly essential for the magnetic cooling application.

4.5 References

- [1] Xue, D.-X.; Cairns, A. J.; Belmabkhout, Y.; Wojtas, L.; Liu, Y.; Alkordi, M. H.; Eddaoudi, M. *J. Am. Chem. Soc.* **2013**, *135*, 7660–7667.
- [2] Yoshinari, N.; Konno, T. *Coord. Chem. Rev.* **2023**, *474*, 214850.
- [3] Woodruff, D. N.; Winpenny, R. E.; Layfield, R. A. *Chem. Rev.* **2013**, *113*, 5110–5148.
- [4] Brunet, G.; Hamwi, M.; Lemes, M. A.; Gabidullin, B.; Murugesu, M. *Commun. Chem.* **2018**, *1*, 88.

- [5] Qin, L.; Yu, Y.-Z.; Liao, P.-Q.; Xue, W.; Zheng, Z.; Chen, X.-M.; Zheng, Y.-Z. *Adv. Mater.* **2016**, *28*, 10772–10779.
- [6] Zheng, Z. *Chem. Commun.* **2001**, 2521–2529.
- [7] Litvinova, Y. M.; Gayfulin, Y.M.; Leusen, J. V.; Samsonenko, D. G.; Lazarenko, V. A.; Zubavichus, Y. V.; Kögerler, P.; Mironov, Y. V. *Inorg. Chem. Front.* **2019**, *6*, 1518–1526.
- [8] Wong, H. Y.; Chan, W. T. K.; Law, G. L. *Inorg. Chem.* **2018**, *57*, 6893–6902.
- [9] Zheng, X. Y.; Xie, J.; Kong, X. J.; Long, L. S.; Zheng, L. S. *Coord. Chem. Rev.* **2019**, *378*, 222–236.
- [10] Singh-Wilmot, M. A.; Kahwa, I. A.; White, A. J. P.; Williams, D. J.; Lough, A. J. *Polyhedron* **2010**, *29*, 270–279.
- [11] Zhang, H.-Y.; Yu, H.-J.; Xu, H.-X.; Ren, J.-S.; Qu, X.-G. *Polyhedron* **2007**, *26*, 5250–5256.
- [12] Ma, B.-Q.; Zhang, D.-S.; Gao, S.; Jin, T.-Z.; Yan, C.-H. *New J. Chem.* **2000**, *24*, 251–252.
- [13] Wang, R.; Liu, H.; Carducci, M. D.; Jin, T.; Zheng, C.; Zheng, Z. *Inorg. Chem.* **2001**, *40*, 2743–2750.
- [14] Das, S.; Dey, A.; Biswas, S.; Colacio, E.; Chandrasekhar, V. *Inorg. Chem.* **2014**, *53*, 3417–3426.
- [15] Schuetz, S. A.; Day, V. W.; Clark, J. L.; Belot, J. A. *Inorg. Chem. Commun.* **2002**, *5*, 706–710.
- [16] Kong, X.-J.; Long, L.-S.; Zheng, L.-S.; Wang, R.; Zheng, Z. *Inorg. Chem.* **2009**, *48*, 3268–3273.
- [17] Savard, D.; Lin, P.-H.; Burchell, T. J.; Korobkov, I.; Wernsdorfer, W.; Clérac, R.; Murugesu, M. *Inorg. Chem.* **2009**, *48*, 11748–11754.

- [18] Wu, H.; Zhang, S.; Li, M.; Qiao, C.; Sun, L.; Wei, Q.; Xie, G.; Chen, S.; Gao, S. *ChemistrySelect* **2016**, *1*, 3335–3342.
- [19] Wang, L.; Yang, W.; Yi, F.-Y.; Wang, H.; Xie, Z.; Tang, J.; Sun, Z.-M. *Chem. Commun.* **2013**, *49*, 7911–7913.
- [20] Kajiwaru, T.; Katagiri, K.; Hasegawa, M.; Ishii, A.; Ferbinteanu, M.; Takaishi, S.; Ito, T.; Yamashita, M.; Iki, N. *Inorg. Chem.* **2006**, *45*, 4880–4882.
- [21] Ivashenko, O.; Perepichka, D. F. *Chem. Soc. Rev.* **2011**, *40*, 191–206,
- [22] Yoshinari, N.; Meundaeng, N.; Tabe, H.; Yamada, Y.; Yamashita, S.; Nakazawa, Y.; Konno, T. *Angew. Chem. Int. Ed.* **2020**, *59*, 18048–18053.
- [23] Goo, Z. L.; Minami, K.; Yoshinari, N.; Konno, T. *Chem Asian J.* **2021**, *16*, 2641–2647.
- [24] Konno, T.; Nakamura, K.; Okamoto, K.-I.; Hidaka, J. *Bull. Chem. Soc. Jpn.* **1993**, *66*, 2582–2589.
- [25] CrysAlisPRO software system (ver.71.39.46); Rigaku Corporation: Oxford, U. K., **2018**.
- [26] Sheldrick, G. M. SADABS; University of Göttingen: Göttingen, Germany, **1996**.
- [27] Spek, A. L. *Acta Cryst.* **2015**, *C71*, 9–18.
- [28] Sheldrick, G. M. *Acta Cryst.* **2008**, *A64*, 112–122.
- [29] Sheldrick, G. M. *Acta Cryst.* **2015**, *C71*, 3–8.
- [30] Dolomanov, O. V.; Bourhis, L. J.; Gildea, R. J.; Howard, J. A. K.; Puschmann, H. *J. J. Appl. Cryst.* **2009**, *42*, 339–341.
- [31] Yoshinari, N.; Yamashita, S.; Fukuda, Y.; Nakazawa, Y.; Konno, T. *Chem. Sci.* **2019**, *10*, 587–593.
- [32] Gyton, M. R.; Leforestier, B.; Chaplin, A. B. *Organometallics* **2018**, *37*, 3963–3971.

- [33] Yamanari, K.; Ito, R.; Yamamoto, S.; Konno, T.; Fuyuhiko, A.; Fujioka, K.; Arakawa, R. *Inorg. Chem.* **2002**, *41*, 6824–6830.
- [34] Groom, C. R.; Bruno, I. J.; Lightfoot, M. P.; Ward, S. C. IUCr. The Cambridge Structural Database, *Acta Cryst.* **2016**, *B72*, 171–179.
- [35] Cotton, S. Lanthanide and Actinide Chemistry, Wiley, Chichester, **2006**.
- [36] Zhang, H. F.; Tao, Z.; Xu, W. G.; Lu, S. X.; Yuan, F. *Comp. Mater. Sci.* **2012**, *58*, 119–124.
- [37] Wawrzyńczyk, D.; Cichy, B.; Stęk, W.; Nyk, M. *Dalton Trans.* **2018**, *47*, 8320–8329.
- [38] Sandmann, A.; Kompch, A.; Mackert, V.; Liebscher, C. H.; Winterer, M. *Langmuir* **2015**, *31*, 5701–5711.
- [39] Ren, T.-B.; Xu, W.; Zhang, W.; Zhang, X.-X.; Wang, Z.-Y.; Xiang, Z.; Yuan, L.; Zhang, X.-B. *J. Am. Chem. Soc.* **2018**, *140*, 7716–7722.
- [40] Forster, L. S. *Coord. Chem. Rev.* **2006**, *250*, 2023–2033.
- [41] Housecroft, C. E.; Sharpe, A. G. Inorganic Chemistry, 3rd Edition, Prentice Hall, **2007**.

CHAPTER 5

Concluding Remarks

In this research, several porous lanthanide coordination polymers (LnCPs) with enhanced solid-state functionalities were newly synthesized through the structural modifications of conventional ligand systems as shown in Fig. 5.1: (i) the introduction of auxiliary poa^- ligand to disrupt dense framework (Chapter 2), (ii) the insertion $-\text{NO}_2$ groups on the lengthy BPDC^{2-} ligand to enlarge the porosity (Chapter 3), and (iii) the replacement of Rh^{III} centers by Ir^{III} ion in $[\text{Zn}_4\text{O}\{\text{Rh}(\text{L-cys})_3\}_4]^{6-}$ ($[\mathbf{L}^{\text{Rh}}]^{6-}$) metalloligands to control the void through the modified hydrogen bonding interactions (Chapter 4). These ligands are different in their rigidity, length, the number of coordinating groups, and functional groups providing different pore sizes, dimensions of the framework structures, and different functionalities of LnCPs. The plausible applications of the resulting LnCPs were also explored.

In chapter 2, the combination of two ligands, dicarboxylate $2,5\text{-pydc}^{2-}$ and monocarboxylate poa^- was proposed to synthesize microporous LnCPs. Under the appropriate synthesis condition, a new series of robust porous LnCPs $[\text{Ln}(\text{poa})(2,5\text{-pydc})(\text{H}_2\text{O})_2]\cdot 3\text{H}_2\text{O}$ ($\mathbf{1}_{\text{Ln}}$; $\text{Ln} = \text{Eu}^{\text{III}}$, Gd^{III} , Tb^{III} , and Sm^{III}) were obtained. In the crystal structure, the one-dimensional coordination polymer structure of $\mathbf{1}_{\text{Ln}}$ was further assembled into three-dimensional supramolecular structures *via* hydrogen bonding and π - π interactions. The supramolecular structure provided the one-dimensional channel with an effective opening size of $4.2 \times 5.5 \text{ \AA}^2$. It should be mentioned that the opening channels in $\mathbf{1}_{\text{Ln}}$ are quite larger than those of our previous LnCPs having only $2,5\text{-pydc}^{2-}$ ligand, *i.e.* $[\text{Ln}_{1.375}(\text{pydc})_2(\text{H}_2\text{O})_4]$ ($\text{Ln} = \text{Sm}^{\text{III}}$, Eu^{III} , Gd^{III} , Tb^{III} , Dy^{III} , Ho^{III} , and Er^{III}), which are non-porous. This result indicated that the poa^- ligand act as a fulfilled ligand in coordination with Ln^{III} centers, which expanded the pore space in the framework. Motivated by specific pore size, it is suitable to act as a molecular sieve for ammonia. The decorated channel by the functional groups of the ligand, *i.e.* phenyl and free O atom

from poa^- as well as O atoms from the carboxylate groups on $2,5\text{-pydc}^{2-}$ was also indicated as possible interaction sites for ammonia adsorption. Encouraged by the excellent photoluminescent properties of these complexes, which are enhanced by effective sensitization of those ligands to Ln^{III} , and high selective interaction with ammonia, the sensing application was investigated. For further practical use, the fabricating film of $1\text{Eu}/\text{PVA}$ was then established. The ammonia sensing of $1\text{Eu}/\text{PVA}$ showed a working range of 0.50 – 10.0 ppm with an excellent sensitivity of $4.04\% \cdot \text{ppm}^{-1}$ and a detection limit of 0.14 ppm. The accuracy and precision of this sensing manifested through the percentage recoveries of 103 – 111% and %RSD of 1.5 – 8.2%. The proposed interacting sites were supported by the DFT calculation and spectroscopic data. The reusable $1\text{Eu}/\text{PVA}$ film for ammonia sensing could be achieved in at least ten cycles with 95 – 97% repeatability.

In chapter 3, the use of a longer divergent dicarboxylate ligand *di*-nitro-BPDC²⁻ was adopted to achieve the nanoporous LnCPs with expanded pore size. As a result, a new series of $[\text{Ln}_4(\textit{di}\text{-nitro-BPDC})_4(\text{NO}_2)_3(\text{OH})(\text{H}_2\text{O})_5] \cdot (\text{solvent})_n$ (2Ln ; Ln = Pr^{III}, Nd^{III}, Sm^{III}, Eu^{III}, and Gd^{III}) were successfully synthesized and characterized. The three-dimensional frameworks with the effective one-dimensional window opening size of $2.0 \times 1.1 \text{ nm}^2$ to $1.5 \times 1.1 \text{ nm}^2$ were observed. The channel surface was decorated by NO₂ groups. In previous LnCPs with non-functionalized BPDC²⁻, e.g. $[\text{Tb}(\text{BPDC})_2] \cdot (\text{CH}_3)_2\text{NH}_2$, the pore size was small (*ca.* $5.6 \times 8.3 \text{ \AA}^2$). The small opening channels and low porosity in $[\text{Tb}(\text{BPDC})_2] \cdot (\text{CH}_3)_2\text{NH}_2$ might be due to the crowded environment around Ln^{III} center. On the other hand, in this system the introduction of electron-rich –NO₂ functional groups on the *di*-nitro-BPDC²⁻ ligand, prevented the crowned coordination sphere around Ln^{III} centers through the electronic repulsion, resulting in the large pore size. Prompted by their large porosity and available –NO₂ groups along the channel, several potential functionalities were surveyed, proton conductions, temperature and humidity sensing, CO₂ gas adsorption and selectivity, and catalytic properties. On the proton conductivities results, 2Ga exhibited a maximum value of $6.17 \times 10^{-2} \text{ S} \cdot \text{cm}^{-1}$ (1 V applied voltage, 55 °C, and 99 RH%), which could be accounted for a superprotonic conducting material. The compound 2Ga was also applicable as the humidity and temperature sensor with a working range of 55 – 99 RH%

at 25 °C and 25 – 40 °C at 99 RH%, respectively. The reusable abilities of **2_{Gd}** for both humidity and temperature sensing manifested through the repeatability of 97% with the standard deviations of 1 RH% and 0.42 °C. Moreover, these complexes showed excellent selectivity with CO₂ over other gases (N₂, O₂, and H₂). This exceptional selectivity could be encouraged for further catalytic activities with CO₂. In this work, the CO₂ cycloaddition reaction with epoxides was selected as a model reaction to study the catalytic performance of these complexes. The excellent performances with high selectivity under ambient CO₂ pressure and 80 °C manifested through the maximum TON of 1,106 and TOF of 276 h⁻¹ for **2_{Eu}**. The effect of lanthanide contraction was also investigated providing the increased performance with the gradual diminishing in ionic radii from Pr^{III} to Gd^{III}. Due to the high disordering in the framework, DFT calculation was performed on the evaluation of the possible catalytic sites, which suggested the effective catalytic sites at larger available space around Ln^{III} centers. These would be very helpful for the further development of a catalyst for this reaction.

In chapter 4, the tuning of the porosity in the supramolecular frameworks based on multicarboxylate metalloligands K₆[L^{Rh}]_nH₂O was examined. The use of a heavier Ir^{III} instead of Rh^{III} led to the highly stabilized Ir^{III}—N bonds resulting in the weaker interaction of N—H···O_{COO} hydrogen bonding in the [L^{Ir}]⁶⁻ framework. The metal substitution caused the enhancement of the porosity from 46% to 53% and the pore size from 4.7 × 11.5 Å² to 6.0 × 12.2 Å². As in the case of K₆[L^{Rh}]_nH₂O, lanthanide cubane clusters were grown inside the crystal lattice of K₆[L^{Ir}]_nH₂O, leading to a series of LnCPs with the lanthanide hydroxide cubane clusters, Ln_{0.33}[Ln₄(μ₃-OH)₄(μ₂-OAc)₃(H₂O)₇][L^{Ir}]_nH₂O (**4_{Ln}**, [L^{Ir}]⁶⁻ = [Zn₄O{Ir(L-cys)₃}₄]⁶⁻, Ln = Sm^{III} to Lu^{III}, and Y^{III}). However, due to the improvement of the porosity in the [L^{Ir}]⁶⁻ framework, the border of the cubane clusters installation had been successfully modified from Eu^{III}/Gd^{III} to Nd^{III}/Sm^{III}. By replacing the metal centers from Rh^{III} to Ir^{III}, the photoluminescence properties of this class of LnCPs could also be improved.

To sum up the present study, three practical approaches for the design and fabrication of porous LnCPs were proposed. First, the use of divergent dicarboxylate ligands could provide a high dimensionality of the framework. While introducing a small

molecule to fulfill the coordination requirement of Ln^{III} centers could avoid the formation of dense frameworks. Second, the pore size could enlarge by using the longer ligands and functionalized ligands with steric groups of electron-rich moieties, which could also disrupt dense frameworks. Third, the use of multicarboxylate metalloligands could provide exceptional possibilities to control the hydrogen-bonded framework by the metal substitution in the metalloligands.

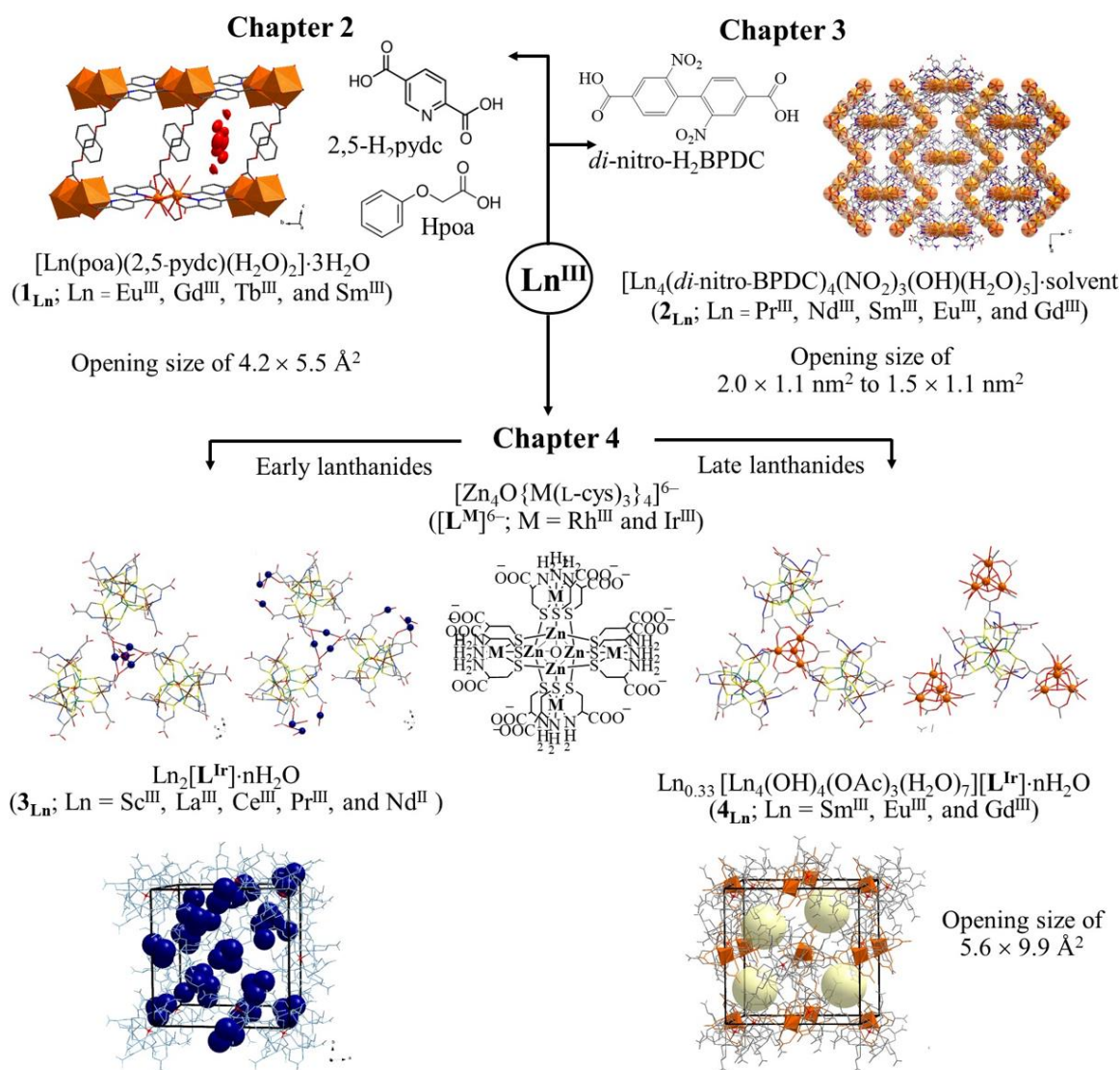


Fig. 5.1 Diagrams summarizing all reported LnCPs in this thesis.

CURRICULUM VITAE

Name	Ms. Supaphorn Thammakan
Date of Birth	7 th November 1994
Education	<p>2023 Doctor of Philosophy in Chemistry (Double Degree Program), Department of Chemistry, Faculty of Science, Chiang Mai University, Chiang Mai, Thailand and Department of Chemistry, Graduate School of Science, Osaka University, Osaka, Japan</p> <p>2019 M.S (Chemistry Major), Department of Chemistry, Faculty of Science, Chiang Mai University, Thailand</p> <p>2016 B.S. (Chemistry Major, 1st class honor), Department of Chemistry, Faculty of Science, Chiang Mai University, Thailand</p>
Scholarship	<p>2016 The Human Resource Development in Science Project (Science to Achievement Scholarship of Thailand, SAST), supported by</p> <p>2022 the Office of Higher Education Commission, Ministry of Education, Thailand</p> <p>2019 International Summer Program: a short term research at Osaka University, Japan, financial support by The Japan Student Service Organization (JASSO) Scholarship</p> <p>2017 International Internship Program (IIP): a short term research at Academia Sinica, Taipei, Taiwan, financial support by Taiwan International Graduate Program (TIGP) Scholarship</p> <p>2015 Research funding from Department of Chemistry, Faculty of Science, Chiang Mai</p> <p>2014 A short term research at Chiang Mai University, Thailand, financial support by The Human Resource Development in</p>

Science Project (Science Achievement Scholarship of Thailand, SAST), supported by the Office of Higher Education Commission, Ministry of Education, Thailand

Publication Thammakan, S.; Sinchow, M.; Chiangraeng, N.; Yoshinari, N.; Konno, T.; Ngamjarrojana, A.; Nimmanpipug, P.; Rujiwatra, A. Robust and Reusable Film of New Lanthanide Coordination Polymers for Room-Temperature Ammonia Gas Sensing. *Sens. Actuators B Chem.* **2023** (In Press)

Chuasaard, T.; Thammakan, S.; Semakul, N.; Konno, T.; Rujiwatra, A. Structure and Photoluminescence of Two-Dimensional Lanthanide Coordination Polymers of Mixed Phthalate and Azobenzene Dicarboxylate. *J. Mol. Struct.* **2022**, *1251*, 131940.

Thammakan, S.; Kuwamura, N.; Chiangraeng, N.; Nimmanpipug, P.; Konno, T.; Rujiwatra, A. Highly Disordering Nanoporous Frameworks of Lanthanide-Dicarboxylates for Catalysis of CO₂ Cycloaddition with Epoxides. *J. Solid State Chem.* **2021**, *303*, 122464.

Thammakan, S.; Rodlamul, P.; Semakul, N.; Yoshinari, N.; Konno, T.; Ngamjarrojana, A.; Rujiwatra, A. Gas Adsorption, Proton Conductivity, and Sensing Potential of a Nanoporous Gadolinium Coordination Framework. **2020**, *59*, 3053–3061.

Thammakan, S.; Panyarat, K.; Rujiwatra, A. Organically Pillared Layer Framework of [Eu(NH₂-BDC)(ox)(H₃O)]. *Acta Cryst.* **2019**, *E75*, 1833–1838.

Panyarat, K.; Thammakan, S.; Ngamjarrojana, A.; Rujiwatra, A. Ratiometric Luminescence Behavior of Lanthanide-Mixed Benzenedicarboxylates Frameworks, *Mater. Lett.* **2018**, *213*, 166-169.

- Experience
- 2018 Sakura Science Exchange Program, Osaka, Japan
 - 2017 The 5th ASEAN Synchrotron Science Camp, held by Synchrotron light research institute (public organization)
 - 2016 Student trainee at Osoth Inter Laboratories Company Limited, Sahapat Group, Thailand
Single Crystal X-ray Diffraction Workshop, at Vidyasirimedhi Institute of Science and Technology (VISTEC), Rayong, Thailand
- Conferences
- 2022 Poster presentation “Post-Synthetic Installation of $\text{Ln}_4(\text{OH})_4$ Cubanes into Ionic Crystals of an Ir_4Zn_4 Complex Anion”, The 4th International Symposium of Ionic Coordination Compounds (ISICC-4) on December 2022, Osaka, Japan
Poster presentation “Highly Disordering Nanoporous Frameworks of Lanthanide-Dicarboxylates for Catalysis of CO_2 Cycloaddition with Epoxides”, 8th Asian Conference on Coordination Chemistry on August 2022, Taipei, Taiwan
 - 2020 Best poster presentation award “Organically Pillared Layer Framework of $[\text{Eu}(\text{NH}_2\text{-BDC})(\text{ox})(\text{H}_3\text{O})]^\text{n}$ ”, Pure and Applied Chemistry International Conference (PACCON 2020) on February 2020 at Bangkok, Thailand.

Oral presentation “Proton Conductivity-based Temperature and Humidity Sensing by Nanoporous Gadolinium Coordination Polymers”, The 21st International Union of Materials Research Societies-International Conference in Asia (IUMRS-ICA-2020) on February 2020 at Chiang Mai, Thailand
 - 2019 Poster presentation “Toward Nanoporous Lanthanide Metal-Organic Frameworks”, The 3rd Thailand-Korea mini symposium on integrated materials research on January, 2019, Chiang Mai, Thailand

- 2018 Oral presentation “Crystal Structures and Temperature-Dependent Photoluminescence of $[\text{Ln}(\text{L})_{0.5}(\text{NO}_2\text{-BDC})\text{H}_2\text{O}]\cdot 3\text{H}_2\text{O}$ ”, 2nd South East Asian Conference on Crystal Engineering (SEACCE-2) on August 2018, Sunway University, Malaysia
- 2017 Oral presentation “Synthesis, characterization and photoluminescence of new lanthanide organic framework; $[\text{Eu}(\text{NO}_2\text{-BDC})_{0.37}(\text{BDC})_{0.63}(\text{ox})_{0.5}(\text{H}_2\text{O})_2]$ ”, on April 2017, Chiang Mai, Thailand
- 2017 Poster presentation “Single Crystal Structure and Topology of $[\text{Eu}(\text{C}_8\text{H}_3\text{NO}_6)_{0.25}(\text{C}_8\text{H}_4\text{O}_4)_{0.75}(\text{C}_2\text{O}_4)_{0.5}(\text{H}_2\text{O})_2]$ ”, Pure and Applied Chemistry International Conference (PACCON 2017) on February 2017, Bangkok, Thailand.
- 2015 Oral presentation “Development of Digital Image Calorimetric Technique for Determination of Silver (I) Ion Using Caffeic Acid as Color Developing Agent”, Scholarship Student Conference on November 2015, Chiang Mai, Thailand.